Interface Layer Design and Analysis for Small Molecule Organic Solar Cells



Hanyang Ye
St Hugh's College
University of Oxford

A thesis submitted for the degree of
Doctor of Philosophy

Michaelmas 2019

This thesis is dedicated to

my grandmother Mrs Yuemei Wang

for her endless love.

Acknowledgements

As I recall all the memories through my entire DPhil studies, I find it a thrilling journey which finishes faster than my wildest expectation. When writing this thesis to summarize my work undertaken during my DPhil, I remember many amazing people who have helped me all along the way.

I would love to thank my supervisor, Dr Moritz Riede, for all the encouragement, patience, understanding, and guidance he offered me during these years. I will never be lucky enough to finish my DPhil studies without his sincere help. I would like to show my gratitude to my beloved parents and families, especially my consin Mengjia Wang. It is their support that helps me go through some difficult time during my DPhil studies.

In my DPhil study, my colleagues in my research group provide me with the most help, either in research or in life. I would love to thank Sameer Kesava, Josue Hardigree, Giulio Mazzotta, Ivan Ramirez, Ross Warren, Grey Christoforo, Alberto Privitera, Pascal Kaienburg, Andreas Lauritzen, Anna Jungbluth, Irfan Habib, and Bernd Sturdza for their fruitful discussions. I also would love to send my regards to my collaborators: Roisin Brown and Prof. Peter Skabara for their help. I am very grateful to have great advisors who sit nearby. I thank Jian Huang, Alexandra Ramadan, Bernard Wenger, Nobuya Sakai, Pabitra Nayak, Yasser Hassan, Zhiping Wang, Sai Bai, Rebecca Sutton, and Rick Hamilton for their sincere guidance. I would love to thank Alice Smith, Bingjun Wang, Florian Le Roux, Nikol Lambeva, Markus Dollmann, Adam Wright, Qiushi

Xia, Hao Ye, Suer Zhou, Yun Xiao and Chen Sun for a relaxed work environment.

During my DPhil studies, many lovely people came into my life, and they shared with me advice, care, and encouragement. I would love to thank Lianbo Li, Huan Qi, Zixuan Wang, Rong Hao, Guolong Wang, Xi Liu, Chunying Zhang, Yuxuan Zhai, Jiexin Li, Yiran Zhou, Yanru Zhou, Mufan Zheng, Ye Ma, Libei Wu, Zheng Wang, Zonghao Sheng, Weijie Chen, Shuxiang Cao, Rubi Wu, Xingliang Fang, and Shijie Zhan for all their support. I would like to thank Juliane Borchert, Timothy Davis, Fiona Money, Diwakar Kishore, Behnam Najafi, Clare Dobson, Maie Khalil, Rhory Ashworth, Ágota Márton, and Marwan Mohammed for their accompany. I also thank Linwei Li, Yiwei Li, Honghao Fang, Yutian Wen, Peimei Da, Jingyuan Liu, Yuzhou Sun, Guowei Tao, Kuan Yang, Xuanyi Sheng, and Xian Guan for all the great memories in Oxford.

My studies of the DPhil programme in Oxford also involves the practice of self-development. In particular, I own my gratitude to Dr Jonathan Brant, Mr Timothy Beardson, Edward Brooks, Wei Wang, Annika Wythes, and Tejas RK Motwani for their guidance towards my life. I also would love to thank my dancing fellows for their embraces. Particularly, I would like to thank Xiaoyu Lu, Nicole Lim, Ronald Li, Aisulu Bakchieva, Hongbae Jeong, Dan Florin Berbec, Sarah Picaflores, Victor Hernandez-Urbina, Ksenia Mus, Ella Saxén, and Benjamin Schuster-Böckler.

I acknowledge the China Scholarship Council, Pacific Alliance Group, and China Oxford Scholarship Fund for their financial support.

Finally, I would love to thank everyone who passed by, cheered me up, and inspired me during my stay in Oxford.

Abstract

Recently, the fast technological development of organic solar cells (OSCs) proves that it has a promising future in the sustainable energy market. Interlayers play a significant role in OSCs, which can enhance device performance and stability. However, many of the fundamental mechanism and design principles of the interlayers have not been adequately studied.

The theoretical chapters of this thesis deliver a summary of the state-of-the-art photovoltaic (PV) technologies and the fundamentals of organic photovoltaics (OPVs). The basic knowledge of interlayers within OSCs is introduced, too.

The methodology chapter introduces the materials used in this thesis. Besides, fundamentals and technical parameters of the methodologies are summarised in this chapter, e.g. X-ray diffraction (XRD), grazing-incidence wide-angle X-ray scattering (GIWAXS), photoluminescence (PL), spectroscopic ellipsometry, external quantum efficiency (EQE), and internal quantum efficiency (IQE).

In the experimental chapters, a new molecule (hexapropyltruxene) is introduced as an interlayer material in small molecule organic solar cells (SMOSCs), and its functions within OSCs are investigated. Firstly, hexapropyltruxene is used as an interlayer in the SubPc/C60 solar cell stack. The experimental results show that hexapropyltruxene works well as an exciton blocking layer (ExBL) between the MoO_x and SubPc layers. By adding

3.8 nm of hexapropyltruxene between MoO_x and SubPc layers, the power conversion efficiency (PCE) of the SubPc/C60 solar cells is enhanced from 2.6 % to 3.0 %, achieving a ca. 15 % improvement. Besides, it is found that hexapropyltruxene has a weak molecular template growth effect on the growth of SubPc thin film. Secondly, the application of hexapropyltruxene as an interlayer in the solar cell stack first demonstrated by interuniversity microelectronics centre (IMEC) is also investigated. The results reveal that hexapropyltruxene has a very weak exciton blocking effect between MoO_x layer and α-6T donor layer. The structural characterization also suggests that hexapropyltruxene can induce the growth of different α-6T polymorphs.

In the final experimental chapter, the polymorphism of α-6T induced by different substrates with hole contact layers (HCLs) is studied. The competing growth of low temperature (LT)-, high temperature (HT)-, and β-phases of α-6T is observed in the thin film growth. The results of the experiments suggest that widely-used HCLs such as MoO_x, PEDOT:PSS, and MeO-TPD have the template growth effect on α-6T molecules. In addition, the substrate temperature in the deposition process is significant in the competing growth of α-6T polymorphs. Corresponding solar cell performances show a correlation with the polymorph composition within α-6T layers and the performances of OSCs. To conclude, less "standing-up" but more "lying-down" molecules lead to better light absorption, which results in better solar cell performance. PEDOT:PSS is the most appropriate HCL for our α-6T/SubPc solar cell stack, and low substrate temperature (20 °C) is more suitable than high temperature (120 °C) in the growth of α-6T thin films for solar cell application.

Contents

List of Figures vi

List of Tables xi

List of Abbreviations xiii

1 Introduction 1

1.1 Problems of the Current Energy System 1

1.2 Current Solar Energy Technology 3

1.3 Next Generation of PVs 6

1.4 Scope and Structure of the Thesis 8

2 Organic Photovoltaics 11

2.1 Basic Principles of Semiconductor: Bands and Fermi Level 11

2.2 Organic Semiconductors 14

2.2.1 Exciton Generation 16

2.2.2 Exciton Transport 16

2.2.3 Marcus Theory and Transition Rates 16

2.2.4 Charge Transport and Gaussian Discorder Model 18

2.2.5 Electron-hole Recombination 19

2.3 Organic Solar Cells 20

2.3.1 Processes in Organic Solar Cells & Charge Transfer (CT) States 20

2.3.2 Structure of Organic Solar Cells 23

2.3.3 Fundamental Principles of Solar Cell Characterization 25

3 Interface Effects Inside Solar Cells 29

3.1 Interlayers in Organic Solar Cells 29

3.2 Electronic Effects 31

3.3 Microstructural Effects 32

3.3.1 Molecular Template Growth (MTG) Effects 32

3.3.2 Substrate-induced Phases (SIPs) 34

3.3.3 Polymorphs of Organic Semiconductors 36

4 Materials and Methods 37

4.1 Materials 38

4.1.1 Hexapropyltruxene 39

4.1.2 Boron Subphthalocyanine Chloride (SubPc) 39

4.1.3 A-sexithiophene (α-6T) 40

4.1.4 Other Materials 41

4.2 Sample Preparation 42

4.2.1 Fabrication Facilities 42

4.2.2 Fabrication Procedure 43

4.3 Material and Thin Film Characterization 44

4.3.1 X-Ray Diffraction 44

4.3.1.1 Fundamentals and Bragg's Law 45

4.3.1.2 Scherrer Equation 47

4.3.1.3 Technical Parameters 48

4.3.2 Grazing-incidence Wide-angle X-ray Scattering (GIWAXS) . . 48

4.3.2.1 Fundamentals of GIWAXS 48

4.3.2.2 GIWAXS Analysis Technique 49

4.3.3 Spectroscopic Ellipsometry 52

4.3.3.1 Fundamentals of Spectroscopic Ellipsometry 52
4.3.3.2 Data Analysis of Spectroscopic Ellipsometry 53
4.3.3.3 Real-time Spectroscopic Ellipsometry (RTSE) 55
4.3.3.4 Technical Parameters 55
4.3.4 Photoluminescence (PL) 56
4.3.4.1 Fundamentals of PL 56
4.3.4.2 Steady-state Photoluminescence (SSPL) 58
4.3.4.3 Time-resolved Photoluminescence (TRPL) 59
4.3.4.4 Technical Parameters 60
4.3.5 Cyclic Voltammetry (CV) 61
4.3.6 Ultraviolet–visible (UV-vis) Spectroscopy 61
4.3.7 Atomic Force Microscopy (AFM) Measurement 63
4.4 Solar Cell Characterization 64
4.4.1 Current-Voltage (JV) Characterization 64
4.4.2 External Quantum Efficiency (EQE) Measurement 64
4.4.3 Internal Quantum Efficiency (IQE) Measurement 64
4.5 Transfer Matrix Modelling 65

5 Efficiency Enhancement of Small Molecule Organic Solar Cells Using Hexapropyltruxene as an Interface Layer 68

5.1 Introduction 68
5.2 Experimental Details 69
5.3 Results and Discussion 72
5.3.1 Basic Properties of Hexapropyltruxene Layer 72
5.3.2 Current-Voltage (JV) Characterization of Solar Cells 72
5.3.3 External Quantum Efficiency (EQE) and Internal Quantum Efficiency (IQE) Analysis 74
5.3.4 Ellipsometry Analysis 79

5.3.5 Grazing-incidence Wide-angle X-ray Scattering (GIWAXS) Analysis . . . 81
5.3.6 AFM Analysis of the in-situ GIWAXS samples . . . 83
5.3.7 Steady-state Photoluminescence (SSPL) Analysis . . . 86
5.3.8 Time-resolved Photoluminescence (TRPL) Analysis . . . 88
5.4 Conclusions . . . 90

6 Hexapropyltruxene in IMEC Solar Cell Stack **92**
6.1 Introduction . . . 92
6.2 Experimental Details . . . 94
6.3 Results and Discussion . . . 95
6.3.1 Current-Voltage (JV) Characterization of Solar Cells (IMEC with molybdenum oxide (MoO_x)) . . . 95
6.3.2 Current-Voltage (JV) Characterization of Solar Cells (IMEC without MoO_x) . . . 96
6.3.3 External Quantum Efficiency (EQE) Analysis (IMEC with MoO_x) 100
6.3.4 Device Absorption Simulation . . . 100
6.3.5 Ultraviolet-visible (UV-vis) Spectroscopy Absorption Analysis 102
6.3.6 X-ray Diffraction (XRD) Analysis . . . 104
6.3.7 Atomic Force Microscopy (AFM) Analysis . . . 106
6.3.8 Steady-state Photoluminescence (SSPL) & Time-resolved Photoluminescence (TRPL) Analysis . . . 106
6.4 Conclusions . . . 109

7 Controlled Growth of α-sexithiophene Polymorphs via Substrate Treatment & Substrate Temperature Variation **113**
7.1 Introduction . . . 113
7.2 Experimental Details . . . 114

7.3 Results and Discussion . . . 117
7.3.1 Ultraviolet–visible (UV-vis) Spectroscopy Analysis . . . 117
7.3.2 X-ray Diffraction (XRD) Analysis . . . 118
7.3.3 Grazing-incidence Wide-angle X-ray Scattering (GIWAXS) Analysis . . . 121
7.3.4 Atomic Force Microscopy (AFM) Analysis . . . 129
7.3.5 Current-Voltage (JV) Characterization of Solar Cells . . . 131
7.3.6 External Quantum Efficiency (EQE) and Internal Quantum Efficiency (IQE) Analysis . . . 134
7.4 Conclusions . . . 135

8 Conclusions and Outlook **138**
8.1 Conclusions . . . 138
8.2 Outlook . . . 141

A Appendix **143**

B List of Publications **149**
B.1 Journal Publications . . . 149
B.2 Conference Contributions . . . 149

Bibliography **150**

List of Figures

1.1 World population growth, world energy consumption, and monthly average CO_2 concentration. 2

1.2 PV production by technology (percentage of global annual production.) 6

1.3 Applications of emerging solar cells. 8

1.4 PCEs of best research solar cells worldwide from 1976 through 2019 for various PV technologies. 9

2.1 Graph of bands and bandgaps. 12

2.2 Differences of bands in highly ordered crystals and amorphous films. . 15

2.3 Schematics of Marcus theory. 17

2.4 Recombination mechanisms in semiconductors. 19

2.5 Schematic illustrating the main process ocuring in the photoactive layer in OSCs. 21

2.6 Diagrams on charge transfer (CT) process. 22

2.7 Schematics of OSC structures. 24

2.8 Equivalent circuit of a basic solar cell and graphs of current-voltage (JV) curves. 26

3.1 Schematic representation of different types and material categories of interlayers. 30

3.2 Schematics of molecular template growth (MTG) method. 33

3.3 Various molecular packing structure of pentacene molecules in thin films. 35

4.1 Schematics of the sample fabrication procedure. 37
4.2 Chemical structures of the organic materials used in this thesis. . . . 38
4.3 Crystal structures of α-sexithiophene (α-6T) polymorphs. 41
4.4 Vacuum thermal deposition chambers used in this thesis. 43
4.5 Schematics of XRD technique. 45
4.6 Illustration of the geometry used for the simplified derivation of Bragg's law. 46
4.7 Schematics of GIWAXS technique. 50
4.8 Schematics of ellipsometry technique. 53
4.9 Optical model including an air/thin film/substrate structure. 54
4.10 Schematic diagram of a steady-state photoluminescence (SSPL) spectrofluorimeter. 59
4.11 Schematic diagram of a time-resolved photoluminescence (TRPL) spectrofluorimeter. 60
4.12 CV experiment set-up. 62
4.13 Schematic presentation of UV-vis spectroscopy measurements of thin film and solar cell samples. 63
4.14 Schematic presentation of the transfer matrix method. 65

5.1 Solar cell stack, and energy levels of the solar cells (hexapropyltruxene in boron subphthalocyanine chloride (SubPc)/buckminsterfullerene (C60) stack). 71
5.2 Basic properties of hexapropyltruxene. 73
5.3 JV curves of the solar cells with different thicknesses of a hexapropyltruxene interlayer between MoO_x and SubPc. 74
5.4 Solar cell performance versus the thickness of the hexapropyltruxene layer between MoO_x and SubPc. (hexapropyltruxene in SubPc/C60 stack). 75

5.5 EQE and UV-vis reflectance measurement results of reference devices without a hexapropyltruxene layer and the devices with 3.8 nm hexapropyltruxene. 76
5.6 Absorption simulation of solar cell stack with/without hexapropyltruxene using a transfer matrix approach. 77
5.7 IQE calculations for the reference devices without hexapropyltruxene and the devices with 3.8 nm hexapropyltruxene. 78
5.8 In-plane and out-of-plane refractive overall indices n, k of the reference device stack and a device stack with hexapropyltruxene. 80
5.9 Plots of the GIWAXS results of hexapropyltruxene project. 82
5.10 Radial distribution of the GIWAXS peak from 0.65 $Å^{-1}$ to 0.75 $Å^{-1}$. 84
5.11 AFM images of the surface morphology of 13 nm SubPc deposited on different layers. 85
5.12 SSPL spectra of glass/SubPc(13 nm), glass/MoO_x (5 nm)/SubPc (13 nm), and glass/ MoO_x (5 nm)/hexapropyltruxene (3.8 nm)/SubPc (13 nm). 87
5.13 TRPL decay dynamics of glass/SubPc(13 nm), glass/MoO_x (5 nm)/SubPc (13 nm), glass/hexapropyltruxene (3.8 nm)/SubPc (13 nm) and glass/ MoO_x (5 nm)/hexapropyltruxene (3.8 nm)/SubPc (13 nm). 89

6.1 Solar cell stack, energy levels of the solar cells (hexapropyltruxene in IMEC stack), and an explanation of the two-step exciton dissociation mechanism in the IMEC stack. 93
6.2 JV curves of the solar cells with different thicknesses of a hexapropyltruxene interlayer between MoO_x and α-6T (hexapropyltruxene in IMEC stack). 96
6.3 Solar cell performance versus the thickness of the hexapropyltruxene layer between MoO_x and α-6T (hexapropyltruxene in IMEC stack). . 97

6.4 JV curves of the solar cells with different thicknesses of a hexapropyltruxene interlayer between indium-doped tin oxide (ITO) and α-6T (hexapropyltruxene in IMEC stack). 98
6.5 Solar cell performance versus the thickness of the hexapropyltruxene layer between ITO and α-6T (hexapropyltruxene in IMEC stack). . . 99
6.6 EQE of the solar cells with different thicknesses of hexapropyltruxene interlayers between MoO_x and α-6T (hexapropyltruxene in IMEC stack). 101
6.7 Absorption simulation of IMEC solar cell stack with different thicknesses of hexapropyltruxene using a transfer matrix approach. 102
6.8 UV-vis absorption measurement results of the α-6T thin films on different substrates. (hexapropyltruxene in IMEC stack). 103
6.9 XRD measurement of the α-6T thin films on different substrates (IMEC stack). 105
6.10 AFM height images of the α-6T thin films on different substrates. (hexapropyltruxene in IMEC stack). 107
6.11 SSPL result of the α-6T thin films on different substrates. (hexapropyltruxene in IMEC stack). 108
6.12 TRPL result of the α-6T thin films on different substrates. (hexapropyltruxene in IMEC stack). 110

7.1 Thin film and solar cell stack schematics, with energy levels of the solar cell materials. 116
7.2 UV-vis absorption of α-6T layer in the films of the Thin Film Set 1. . 118
7.3 XRD measurement of the Thin Film Set 1. 120
7.4 Summary of GIWAXS results of the Thin Film Set 2. 122
7.5 Comparison of GIWAXS peak intensity, Scherrer coherence length, and UV-vis absorption. 128
7.6 AFM height images of different HCLs. 130

7.7 AFM height images of α-6T thin films on different HCLs. 131
7.8 JV curve summary of solar cells with different HCLs and substrate treatments. 133
7.9 Comparison of UV-vis absorption and short-circuit current (J_{sc}). . . . 133
7.10 EQE summary of solar cells with different HCLs and substrate treatments. 135
7.11 IQE summary of solar cells with different HCL and substrate treatment. 136

A.1 X-ray reflectivity (XRR) Analysis of a glass/hexapropyltruxene/SubPc thin film sample. 144
A.2 Summary of GIWAXS results of Thin Film Set 2. 145
A.3 Schematic presentation of the molecular orientation of α-6T polymorphs with different parallel plane. 146

List of Tables

1.1 PV technologies and their market share 5

4.1 Crystal structures of α-6T polymorphs reported in literature. 40

5.1 Thin film/device stacks in different experiments (hexapropyltruxene in SubPc/C60 stack). 70

5.2 Device performance summary of solar cells with different thicknesses of hexapropyltruxene. 76

5.3 Photon number absorbed in each layer calculated by absorption simulation using a transfer matrix approach. 77

5.4 Fitted peak properties of the GIWAXS line cut of hexapropyltruxene project. 81

5.5 Time-resolved photoluminescence lifetimes of SubPc thin films on quartz glass with different interlayers. 88

6.1 Thin film/device stacks in different experiments (hexapropyltruxene in IMEC stack). 94

6.2 Solar cell mismatch factor calculation result for IMEC stack. 95

6.3 IMEC solar cell (with MoO_x) device performance summary of solar cells with different thicknesses of hexapropyltruxene. 95

6.4 IMEC solar cell (without MoO_x) device performance summary of solar cells with different thicknesses of hexapropyltruxene. 98

6.5 Time-resolved photoluminescence lifetimes of α-6T thin films on glass with different interlayers. 111

7.1 Thin film/device stacks in different experiments (α-6T polymorphism). 115
7.2 GIWAXS peak intensity analysis of Figure 7.4. 123
7.3 Scherrer coherence length analysis of Figure 7.4. 124
7.4 Summary of root mean square roughness (RMS) of the AFM heigh images in Figure 7.6 and 7.7. 129
7.5 Device performance summary of solar cells with different HCLs and substrate treatments. 132

A.1 List of the Q-space values of representative GIWAXS diffraction peaks. 143
A.2 GIWAXS peak intensity analysis with R-square data. 147
A.3 GIWAXS Scherrer coherence length analysis with R-square data. . . . 148

List of Abbreviations

120 °C stands for the treatment during which substrate temperature was 120 °C when α-6T thin film was deposited.

1H NMR proton nuclear magnetic resonance

α-6T α-sexithiophene

AFM atomic force microscopy

AIL anode interface layer

ANL indicates that the substrates of the "ANL"-labelled samples were annealed for the same duration as the "120 °C" samples and then were cooled down to room temperature before the deposition of α-6T.

a-Si:H hydrogenated amorphous silicon solar cell

BCP bathocuproine

BIPV building-integrated photovoltaic

BPhen bathophenanthroline

C60 buckminsterfullerene

CBP 4,4′-bis(N-carbazolyl)-1,1′-biphenyl

CCDC Cambridge Crystallographic Data Centre

CdTe cadmium telluride solar cell

CIGS copper indium gallium selenide solar cell

CIL cathode interface layer

COD Crystallography Open Database

CSP concentrated solar power

CT charge transfer

CuPc copper phthalocyanine

CV cyclic voltammetry

CZTSSe copper zinc tin sulfur-selenium solar cell

D-A donor-acceptor

DC direct current

DIP di-indenoperylene

DIW deionized water

DOS density of states

DPC Diffraction Pattern Calculator

DSSC dye-sensitized solar cell

EBL electron blocking layer

ECL energy cascading layer

ExBL exciton blocking layer

$\mathbf{E}_g$ energy bandgap

EQE external quantum efficiency

FF fill factor

FWHM full width at half maximum

GaAs gallium arsenide solar cell

GIWAXS grazing-incidence wide-angle X-ray scattering

HCL hole contact layer

HIT Si heterostructures

HOMO highest occupied molecular orbital

HT high temperature

HTL hole transporting layer

ICL interconnecting layer

IMEC interuniversity microelectronics centre

IPA isopropyl alcohol

IPES inverse photoemission spectroscopy

IRF instrument response function

ITO indium-doped tin oxide

IQE internal quantum efficiency

J_{sc} short-circuit current

JV current-voltage

L_D exciton diffusion length

LFR linear Fresnel reflector

LUMO lowest unoccupied molecular orbital

LT low temperature

MBB multi-busbar

MeO-TPD N,N,N′,N′-tetrakis(4-methoxy-phenyl)benzidine

MoO_x molybdenum oxide

MPP maximum power point

MTG molecular template growth

ND neutral density

OPV organic photovoltaic

OSC organic solar cell

PCE power conversion efficiency

PDS parabolic dish systems

PEDOT:PSS poly(3,4-ethylenedioxythiophene) polystyrene sulfonate

PERC passivated emitter and rear cell

PL photoluminescence

PMT photomultiplier tube

PTC parabolic trough collector

PTFE polytetrafluoroethylene

PV photovoltaic

QCM quartz crystal microbalance

RMS root mean square roughness

R_s series resistance

R_{sh} shunt resistance

RT means that the thin film was fabricated with the substrate held at room temperature (20 °C).

RTSE real-time spectroscopic ellipsometry

SAM self-assembled monolayer

SIP substrate-induced phase

SMOSC small molecule organic solar cell

SPT solar power tower

SSPL steady-state photoluminescence

SubNc chloroboron subnaphthalocyanine

SubPc boron subphthalocyanine chloride

TAPC 4,4′-cyclohexylidenebis[N,N-bis(4-methylphenyl)benzenamine]

TCSPC time-correlated single photon counting

TRPL time-resolved photoluminescence

TTF-TCNQ tetrathiofulvalene-7,7,8,8-tetracyanoquinodimethane

UV-vis ultraviolet–visible spectroscopy

UPS ultraviolet photoelectron spectroscopy

VC-A Vacuum Chamber A

VC-B Vacuum Chamber B

VC-C Vacuum Chamber C

$\mathbf{V}_{MPP}$ maximum power point voltage

$\mathbf{V}_{oc}$ open circuit voltage

XRD X-ray diffraction

XRR X-ray reflectivity

Chapter 1

Introduction

1.1 Problems of the Current Energy System

The world population is growing tremendously with the development of human society, requiring a high demand for energy resources. Figure 1.1 (a) shows world population growth over the last half-century [1]. From this figure, we can observe that the world population has risen quickly during the last 50 years. This is due to the industrial revolution bringing increased productive capacity. However, the increase in population has also brought the problem of high energy consumption. Especially in the last decades, the rapid development of modern technology, e.g. the blooming of the Digital Revolution, has set a challenging demand on the energy supply, which cannot be fulfilled sustainably by the traditional fossil energy supply system.

Figure 1.1 (b) shows the steadily increasing world consumption of energy during the last 50 years [2]. Comparing Figure 1.1 (a) with (b), we can find that the consumption of energy resources is related to the growth of the world population. Figure 1.1 (b) also demonstrates that world energy consumption still heavily depends on fossil energy resources (oil, coal, and natural gas). However, fossil energies have limited reserves on Earth, even though we keep discovering new reserves of fossil fuels. Report about the proven reserves and consumption of fossil fuels indicates that in ca. 50 years we are likely to run out of oil and natural gas, and in ca. 100 years we are going to use up the coal reserves if no new reserves are being detected in the

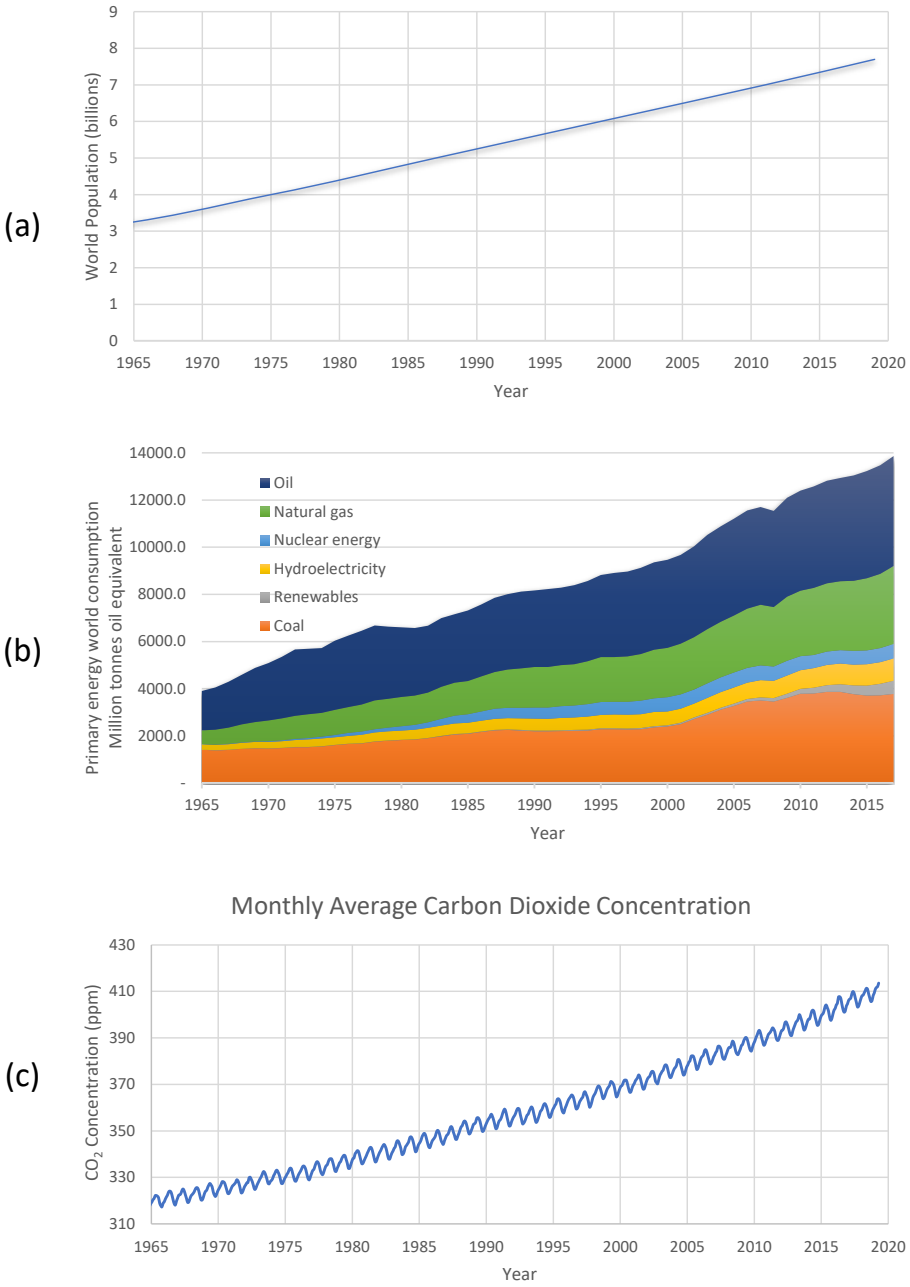


Figure 1.1: (a). Graph of world population growth. This graph is replotted from Reference [1]. (b). Graph of world energy consumption. The unit in this graph is million tonnes of oil equivalent. This graph is modified from Reference [2]. (c). Monthly average CO_2 concentration. This graph is replotted from Reference [3].

future [4]. It is vital to discover new energy resources to sustain the development of human civilization.

Besides, the use of fossil fuels causes detrimental problems such as air/water pollution and climate change. Figure 1.1 (c) shows the CO_2 concentration changes with time [3]. From this figure, we find that during the last 50 years, the CO_2 concentration has been increasing steadily. This steadily increasing CO_2 concentration in the atmosphere has triggered global warming [5, 6]. Nowadays, extreme climate events caused by global warming are affecting human beings' everyday life [7, 8] and agricultural production [9, 10]. These consequences of the use of fossil fuels warn us to investigate sustainable energy resources for development.

The rise in awareness about the need for sustainable and environmentally-friendly development requires investment in sustainable resources of energy, including biomass [11], hydroelectric power [12], wind power [13], photovoltaic (PV) [14], and carbon capture and storage [15]. Among these potential technologies, PV technology is probably one of the most promising applications to provide a large scale of energy at a reasonable cost [16–18].

1.2 Current Solar Energy Technology

At present, there are two major technologies to utilize solar energy directly. One is the so-called concentrated solar power (CSP), and the other is photovoltaic (PV).

CSP is also referred to as "concentrated solar thermal". It is a technology to utilize solar thermal energy. There exist several CSP technologies, such as parabolic trough collector (PTC), solar power tower (SPT), linear Fresnel reflector (LFR) and parabolic dish systems (PDS) [19, 20]. Its general principle is to use lenses or mirrors to concentrate the sunlight. Thus, solar thermal energy is accumulated to heat the heat transfer fluid (water and synthetic thermal oil are commonly used, and molten salts, as well as nanofluids, have their potential applications as heat transfer fluids [21, 22]). The generated hot fluids can be applied to generate electricity via conventional steam-driven turbines. Compared to PV, this system has advantages

such as being cost-effective, simple implementations and operations [22], a relatively constant source of electricity (with the thermal storage technology) [23]. However, it also has disadvantages such as low efficiency, large land resource consumption, and the cost implications of thermal storage materials [23].

PV is a technology that uses semiconductors to convert sunlight directly into direct current (DC) electricity [24]. PV devices are also called as solar cells. Nowadays, solar cells in labs are reported to have power conversion efficiency (PCE) over 20 % [25], and PV power plant efficiency is around 10 % [26]. PV installations have higher overall efficiency than CSP systems occupying the same area, due to its small land area demand [23].

The first commercialization of a distributed yet grid-connected PV system called "The PV Pioneer Program" started in 1993 [27]. The first wave of mass-production of PV modules was in 2000 [28]. Due to the development of PV technology and the supportive policy from governments around the world, crystalline silicon (Si) solar cell technology has developed fast in the last decades. The cost of commercialized solar cell production has dropped dramatically since 2008 [29].

There exist several state-of-the-art PV technologies other than crystalline Si solar cells, including thin-film technologies (e.g. gallium arsenide solar cells (GaAs), copper indium gallium selenide solar cells (CIGS), cadmium telluride solar cells (CdTe), hydrogenated amorphous silicon solar cells (a-Si:H)), and emerging PV technologies (e.g. dye-sensitized solar cells (DSSCs), perovskite solar cells, perovskite/Si tandem solar cells, organic solar cells (OSCs), organic tandem cells, copper zinc tin sulfur-selenium solar cells (CZTSSe), and quantum dot solar cells). Table 1.1 summarises the major solar cell technologies at present. According to the time when the technologies were invented, these PV technologies can be generally divided into three categories: crystalline Si solar cells, thin-film technologies, and emerging PV technologies. Si and thin-film technologies have already been commercialized, and the global solar

cell market is dominated by crystalline Si solar cells. Now it shares about 95 % of the total market [30]. Among the numerous crystalline Si solar cells, passivated emitter and rear cells (PERCs) and multi-busbar (MBB) technologies are the most up-to-date ones [31, 32]. Thin-film PV has only around 5 % market share nowadays [30]. The PCEs of thin film solar cell modules are still lower than those of the crystalline Si solar cell modules [25]. However, because of the marginally smaller production cost and government subsidies [33, 34], thin film solar cell technologies have a small share of the entire market, of which the majority is cadmium telluride solar cell (CdTe) and copper indium gallium selenide solar cell (CIGS). Due to the patent restriction on CdTe technology, companies other than First Solar (who owns the most patents on CdTe technology [35]) are developing CIGS technology. Figure 1.2 indicates the market share change of the different technologies in the solar cell industry. Because of the cost reduction of crystalline Si solar cells, thin film solar cells are gradually losing their price advantage. The market share of thin film solar cell technologies is gradually decreasing since 2009 [36].

Table 1.1: PV technologies and their market share

Category	Technology	Market share	Comments
Crystalline Si solar cells	single crystal Si, multicrystalline Si, HIT, PERC, MBB, etc.	$\sim$ 95 % [30]	Crystalline Si solar cells dominate the market. PERC and MBB are the most up-to-date technologies.
Thin film technologies	GaAs, CIGS, CdTe, a-Si:H, etc.	$\sim$ 5 % [30]	The majority of the thin film solar cell market is controlled by CdTe. CIGS is developed fast due to the patent restriction on CdTe technology.
Emerging PV technologies	DSSC, provskite cells, perovskite/Si tandem, OSC, organic tandem cells, CZTSSe, quantum dot solar cells, etc.	$\sim$ 0 % [30]	in the process of commercialization

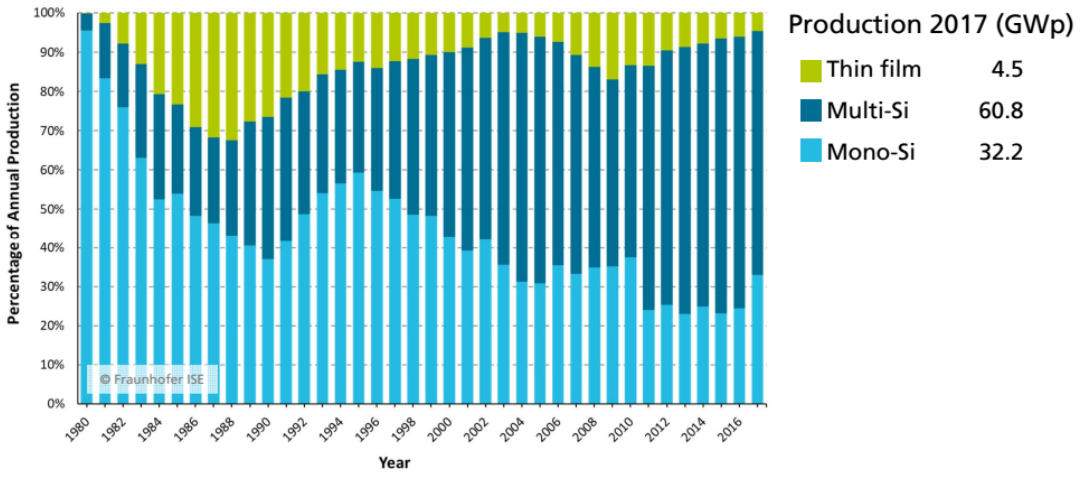


Figure 1.2: PV production by technology (percentage of global annual production). "Multi-Si" refers to multicrystalline silicon technology and "Mono-Si" refers to monocrystalline silicon technology. This graph is taken from reference [36].

PV technology is the most widely used solar energy technology nowadays. Due to the development of PV technology (mainly because of the maturation of the crystalline silicon technology) and political subsidies from governments, the electricity generated by PV has the comparable price as the conventional electricity produced from fossil fuels [33]. This competitive price, together with the sustainability benefits of solar energy, makes PV technology a promising alternative to fossil fuels.

1.3 Next Generation of PVs

Even though current crystalline Si PV technology is already matured and the price of the electricity generated by crystalline Si solar cells is comparable with that generated by commercial fossil resources, we still find it has several disadvantages to overcome. The biggest problem of the crystalline Si PV technology is that it is an energy-intensive industry. Crystalline Si solar cells are assumed as sustainable productions, yet the manufacture of these products is not an environmentally-friendly process. On the contrary, due to the energy consumption as well as the environmental

pollution caused by the manufacturing process, the fabrication of crystalline Si solar cells generates many problems to the local environment [37]. It provides alternative PV technologies with a chance to enter the playground.

Besides, both the production and purchase of Si solar cells are capital-intensive [38], which prevents less-developed economies from developing this technology. It is estimated that investment required for a crystalline Si solar cell factory is more than 100 million USD per gigawatt [39]. These disadvantages leave other potential technologies, e.g. solution-based fabrication technology or vacuum-evaporation small molecule organic solar cell (SMOSC) technology, a promising future.

Last but not least, the need in some special application fields such as wearable devices, building-integrated photovoltaics (BIPVs), and travel/military applications cannot be completely fulfilled by commercial crystalline Si solar cells due to its heavy-weight, rigid shape and a lack of transparency. Figure 1.3 summarizes potential applications of the emerging solar cells. Because of these reasons, the new generation of PVs which are cost-efficient, portable, light-weight, flexible has the potential for further development.

So far, as shown in Table 1.1, there are several emerging PV technologies appearing in labs and industries, such as DSSCs, perovskite solar cells, perovskite/Si tandem, OSCs, organic tandem cells, copper zinc tin sulfur-selenium solar cells (CZTSSes), quantum dot cells. These technologies can also be categorized as thin film solar cell technology since their active layers are thin films comparing with the crystalline Si solar cells. However, most of them are still in the process of lab-based research and not commercialized yet.

In Figure 1.4 the records of the up-to-date best research-cell efficiencies are shown [44]. From this figure, we can find that the development of emerging PV has accelerated in recent years. OSCs and quantum dot solar cells have shown remarkable progress in their PCE records while perovskite solar cells have comparable PCE

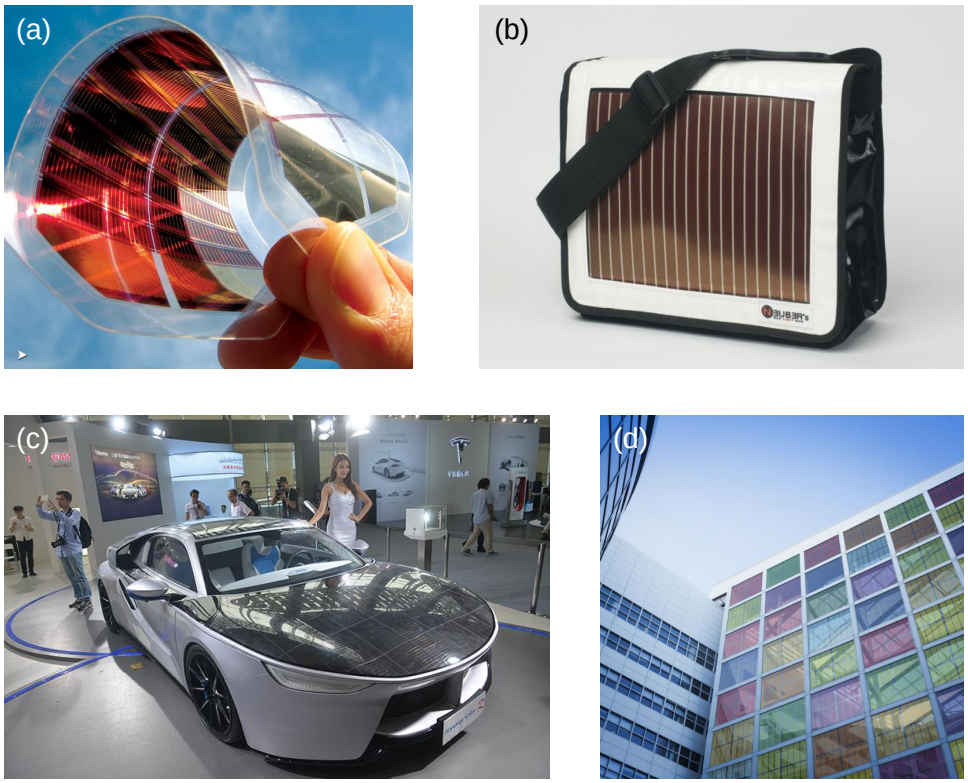


Figure 1.3: Applications of emerging solar cells. (a) A flexible organic solar cell module. This photo is amended from Reference [40]. (b). An organic solar cell integrated bag for travelling. This photo is amended from Reference [41]. (c). A solar-roof car. This photo is amended from Reference [42]. (d). A wall of semi-transparant solar cell windows (an example of BIPVs). This photo is amended from Reference [43].

records to crystalline Si solar cells. Among the emerging PV technologies, perovskite solar cells, OSCs, and quantum dot cells are the most promising alternatives to Si solar cells.

1.4 Scope and Structure of the Thesis

This thesis focuses on the idea of using the template layer to perform morphology control of organic thin films and investigating its relationship with solar cell performance.

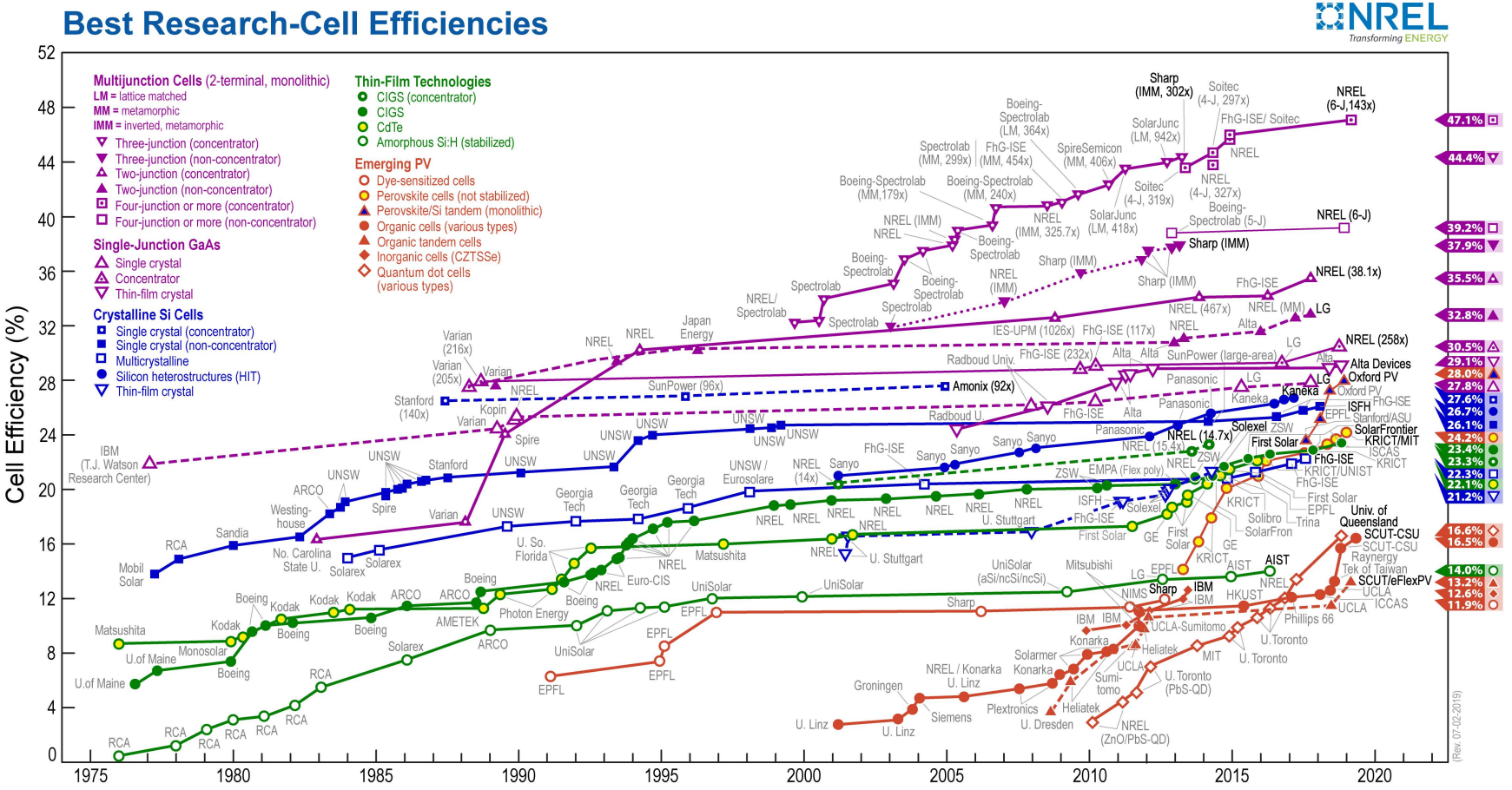


Figure 1.4: Conversion efficiencies of best research solar cells worldwide from 1976 through 2019 for various PV technologies. Efficiencies determined by certified agencies/laboratories. This plot is courtesy of the National Renewable Energy Laboratory, Golden, CO [44].

In the first theoretical part, Chapter Two and Chapter Three illustrate the fundamental concepts of organic semiconductors, organic solar cells (OSCs), and interface effects within OSCs, such as molecular template growth (MTG) effect and substrate-induced phase (SIP) effect. These chapters provide the readers with the necessary knowledge to understand the latter experimental chapters.

Chapter Four starts the experimental part of this thesis. It is a detailed introduction of the materials and methods used in this thesis. Chapter Five describes the research about the function of hexapropyltruxene interlayer (a novel truxene-based molecule) in the SubPc/C60 solar cell stack. Solar cell performances are found to be improved by hexapropyltruxene interlayer. Chapter Six introduces the application of hexapropyltruxene as an interlayer in the solar cell stack first invented by the interuniversity microelectronics centre (IMEC) (For readers' benefit, "IMEC stack" is used to refer to this solar cell stack in the later chapters). Chapter Seven explains the polymorphism of α-sexithiophene (α-6T). The substrate surfaces and substrate temperatures are controlled to modify the growth of different polymorphs of α-6T. It also studies the influence of polymorphism on solar cell performances.

Finally, Chapter Eight summarizes and concludes the work in this thesis, and explains the outlook for future work.

Chapter 2

Organic Photovoltaics

This chapter summarises the fundamentals of organic photovoltaic (OPV) devices. It starts with the basic concepts of semiconductors and then explains the processes within OSCs and their typical device structure. This chapter is based mainly on Peter Würfel, *Physics of Solar Cells: From Basic Principles to Advanced Concepts*, 2nd ed. 2009, Wiley [45]; and Wolfgang Tress, *Organic Solar Cells: Theory, Experiment, and Device Simulation*, 2014, Springer [46].

2.1 Basic Principles of Semiconductor: Bands and Fermi Level

Semiconductors are a category of materials that have electrical conductivity between conductors and insulators. Classic semiconductors have continuous ranges of allowed energies known as bands, which is caused by the Pauli exclusion principle. Pauli exclusion principle allows only one electron in one state. Thus, when the atoms are brought together, the energy levels split from each other to form a continuous set of allowed states (shown in Figure 2.1 (b)). Specifically, semiconductors are defined by an energy bandgap (E_g) in the range of 0.5 — 4 eV [46]. The energy range below the gap is defined as the valence band, while the energy range above this gap is defined as the conduction band. The valence band is nearly fully occupied by electrons while the conduction band is almost empty. The existence of an energy gap can be illustrated by

assuming a free electron with parabolic dispersion in a periodic crystal. The periodic dispersion is described by the Equation 2.1 below:

$$E = \frac{1}{2}mv^2 = \frac{p^2}{2m} = \frac{\hbar^2 k^2}{2m} \tag{2.1}$$

where k is the wavenumber and it has the value $k = p/\hbar = 2\pi/\lambda = Na$ with $N \in \mathbb{N}$, a is the the distance between atoms in the one-dimensional lattice in Figure 2.1 (a).

In a periodic crystal, because of the existence of a repeating lattice, waves interfere with each other and thus lead to two standing waves. One of the standing waves has higher potential energy than the average energy of a free electron as propagating wave while the other has lower potential energy, which leads to an energy gap close to $k = \frac{\pi}{a}N$. A schematic of the formation of bandgaps is shown in Figure 2.1 (a).

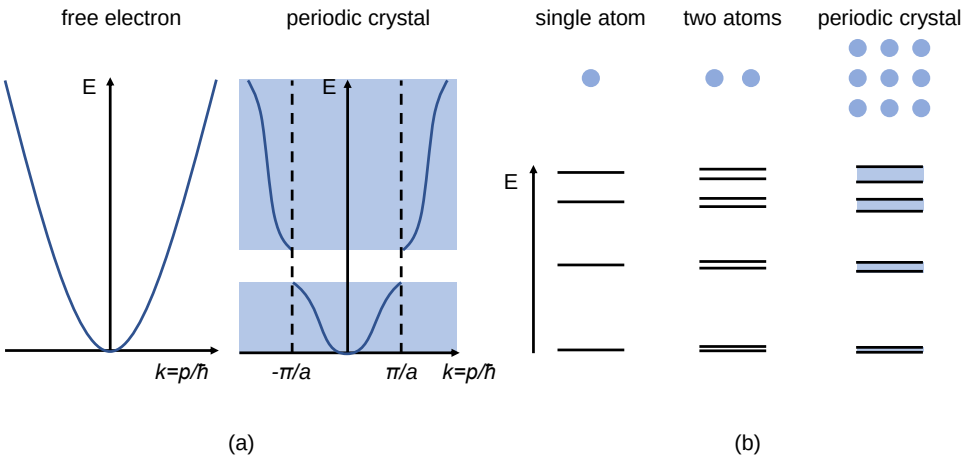


Figure 2.1: Graph of bands and bandgaps. (a). Free-electron approximation with parabolic dispersion relation of a free electron (left) and an electron in periodic crystal lattice (right). (b). Tight-binding-model, where discrete degenerate atomic levels split as atoms influence one another. Adapted by permission from Reference [46]. Copyright 2014 Springer Nature.

The concept density of states (DOS) is introduced to illustrate the distribution of the number of states at each energy level that can be occupied. The integral of the

product of DOS $g(E)$ and the probability of occupation $f(E)$ explains the occupation of the bands in thermal equilibrium.

$$\int_{band} g(E) \cdot f(E) dE \tag{2.2}$$

If we ignore the mutual interaction of the particles, the state occupation probability can be explained by the Fermi-Dirac statistics:

$$f(E) = \frac{1}{e^{\frac{E - E_F}{k_B T}} + 1} \overset{(E - E_F > 3k_B T)}{\approx} e^{-\frac{E - E_F}{k_B T}} \tag{2.3}$$

where E_F is the Fermi level and k_B is the Boltzmann constant.

The DOS $g(E)$ can be a complicated function [46]. However, it can be described as Equation 2.4:

$$g(E) = \frac{dN}{V dE} = \frac{1}{2\pi^2} \cdot (\frac{2m^*}{\hbar^2})^{3/2} E^{1/2} \tag{2.4}$$

where m^* is the effective mass of the charge carrier.

Thus, electron density n in the conduction band can be solved by calculating the integral of Equation 2.2:

$$\begin{aligned} n = \int_{E_C}^{\infty} g(E) \cdot f(E) dE = \int_{E_C}^{\infty} 4\pi (\frac{2m^*}{\hbar^2})^{3/2} (E - E_C)^{1/2} \frac{1}{e^{\frac{E - E_F}{k^B T}} + 1} dE \\ \overset{(E - E_F > 3k_B T)}{\approx} \int_{E_C}^{\infty} 4\pi (\frac{2m^*}{\hbar^2})^{3/2} (E - E_C)^{1/2} e^{-\frac{E - E_F}{k_B T}} dE = N_C e^{-\frac{E_C - E_F}{k_B T}} \end{aligned} \tag{2.5}$$

where N_C is defined as the effective density of states and $N_C = 2 \cdot \left(\frac{2\pi m_e^* k_B T}{h^2} \right)^{3/2}$.

In semiconductors, we use the concept hole density p to describe the charge transport in the valence band. Holes are missing (or defect) electrons, so holes carry one positive elementary charge. Similar to Equation 2.5, hole density can be described as the following equation:

$$p = N_V e^{-\frac{E_F - E_V}{k_B T}} \tag{2.6}$$

where $N_V = 2 \cdot \left(\frac{2\pi m_p^* k_B T}{h^2}\right)^{3/2}$. Multiply 2.5 and 2.6, we get:

$$n_0 p_0 = n_i^2 = N_C N_V e^{-\frac{E_g}{k_B T}} \tag{2.7}$$

In Equation 2.7 the product of electron and hole densities is independent of the position of E_F. Impurities in semiconductors can increase n_0 or p_0 by donating free charges, which can be applied to manipulate the conductivity of semiconductors. A typical doping process is to replace a small amount of the crystal atoms with another species of atoms that have one more (or less) valence electron not forming a covalent bond.

Once illuminated, electrons in the valence band will be excited into the conduction band, leading to lager values of n and p, which breaks the equilibrium we described in Equation 2.7. However, because of the difference between relaxation (intra-band, normally less than 1 picosecond ps) and recombination (band-band, typically in the range of ps), thermalized electrons and holes still obey the Fermi-Dirac statistics in their bands. With the increased value of n and p, E_F is shifted to describe the distribution of them, respectively. Thus, we have the so-called quasi-Fermi levels: E_F^n which is close to the conduction band, and E_F^p which is close to the valence band. Thus, we have:

$$n \cdot p = N_C e^{-\frac{E_C - E_F^n}{k_B T}} \cdot N_V e^{-\frac{E_F^p - E_V}{k_B T}} = n_i^2 e^{-\frac{E_F^n - E_F^p}{k_B T}} \tag{2.8}$$

2.2 Organic Semiconductors

Organic semiconductors are a class of organic materials that exhibit semiconductor properties. They are π-conjugated systems, such as π-conjugated polymers, oligomers, and small molecules [47].

The physics of single molecules is discussed in details in books such as Reference [46]. Readers are encouraged to refer to the textbooks for information about

absorption and emission behaviours of single molecules, such as molecular orbital theory and Franck-Condon principle. In the following sections, the basics of organic semiconductor solids are discussed.

Molecules in organic semiconductors are coupled by intermolecular forces, e.g. van der Waals forces, which is much weaker than atomic bonds within inorganic semiconductors (van der Waals forces are one or two orders of magnitude smaller than atomic bonds [48]). Thus, the energy level splitting of electrons in these organic semiconductor solids is much more moderate than those in inorganic semiconductors, resulting in narrower bands or more localized states. A schematic comparison of the band/energy level difference between highly ordered crystals and amorphous films is shown in Figure 2.2. The properties of organic semiconductors fall in between isolated molecules and inorganic semiconductors.

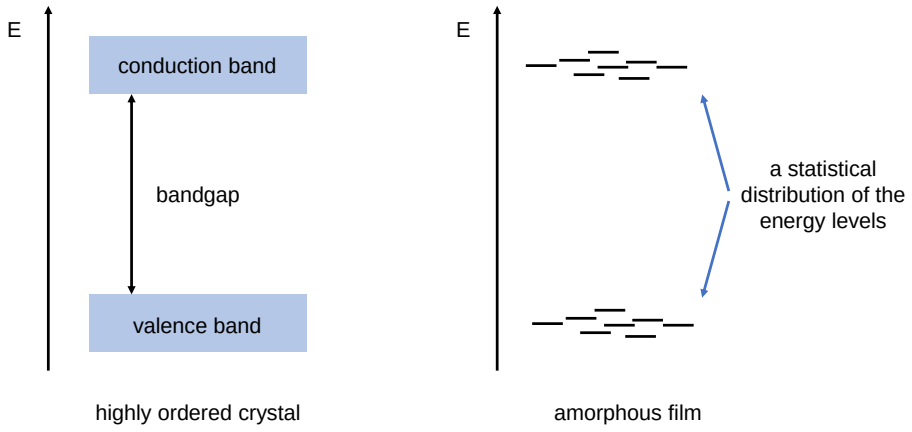


Figure 2.2: Differences of bands in highly ordered crystals and amorphous films. In highly ordered crystals, strong interactions of the atoms lead to energy bands (left). In amorphous films, the disorder of molecules leads to a statistical distribution of the energy levels.

2.2.1 Exciton Generation

Once the semiconductor absorbs a photon with the energy more than E_g, it can generate an exciton. In organic semiconductors, the generated exciton is often located in one molecule or one conjugated segment of a polymer. It can be regarded as a bounded electron-hole pair with binding energy, which is around several hundred meV [49, 50]. However, not every photon passing through the solar cells will be absorbed. The term absorption coefficient $\alpha(\omega\hbar)$ is used to describe the probability of photon absorption. Thus, the number of absorbed photons can be defined as the following equation:

$$j_{\gamma,abs} = \alpha j_{\gamma,in} \tag{2.9}$$

where $j_{\gamma,in}$ is the incident photon current density.

2.2.2 Exciton Transport

In organic semiconductors, the generated exciton can be transferred to a nearby molecule via Föster energy transfer or Dexter energy transfer. Föster energy transfer is a dipole-dipole interaction between the emitter molecule and receiver molecule. The energy is transferred via a resonant process, and it is typically in the range of several nanometres. It only allows for singlet transfer. In Dexter energy transfer process, electrons can be exchanged via a wave function overlap between two neighbouring molecules. Both singlet and triplet transfer are allowed, and it has a distance range of 1 - 2 nm. In organic semiconductors, exciton transport is a multi-step diffusion (hopping) process, where both Föster and Dexter energy transfers take places.

2.2.3 Marcus Theory and Transition Rates

Non-adiabatic Marcus theory is often used to describe the charge transport process (hopping between weakly coupled molecules or segments) within organic semiconductors. This theory is described in Figure 2.3.

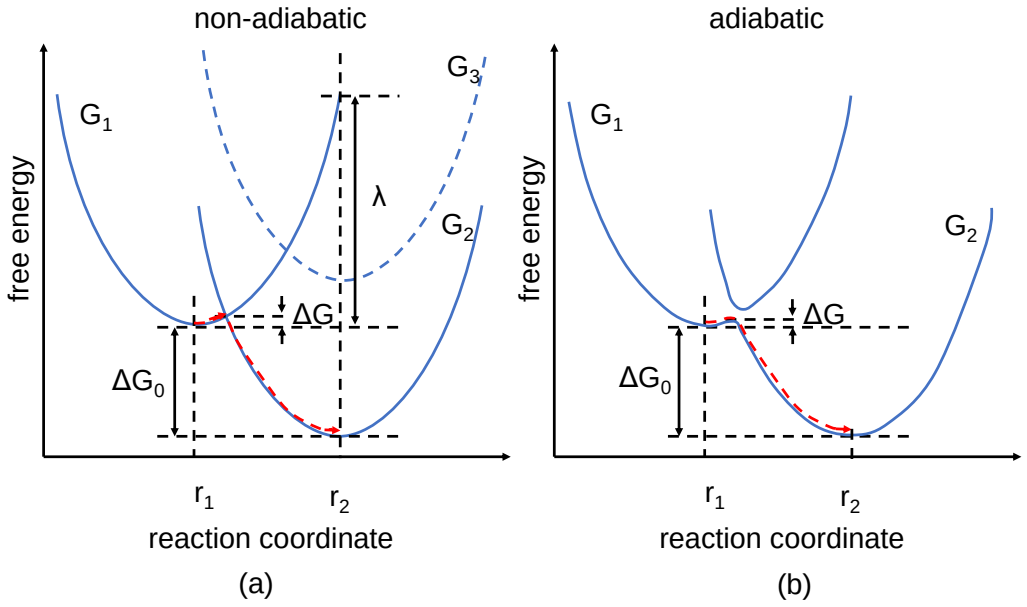


Figure 2.3: Schematics of Marcus theory. (a). Non-adiabatic Marcus theory (for weakly coupled molecules), (b). Adiabatic Marcus theory (for strongly coupled molecules). G_1 is the free energy of the educt, G_2 and G_3 are the free energy of products. r_1 and r_2 represent the reaction coordinates of the educt and product. ΔG_0 is the energy change between these two states. ΔG_0 can be negative for down-hill (from G_1 to G_2) process or positive for up-hill (from G_1 to G_3) process. ΔG is the activation energy. λ is the reorganization energy the molecule needs to reach the equilibrium geometry of the product without electron transfer. Red arrows indicate the transfer process from G_1 to G_2. Adapted by permission from Reference [46]. Copyright 2014 Springer Nature.

In the charge transfer process, the educt (the molecule before the charge transfer) and product (the molecule after the charge transfer) have different states. The transition between the educt and product states can be described as a non-adiabatic process, which requires a quantum jump. Due to Franck-Condon principle and the conservation of energy, the transition between these two states (G_1 and G_2 in Figure 2.3 (a)) can only happen at the intersection of the two energy curves. The transition needs to overcome an activation energy, which is

$$\Delta G = \frac{(\Delta G_0 + \lambda)^2}{4\lambda} \tag{2.10}$$

where ΔG_0 is the energy change between these two states, λ is the reorganization

energy the molecule needs to reach the equilibrium geometry of the product without electron transfer. ΔG_0 and λ is sketched in Figure 2.3 (a). The probability of the transition is given in the following equation:

$$\nu_{ij} = \frac{|I_{ij}|^2}{\hbar}\sqrt{\frac{\pi}{\lambda k_B T}}\exp\left(-\frac{(\Delta G_0 + \lambda)^2}{4\lambda k_B T}\right) \tag{2.11}$$

where $|I_{ij}|^2$ is the electronic coupling term, which depends on the orbital overlap.

For strongly coupled molecule systems, the transition does not need a quantum jump. The transition mainly depends on the reorganization ability of the molecules and does not depend on the electron transfer at the intersection of the two energy curves (shown in Figure 2.3 (b)).

2.2.4 Charge Transport and Gaussian Discorder Model

In amorphous organic solids, electrons are localized within the intermolecular scale due to the disorder of the molecule packing. Charge transport inside amorphous organic solids is described as a "hopping" process. Gaussian disorder model is often applied to describe the charge transport within organic semiconductors. The density of states (DOS) of the hopping sites (molecules or π-systems) within the organic semiconductors can be described by Gaussian distribution:

$$g(E) = \frac{N_{sites}}{\sqrt{2\pi}\sigma}\exp\left(-\frac{(E - E_0)^2}{2\sigma^2}\right) \tag{2.12}$$

where E_0 is the centre of DOS and N_{sites} is the density of the enegies of hopping sites. σ is the width of Gaussian distribution.

For weakly coupled molecule system, the jump rate of charge carriers hopping from site i to site j can be described as the non-adiabatic Marcus theory as Equation 2.11. If the polaronic effects is neglected, the jump rate can be describes as Miller-Abrahams equation:

$$\nu_{ij} = \nu_0 \exp(-2\gamma\Delta R_{ij}) \cdot \begin{cases} \exp\left(-\dfrac{E_j - E_i}{k_B T}\right), & E_j > E_i \\ 1, & E_j < E_i \end{cases} \tag{2.13}$$

where E_i and E_j are the energies of the hopping sites, ν_0 is the attempt frequency at which the electron tries jumping. γ is the wave function decay parameter and ΔR_{ij} is the site distance.

2.2.5 Electron-hole Recombination

Opposite to the mechanism described in Section 2.2.1, the reverse process of generation exists, which is defined as electron-hole recombination. Depending on the reaction either emitting photons or not, recombination processes are divided into radiative recombination and non-radiative recombination. Non-radiative recombination can be further divided into Auger recombination and impurity recombination. A diagram of different recombination mechanisms in semiconductors is illustrated in Figure 2.4.

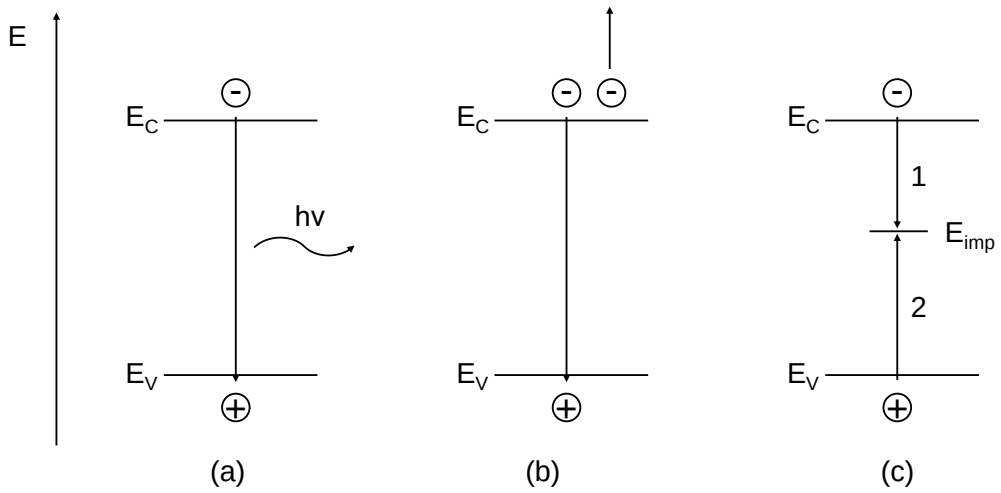


Figure 2.4: Recombination mechanisms in semiconductors. (a). A diagram of radiative recombination. The energy from the recombination is emitted as a photon; (b). A diagram of Auger recombination. In this process, the emitted energy of an excited electron is transferred to another electron; (c). A diagram of impurity recombination. The electron is trapped by an impurity-generated state, and subsequently, recombines with a hole.

In the radiative recombination process, an electron and a hole meet and annihilate to produce a photon carrying the energy, which is exactly the reverse reaction of electron-hole generation. This process is unavoidable and depends on the concentration of charge carriers.

Apart from the radiative recombination, the electron-hole annihilation sometimes will not produce any photon. Instead, the energy generated from the electron-hole recombination is taken by other particles. This process is defined as non-radiative recombination. In the Auger recombination process, other electrons or holes absorb the emitted energy while in impurity recombination phonons absorb the emitted energy.

2.3 Organic Solar Cells

Organic solar cells (OSCs) are a class of PVs that are composed of one or more layers of organic semiconducting materials sandwiched between metallic and transparent electrodes [51]. Recent performance development in OSCs shows a remarkable progress [26, 52–55], achieving PCE of more than 16% in single-junction devices [56]. Advantages such as their mechanical flexibility, portability, lightweight and potentially cost-efficient production on large area make OSCs a promising alternative technology to silicon wafer-based solar cells [57, 58], especially in the BIPV market [58, 59].

2.3.1 Processes in Organic Solar Cells & Charge Transfer (CT) States

Figure 2.5 illustrates a schematic presentation of the process inside OSCs. Here we use a simple planar donor-acceptor (D-A) heterojunction structure to explain the process. Donor and acceptor layers are the active layers in light absorption. (More detailed information about different types of solar cell structures will be discussed in Section 2.3.2.) Once light shines on the active layers of the solar cell, a bound electron-hole pair (exciton) is generated. Excitons can transport through the organic

semiconductor. Then, the electron and hole may separate from each other at the interface of donor and acceptor materials. Electron-hole pairs also have the chance to recombine. Later, the separated charge carriers transport through the organic semiconductor with the influence of the electric field inside the solar cell. Finally, the remaining charges will be collected by the corresponding electrodes, and thus the photocurrent is generated.

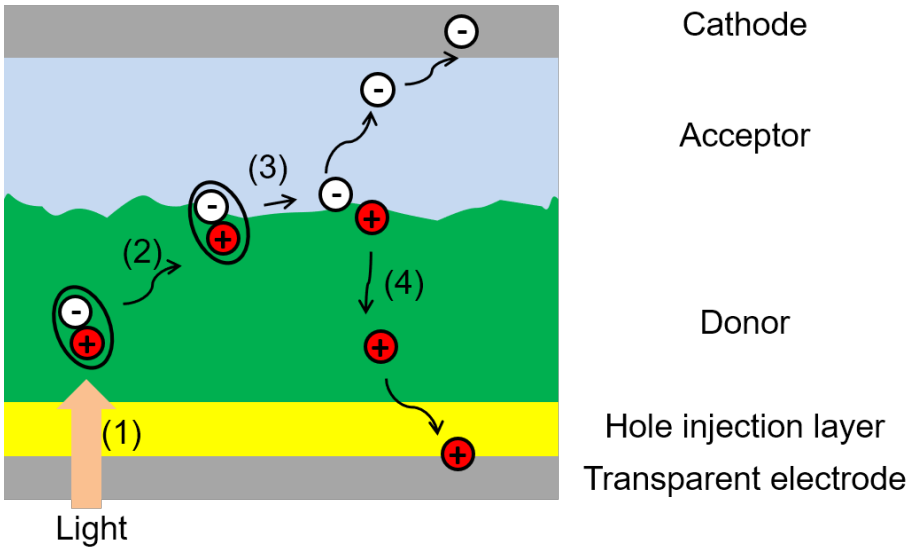


Figure 2.5: Schematic illustrating the main process ocuring in the photoactive layer in OSCs: (1). photon absorption and exciton generation. (2). exciton diffusion. (3). exciton splitting at D-A interface. (4). charge collection.

The processes of exciton generation and transport, charge transport and recombination have already been discussed in Section 2.2. In this section, the concept of charge transfer (CT) states is briefly introduced.

Charge Transfer (CT) States

As shown in Figure 2.5, an exciton is split into an electron and a hole at the interface of the D-A materials due to the difference of electron transport energy ΔE_{et} ($\approx \Delta LUMO_{film}$). This process is known as the charge transfer (CT) process. Energy levels of the charge transfer complexes are known as the charge transfer (CT) states.

The actual process of CT is still not yet well understood by researchers. There exist mainly two possible models to explain the exciton dissociation processes, as shown in Figure 2.6 (b). In brief, one model (solid red arrows) explains that the exciton dissociation process undergoes an intermedium short-lifetime state as the CT complex, where the CT state energy is smaller than the charge-separated (CS) state due to the existence of CT binding energy. The other model (black dashed arrows) suggests that the exciton dissociation process goes through a so-called "hot CT states" path, where the energy gained from the energy level offset is used to generate free charge carriers directly.

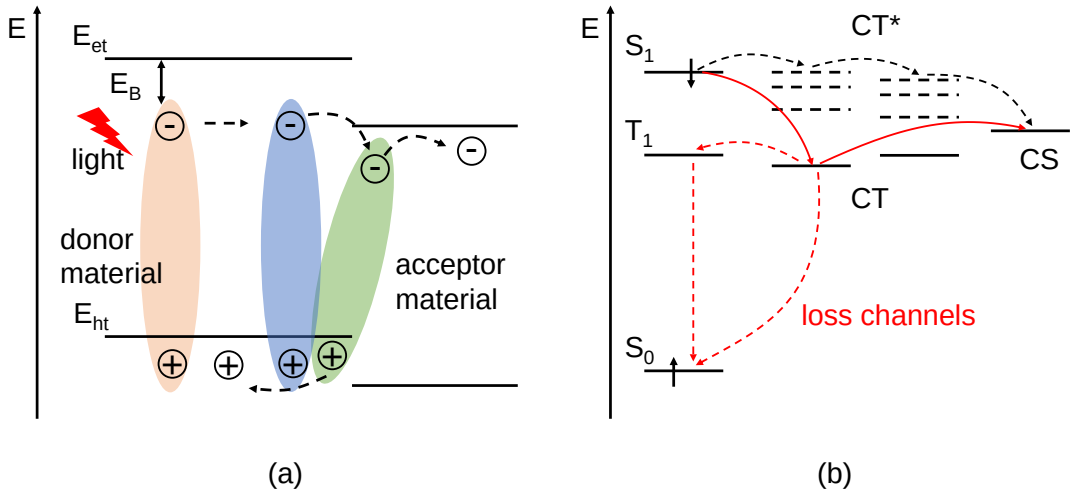


Figure 2.6: Diagrams on charge transfer (CT) process. (a). Diagram of energy conversion steps in the one-electron picture. E_{et} and E_{ht} are the charge carrier transport energies, where $E_{et} \approx LUMO_{film}$ and $E_{ht} \approx HOMO_{film}$. ΔE_{et} is the driving force to overcome the exciton binding energy E_B. (b). CT states and hot CT states. S_0, T_1, S_1 are the ground state, triplet state and singlet state of the exciton, respectively. CT represents the charge-transfer states. CT* represents the hot CT states. CS represents the charge separated states. Red solid arrows show the dissociation process of an exciton by CT states. Black dashed arrows show the exciton dissociation process via hot CT states. Red dashed arrows show the loss channels. Adapted by permission from Reference [46]. Copyright 2014 Springer Nature.

During the charge transfer process, there exist chances for energy loss, shown as

the red dashed arrows in Figure 2.6 (b). One channel for energy loss is the relaxation of CT states to the ground state of the exciton. The other possible loss channel is the back transfer of energy to the triplet state T_1, if the energy level of T_1 is lower than CT states.

2.3.2 Structure of Organic Solar Cells

The most successful structure so far for OSCs is the donor-acceptor (D-A) heterojunction structure [46]. Heterojunction comprises a junction of two different materials. A schematic of a bilayer heterojunction solar cell is shown in Figure 2.7 (a). In particular, planar heterojunction (Figure 2.7 (b)) and bulk heterojunction (Figure 2.7 (c)) are two typical types of solar cell stacks that have been extensively studied.

As discussed in Section 2.1, photocurrent is generated by the absorption of photons. The absorbed photon is extracted as an exciton, which then has to be separated in a subsequent step taking place in the interface of donor and acceptor materials. The planar heterojunction provides this interface. However, the exciton diffusion length (L_D) in many organic semiconductors is only of the order of 10 nm [61]. To achieve the optimal light absorption, however, the thicknesses of thin films inside heterojunction usually need to be longer than the L_D. This contradiction limits the design of OSCs with high PCE. Hence, it is vital to minimize the exciton travel distance before reaching a donor-acceptor interface. Shown in Figure 2.7 (c), the donor and acceptor materials in bulk heterojunctions are better mixed, providing shorter diffusion length for excitons. When the electron and hole separate, they are transported through an ideally continuous interpenetrating network morphology with optimal domain size [62]. Despite this advantage, bulk heterojunction causes several disadvantages, e.g. the semiconductor in contact with "wrong" electrode, large domains, small or isolated domains, and disrupted molecular packing. They are explained in Figure 2.7 (c). In order to combine the advantages of planar and bulk

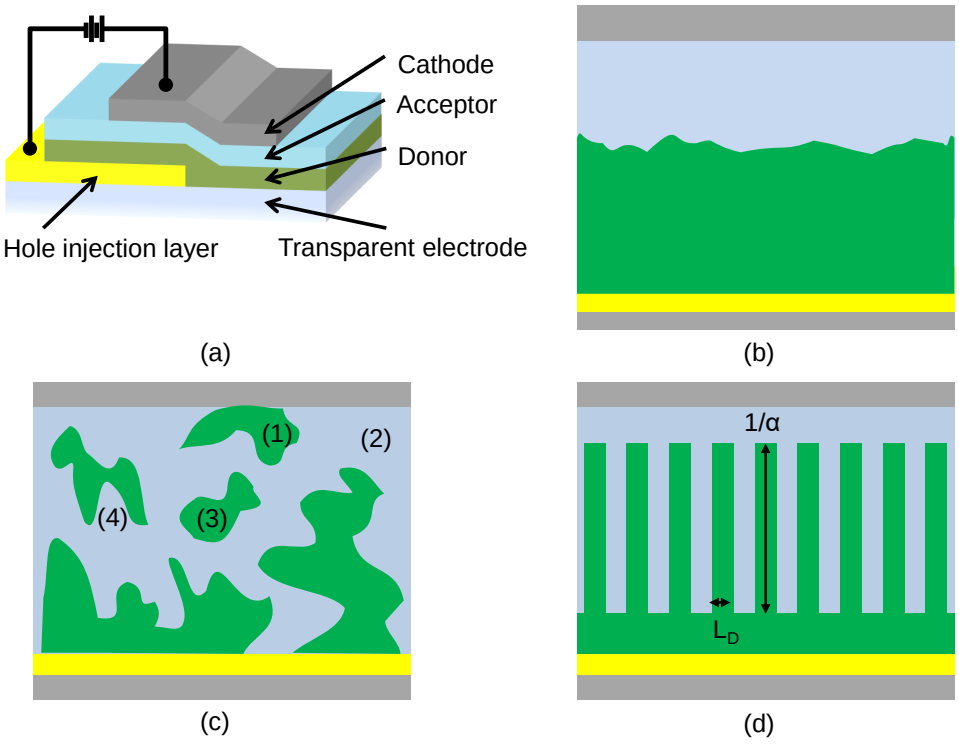


Figure 2.7: Schematics of OSC structures. (a). Schematic of a planar bilayer OSC structure. (b). Side view of planar heterojunction D-A blend film microstructure. (c). Side view of the bulk heterojunction D-A blend film microstructure, indicating different non-optimum microstructures and their influences on device performance: (1). The semiconductor in contact with the "wrong" electrode, which can cause charge leakage and result in limited voltage. (2). Large domains, which can make excitons decay before reaching interfaces, leading to limited charge separation. (3). Small or isolated domains, which can result in trapped charge recombination. (4). Disrupted molecular packing, which can lead to poor charge transport. (d). Side view of microstructure of an "ideal" comb-like bulk heterojunction solar cell [60].

heterojunction, a comb-like interpenetrating morphology for OSCs is designed. This model is the most widely desired morphology for D-A heterojunction structure [60]. The device thickness is the inversion of the absorption coefficient α, approximately 50 - 200 nm.

Summarized in Reference [46], the morphology of the donor-acceptor interfaces is influenced by several factors, including mixing ratio of donor and acceptor, choice of

solvents and additives (in the case of solution processing), concentration and molecular weight of compounds in the solution, drying condition of the films, heating of the substrates during deposition (in the case of vacuum deposition), and pretreatment of the substrates. However, it has to be checked individually on how the methods mentioned above affect the morphology.

2.3.3 Fundamental Principles of Solar Cell Characterization

The current-voltage (JV) characterization of solar cells is to measure the device's output current and voltage when it is connected to a load. A graph of the equivalent circuit of a basic solar cell is shown in Figure 2.8 (a). When there is no load, the potential difference across the device is zero. This is the so-called short-circuit condition. In this condition, the measured output current is defined as short-circuit current (J_{sc}) (See Figure 2.8 (b)). When the load for the device is infinitely large, the device is under the open-circuit condition, where no current is flowing. The measured output voltage is defined as open circuit voltage (V_{oc}), See Figure 2.8 (b).

When incident light of required energy illuminates the device, there is photocurrent generated inside the device. The external quantum efficiency (EQE) describes the probability of a photon with energy E to be absorbed and deliver an electron to the external circuit. The internal quantum efficiency (IQE) eliminates the absorption effect of EQE via dividing EQE by the solar cell stack absorption spectra to demonstrate the probability of a photon with energy E to be absorbed and delivers an electron to the external circuit. Sometimes the absorption spectra of the active layer are used instead of the stack absorption spectra, which depends on the definition of IQE [51]. J_{sc} can be derived as the integral of the incident light spectra and EQE, which is given in the following Equation 2.14:

$$J_{sc} = e \int j_{\nu,in}(E) EQE(E) d(E) \tag{2.14}$$

where e is the elementary charge and $j_{\nu,in}$ is the incoming photon flux.

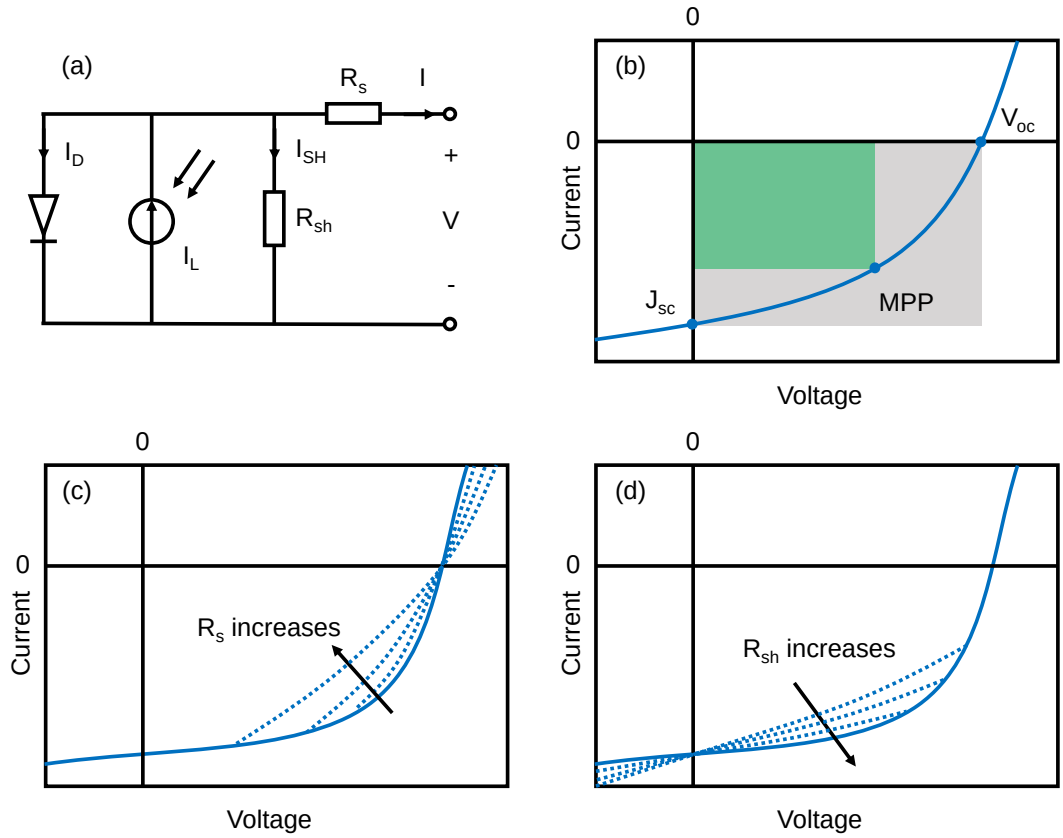


Figure 2.8: Equivalent circuit of a basic solar cell and graphs of current-voltage (JV) curves. (a). Equivalent circuit of a basic solar cell. R_s is the serues resistance, R_{sh} is the shunt resistance, I_D is the diode current, I_L is the light current, I is the measured current out of the positive terminal of the cell, and V is the measured voltage across the cell; (b). JV curve of a solar cell under illumination. MPP stands for the maximum power point. J_{sc} is the short-circuit current, and V_{oc} is the open circuit voltage; (c). JV curve change caused by a change in series resistance; (d). JV curve change caused by a change in shunt resistance. Adapted by permission from Reference [46]. Copyright 2014 Springer Nature.

A typical inorganic solar cell has a diode-like behaviour in the dark environment. The ideal JV curve can be described with the following Shockley equation:

$$J_{dark} = J_0 \left(e^{\frac{eV}{k_B T}} - 1 \right) \tag{2.15}$$

where $J_0 \propto exp(-E_g/k_B T)$ is the saturation current.

Thus, the JV curve of a typical inorganic solar cell can be derived via Equation

2.16:

$$J = -J_{sc} + J_0 \left(e^{\frac{eV}{k_B T}} - 1 \right) \tag{2.16}$$

However, in real OSC devices, the ideal diode-like condition is not always achievable in reality. Thus we have to introduce an ideality facter in Equation 2.16:

$$J = -J_{sc} + J_0 \left(e^{\frac{eV}{mk_B T}} - 1 \right) \tag{2.17}$$

where m is the ideality factor, whose value is generally between 1 and 2.

In addition, in real devices, the electrical resistance of the materials and leakage currents through the cells introduce the series resistance (R_s) and shunt resistance (R_{sh}) to the solar cells, respectively. The influence of series and shunt resistances can be found in Figure 2.8 (c) and (d). Equation 2.17 can be modified as:

$$J = -J_{sc} + J_0 \left(e^{\frac{e(V - JAR_s)}{mk_B T}} - 1 \right) + \frac{V - JAR_s}{R_{sh}} \tag{2.18}$$

where A is the area of the device, J is the current density.

The model developed above is a commonly used working model for OSCs. There exist other non-ideality factors, and they can be modelled based on their effects, e.g. S-kinks in JV curves caused by the injection/extraction barrier in solar cells.

Since power is the product of voltage and current, The optimum output power is reached when the product of voltage and current is the maximum. This point is defined as the maximum power point (MPP) (See Figure 2.8 (b)). The ratio of MPP and the product of J_{sc} and V_{oc} is the fill factor (FF):

$$FF = \frac{J_{MPP} V_{MPP}}{J_{sc} V_{oc}} \tag{2.19}$$

FF is a term to describe the quality of the solar cell. Because the power output at MPP (p_{MPP}) is highest, we can define PCE of the solar cell via dividing p_{MPP} by the

incident light power density p_S:

$$PCE = \frac{p_{MPP}}{p_S} \tag{2.20}$$

Due to the mismatch of the spectra between the solar simulator and the sun (well-known and frequently used as the AM 1.5G reference spectrum), as well as the different spectral responses between the reference and tested solar cells, it is vital to make an appropriate calculation of the difference between the measured and actual solar cell performances, which is known as the mismatch factor. A detailed calculation method can be obtained from literature [64, 65]. In this thesis, the fundamentals of mismatch calculation are not introduced in details to keep it concise, but the mismatch factors were calculated and reported where necessary.

Chapter 3

Interface Effects Inside Solar Cells

3.1 Interlayers in Organic Solar Cells

As discussed in 2.3.2, in both planar heterojunction and bulk heterojunction OSCs, the photoactive layer (i.e. donor and acceptor layers) is sandwiched between charge-selective layers on the anode and cathode sides [66]. Moreover, most OSC stacks have multilayer systems which are more complex than the simple D-A structure. The interfaces of the electrodes play a significant role in the performance of OSCs. Interlayers between the photovoltaic active layer and the electrodes inside OSC stacks have been studied meticulously as OSCs have developed [67, 68].

Generally speaking, interlayers can be divided into many categories depending on their positions and functions within the OSC stacks. Typical types are: (1) anode interface layer (AIL) which is sandwiched between the anode material and the donor material; (2) cathode interface layer (CIL) that is between the cathode material and acceptor material; (3) interconnecting layer (ICL) whose place is between the sub-cells in tandem solar cells; (4) D-A interlayer which is located at the interface of the donor and acceptor materials [67, 69, 70]. A schematic of different types of interlayers and their locations inside the solar cell stack is shown in Figure 3.1 (a).

According to the material properties, interlayers can be classified as five major categories (shown in Figure 3.1 (b)): inorganic metal oxides, metal salts and complexes, organic interlayers (including polymer and small molecule organic materials),

hybrids and composites, and promising alternatives [67].

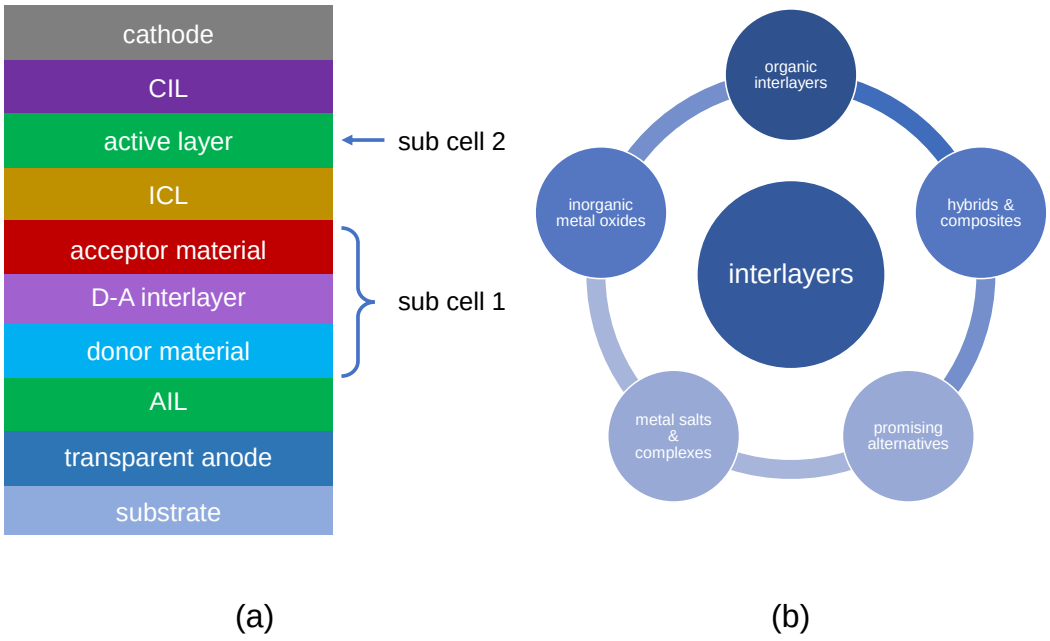


Figure 3.1: Schematic representation of different types and material categories of interlayers. (a). The locations of different types of interlayers in the device. AIL: anode interlayer; D-A interlayer: donor-accepter interlayer; ICL: interconnecting layer; CIL: cathode interlayer. (b). Different material categories of interlayers.

Interlayers have been shown to improve the performance [71,72] as well as the stability [70] of the OSC devices. AILs and CILs are often applied to amend and stabilize the work function of the electrodes. In addition, AILs and CILs in OSCs sometimes have multiple functions, such as electron blocking layers (EBLs), exciton blocking layers (ExBLs), hole transporting layers (HTLs), energy cascading layers (ECLs), as well as templating layers for morphology modification of the subsequent grown layer. These layers can also be tuned to act as a spacer layer to adjust the optical field intensity within the absorbing layers [73]. ICLs are designed for extracting charge carriers from the neighbouring sub-cells and then completing the charge recombina-

tion within them [67]. Interlayers between donor and acceptor layers sometimes serve as a surface modification layer to reduce the voltage loss [69].

A significant consequence of the insertion of interlayers is the change in morphology of the subsequent layer. Such a template layer can be used to modify the molecular ordering, which has a significant effect on the performance of the photovoltaic active layer, leading to higher absorption and more efficient charge carrier transport [74–77]. As a result, the PCE of OSCs can be improved [74, 78–80]. Furthermore, the energy levels of the electrode materials can also be modified by the template layer [78,81,82], which is important for device performance [81].

3.2 Electronic Effects

Interlayers inside OSCs have various functions, such as electron blocking effect, exciton blocking effect, hole transporting, and energy tuning. Among those diverse functions, a significant role that interlayers play is to block the excitons from being quenched [68]. This so-called exciton blocking effect makes the excitons get reflected rather than be quenched at the interface between absorber materials and AILs. The interlayer which has this effect is defined as an exciton blocking layer (ExBL).

MoO_x is a widely used interface modifier material in OSCs that facilitates an efficient hole contact between anode and the photovoltaic active layer [50, 54, 55, 83–85]. However, it is reported that the ITO/MoO_x anode quenches excitons generated in the active layer in OSCs if MoO_x and excitons can come into direct contact [86–88]. This quenching effect reduces the PCE of OSCs. By inserting an ExBL between the MoO_x layer and the photovoltaic active organic layer, the quenching effect can be effectively reduced by stopping excitons from reaching the MoO_x surface [89]. Several small organic molecules are shown to have this effect, e.g. rubrene, 4,4′-cyclohexylidenebis[N,N-bis(4-methylphenyl)benzenamine] (TAPC), and 4,4′-bis(N-carbazolyl)-1,1′-biphenyl (CBP) [86].

3.3 Microstructural Effects

The microstructural properties of organic semiconductor thin films such as domain size and molecular orientation have a vital influence on the device performance [81, 90, 91]. In order to modify the organic semiconductor thin films to have specific optical and electrical properties, controlled growth of organic semiconductor materials is of high interests to researchers in this field. There are quite a few techniques developed to control the growth of organic semiconductor thin films, including self-assembled monolayer (SAM) methods [92–94], micro-and nano-patterning methods [95–97], molecular template growth (MTG) methods [74, 81, 98], and substrate-induced phase (SIP) methods [98]. Most of these methods depend on the molecular force interaction of the substrate surface and the subsequently grown molecules. Besides, substrate temperature also plays an important role in the crystal growth of organic semiconductor thin films, especially those with different polymorphs at different temperatures [99, 100].

3.3.1 Molecular Template Growth (MTG) Effects

As Yang *et al.* reviewed, molecular template growth (MTG) is a method for fabricating high-quality organic semiconductor thin film with controllable morphologies, molecular orientations, electronic structures, and interface properties, to produce high-performance organic electronic and optoelectronic devices [74]. As shown in Figure 3.2 (a) and (b), MTG method uses an ultra-thin layer of small organic molecules as the template for other organic molecules to grow on. Via the influence of molecular interactions, e.g. van der Waals force, this ultra-thin template layer can induce the growth of subsequently-deposited thin film layers. Specifically for solar cells, the ideal molecular orientation is shown in Figure 3.2 (c). With the π-π stacking direction close to the light direction, OSCs will absorb the maximum amount of light, which gives rise to the highest PCE. In addition, this π-π stacking direction is beneficial

to the charge transport within the solar cell, leading to less voltage loss and better performance.

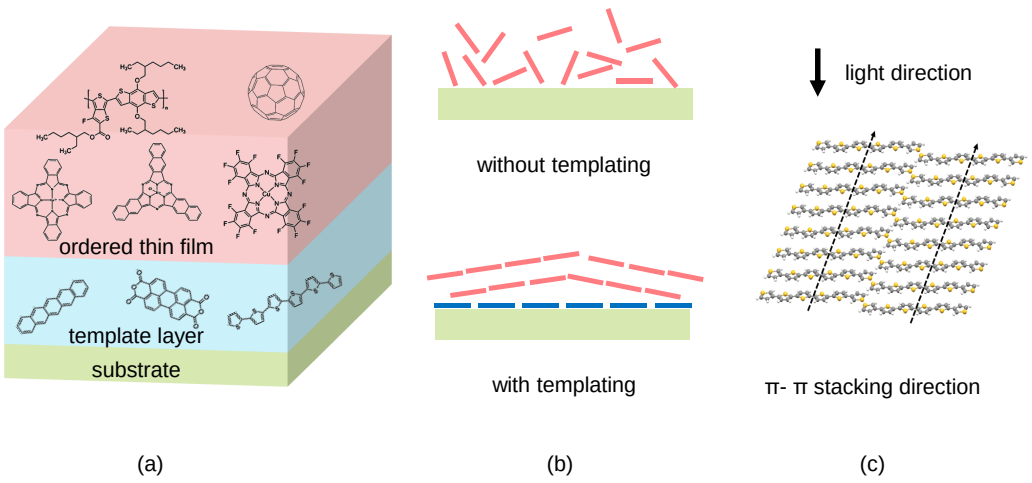


Figure 3.2: Schematics of molecular template growth (MTG) method. (a). Definition of each layer in MTG. (b). Effects with and without insertion of template layers. (c). An desirable orientation of the molecules (α-6T) within OSCs. The π-π conjugated direction close to the light direction helps increase the light absorption and as well improve the charge transport.

In contrast to the epitaxy growth method which is frequently utilized in inorganic thin film growth by matching the crystal unit cell parameters of the substrate and the subsequent-grown thin film, MTG technique is commonly applied in the growth of organic thin films. It takes advantage of van der Waals force, π-π interactions, H-bonding interactions, and other molecular interactions to induce the growth of high-quality organic thin films. Research on the MTG effect has been conducted with numerous organic small molecules, e.g. perylene-derivatives [101–103], acene [104, 105], phenyl- and thiophene-based molecules [100, 106, 107], and graphene/graphene oxide [108–111]. In practice, a template layer can take multiple functions in the solar cell stack. For instance, it has been reported that a template layer can be used to increase OSC efficiency, which in the meantime of acting as the HTL [112].

Although MTG method has such significant advantages discussed above, there are still some challenges to overcome: (1) The mechanism of MTG effect heavily depends on the materials being used. It is difficult to summarize a universal theory of MTG mechanism since different types of molecular interactions lead to different modes of MTG growth. (2). Side effects will occur when a molecular template layer appears in the device film stack. A template layer may have multiple functions in devices, some of which are not desirable. It is hard to design materials to meet all the demands. (3). Some template materials cannot form good crystalline film for templating, even though they may have some potential in templating the subsequent-deposited films. The concept of MTG should be extended to explain these phenomena.

3.3.2 Substrate-induced Phases (SIPs)

In the case of molecular materials grown on a substrate surface, new crystalline structures different from those in bulks can be formed, which are known as substrate-induced phases (SIPs) [98]. The definition of SIPs is different from SAMs and MTG effect, although they have many similarities. SIPs do not necessarily require a monolayer of self-assembly molecules for the subsequent layer to grow on. In addition, SIPs are not strictly the same as the MTG effect, since MTG method requires ultra-thin template layer whereas SIP method does not. The manipulation of SIPs can be a promising controlling method for modifying the organic semiconductor thin film properties. Molecules such as pentacene, perfluoropentacene, *p*-sexiphenyl, α-sexithiophene (α-6T), di-indenoperylene (DIP), tetrathiofulvalene-7,7,8,8-tetracyanoquinodimethane (TTF-TCNQ), and hexa-peri-hexabenzocoronene have been observed to have SIPs in the vicinity of a solid substrate [98]. Figure 3.3 shows typical SIPs of pentacene films.

Though there are numerous reports about the SIPs in organic semiconductors, the origins of SIPs are not well understood. This is because the formation of SIPs is

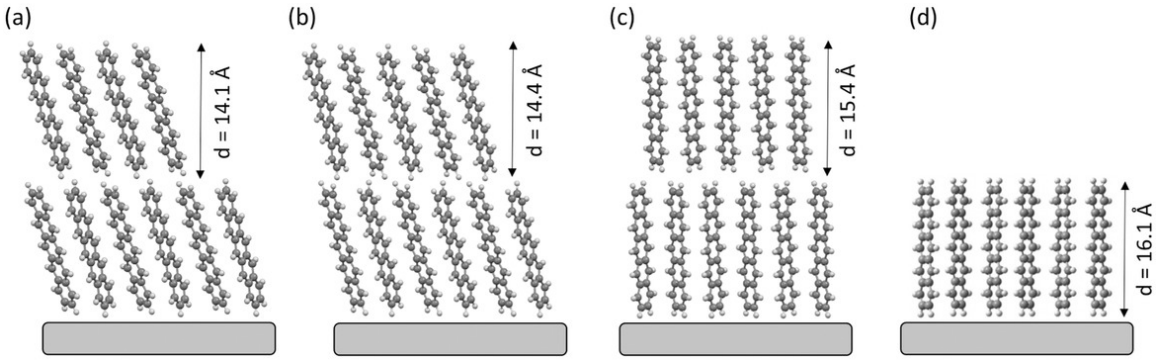


Figure 3.3: Various molecular packing structure of pentacene molecules in thin films: (a). Molecules in the LT phase with a tilted angle of $\approx 24°$ towards the substrate normal [113]. (b). Molecules in the HT phase with a tilted angle of $\approx 21°$ [114] towards the substrate normal. (c). Molecules in 15.4 Å SIP with a tilted angle of $\approx 3°$ towards the substrate normal [115]. (d). Molecules in monolayer of pentacene standing upright with no tilted angle towards to the substrate normal [116, 117]. Adapted by permission from Reference [98]. Copyright 2016 John Wiley and Sons.

influenced by several effects. One growth condition which will influence the SIPs is the formation of an interfacial or wetting layer on the substrate surface, which provides mediator for the subsequent layer to grow on [118]. This effect is very similar to the MTG effect, except that the template molecule is the same as the subsequent growing molecules. Another growth condition is the choice of the film deposition method. The films fabricated via vacuum deposition method are usually different from those made via solution process, due to the absence of the solvent influence on the films [119]. Besides, the parameters chosen in the film deposition also play an essential role in the formation of SIPs, e.g. deposition rate [120]. Finally, the properties of the substrate are also crucial to the growth of SIPs. These properties include the substrate geometry, roughness, chemical properties, and substrate temperature [121, 122]. The origins of the SIPs mentioned above usually influence the nucleation process of the crystals. This change in the nucleation procedure will further control the growth of SIPs.

3.3.3 Polymorphs of Organic Semiconductors

As discussed in Section 2.3.2, molecular orientation and molecular packing inside the organic semiconductor thin film is vital to their optical and electronic properties. Many organic compounds have multiple possible crystal structures, i.e. polymorphism. Polymorphism is a common phenomenon in crystals, and it has been extensively studied. It exists inside organic thin films, too. Materials such as pentacene [123, 124], rubrene [125, 126], tetracene [127, 128], α-6T [120, 122, 129], DIP [130, 131], copper phthalocyanine (CuPc) [132, 133] have shown the existence of polymorphism. However, much less research has been done about the relationship between polymorphism and device performance. Different polymorphs of the same organic compound tend to show different properties, e.g. different absorption properties arising from molecule orientations [134, 135]. Besides, changes in π-π stacking mode within crystal domains can result in orders of magnitude difference in the mobility of charge carriers [136]. Thus, it is crucial to control the polymorphism of organic semiconductor films to achieve desirable properties. However, it is challenging to achieve this goal, as different polymorphs of the same organic semiconductor have closely matched cohesive energies and low kinetic barriers to solid-solid transformation due to the weak interaction between molecules [137]. Nevertheless, several methods have been developed to control the polymorphism, including the tuning of film thickness [138], MTG [139, 140], tuning of substrate temperature [120, 141], the SIP method [98, 142], the SAM method [143, 144], and solvent annealing method [145, 146].

Chapter 4

Materials and Methods

This chapter provides a brief description of the materials as well as experimental methods and techniques used in this thesis. A schematic presentation describing the sample fabrication is shown in Figure 4.1. The entire experimental procedure includes substrate cleaning, UV-Ozone treatment, thermal evaporation, encapsulation (for solar cells), and characterisations. Information about the materials is reported as provided by the suppliers.

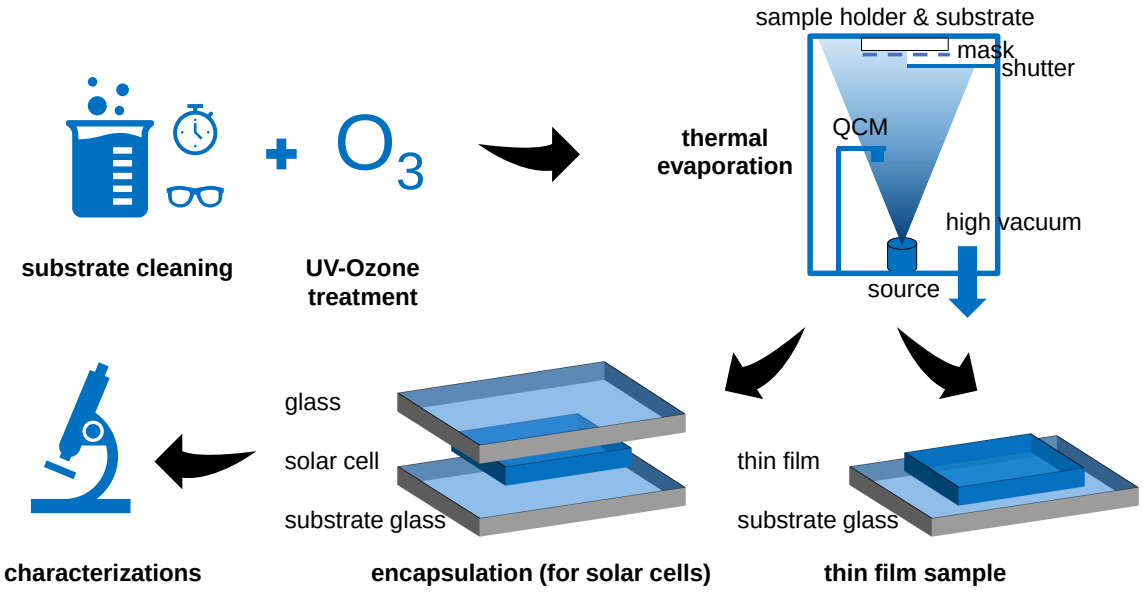


Figure 4.1: Schematics of the sample fabrication procedure.

4.1 Materials

Several small molecule organic molecules were used in this thesis, including hexapropyltruxene, SubPc, chloroboron subnaphthalocyanine (SubNc), α-6T, bathophenanthroline (BPhen), N,N,N′,N′-tetrakis(4-methoxy-phenyl)benzidine (MeO-TPD), C60, and poly(3,4-ethylenedioxythiophene) polystyrene sulfonate (PEDOT:PSS). The chemical structures of molecules used in this thesis are summarized in Figure 4.2.

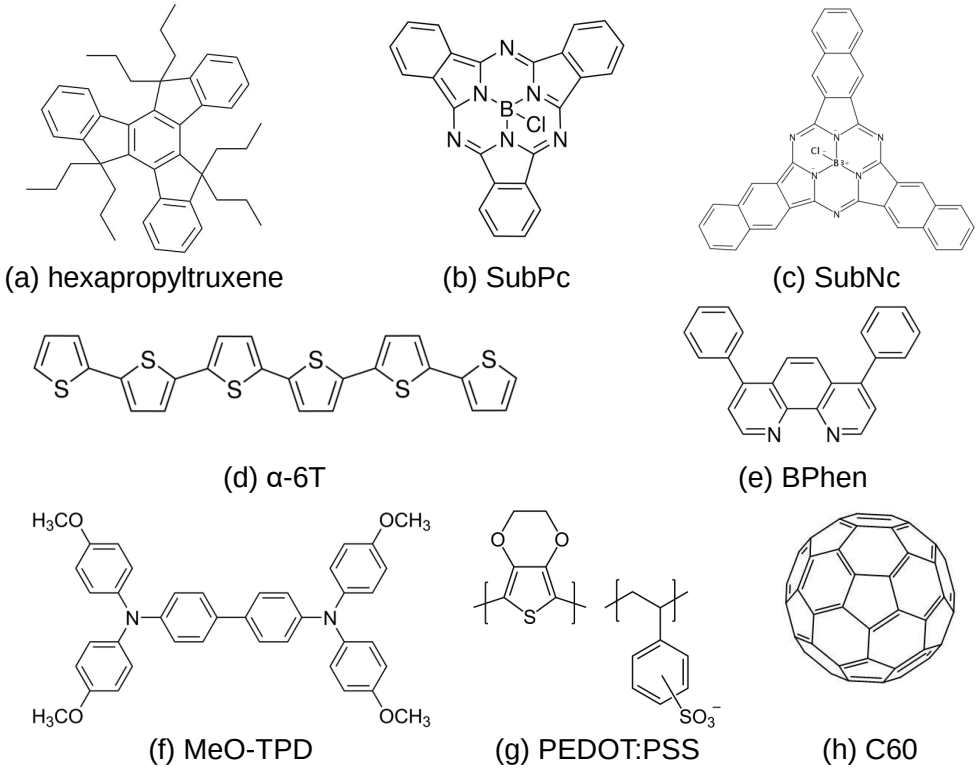


Figure 4.2: Chemical structures of the organic materials used in this thesis. (a). hexapropyltruxene, (b). boron subphthalocyanine chloride (SubPc), (c). chloroboron subnaphthalocyanine (SubNc), (d). α-sexithiophene (α-6T), (e). bathophenanthroline (BPhen), (f). N,N,N′,N′-tetrakis(4-methoxy-phenyl)benzidine (MeO-TPD), (g). poly(3,4-ethylenedioxythiophene) polystyrene sulfonate (PEDOT:PSS), (h). buckminsterfullerene (C60).

4.1.1 Hexapropyltruxene

Hexapropyltruxene is an alkylated derivative of the parent truxene molecule, in which the six propyl groups are positioned at the three C sp^3 sites of the compound [147]. Truxene derivatives have been applied as photosensitizers [148], electron donor molecules [149–151], and hole transporting layers [152] in OSCs due to their good thermal stability, optoelectronic properties and ease of being modified [152–154]. The molecule structure of hexapropyltruxene is shown in Figure 4.2(a). Hexapropyltruxene used in this thesis was synthesised by Dr Roisin E. Brown in the University of Strathclyde, following Goubard et al. 's report [147]. The material for single film UV-vis measurement had a purity of more than 95%, determined by proton nuclear magnetic resonance (1H NMR). The material for cyclic voltammetry, multilayer thin film, and device fabrication was triple purified by thermal sublimation under vacuum.

4.1.2 Boron Subphthalocyanine Chloride (SubPc)

Boron subphthalocyanine chloride (SubPc) has an aromatic bowl-shaped small molecular structure comprising three diimino-isoindoline units around a central boron atom [155, 156]. The chemical structure of SubPc is shown in 4.2 (b). It is a typical small organic molecule being extensively studied for organic electronic applications. SubPc can be used as a donor as well as acceptor material in small molecule organic solar cells [157, 158]. Power conversion efficiency as high as 8.4% was achieved with SubPc in fullerene-free organic solar cells indicates its potential of being an excellent PV material [159]. The SubPc used in the experiments of this thesis was purchased commercially in its sublimed versions (state purity $>$ 99%, from Luminescence Technology Corp., Taiwan).

4.1.3 A-sexithiophene (α-6T)

A-sexithiophene (α-6T) is a widely used small organic molecule in OSCs and organic transistors [159, 160]. Shown in Figure 4.2 (d) and Figure 4.3 (a), α-6T is a linear molecule with six thiophene subunits. It forms poly-crystalline films when deposited on substrates. Previous research reports that it has two single-crystal phases: a low temperature (LT)-phase and a high temperature (HT)-phase [161–163]. The crystal unit cell structures of LT-phase and HT-phase are shown in Figure 4.3 (b) and (c), respectively. These two phases have different lattice parameters and tilt angle ϕ (which is defined between the long molecular axis and the small basal plane of the unit cell [134,164]). The absorption behaviours of these two polymorphs are different [134]. Moreover, previous research by Servet *et al* suggests that there exist another four different polymorphs (α, β, γ, and δ) especially in α-6T thin films [120], among which the β-phase is kinetically favored [129]. However, according to the reported crystal lattices, the γ- and δ-phases are very similar to LT- and HT-phases. Other researches also mention that α-6T has several monoclinic unit cell structures [135, 162, 163] and a mesophase at high substrate temperature during evaporation [122]. A summary of the lattice parameters of different polymorphs described in the literature is included in Table 4.1.

Table 4.1: Crystal structures of α-6T polymorphs reported in literature.

Name	a (nm)	b (nm)	c (nm)	α (°)	β (°)	γ (°)	Tilt angle (°)	Lattice spacing (Å)	Type	Reference
LT-phase	4.4708	0.7851	0.6029	90	90.76	90	65.9	22.35	single crystal	161, 134
HT-phase	0.914	0.568	2.067	90	98	90	56.3	20.67	single crystal	162, 134
α-phase	-	-	-	-	-	-	-	24.4	thin film	120
β-phase	0.5667	0.78	4.7288	90	100.6	90	-	23.7	thin film	120, 165, 76
γ-phase	-	-	-	-	-	-	-	22.42	thin film	120
δ-phase	-	-	-	-	-	-	-	36.3	thin film	120
mesophase	-	-	-	-	-	-	-	-	thin film	122

The α-6T used in the experiments of this thesis was purchased commercially in

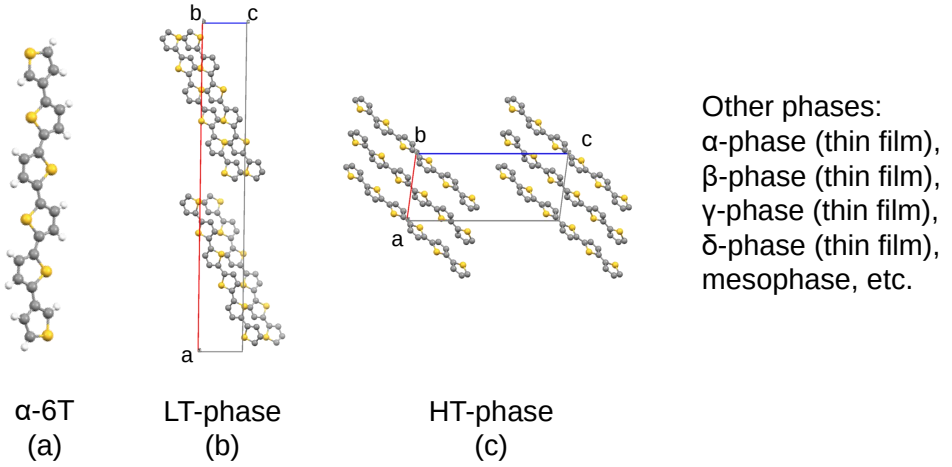


Figure 4.3: Crystal structures of α-6T polymorphs. (a). Chemical structure of α-6T. (b). Crystal unit cell of α-6T LT-phase. (c). Crystal unit cell of α-6T HT-phase.

its sublimed versions (state purity $>$ 99%, from Luminescence Technology Corp., Taiwan).

4.1.4 Other Materials

Other small molecule organic materials used for thermal evaporation (SubNc, C60, MeO-TPD, and BPhen, shown in Figure 4.2(c)(e)(f)(h)) were purchased commercially in their sublimed versions (state purity $>$ 99%, from Luminescence Technology Corp., Taiwan). They were used along with MoO_x (Luminescence Technology Corp., Taiwan) and Aluminium pellets (K. J. Lesker) as received. PEDOT:PSS (shown in Figure 4.2(g)) solution (PEDOT:PSS ratio by weight is 1:6) was purchased from Heraeus Holding GmbH, Germany with the product name as CLEVIOS P VP. AI 4083. PEDOT:PSS solution was filtered by a 0.45 μm polytetrafluoroethylene (PTFE) filter before the spin coating process.

4.2 Sample Preparation

4.2.1 Fabrication Facilities

A simplified schematic graph of the thermal deposition chamber is shown in Figure 4.4(a), which illustrates the basics of the vacuum thermal evaporation facility. As shown in this figure, a typical deposition chamber is made of these parts: a vacuum chamber, material sources, quartz crystal microbalances (QCMs), sample holder, masks, shutter, and a pump system (which consists of a scroll pump to provide the background vacuum and a turbopump to generate the high vacuum). A typical evaporation procedure is: After the cleaned substrates and source materials are loaded into the vacuum chamber, the chamber will be pumped down by the pump system to its base vacuum pressure. Then the materials inside the sources are heated up to their sublimation/evaporation point via resistive heating. The deposition rates of the materials are monitored by QCMs, and we control the thickness of thin films via switching the shutter open/closed. Once the designed thin-film stacks are fabricated, the chamber vacuum is vented, and the fabricated samples are transferred to a glove box or the air.

Shown in Figure 4.4(b)-(f), three different vacuum chambers were used to fabricate our samples. They were: a multi-source bell-jar type "B30" vacuum deposition chamber (base pressure approx. 5×10^{-6} mbar, Oerlikon Leybold Vacuum Dresden GmbH, Germany) with major parts upgraded (CreaPhys GmbH, Germany). Samples fabricated in this chamber are exposed to air when being removed from the chamber for further measurements, (Vacuum Chamber A (VC-A), shown in 4.4(b)); a multi-source vacuum deposition chamber (base pressure approx. 5×10^{-7} mbar, CreaPhys GmbH, Germany) connected to a glovebox (LC Technology Solutions Inc., USA) where samples can be loaded from and unloaded to N_2 atmosphere without exposure to air after sample fabrication (Vacuum Chamber B (VC-B), shown in 4.4(d)-(f)). VC-B has an attachment specially designed for connecting an in-situ spectroscopic ellipsometer

(J.A. Woollam Spectroscopic SE RC2); a small dual-source vacuum deposition chamber ("MINERVA" system, base pressure approx. 5×10^{-7} mbar, co-developed with K.J. Lesker Ltd., UK) specially designed for in-situ GIWAXS measurement (Vacuum Chamber C (VC-C), shown in 4.4(c)) at Diamond Light Source [166].

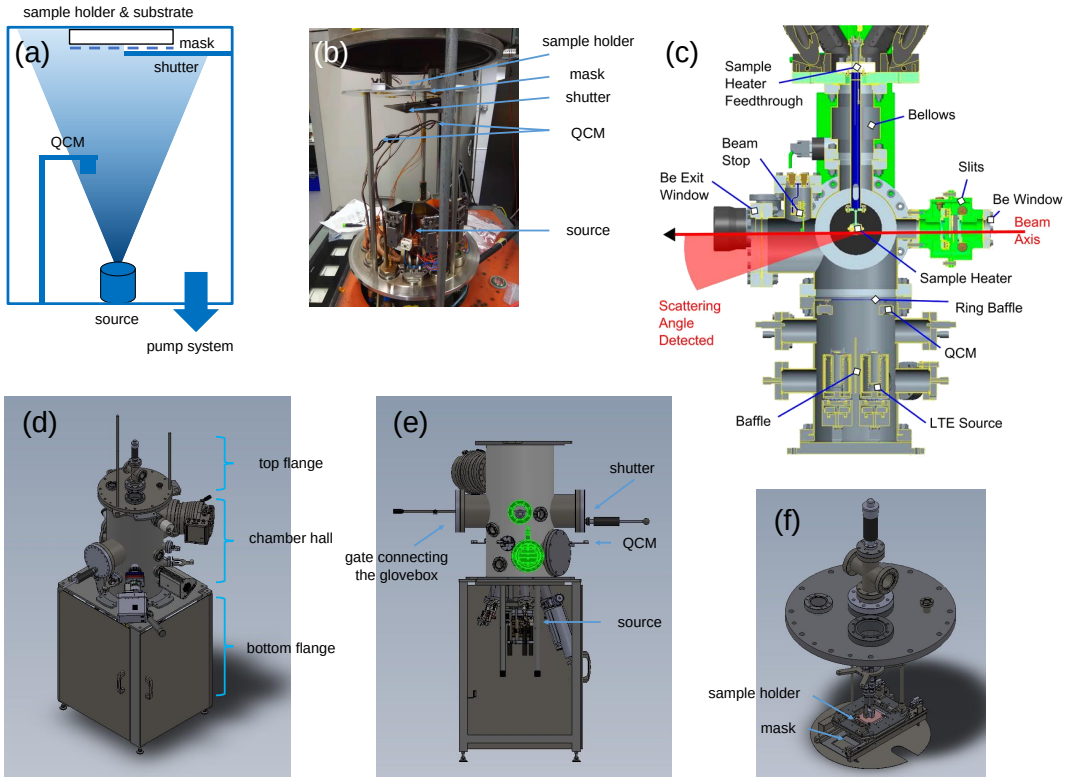


Figure 4.4: Vacuum thermal deposition chambers used in this thesis. (a). A simplified graph of the deposition chamber. (b). A picture of the B30 chamber (VC-A). (c). A cut-through schematic presentation of the "MINERVA" system (VC-C). Adapted by permission from Reference [166]. Copyright 2017 AIP Publishing. (d)-(f). Schematic presentations of VC-B. These figures are modified from Reference [167].

4.2.2 Fabrication Procedure

Si wafers (IDB Technologies ltd., UK), Corning Eagle XG glass substrates and ITO-coated glass substrates (both from TFD Inc., USA), were purchased commercially for use in this thesis.

Substrates (glass/ITO-coated glass/Si wafer) were sonicated in 2.5% Hellmanex III soap solution, deionized water (DIW), acetone and isopropyl alcohol (IPA) each at 50 °C for 10 minutes. Subsequently, the substrates were UV-Ozone cleaned for 10 minutes before the deposition of films.

To prepare the PEDOT:PSS substrates used in the experiments, 100 μl of filtered PEDOT:PSS solution was spin-coated on each UV-Ozone treated substrate at a rate of 5000 rpm for 60 s (acceleration rate is 12000 rpm^2). Then the substrate was immediately transferred to a 120 °C hotplate to be thermally annealed for 10 min. The annealed PEDOT:PSS samples were then transferred into the glovebox for being loaded into the vacuum deposition chambers.

After the substrates were loaded into one of the vacuum deposition chambers, organic layers as well as MoO_x and metal electrodes (full film stacks will be explained in each chapter) were thermally evaporated under vacuum. The fabricated devices in VC-B were then encapsulated with a glass cover slide (AMG Tech ltd, South Korea) and epoxy glue (UHU PLUS Endfest 2-K-Epoxidharzkleber, UHU GmbH & Co KG, Germany) in a N_2-filled glovebox for further measurements.

4.3 Material and Thin Film Characterization

4.3.1 X-Ray Diffraction

In this section, essential background knowledge of XRD is summarised to help the reader better understand this thesis. It is based on the book Jens Als-Nielsen and Des McMorrow, *Elements of modern X-ray physics*. John Wiley & Sons, 2011 [168]; and Armel Le Bail, *Powder diffraction: theory and practice*. Royal Society of Chemistry, 2008 [169].

4.3.1.1 Fundamentals and Bragg's Law

Figure 4.5 shows a simplified sketch of a typical XRD experiment instrument. The whole instrument consists of an X-ray source, several monochromators, a sample holder, a crystal (sample), and a detector. The incidence X-ray is generated via the X-ray source, passes through monochromators (not included in Figure 4.5), and reaches the sample, where it gets diffracted by the lattice of the atoms. The diffracted X-ray will be collected by the detector, which is further analysed via the computer to reveal the structure of the characterised matter.

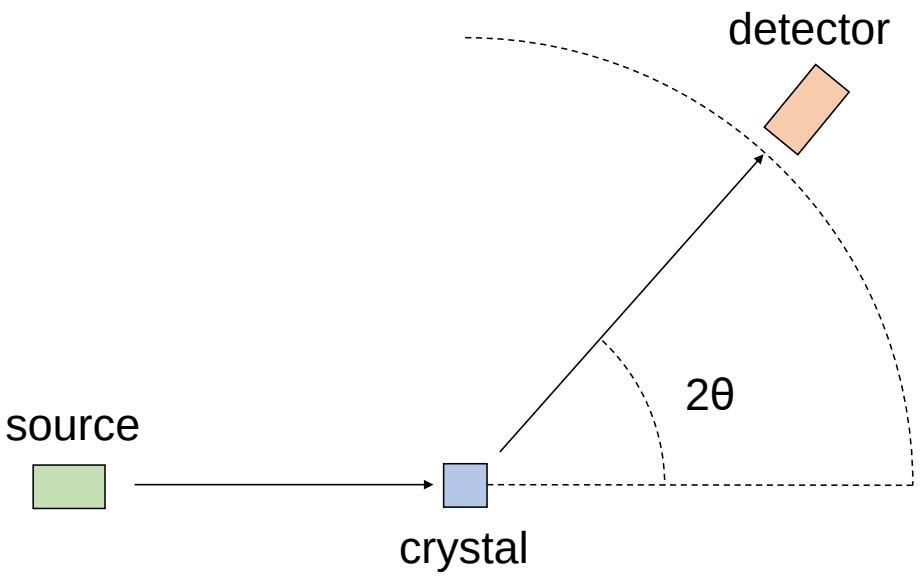


Figure 4.5: Schematics of XRD technique. A X-ray source, a crystal (sample), and a detector are included in this figure. 2θ represents the angle between the incidence and reflected X-rays. Monochromators are omitted.

.

The basics of the XRD can be attained via textbooks talking about solid-state physics. Introductions about basic concepts in solid-state physics, e.g. reciprocal lattice, Miller indices are skipped in this thesis. However, Bragg's law is explained, which is frequently used to analyse XRD data.

Using Bragg's law is considered the easiest way to access the structure information in powder diffraction [170]. It describes XRD in terms of a reflection of X-rays by sets of lattice planes, which have the same Miller indices and are parallel to each other. Illustrated in Figure 4.6, X-rays are specularly reflected by the lattice planes of the crystallite. Because of the high energy of X-rays, they penetrate the crystalline, and additional reflection occurs at the parallel lattice planes, leading to a constructive interference when the distance of the light travelled (Δ=PN+NQ) equals to a multiple n of the wavelength λ ($n = 0, \pm1, \pm2, ...$). Then we have:

$$\Delta = n\lambda \tag{4.1}$$

Δ can be derived from the distance between two parallel planes, which is

$$\Delta = 2dsin\theta \tag{4.2}$$

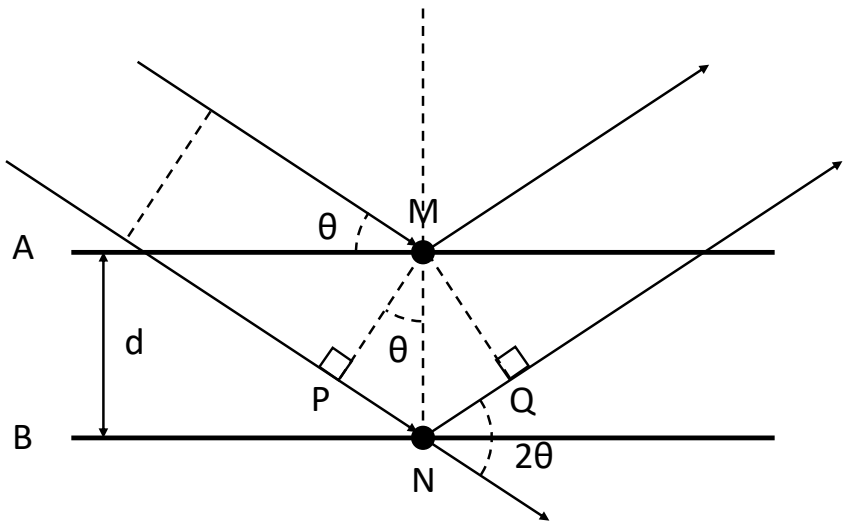


Figure 4.6: Illustration of the geometry used for the simplified derivation of Bragg's law. AM and BN are two parallel lattice planes with a distance of d. θ is the angle between the incidence X-ray and the lattice plane.

.

Combining Equation 4.1 and Equation 4.2, we have the famous Bragg's law:

$$n\lambda = 2dsin\theta \tag{4.3}$$

This illustration is just a simplified derivation of the Bragg's law, although it leads to the right answer. A more complex discussion can be found in Reference [169].

Bragg's law is very useful in our analysis of the XRD and GIWAXS data to calculate the distance between two parallel lattice planes of the small organic molecule crystallites. It has a frequently-used derivation as followed:

$$|q| = \frac{4\pi sin\theta}{\lambda} = \frac{2\pi}{d} \tag{4.4}$$

where q is the momentum transfer on scattering (The notation Q is also used in this thesis for this parameter.).

XRD profile contains much information about the crystalline being characterised. There are several practical tricks to analyse XRD data. Take the ordinary powder XRD scan result for example. The peak locations will indicate the crystallites planes according to Bragg's law. The intensity of the peaks is a sign of the crystallinity of the crystallites. Moreover, the broadening of the peak information can be used to analyse the size of the crystallites.

4.3.1.2 Scherrer Equation

Another useful equation used to analyse the size of the crystallites domains inside thin films is the Scherrer equation. It is a formula used to estimate the size of sub-micrometre particles, or crystallites in a solid via the broadening of the diffraction peak. The equation is as follows:

$$\tau = \frac{K\lambda}{\beta cos\theta} \tag{4.5}$$

where τ stands for the mean size of the crystallites domains; K is defined as the shape factor, for sphere-like features it has the value of 0.89 [171, 172]; λ is the X-ray

wavelength; β is the line broadening at full width at half maximum (FWHM) with subtracting the instrumental line broadening (in radians); θ is the Bragg angle.

4.3.1.3 Technical Parameters

XRD measurements were used in this thesis to identify the crystal structure inside thin films. Two instruments were used: (a). A Phillips X'pert Pro MRD with Cu as X-ray source. The wavelength of K-α is 1.540598 Å. (b). A Rigaku SmartLab system (Rigaku Innovative Technologies Europe s.r.o.) with Cu as X-ray source. The wavelength of K-α is 1.540598 Å. Gaussian function in Origin software was used to fit the results. Detailed scanning parameters can be found in relevant chapters.

4.3.2 Grazing-incidence Wide-angle X-ray Scattering (GIWAXS)

XRD measurement is vital to the characterisation of the crystallites structure inside thin films. However, because XRD measurement only reveals the crystallite structural information of the thin film in the out-of-plane direction, researchers may have to turn to the GIWAXS technique to characterise the 2D structural information of the thin film, i.e. in both in-plane and out-of-plane directions. In this section, the basics of GIWAXS technique are summarised, which is mainly based on the review paper: Jonathan Rivnay et al. *Quantitative determination of organic semiconductor microstructure from the molecular to device scale.* Chemical reviews 112.10 (2012): 5488-5519. [173] and the book: Mario Birkholz. *Thin film analysis by X-ray scattering.* John Wiley & Sons, 2006 [171].

4.3.2.1 Fundamentals of GIWAXS

GIWAXS is an X-ray surface structural measurement technique used to probe molecular length scales. A sketch of the experimental basis is shown in Figure 4.7 (a) [173]. A typical GIWAXS experiment set-up consists of a light source, a sample holder, a 2D detector, and a control unit. It is very similar to the set-up of XRD. Because of

the demand for high resolution to identify the weakly scattering samples such as organic thin films, synchrotron radiation sources are often used to perform the GIWAXS measurement. The angle α in the sketch is the incidence angle of the X-ray, which is slightly larger than the critical angle of the characterised material but smaller than the critical angle of the substrate, usually between 0.1 ° and 0.3 °. L is the distance between the sample and the 2D detector. The distance is normally between 300 mm to 400 mm, whose actual value depends on the experimental design. In this thesis, the actual GIWAXS set-up parameters are different in each experiment, so they are indicated separately in the relevant experimental chapter.

4.3.2.2 GIWAXS Analysis Technique

Similar to XRD, when incident X-rays penetrate a thin film, a number of them are diffracted by the atom lattice planes in GIWAXS measurement. The constructive interference of reflections from adjacent planes results in a high intensity spot on the 2D detector. The angle where the diffraction occurs is determined by the lattice plane distance (d spacing). In the meantime, the direction/position of the diffracted pattern is determined via the orientation of corresponding lattice planes. The magnitude of the scattering vector is defined by the well-known Bragg equation in Equation 4.4.

Shown in Figure 4.7 (a), the diffraction pattern observed in the normal direction of the sample plane (q_z) describes the periodicity of the lattice planes out of the substrate plane. Similarly, the diffraction pattern observed in the horizontal direction of the sample plane (q_{xy}) illustrates the periodicity of the lattice planes in the substrate plane [173]. Thus, from the patterns of observed signal intensity maps, researchers can quickly analyse the crystallites structure of the sample. However, due to the scattering geometry, nominal cuts along q_z direction on the 2D detector (which are images on a flat coordinate plane) do not match with the actual specular scans of the planes (which are images on the sphere-curved coordinate plane). Instead, they have slight shifts in degrees compared with the exact scattered patterns. The similar effects

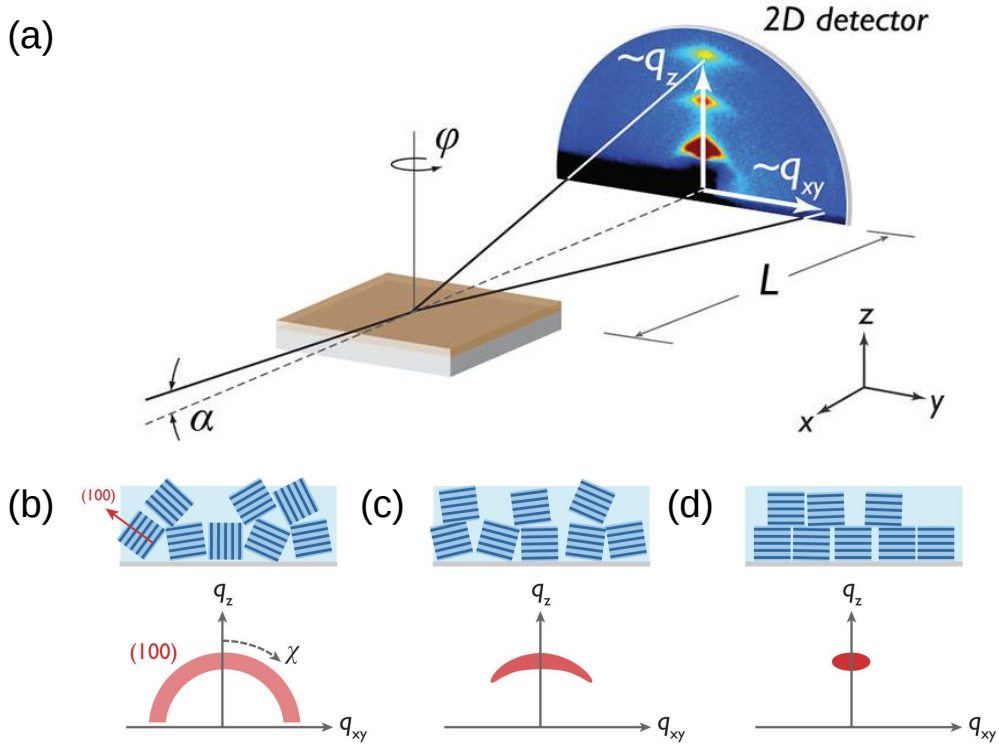


Figure 4.7: Schematics of GIWAXS technique. (a). GIWAXS scattering geometrics on thin films, α is the incidence angle, and φ is an in-plane azimuthal rotation; (b). Randomly oriented arrangement of crystallites in thin films, with no preference for a specific crystallographic orientation (100) with respect to the substrate normal produce rings in the diffraction patterns, χ is the polar angle; (c). Textured or oriented films with a distribution of crystallites orientations produce arcs of diffracted intensity; (d). Highly oriented films produce spots or ellipses. Adapted with permission from Reference [173]. Copyright 2012 American Chemical Society.

also apply to q_{xy}. Thus, the raw data are usually corrected by the analysis software. In this thesis, DAWN software is used to process the raw GIWAXS data [174, 175].

Figure 4.7 (b)-(d) show different diffracted patterns of the scattering. (b) illustrates a randomly oriented arrangement of crystallites in thin films leads to power rings in the diffraction pattern; (c) demonstrates that textured or semi-oriented films with a distribution of lattice plane orientations result in arcs in the diffraction pattern; (d) expresses highly oriented films produce small spots or ellipses in the diffraction

pattern.

Molecular Crystal Packing

To identify the molecular packing of the poly- or semi-crystalline films, the unit cell parameters such as size, symmetry, and basis or atomic arrangement are required in advance, which can be obtained from databases such as Cambridge Crystallographic Data Centre (CCDC) and Crystallography Open Database (COD) [176, 177].

The diffraction of GIWAXS also obeys the Bragg's law which is expressed by the Bragg condition (Equation 4.4). The Bragg condition links the allowed q values (q_B) to the interplanar lattice spacings in the crystallites [178, 179]. Reciprocal lattice vectors ($\mathbf{a}^*$, $\mathbf{b}^*$, $\mathbf{c}^*$) are used to calculate the q values. The reciprocal lattice vectors can be calculated by the real lattice vectors ($\mathbf{a}$, $\mathbf{b}$, $\mathbf{c}$) as:

$$\mathbf{a}^* = 2\pi \frac{\mathbf{b} \times \mathbf{c}}{\mathbf{a} \cdot (\mathbf{b} \times \mathbf{c})} \tag{4.6}$$

$$\mathbf{b}^* = 2\pi \frac{\mathbf{c} \times \mathbf{a}}{\mathbf{a} \cdot (\mathbf{b} \times \mathbf{c})} \tag{4.7}$$

$$\mathbf{c}^* = 2\pi \frac{\mathbf{a} \times \mathbf{b}}{\mathbf{a} \cdot (\mathbf{b} \times \mathbf{c})} \tag{4.8}$$

Thus, q values can be written in reciprocal lattice vectors as:

$$\mathbf{q}_{hkl} = (h\mathbf{a}^* + k\mathbf{b}^* + l\mathbf{c}^*) \tag{4.9}$$

With Equation 4.6,4.7,4.8, and 4.9, researchers can reconstruct the real space unit cell from the GIWAXS data or simulate the GIWAXS scattering patterns from the real space unit cell by calculating. In practice, there are several program packages available such as SimDiffraction and Diffraction Pattern Calculator (DPC) toolkit [180, 181]. In this thesis, DPC toolkit is used to calculate the diffraction spot positions of the α-6T polymorphs.

4.3.3 Spectroscopic Ellipsometry

Spectroscopic ellipsometry is an optical characterisation technique that investigates light reflection (or transmission) from samples [182]. The key feature of spectroscopic ellipsometry is that it measures the difference of the polarised light before and after interacting with the sample (reflection or transmission). This section is based on the book: Hiroyuki Fujiwara, *Spectroscopic ellipsometry: principles and applications*. John Wiley & Sons, 2007 [182] and the book: Daniel Abou-Ras, Thomas Kirchartz, and Uwe Rau, eds. *Advanced characterisation techniques for thin-film solar cells*. John Wiley & Sons, 2016 [183].

4.3.3.1 Fundamentals of Spectroscopic Ellipsometry

As shown in Figure 4.8, a typical ellipsometry instrument set-up includes a light source, monochromators (optional), a polariser, compensators (optional), samples, an analyser, and a detector. The light from the light source passes through the polariser and gets linearly polarised. Then the light can go through the optional compensator and is reflected by the thin film sample. The reflected light passes through the optional compensator and analyser (another polariser) then reaches the detector. The compensators are optional. Some ellipsometer systems are equipped with phase modulators instead. Because the result of this technique is wavelength-related, a monochromator should be applied in conjunction with the light source or a spectrometer should be used together with the detector [183].

Spectroscopic ellipsometer measures the amplitude ratio ψ and phase difference Δ between p- and s- polarised light waves. These parameters are defined as ellipsometry angles. With further optical model simulation based on the measured data, researchers can calculate the optical constants (complex refractive index n and k ($N = n - ik$), complex dielectric constant ε_1 and ε_2 ($\varepsilon = \varepsilon_1 - i\varepsilon_2$), absorption coefficient α ($\alpha = 4\pi k/\lambda$)) and film structure (film thickness and surface roughness).

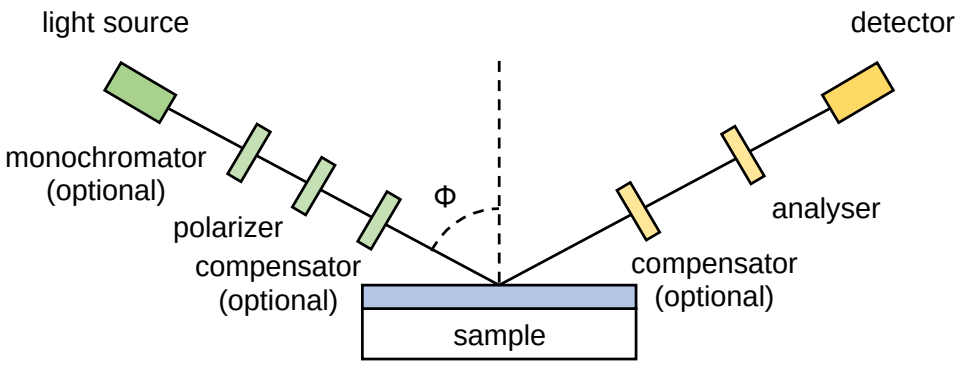


Figure 4.8: Schematics of ellipsometry technique. ϕ is the incidence angle.

.

Moreover, other information such as the bandgap (E_g), grain size, carrier concentration, carrier mobility, and conductivity can be analysed based on this information. Besides, the applications of ellipsometry have been expanded with the development of this technology. Particularly, nowadays, it provides the potential to analyse on the atomic scale at real-time measurement.

The advantages of spectroscopic ellipsometry technique include high precision (thickness sensitivity is as high as 0.1 Å), nondestructive and fast measurement, wide application area, and rich out-put information of the sample. However, the limitations of this technique should as well be considered, such as indirect measurement, complicated data analysis, low spatial resolution (spot size: several mm), and difficulty in the characterisation of low absorption coefficients (α<100 cm^{-1}).

4.3.3.2 Data Analysis of Spectroscopic Ellipsometry

Figure 4.9 shows a typical optical model, including air, a thin film, and a substrate. N_0, N_1, N_2 are the complex refractive indices of air, the thin film, and the substrate,

respectively. This model illustrates the light's passage through the thin film sample and shows the optical interference where the optical wave is superimposed.

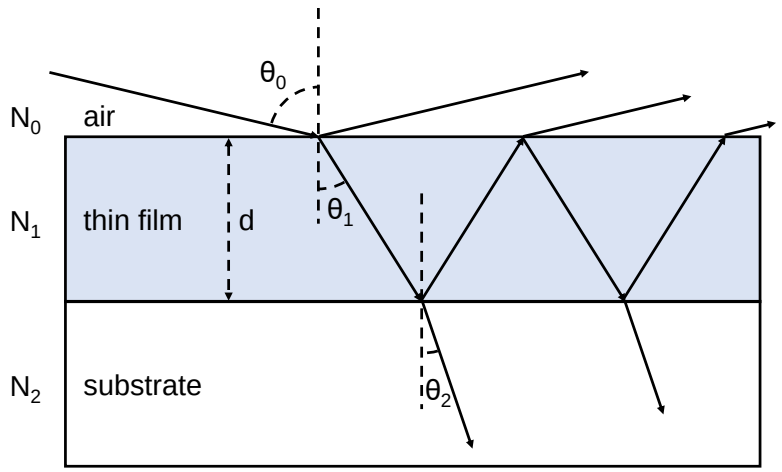


Figure 4.9: Optical model including an air/thin film/substrate structure. θ_0 is the incidence angle of the light. θ_1 and θ_2 are the refraction angles of the light. N_0, N_1, and N_2 are the complex refractive indices of the air, the thin film, and the substrate, respectively.

In ellipsometry, the measured parameters ψ and Δ have the relationship as:

$$\rho \equiv \tan\psi \exp(i\Delta) = r_p/r_s \tag{4.10}$$

where r_p and r_s stand for the complex amplitude reflection coefficients of the sample for linear polarization states. p and s indicate that the electric field is parallel and perpendicular to the plane of incidence, respectively [183]. In the optical model, ρ is expressed as:

$$\tan\psi \exp(i\Delta) = \rho(N_0, N_1, N_2, d, \theta_0) \tag{4.11}$$

where the values of N_0, N_2, θ_0 are already known. The layer thickness d can be determined by analysing the interference pattern in the low-energy range. Thus, in Equation 4.11 only the complex refractive index $N_1 = n_1 - ik_1$ is unknown. In this

case, n_1 and k_1 can be determined from the measured values ψ and Δ. In the high-energy range of the interference pattern, optical interference is negligible because of the increase of the light absorption of the sample. By analysing the spectra data in this range, band structure and surface roughness can be determined. In this way, various physical parameters of the sample can be analysed via the data of (ψ, Δ) spectra measured with a wide energy range.

4.3.3.3 Real-time Spectroscopic Ellipsometry (RTSE)

In RTSE measurement, the amplitude ratio ψ and phase difference Δ are continuously recorded. With the real-time analysis of the data, this technique can help analyse the thin-film growth behaviour, e.g. the initial growth process of the thin film and the in-situ observation of the interface structure of multilayer thin film. Other benefits include analysing the compositionally modulated layer, monitoring the reaction rate during processing. Besides, because of the sensitiveness of real-time spectroscopic ellipsometry measurement, it can also be applied as a process control method.

4.3.3.4 Technical Parameters

A J.A. Woollam Spectroscopic Ellipsometer (SE RC2; J. A. Woollam, USA) system was used for the spectroscopic ellipsometry measurements (210 nm – 1690 nm), both for in-situ (VC-B) and ex-situ measurements as well as transmittance and reflectance measurement of thin films in Chapter 5. In-situ measurements were carried out at an angle of 65 ° and an acquisition rate of one measurement per 10 s. CompleteEASE software (also J.A Woollam) was used to analyse the measured data. In the thin film thickness analysis, a calibration Si wafer with 25 nm SiO_2 thin layer on the surface was used to calibrate the instrument. The thickness of the characterised thin film was obtained by fitting Cauchy model to the ellipsometry data which fits for the refractive indices, n, in the transparent region (k=0) and the thickness d of the film. The Levenberg-Marquardt Algorithm is used by the software to perform the

fitting. The in-situ ellipsometry experiment and data modelling were performed by Dr Sameer V. Kesava (University of Oxford).

X-ray reflectivity (XRR) analysis of a glass/hexapropyltruxene (30 nm)/SubPc (20 nm) thin film sample was performed with Rigaku SmartLab system and modelled by GlobalFit software (Rigaku Innovative Technologies Europe s.r.o.) to confirm the thickness analysis by ellipsometry. The XRR fitting result is shown in Figure A.1 in the appendix. The XRR fitted thickness of the hexapropyltruxene layer is comparable with that recorded by QCM, which is calibrated using the fitted parameters (such as the material density) from ellipsometry modelling. Thus, the thickness analysis by ellipsometry is confirmed trustworthy.

4.3.4 Photoluminescence (PL)

Photoluminescence (PL is a common phenomenon where light is emitted after the solid absorbs photons of sufficient energy. PL emission is caused by the transition of electrons from higher occupied electronic states into lower unoccupied states, leading to the emission of photons if the transition is dipole-allowed [183]. In this section, the basics of PL are given for the readers to understand the experimental sections. This section is largely based on the books: Daniel Abou-Ras, Thomas Kirchartz, and Uwe Rau, eds. *Advanced characterisation techniques for thin-film solar cells.* John Wiley & Sons, 2016 [183], and the book: Vaidhyanathan Ramamurthy, and Kirk S. Schanze. *Organic photochemistry and photophysics.* CRC Press, 2005 [184].

4.3.4.1 Fundamentals of PL

The presence of luminescence provides information about the emitting excited states [185]. Thus, the PL characterisation method becomes a significant technique to characterise the properties of PV materials. Fundamentals of PL phenomenon are detailed explained in textbooks about photochemistry and photophysics such as Vaidhyanathan Ramamurthy, and Kirk S. Schanze, *Organic photochemistry and photo-*

physics, 2005, CRC Press [184]. In this section, the basic knowledge about PL technology is introduced to the reader's benefit.

The spontaneous emission rate (R^0_{sp}) has a relationship with the absorption coefficient $\alpha(E)$ in thermal equilibrium:

$$R^0_{sp} = \frac{8\pi n_r^2}{h^3 c^2} \frac{\alpha(E) E^2}{\exp(E/k_B T) - 1} \tag{4.12}$$

where n_r stands for the complex refractive index of the material in vacuum, h is the Planck's constant, c is the velocity of light, k_B is the Boltzmann constant.

In practice, the deviations from thermal equilibrium are of more interests, thus, the above equation can be written as:

$$R_{sp} = R^0_{sp} \frac{np}{n_0 p_0} - R^0_{sp} = B(np - n_0 p_0) = B n_i^2 (\exp(\Delta\mu / k_B T) - 1) \tag{4.13}$$

where n and p stand for the total carrier densities, n_0 and p_0 stand for the equilibrium carrier densities associating with the intrinsic carrier density as $n_i^2 = n_0 p_0$. $\Delta\mu$ stands for the quasi-Fermi level splitting ($\Delta\mu = E_{F_n} - E_{F_p}$). B is defined as the material-specific relative recombination coefficient:

$$B = \frac{1}{n_i^2} \frac{8\pi}{h^3 c^2} \int_0^\infty n_r^2 \alpha(E) \exp(-E/k_B T) E^2 dE \tag{4.14}$$

From Equation 4.13 we can distinguish two experimental conditions: (1). When $n \gg n_0$ and $p \gg p_0$, it is referred as the high-injection condition, and the PL photon flux is $Y_{PL} \propto Bnp$. In this condition, the radiative lifetime is $\tau_{rad} = 1/(Bn)$, which depends on the injection ratio. (2). When $n \approx n_0$ for n-type material (or $p \approx p_0$ for p-type material), the PL flux depends on the density of major carriers, $Y_{PL} \propto Bn_0 p$ and $\tau_{rad} = 1/(Bn_0)$.

The total lifetime of the recombinations can be derived from the sum of the lifetime of radiative and nonradiative recombinations.

$$\tau_{tot}^{-1} = \tau_{rad}^{-1} + \tau_{nonrad}^{-1} \tag{4.15}$$

And the PL efficiency of a material can be defined as

$$\eta_{PL} = \tau_{tot}/\tau_{rad} \tag{4.16}$$

Considering the experimental situation of the sample, e.g. absorption profile, diffusion, drift, and recombination of charge carriers within the sample, and the propagation of the emitted photons going through the sample surface, the photon flux detected outside the sample can be expressed as:

$$Y_{PL}(E) = \frac{1}{4\pi^2\hbar^3c^2}\frac{\alpha(E)E^2}{\exp(E-\Delta\mu/k_BT)-1} \tag{4.17}$$

where $\alpha(E) = (1-R_f)(1-\exp(-\alpha(E)d))$, R_f is the front surface reflectivity, d is the sample thickness.

For further analysis about the characteristic analysis (e.g. lineshape and intensity), readers are recommended to refer some specialised books about the PL analysis such as Page 151-157 in Daniel Abou-Ras, Thomas Kirchartz, and Uwe Rau, eds. *Advanced characterisation techniques for thin-film solar cells*. John Wiley & Sons, 2016 [183].

4.3.4.2 Steady-state Photoluminescence (SSPL)

Figure 4.10 shows the schematic diagram of a spectrofluorimeter, which is a typical instrument for the steady-state photoluminescence (SSPL). The instrument consists of a lamp, an excitation monochromator, a beam splitter, a reference detector, a sample holder, an emission monochromator, and a detector. SSPL can be run in two modes: emission spectra mode and excitation spectra mode. When the instrument is set to emission spectra mode, the wavelength of the excitation light is fixed, and the detector scans the emitted light in a range of wavelength. In contrast, when the instrument is set to excitation spectra mode, the wavelength of the detected light is fixed, and the wavelength of the excitation light is changing. In this thesis, the emission mode is used.

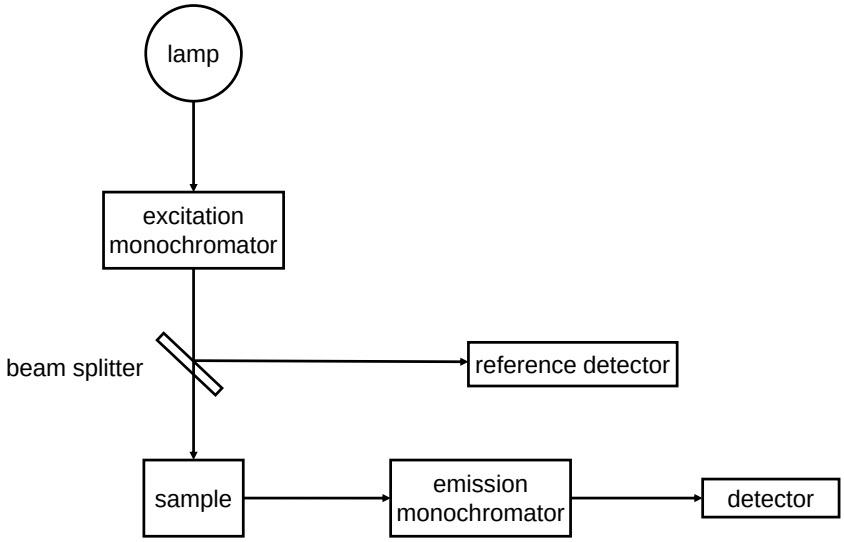


Figure 4.10: Schematic diagram of a SSPL spectrofluorimeter.

4.3.4.3 Time-resolved Photoluminescence (TRPL)

Figure 4.11 shows a typical instrument set-up for TRPL. Similar to SSPL instrument, it consists of a light source (laser head controlled with the diode laser driver), filters (neutral density (ND) filter and cut-off filter), a sample holder, a detector (a photomultiplier tube (PMT) and timing electronics).

TRPL is based on recording the change of the excited state concentration as a function of time [184], i. e. measuring the luminescence change as a function of time. The simplest model for the excited state decay follows the first-order kinetics. The decay of the lumenscence intensity follows an exponential law, which is:

$$I(t) = I_0 \exp\left(\frac{-t}{\tau}\right) \tag{4.18}$$

$$\ln I(t) = \ln I_0 - \frac{t}{\tau} \tag{4.19}$$

However, due to the complexity of the mechanism of luminescence, multiexponential or nonexponential decays are observed in many experiments [66, 186–188]. Any decay

can be fitted properly with a sum of multiple exponential terms:

$$I(t) = A_1 \exp\left(\frac{-t}{\tau_1}\right) + A_2 \exp\left(\frac{-t}{\tau_2}\right) + A_3 \exp\left(\frac{-t}{\tau_3}\right) + \cdots \tag{4.20}$$

or a stretched exponential model as:

$$I(t) \approx \exp\left(\frac{-t}{\tau}\right)^{\beta} \tag{4.21}$$

but we need to carefully choose the fitting method to precisely describe the recombination mechanism inside the semiconductor materials [189], i. e. choosing the model based on the recombination mechanism of the materials. If the recombination mechanism is not clear, a rule of thumb in fitting is to start with the simplest model until the fitting result satisfies the statistical criteria.

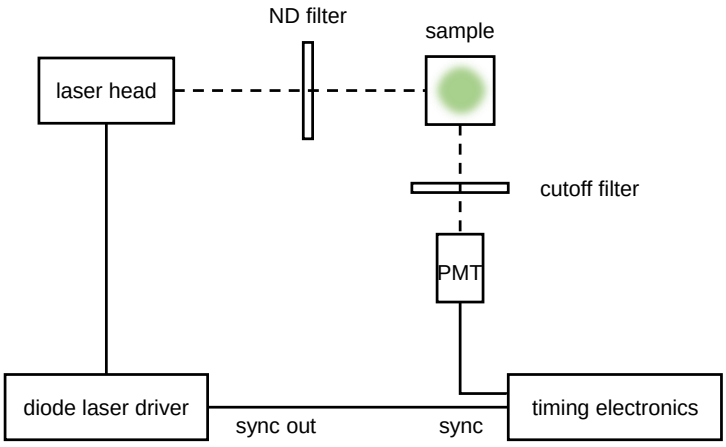


Figure 4.11: Schematic diagram of a TRPL spectrofluorimeter. The dash lines represent light and the solid lines represent the cables. This diagraph is modified from Reference [190].

4.3.4.4 Technical Parameters

Time-resolved Photoluminescence

TRPL was used to identify the exciton lifetime inside the thin films. The measurements were performed with a FluoTime 300 set-up (PicoQuant GmbH, Germany). A specific wavelength of laser (405 or 510 nm, generated by LDH-P-C-405 or LDH-P-C-510 laser diode, respectively, also from PicoQuant) was generated with 128 ps pulse duration at a 10 MHz repetition rate. The excitation fluence of the laser used was ca. 20 nJ cm^{-2}. The scattered light was filtered out from the excitation beam via a long-wavelength pass filter. Detailed parameters of corresponding experiments can be found in each relevant chapter.

Steady-state Photoluminescence

SSPL measurements were carried out with the same instrument as TRPL. The measuring time for each wavelength interval is 0.5 s.

4.3.5 Cyclic Voltammetry (CV)

Cyclic voltammetry (CV) measurement was used to measure the energy levels of hexapropyltruxene molecules. Hexapropyltruxene, PTFE, and carbon black were mixed 1:1:1 by mass ratio to make the working electrode. Reference and counter electrodes were both lithium [191, 192]. A schematic presentation of the experimental set-up is shown in Figure 4.12. The CV measurement was performed, and the data were analysed by Dr Jingyuan Liu (University of Oxford).

4.3.6 Ultraviolet–visible (UV-vis) Spectroscopy

The ultraviolet–visible spectroscopy (UV-vis) was used to observe the optical absorption behaviours of the thin film and solar cell samples. A schematic presentation of UV-vis spectroscopy measurements of thin film and solar cell samples is shown in Figure 4.13. Shown in Figure 4.13(a), for a thin film sample, the light absorption of the sample is calculated as

$$A = 1 - R - T \tag{4.22}$$

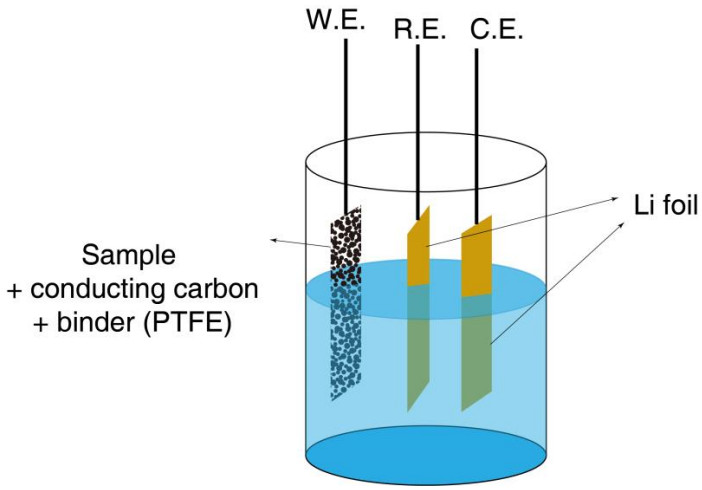


Figure 4.12: CV experiment set-up. W.E.: working electrode, R.E.: reference electrode, C.E.: counter electrode.

where A is light absorption, R is light reflectance, and T is light transmission.

For a solar cell sample, because of the existence of 100 nm fully opaque Al electrode, the transmitted light will be reflected (shown in Figure 4.13(b)). Thus, the transmission could be neglected in the calculation of solar cell absorption. When measuring absorption in reflection and using this to deduce, e.g. the maximum short circuit current of the full device, it is paramount to take into account the complex interference patterns in the OSC stack [193]. The absorption of the device is thus estimated via

$$A = 1 - R \tag{4.23}$$

Three different UV-vis set-ups were used for thin film samples in this thesis: (a). A Cary 300 UV-vis Spectrophotometer with a nominal step size as 1 nm (Agilent Technologies); (b). A Perkin-Elmer Lambda 1050 UV-vis NIR spectrophotometer with nominal step size as 1 nm (PerkinElmer Inc.); (c). A UV-vis set-up which consists of an Ocean Optics ISP-REF Integrating Sphere, optical fibres, and an Ocean Optics USB2000 spectrometer (Ocean Optics Inc., US). The integration time was 35 ms with ten scans for averaging the signal. (a) is used to characterise the absorption of hexapropyltruxene thin films. (b) and (c) are used to characterise other thin films

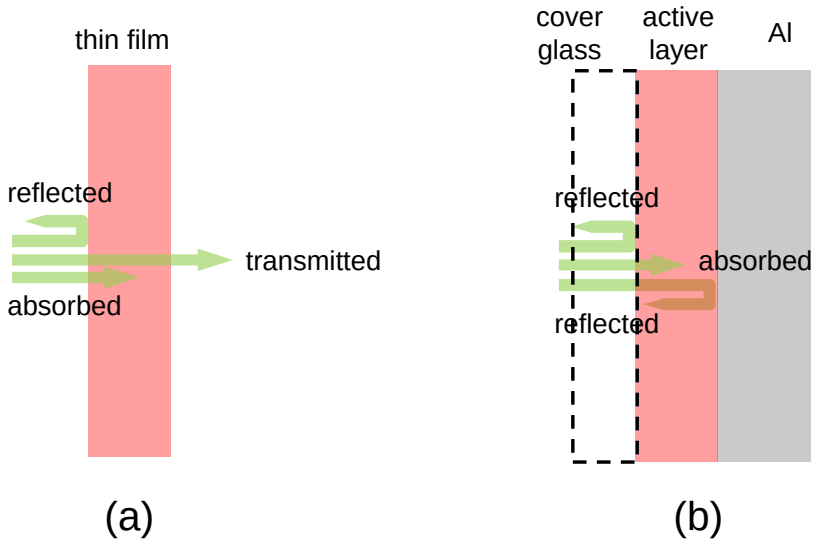


Figure 4.13: Schematic presentation of UV-vis measurements of (a). thin film and (b). solar cell samples. To simplify the graph, the optical effect of the cover glass of solar cells is neglected in sub figure (b).

in this thesis, with (b) for transmittance and (c) for reflectance.

A UV-vis set-up consisting of a DH-2000-BAL light source, optical fibre, and a Maya Pro 2000 detector (both Ocean Optics Inc., US) was used to perform UV-vis reflectance spectroscopy for solar cells. Three of the best performing OSCs with different thicknesses of interlayers were measured. In the following chapters, the integration time for solar cells in different experiments varies, and they are indicated in each chapter individually. Ten repeated measurement results of each measuring point are averaged to smooth the acquired data.

4.3.7 Atomic Force Microscopy (AFM) Measurement

Atomic force microscopy (AFM) measurement was applied in this thesis to acquire the surface topography of the thin films. The microscopes used in our experiments were an AutoProbe M5 from ThermoMicroscopes Ltd. (UK) and an MFP-3D from Asylum Research Ltd. (UK). Non-contact mode measurements were carried out with

TAP150Al-G tips purchased from Windsor Scientific Ltd. (UK). The scanning rate was between 0.2 to 1 Hz, and the data were analysed and processed using gwyddion software [194].

4.4 Solar Cell Characterization

4.4.1 Current-Voltage (JV) Characterization

An Abet Class AAB solar simulator was used to perform the solar cell efficiency measurement. The solar cells were illuminated under simulated AM 1.5 sunlight, whose intensity was measured with an NREL-calibrated KG5 filtered silicon reference cell. The dark and illuminated JV curves were recorded with a Keithley 2400 Series Sourcemeter. At least four solar cells were measured for each data point. The active area of the solar cells is defined by the geometric overlap between ITO and Al. Measurement details of each experiment can be found in each relevant chapter.

4.4.2 External Quantum Efficiency (EQE) Measurement

The determination of the EQE was carried out using a home-made EQE set-up. Two of the best performing OSCs in each category were measured and compared.

4.4.3 Internal Quantum Efficiency (IQE) Measurement

The internal quantum efficiency (IQE) was calculated by dividing the EQE data with estimated absorption (1-R) data of each device which was measured from UV-vis reflectance. This IQE measurement method is widely used and has been chosen for its simplicity. Despite the known cavity effect-induced limitations [51], it still provides meaningful information to describe our system.

4.5 Transfer Matrix Modelling

As is already mentioned in Figure 4.9, when light passes through multiple interfaces, it will be reflected by the interfaces, with each is partially transmitted and then partially reflected. These reflections can interfere with each other. This situation makes the simulation of the optical absorption of multiple layers not an easy task. The optical simulation of the solar cell stacks in this thesis was based on a transfer matrix method [195].

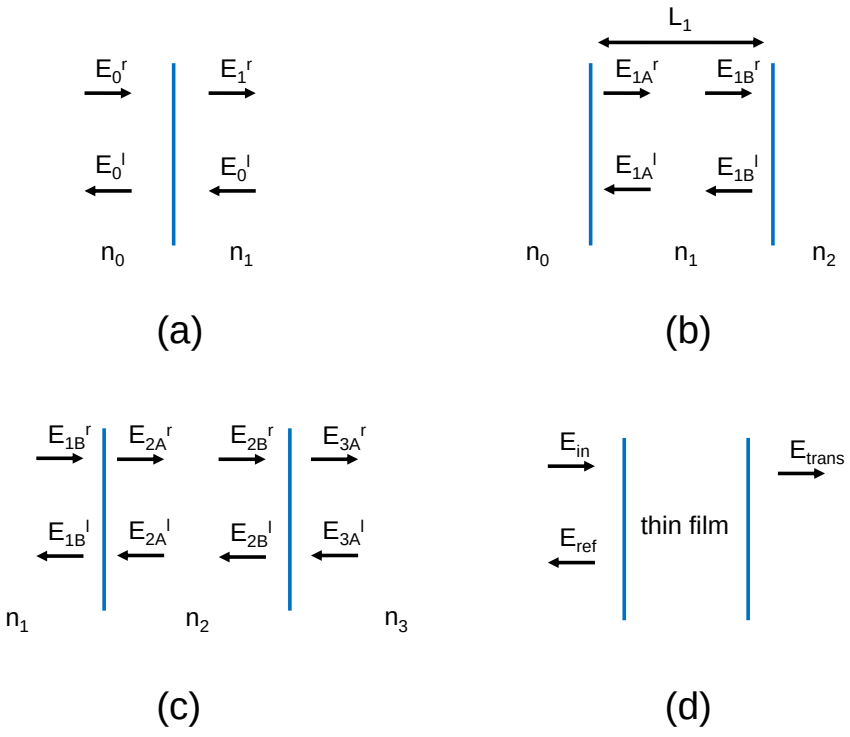


Figure 4.14: Schematic presentation of the transfer matrix method. E is the abbreviation of the electromagnetic wave. The superscript "l" and "r" represent leftward and rightward travelling direction. n is the refractive index of the corresponding material. The subscript "in" is short for incidence, "ref" is short for reflection, "trans" is short for "transmission". The subscripts "A" and "B" are used to distinguish the travelling wave near the different interfaces in the same material.

Shown in Figure 4.14(a), at a certain interface of two materials with refractive

indices n_0 and n_1 (Material 0 and Material 1), there are four different travelling waves: rightward travelling wave E_0^r and E_1^r, as well as leftward travelling wave E_0^l and E_1^l. Thus, we have the equation:

$$\begin{bmatrix} E_0^r \\ E_0^l \end{bmatrix} = D \begin{bmatrix} E_1^r \\ E_1^l \end{bmatrix}, D = \frac{1}{t_{01}} \begin{bmatrix} 1 & -r_{01} \\ r_{01} & 1 \end{bmatrix} \tag{4.24}$$

where D is the so-called transmission matrix. t_{01} and r_{01} are the transmission coefficient and reflection coefficient of the light passing from Material 0 to Material 1.

Shown in Figure 4.14(b), inside Material 1, the relationship of the four travelling waves can be described as he following equation:

$$\begin{bmatrix} E_{1A}^r \\ E_{1A}^l \end{bmatrix} = P \begin{bmatrix} E_{1B}^r \\ E_{1B}^l \end{bmatrix}, P = \begin{bmatrix} e^{ik_1 L_1} & 0 \\ 0 & e^{-ik_1 L_1} \end{bmatrix} \tag{4.25}$$

where P is the so-called propagation matrix. k_1 is the wave number in Material 1 and L_1 is the thickness of this film.

For a multilayer system as shown in Figure 4.14(c), by applying transmission and propagation matrix to each layer, we have

$$\begin{bmatrix} E_{2B}^r \\ E_{2B}^l \end{bmatrix} = D_{23} \begin{bmatrix} E_{3A}^r \\ E_{3A}^l \end{bmatrix} \tag{4.26}$$

$$\begin{bmatrix} E_{2A}^r \\ E_{2A}^l \end{bmatrix} = P_2 \begin{bmatrix} E_{2B}^r \\ E_{2B}^l \end{bmatrix} \tag{4.27}$$

$$\begin{bmatrix} E_{1B}^r \\ E_{1B}^l \end{bmatrix} = D_{12} \begin{bmatrix} E_{2A}^r \\ E_{2A}^l \end{bmatrix} \tag{4.28}$$

Combining Equation 4.26,4.27, and 4.28 we have

$$\begin{bmatrix} E_{1B}^r \\ E_{1B}^l \end{bmatrix} = D_{12} P_2 D_{23} \begin{bmatrix} E_{3A}^r \\ E_{3A}^l \end{bmatrix} = M \begin{bmatrix} E_{3A}^r \\ E_{3A}^l \end{bmatrix} \tag{4.29}$$

where $M = D_{12} P_2 D_{23}$ is defined as the transfer matrix, which can be obtained by calculating the optical coefficients of each layer.

Shown in Figure 4.14(d), the incidence light, reflection and transmission of a thin film system have the relationship as

$$\begin{bmatrix} E_{in} \\ E_{ref} \end{bmatrix} = M \begin{bmatrix} E_{trans} \\ 0 \end{bmatrix} \tag{4.30}$$

Thus we have the total transmission coefficient t and reflection coefficient r

$$t = \frac{E_{trans}}{E_{in}} = \frac{1}{M_{11}} \tag{4.31}$$

$$r = \frac{E_{ref}}{E_{in}} = \frac{M_{21}}{M_{11}} \tag{4.32}$$

With this transfer matrix method, the absorption of the solar cell stack can be simulated via computer programmes. In this thesis, optical constants of the materials were acquired by ellipsometry measurement of thin films using the above mentioned J.A. Woollam Spectroscopic Ellipsometer (SE RC2) system, performed by Dr Sameer V. Kesava (University of Oxford). The modelling code was developed by Mr Sergejs Lukanihins (University of Oxford).

Chapter 5

Efficiency Enhancement of Small Molecule Organic Solar Cells Using Hexapropyltruxene as an Interface Layer

The material contained within this chapter has been published as: Ye H., Kesava S. V., Hardigree J. F. M., Brown R. E., Mazzotta G., Warren R., Skabara P. J., & Riede M. Efficiency enhancement of small molecule organic solar cells using hexapropyltruxene as an interface layer, *Journal of Materials Chemistry C* **8**, 4909 (2020). Reproduced by permission of The Royal Society of Chemistry.

5.1 Introduction

Explained in Chapter 3, interlayers inside organic solar cells (OSCs) have various effects such as exciton blocking effect, molecular template growth (MTG) effect, and substrate-induced phase (SIP) effect. Proper interlayers applied within OSCs will help improve the device performances dramatically. Thus, apart from the attempt of searching for high-performance active layer materials for OSCs, finding proper interlayers for existing OSC stacks is an alternative pathway to improve the device performance.

As discussed in Section 4.1.1, truxene derivatives have multiple potential applica-

tions in OSCs, including photosensitizers [148], electron donor molecules [149–151], and hole transporting layers [152]. Hexapropyltruxene is an alkylated derivative of the parent truxene molecule, whose chemical structure is shown in Figure 4.2 (a). Little research about the potential applications of hexapropyltruxene in OSCs has been reported. Nevertheless, according to its optical and electronic properties shown in Section 4.1.1, it is almost transparent in the UV-vis wavelength range, and it has suitable energy levels as interlayers. Thus, it may be suitable to work as an interlayer material inside OSCs to increase the OSC performance.

This chapter investigates the potential application of hexapropyltruxene as an interlayer between MoO_x and SubPc layers in a SubPc/C60 solar cell stack. It shows how the MTG effect of hexapropyltruxene interlayer inside the SubPc/C60 solar cells can affect the growth behaviour of subsequent-grow SubPc layer. It reveals how hexapropyltruxene interlayer can improve the device performance by blocking the excitons from being quenched on the surface of the MoO_x layer. In-situ grazing-incidence wide-angle X-ray scattering (GIWAXS) and in-situ spectroscopic ellipsometry were used hand-in-hand to investigate the change in the growth of a SubPc layer as an electron donor after inserting the hexapropyltruxene layer. atomic force microscopy (AFM) measurements were performed to investigate the surface topology change. Full planar heterojunction solar cell stacks using SubPc/C60 as the photovoltaic active layer were fabricated to examine the performance change caused by insertion of the hexapropyltruxene layer. Steady-state and time-resolved photoluminescence spectroscopy (SSPL and TRPL) were carried out to evaluate the exciton quenching effect.

5.2 Experimental Details

Thin film and device samples were fabricated following the procedure described in Chapter 4. The full solar cell structure is shown in Figure 5.1(a) and the parameters

are detailed in Table 5.1. The energy levels of the materials used in this solar stack are indicated in Figure 5.1(b). It has to be noticed that the energy levels of MoO_x are normally 9.2-9.7 eV (valence band) and 6.2-6.9 eV (conduction band) [112, 196–198]. The schematic presentation of the energy levels of MoO_x in Figure 5.1(b) is adjusted due to the shift of the vacuum level [85, 112, 199]. It is reported that holes transport across the MoO_x by tunnel effect, and the existence of the gap states inside the oxygen-deficient MoO_x thin film helps the hole transporting at the interface [85]. The single layers of hexapropyltruxene were made in VC-A. The multilayers made for in-situ spectroscopic ellipsometry and photoluminescence measurements were fabricated in VC-B, multilayers made for GIWAXS and AFM measurements were made in VC-C. (Please see Section 4.2.1 for details about the different vacuum evaporation chambers.)

Table 5.1: Thin film/device stacks in different experiments.

Experiment	Thin film/device stack
Solar cell	glass/ITO/MoO_x (5 nm, 0.1 Å/s) /hexapropyltruxene (various thicknesses, 0.1 Å/s) /SubPc (13 nm, 1 Å/s) /C60 (35 nm, 0.5 Å/s) /BPhen (8 nm, 0.8 Å/s) /Al (100 nm, 1 Å/s)
In-situ ellipsometry	Si/SiO_2/MoO_x (5 nm, 0.1 Å/s) /hexapropyltruxene (0 or 3.8 nm, 0.1 Å/s) /SubPc (13 nm, 1 Å/s) /C60 (35 nm, 0.5 Å/s)
In-situ GIWAXS	Si/SiO_2/hexapropyltruxene (0 or 3.8 nm, 0.1 Å/s) /SubPc (13 nm, 1 Å/s)
SSPL & TRPL	glass/MoO_x (0 or 5 nm, 0.1 Å/s) /hexapropyltruxene (0 or 3.8 nm, 0.1 Å/s) /SubPc (13 nm, 1 Å/s)

Thin film and solar cell characterisation were carried out according to the experiment procedure explained in Chapter 4.

XRD measurement of the hexapropyltruxene thin film was undertaken via the Phillips X'pert Pro MRD. In-situ GIWAXS was performed during and after the growth of the films in VC-C at beamline I07 of the Diamond Light Source (beamtime SI18016) with a Pilatus 2M detector (Dectris AG, Switzerland) at a distance of 300 mm. The samples were fabricated on an angle-adjustable sample stage for in-situ

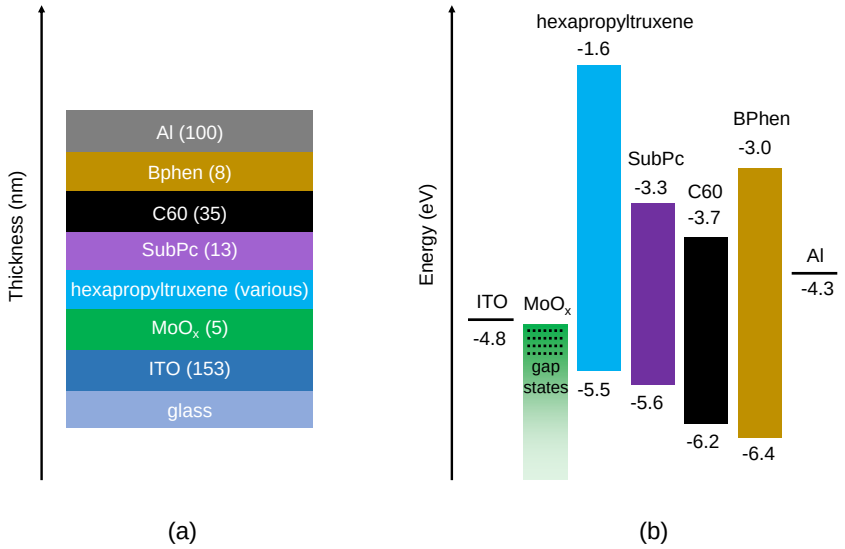


Figure 5.1: Solar cell stack, and energy levels of the solar cells. (a). Schematics of the investigated solar cell stacks with the individual layer thickness given in nanometres, (b). Energy levels of materials used in this work. The indicated energy levels of C60, SubPc, BPhen, and electrodes (UPS & IPES) are taken from literature [112, 158, 200, 201]. The energy levels of MoO_x are normally 9.2-9.7 eV (valence band) and 6.2-6.9 eV (conduction band) [112, 196–198]. The schematic presentation of the energy levels of MoO_x is adjusted due to the shift of the vacuum level [85, 112, 199]. Gap states of MoO_x is shown as dotted lines. The HOMO-LUMO levels of hexapropyltruxene are determined by cyclic voltammetry.

growth observation. The incident angle of the beam on the samples was 0.15°, with a beam energy of 12.5 keV (wavelength $\lambda = 0.992$ Å). The exposure time for each image was 10 s. The beam damage to the samples was reduced by laterally moving the sample area at each exposure. Data were analysed with DAWN software [174, 175]. A sector region of 15° was used to plot the line-cut profile. The experiment at beamline I07 was undertaken by Dr Josue Martinez-Hardigree (Oxford University) and the thesis author. Data analysis were performed by the thesis author.

In TRPL measurement, an LDH-P-C-510 laser source was used to generate incidence laser at 510 nm wavelength, 620 and 720 nm emission wavelengths of SubPc were monitored. In SSPL, the same laser source was applied. The measuring time

for each wavelength interval is 0.5 s.

For solar cell JV curve measurements, six solar cells in two batches (three per batch) with an active area of 7.5 mm^2 (defined by the geometric overlap between ITO and Al) were measured for each thickness of hexapropyltruxene. The exception was the stack with a 0.8 nm hexapropyltruxene layer: here, four devices from the same batch were measured, one of which had an active area of 1.5 mm^2. By following a pre-established protocol [64,65], the mismatch factor for the reference solar cell without hexapropyltruxene and the solar cell with hexapropyltruxene were calculated as 0.980 and 0.977, respectively, which is close to unity.

5.3 Results and Discussion

5.3.1 Basic Properties of Hexapropyltruxene Layer

Measurements of the UV-vis spectra of 100 nm hexapropyltruxene layer made in VC-A show that this thin film is almost transparent in the visible spectrum region, which is desired for being an interlayer in a solar cell stack (Figure 5.2(a)). A Tauc Plot analysis suggests its optical band gap is 3.95 eV. The CV measurement shows the hexapropyltruxene has a reversible oxidation, but no reduction is observed in the scanned range from 1.75 to 5 V. The value used for E_{ox} vs Li/Li^+ is 4.39 V. The HOMO is subsequently calculated as -5.53 eV (Figure 5.2(b)). XRD analysis of the hexapropyltruxene layer (100 nm) shows no X-ray diffraction peak of hexapropyltruxene. The broad peak around 2θ=25 ° belongs to the glass substrate. It suggests that hexapropyltruxene thin film is not well-crystallized (Figure 5.2(c)). AFM analysis of the identical thin film shows its surface roughness is around 0.4 nm. (Figure 5.2(d)).

5.3.2 Current-Voltage (JV) Characterization of Solar Cells

The JV curves of the solar cells are shown in Figure 5.3. A summary of the solar cell performance is included in Figure 5.4 and Table 5.2.

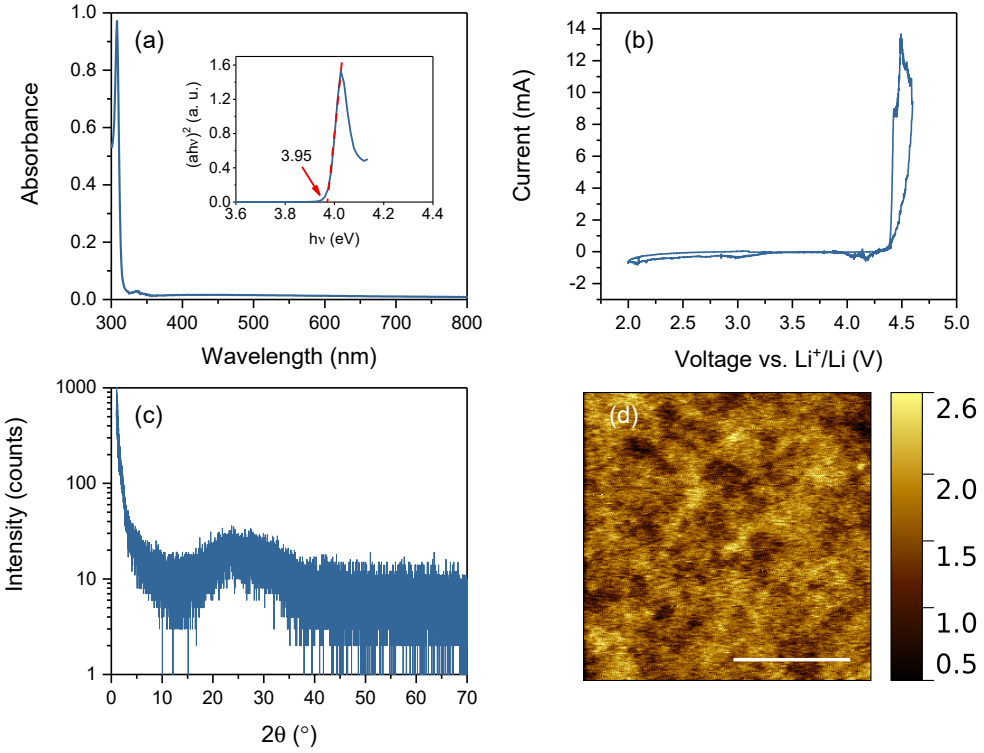


Figure 5.2: Basic properties of hexapropyltruxene. (a). UV-vis spectrum of 100 nm hexapropyltruxene layer, the inset graph is the Tauc Plot of the UV-vis spectrum, (b). Cyclic voltammetry test result of hexapropyltruxene, (c). XRD analysis of 100 nm hexapropyltruxene layer on glass substrate, (d). AFM image of the surface morphology of hexapropyltruxene layer (100 nm). The scale bar in the figure is 2 μm and the unit for the vertical scale is nm.

In Figure 5.4, the PCE of the solar cells is shown with hexapropyltruxene layer thickness systematically increasing from 0 to 3.8 nm. In this range, the PCE increases from 2.6 % to 3.0 %, mainly due to an increase in J_{sc}, leading to an improvement of efficiency of about 15 %. As the thickness of the hexapropyltruxene layer is increased further from 3.8 nm to 7.7 nm, the PCE of the devices begins to drop. This is mainly due to a decrease in FF which changes from ca. 55 % to ca. 28 %. For all the investigated hexapropyltruxene layer thicknesses, the open-circuit voltage V_{oc} of the devices remains the same at around 1.1 V. From the JV curves (Figure 5.3) we can

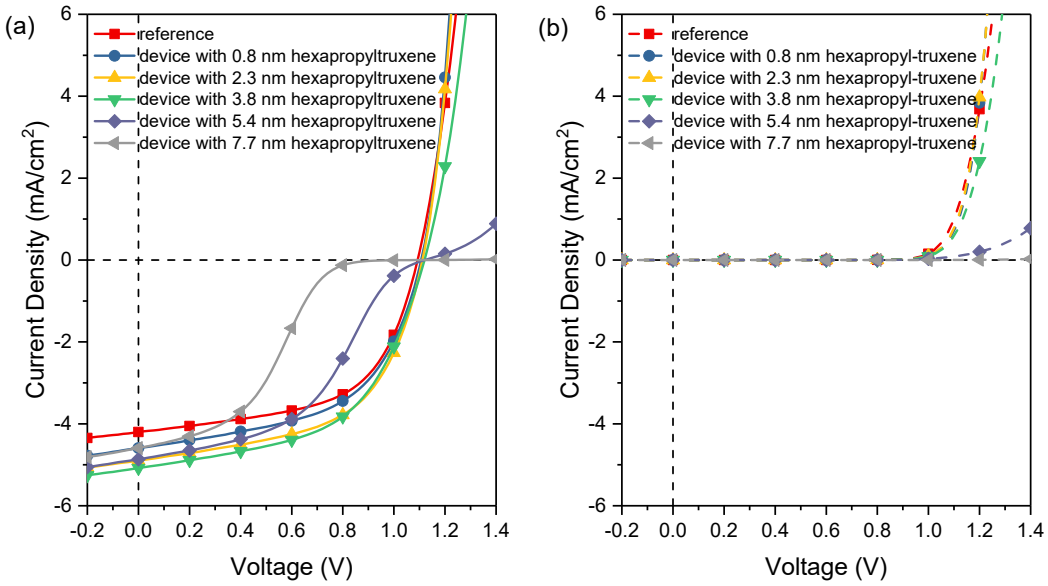


Figure 5.3: JV curves of the solar cells with different thicknesses of a hexapropyltruxene interlayer between MoO_x and SubPc. The reference device does not have a hexapropyltruxene interlayer. (a). Solid lines represent the JV curves under illumination. (b). Dashed lines represent the JV curves in the dark.

see that S-kink features are appearing when the hexapropyltruxene layer exceeds 3.8 nm. According to the shape of the S-kink in the range of 1.2 to 1.4 V, we conclude that this is an injection barrier [202–204]. Overall, we find that the PCE increase with the insertion of a hexapropyltruxene layer is mainly due to the rise of J_{sc}.

5.3.3 External Quantum Efficiency (EQE) and Internal Quantum Efficiency (IQE) Analysis

To investigate the reason for the J_{sc} increases of about 25 % with the insertion of a thin layer of hexapropyltruxene, EQE and UV-vis reflectance measurement of the hexapropyltruxene solar cells with the best performance (devices with a 3.8 nm hexapropyltruxene layer) and reference devices without hexapropyltruxene were carried out.

As shown in Figure 5.5, the EQE curves have two significant peaks: one is in the range from 330 to 400 nm (C60 absorption range), and the other is in the range from

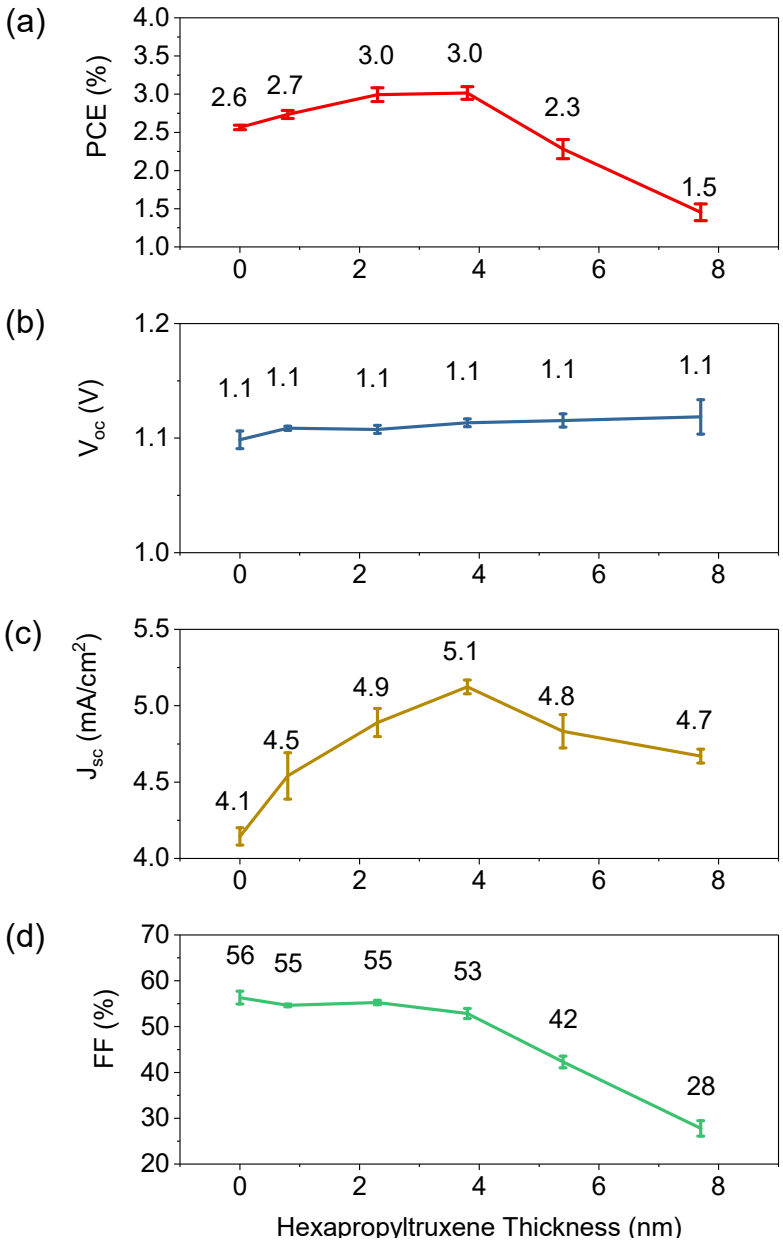


Figure 5.4: Solar Cell performance versus the thickness of the hexapropyltruxene layer between MoO_x and SubPc. (a). PCE, (b). V_{oc}, (c). J_{sc}, (d). FF.

520 to 600 nm (SubPc absorption range). The EQE of the device with hexapropyltruxene is significantly higher than the reference device in the range from about 520 to 600 nm, i.e. in the major SubPc absorption range, with the EQE peak between 520 and 600 nm, rising from 40 % (no hexapropyltruxene) to 56 % (3.8 nm hexapropyltruxene). The improvement of photocurrent generation in the range from 520 nm to

Table 5.2: Device performance summary of solar cells with different thicknesses of hexapropyltruxene.

Hexapropyltruxene thickness (nm)	J_{sc} (mA·cm^{-2})	V_{oc} (V)	FF (%)	PCE (%)
0	4.1 ± 0.06	1.10 ± 0.01	56 ± 1	2.6 ± 0.03
0.8	4.5 ± 0.15	1.11 ± 0.01	55 ± 1	2.7 ± 0.05
2.3	4.9 ± 0.09	1.11 ± 0.01	55 ± 1	3.0 ± 0.09
3.8	5.1 ± 0.04	1.11 ± 0.01	53 ± 1	3.0 ± 0.08
5.4	4.8 ± 0.11	1.12 ± 0.01	42 ± 1	2.3 ± 0.13
7.7	4.7 ± 0.04	1.12 ± 0.02	28 ± 2	1.5 ± 0.11

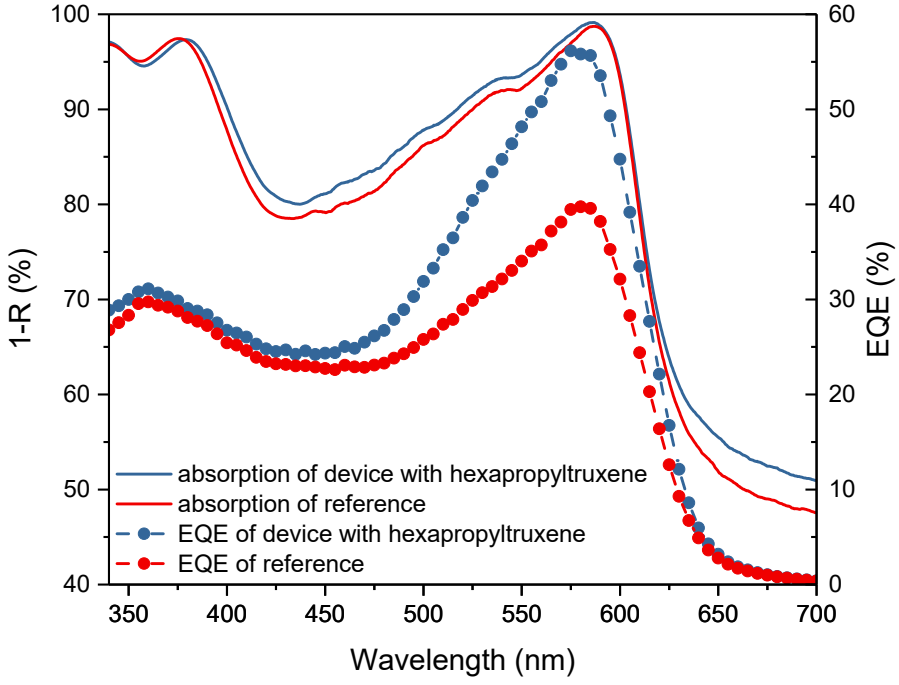


Figure 5.5: EQE and UV-vis reflectance measurement results of reference devices without a hexapropyltruxene layer and the devices with 3.8 nm hexapropyltruxene between MoO_x and SubPc showing the best performance. R is the measured reflectance of the stack.

600 nm is calculated to be ca. 40 %. The estimated absorption (1- reflectivity R) of the devices as measured in UV-vis reflectance measurement shows little change in the absorption behaviour of the active layer after the insertion of hexapropyltruxene. The small absorption difference is not sufficient to explain the high increase of EQE

and photocurrent generation in the SubPc absorption region.

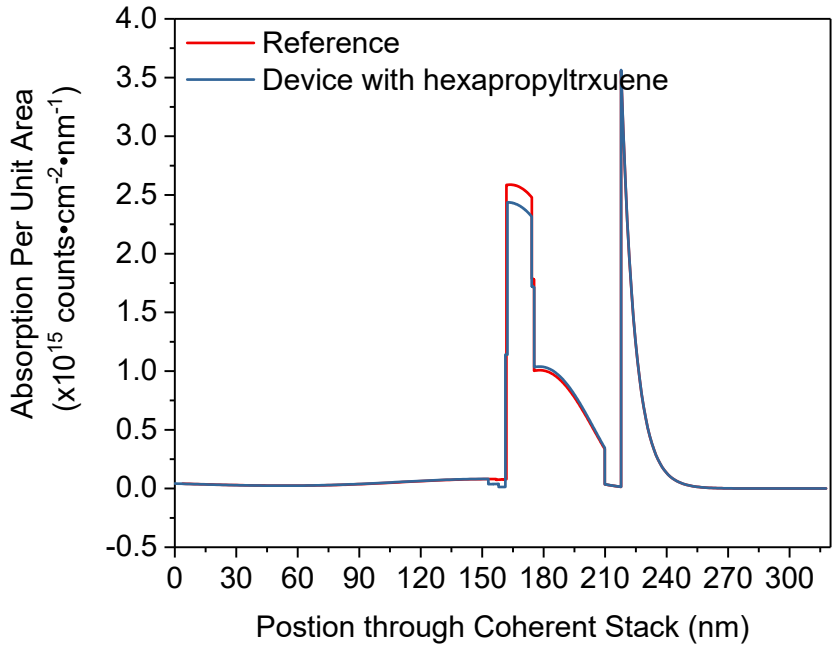


Figure 5.6: Absorption simulation of solar cell stack with/without hexapropyltruxene using a transfer matrix approach.

Table 5.3: Photon number absorbed in each layer calculated by absorption simulation using a transfer matrix approach.

Device	Absorbed photon number ($\times 10^{16}$)			Absorbed photon percentage (%)	
	SubPc	C60	Total	SubPc	C60
Reference device	3.28	2.78	9.19	36	30
Device with 3.8 nm hexapropyltruxene	2.90	2.97	9.05	32	33

Absorption simulations of solar cell stacks with 3.8 nm/without hexapropyltruxene were carried out and shown in Figure 5.6 and Table 5.3. This shows that after the insertion of hexapropyltruxene, the light absorption of the active layer slightly changes: SubPc absorbs less light while C60 absorbs more. Calculations of the absorbed number of photons per unit area and time show that after the insertion of hexapropyltruxene, photon absorption of SubPc layer decreases from 36 % of the to-

tal absorption of the stack to 32 %, while C60 absorption increases from 30 % to 33 %. This is due to changes in the cavity and the slight shift of the light interference before and after the insertion of hexapropyltruxene. However, the total absorption of the photovoltaic active layer stays similar after the insertion of the hexapropyltruxene layer according to the simulations. Thus, the change of the absorption behaviour in SubPc and C60 layers cannot account for the significant rise of EQE and photocurrent generation. We notice that this simulation result shows small difference comparing to the reflectivity measurement (estimated absorption (1-R) calculated from reflectivity measurement shown in Figure 5.5), which might be due to slightly different thicknesses in the measured films and simulation data. In any case, the small change in absorption behaviour of the active layer cannot explain the large increase in EQE and photocurrent generation.

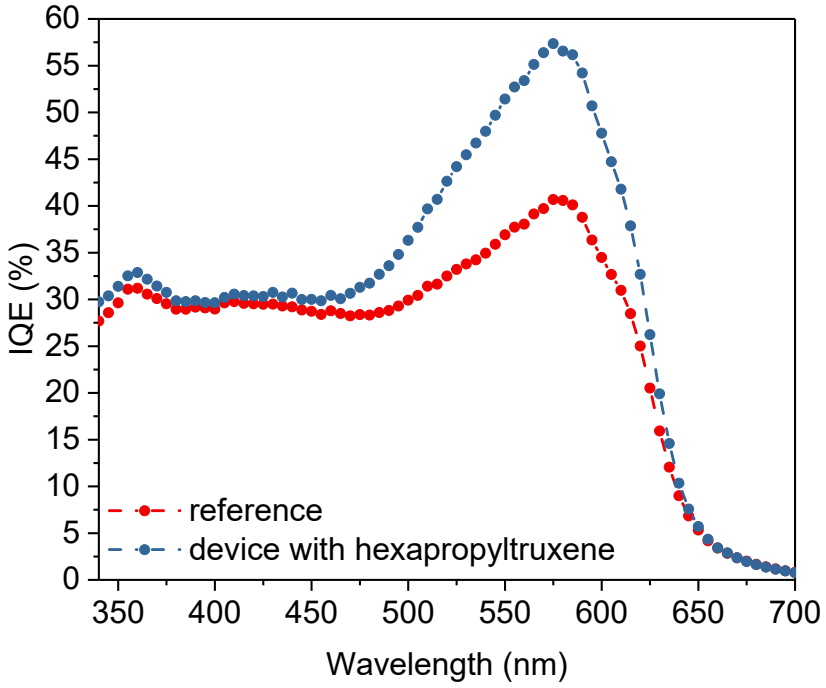


Figure 5.7: IQE calculations based on the EQE and absorption data for the reference devices without hexapropyltruxene and the devices with 3.8 nm hexapropyltruxene as interlayer between MoO_x and SubPc

We further calculated the IQE using the EQE and UV-vis reflectance data to compare the charge generation in the devices. Shown in Figure 5.7 are the results: with the insertion of hexapropyltruxene layer, IQE increases significantly within the wavelength range of 475 nm to 600 nm, which is the main absorption range of the device and the SubPc absorption region. Calculated photocurrent generation increase is 39 % comparing with the reference device. This result shows that the inserted hexapropyltruxene helps to turn more of the photogenerated excitons in the SubPc into current that can be extracted.

5.3.4 Ellipsometry Analysis

In order to examine the effect that the hexapropyltruxene interlayer has on the growth of the subsequent SubPc, spectroscopic ellipsometry measurements of the device stack up to the C60 layer with and without hexapropyltruxene were carried out in-situ during the deposition of the SubPc layer. The SubPc layer was modelled as a uniaxial layer, i.e. with different in-plane and out-of-plane refractive indices. Corresponding data analyses reveal small changes in the optical properties of SubPc with the insertion of hexapropyltruxene. As shown in Figure 5.8, for stacks with hexapropyltruxene and without (reference), both their in-plane refractive index n and k are consistent in the wavelength range 200 nm to 900 nm, except a minor gap around 450 nm to 500 nm. However, SubPc absorbs little light in this range so that this minor difference can be neglected. These results indicate that the in-plane optical property of the stack stays similar after inserting the hexapropyltruxene interlayer, which is in line with the absorptance measurements.

The out-of-plane refractive indices, however, shows a notable difference between the stack with hexapropyltruxene and without. For the out-of-plane refractive indices n, a new peak appears at 633 nm after the insertion of the hexapropyltruxene layer, which shows only as a shoulder in the reference sample. This increase in k at 633 nm

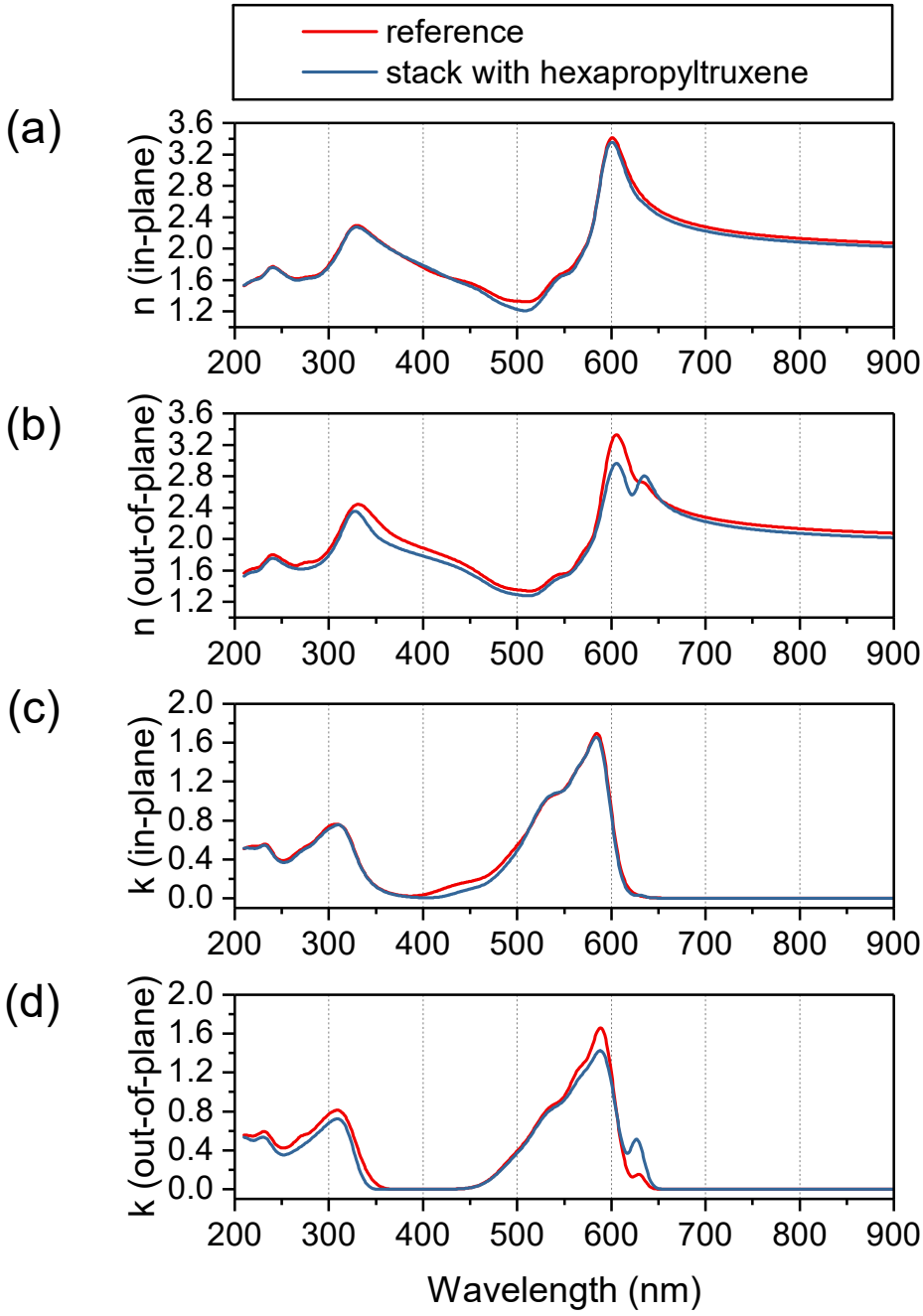


Figure 5.8: In-plane and out-of-plane refractive overall indices n, k of the reference device stack (Si/MoO_x (5 nm)/SubPc (13 nm) /C60 (35 nm)) and a device stack with hexapropyltruxene (Si/ hexapropyltruxene (3.8 nm)/MoO_x (5 nm)/SubPc (13 nm)/C60 (35 nm)). (a). in-plane refractive indices n, (b). out-of-plane refractive indices n, (c). in-plane refractive indices k, (d). out-of-plane refractive indices k.

seems to come at the cost of weakening the peak at 605 nm. Similarly, for the out-of-plane refractive indices k, a trade-off in peak intensities between 590 and 630 nm is observed. These changes in absorption behaviour happen in the absorption wave range of SubPc. This indicates that the insertion of the hexapropyltruxene interlayer between MoO_x and SubPc layers modifies the out-of-plane optical properties of SubPc, which might be a consequence of the change in the molecular ordering of SubPc.

5.3.5 Grazing-incidence Wide-angle X-ray Scattering (GIWAXS) Analysis

In order to corroborate these results, in-situ GIWAXS measurements were carried out using VC-C [166]. The results are shown in Figure 5.9.

Table 5.4: Fitted peak properties of the GIWAXS line cut. (Gaussian function is used in the peak fitting)

Film & orientation (*)	Peak center ($Å^{-1}$)	FWHM (δq, $Å^{-1}$)	d-value (Å)	Scherrer coherence length (D=$2\pi/\delta q$, Å)	Max height (a.u.)
(a)	0.68 ± 0.01	0.31 ± 0.01	9.24 ± 0.14	20.27 ± 0.68	12.1
(b)	0.73 ± 0.01	0.22 ± 0.01	8.61 ± 0.12	28.56 ± 1.36	18.8
(c)	0.70 ± 0.01	0.23 ± 0.01	8.98 ± 0.13	27.32 ± 1.24	26.2
(d)	0.70 ± 0.01	0.20 ± 0.01	8.98 ± 0.13	31.42 ± 1.65	52.8

*:
(a). Si/SiO_2/SubPc (in-plane);
(b). Si/SiO_2/SubPc (out-of-plane);
(c). Si/SiO_2/ hexapropyltruxene/SubPc (in-plane);
(d). Si/SiO_2/ hexapropyltruxene/SubPc (out-of-plane).

The high intensity spot around Q_{xy} = 1.6 $Å^{-1}$ originates from the Si/SiO_2 substrate. We find a SubPc peak at around 0.7 $Å^{-1}$. It could be either SubPc (110) peak (0.67 $Å^{-1}$) or SubPc (011) peak (0.74 $Å^{-1}$). In SubPc single crystal structure, (110) peak is systematically absent [155]. Thus, this broad peak could be SubPc (011) peak. Line-cut profiles (15°) in horizontal (in-plane) and perpendicular (out-of-plane) directions were analysed. The fitting result is shown in Figure 5.9 and Table 5.4. From the

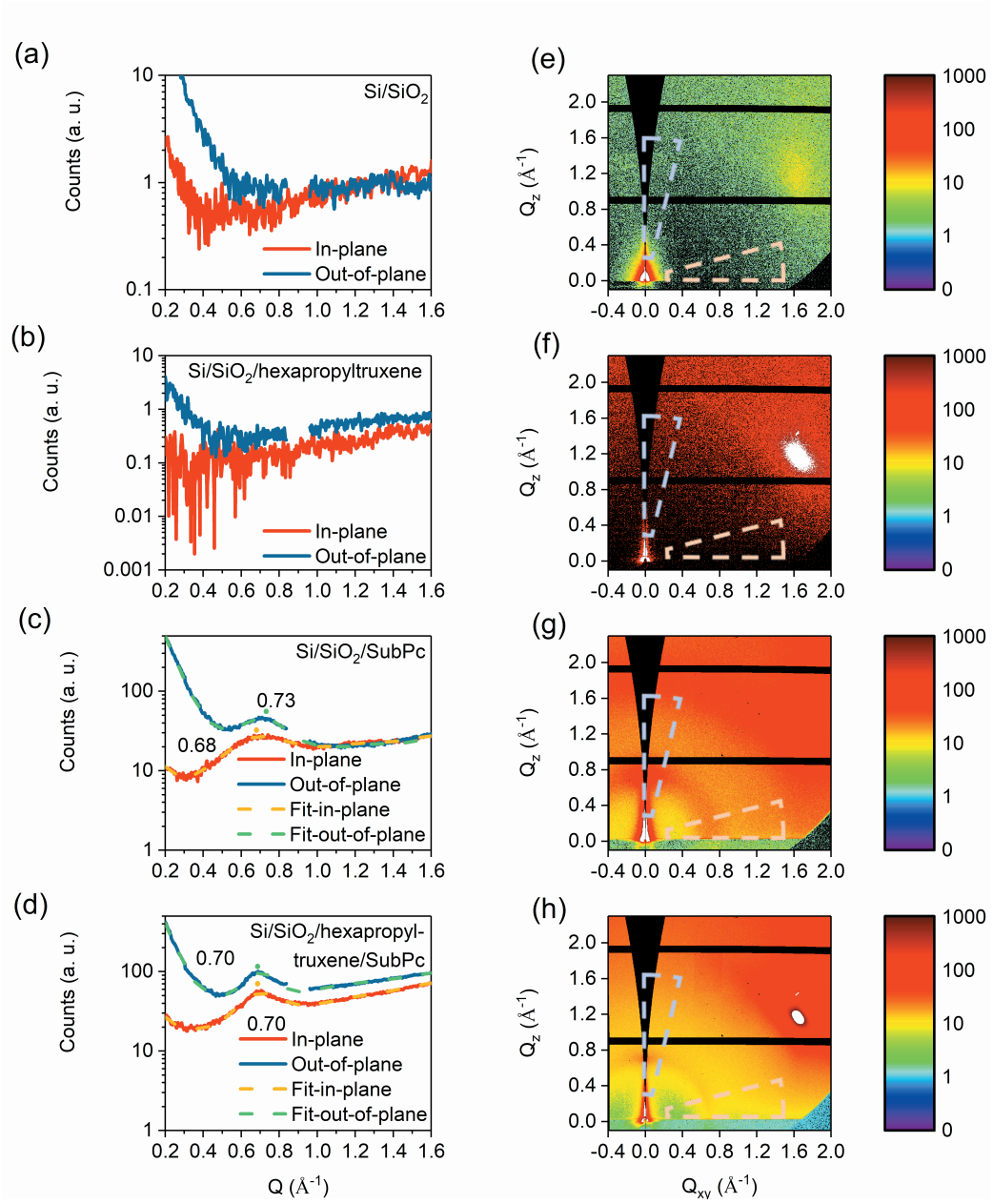


Figure 5.9: Plots of the GIWAXS results obtained through measurements at Diamond Light Source's I07 beamline. In-plane and out-of-plane line cuts for (a) Si/SiO_2, (b) Si/SiO_2/hexapropyltruxene (3.8 nm), (c) Si/SiO_2/SubPc (13 nm), and (d) Si/SiO_2/hexapropyltruxene (3.8 nm)/SubPc (13 nm) multilayer films. GIWAXS images of (e) Si/SiO_2, (f) Si/SiO_2/hexapropyltruxene (3.8 nm), (g) Si/SiO_2/SubPc (13 nm), and (h) Si/SiO_2/hexapropyltruxene (3.8 nm)/SubPc (13 nm) multilayer films. Line-cut sections are indicated with dashed wedges in the figure.

fitted FWHM and peak maximum heights we can find that the SubPc peak becomes narrower in both in-plane and out-of-plane directions after the insertion of hexapropy-

ltruxene. This indicates a larger crystalline size of SubPc after the insertion of the hexapropyltruxene interlayer. The peak center locations of the SubPc (011) plane shift to 0.70 $Å^{-1}$ from 0.68 $Å^{-1}$ (in-plane) and 0.73 $Å^{-1}$ (out-of-plane) after the insertion of the hexapropyltruxene interlayer. This peak shift might be an indication of a change of crystal structure of SubPc after the insertion of hexapropyltruxene, which could explain the difference in optical properties of SubPc in the thin film. A radial distribution of the peaks is shown in Figure 5.10. Comparing the integrated intensities in Figure 5.10 between SubPc on SiO_2 and SubPc on hexapropyltruxene, we can see that the hexapropyltruxene layer affects, along with the crystallite sizes, the orientation distribution of SubPc, with a clear shoulder visible around 30 °. This affect on structure is reflected in the difference in the optical properties (Figure 5.8) of SubPc.

We need to point out that because of the limited organic sources in MINERVA (only two) and the conditions of the experiment at the beamtime, we were not able to perform the characterisation of SubPc and hexapropyltruxene/SubPc thin film on top of MoO_x layer. Thus, this GIWAXS measurement result can only illustrate the template effect of hexapropyltruxene on SubPc, rather than the function of hexapropyltruxene layer in between the MoO_x and SubPc layer in solar cell stack. And the change in ellipsometry experiment result cannot be entirely clarified by GIWAXS data.

5.3.6 AFM Analysis of the in-situ GIWAXS samples

To further confirm the structure change of SubPc on substrates and hexapropyltruxene, AFM measurement of SubPc layer on different substrates (made in VC-C) were carried out.

Figure 5.11(a), (b) and (c) show the surface topology of 13 nm SubPc on Si wafer. It has an RMS of 0.50 nm. Figure 5.11(d), (e), and (f) show the surface morphology

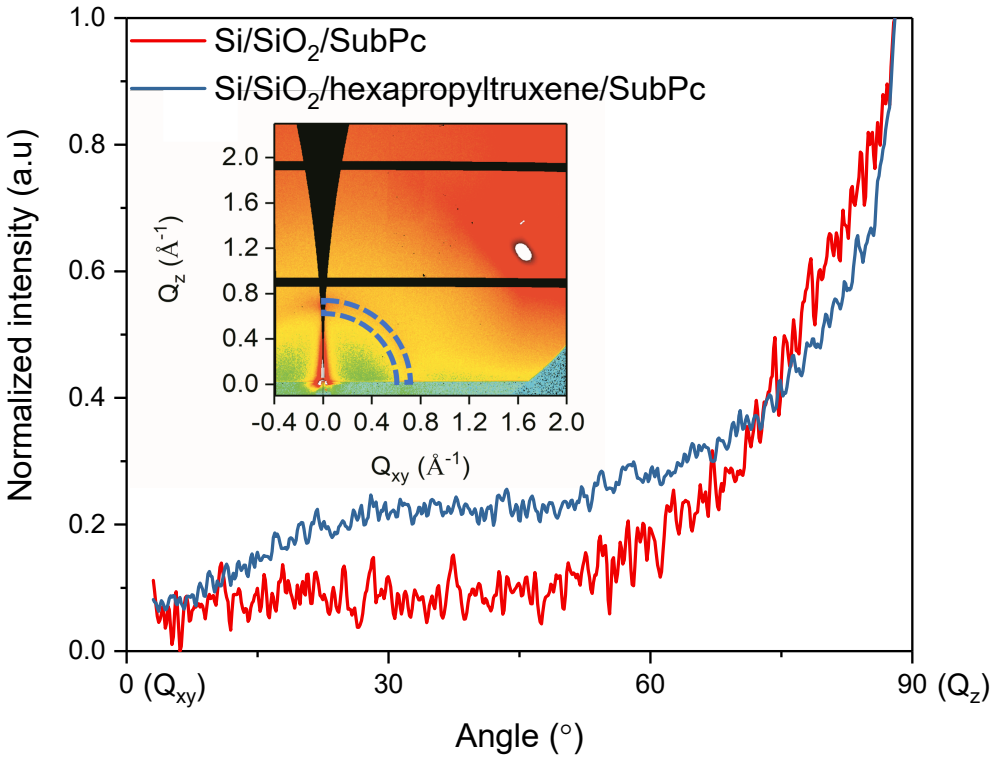


Figure 5.10: Radial distribution of the GIWAXS peak from 0.65 $Å^{-1}$ to 0.75 $Å^{-1}$. The cut section is indicated with dashed sector in the inset figure. The intensities of the peaks are normalized. 0 ° stands for Q_{xy} and 90 ° stands for Q_z.

of 13 nm SubPc on 3.8 nm hexapropyltruxene deposited on Si wafer. The roughness we obtained is 0.64 nm. Figure 5.11(g), (h), and (i) show the morphology of 13 nm SubPc on ITO glass and 5 nm MoO_x, the roughness is 0.45 nm, Figure5.11(j), (k), and (l) show the morphology of 13 nm SubPc on 3.8 nm hexapropyltruxene deposited on ITO glass and 5 nm MoO_x, the roughness is 0.55 nm. From the AFM analysis, we can conclude that both on Si and ITO/MoO_x film, SubPc appears to have a slightly rougher surface morphology if there is a hexapropyltruxene interlayer. Also, from the AFM images, we can see that the feature size of SubPc becomes smaller after inserting the hexapropyltruxene layer. We used the segmentation function in gwiddeon to calculate the domain size of the surface. By comparing this domain

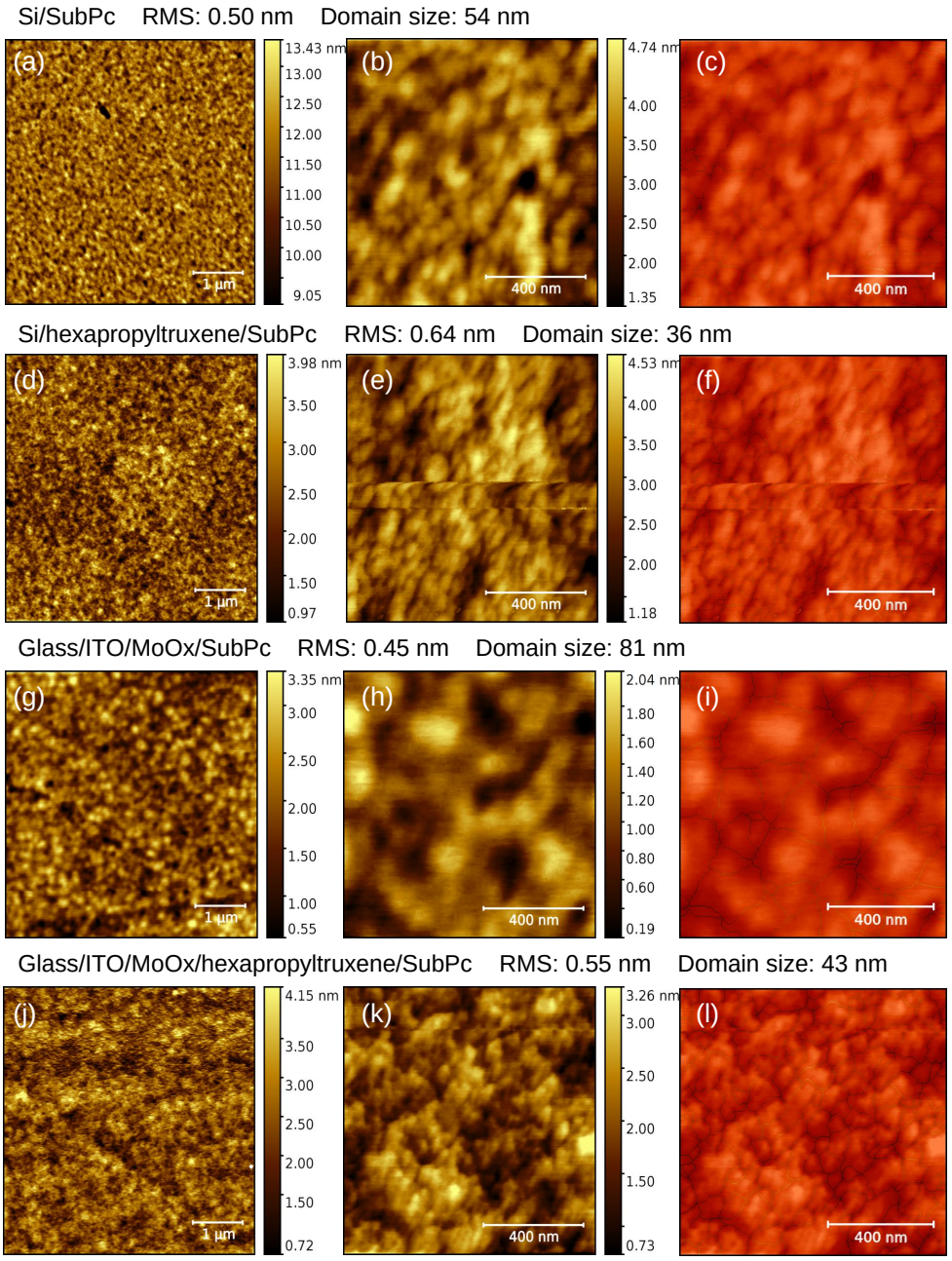


Figure 5.11: AFM images of the surface morphology of 13 nm SubPc deposited on different layers with the left column being 5x5 μm^2, the middle column being a zoomed-in version of 1x1 μm^2, and the right column being the domain-marked image of the 1x1 μm^2 versions: (a)(b)(c): Images of SubPc layer on a Si wafer. (d)(e)(f): images of Si/hexapropyltruxene (3.8 nm)/SubPc multilayer film. (g)(h)(i): Images of ITO/MoO_x(5 nm)/SubPc multilayer film. (j)(k)(l): Images of ITO/MoO_x(5 nm)/hexapropyltruxene(3.8 nm)/SubPc multilayer film.

size between the samples, we can have a visual knowledge about the surface shape and roughness. The calculated mean domain size shrinks from 54 nm to 36 nm after inserting the hexapropyltruxene layer in Si samples (from 81 nm to 43 nm after inserting the hexapropyltruxene layer in ITO/MoO_x samples). This evidence shows that hexapropyltruxene interlayer does modify the morphology of SubPc layer on top of it.

5.3.7 Steady-state Photoluminescence (SSPL) Analysis

To conclude the measurements, steady-state photoluminescence (SSPL) measurements were carried out and the results of the samples glass/SubPc(13 nm), glass/MoO_x (5 nm)/SubPc (13 nm), glass/hexapropyltruxene (3.8 nm)/SubPc (13 nm), and glass/MoO_x (5 nm)/hexapropyltruxene (3.8 nm)/SubPc (13 nm) are shown in Figure 5.12.

From Figure 5.12, we can see that SubPc films have two major emission peaks: around 620 and 720 nm. Comparing the PL peak intensity of bare SubPc and MoO_x/SubPc samples, we can find that the reduction of the emission peak intensity shows the exciton quenching effect of MoO_x layer. Specifically, the peak at 720 nm is more affected than the one at 620 nm. A notable increase in PL peak intensity after inserting the hexapropyltruxene layer indicates it has an exciton blocking effect.

Previous research illustrates that the SubPc PL emission components at these two peaks have different origins. The emission component around 620 nm is said to originate from the direct emission of excitons while the component around 720 nm comes from the emission of trapped excitons in structural defects of the SubPc films [89, 205]. The difference of the peak reduction after the insertion of the MoO_x layer indicates that the trapped excitons (720 nm) are more easily to be quenched by the MoO_x than the free excitons (620 nm). Also because of the exciton component difference, the ratio of the peak intensities (I_{720nm}/I_{620nm}) can be used as an indication of the concentration of microstructural defects inside the SubPc layer.

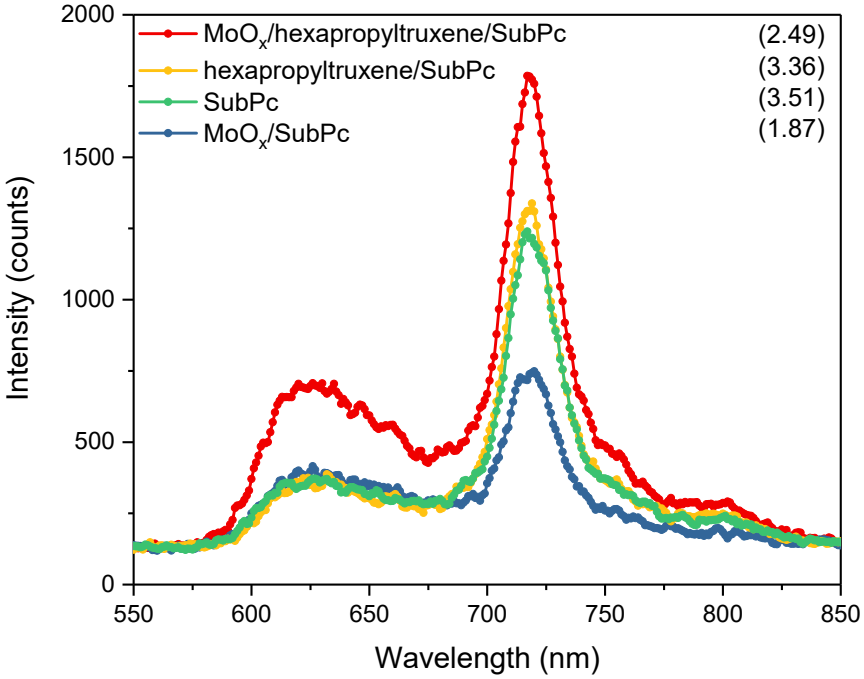


Figure 5.12: SSPL spectra of glass/SubPc(13 nm), glass/MoO_x (5 nm)/SubPc (13 nm), and glass/ MoO_x (5 nm)/hexapropyltruxene (3.8 nm)/SubPc (13 nm). The numbers in brackets on the right side of the graph are the ratios of peak intensities (I_{720nm}/I_{620nm}) of the corresponding samples.

We calculated the peak intensity ratio of the SSPL signal for each sample (see Figure 5.12): SubPc 3.51, MoO_x/SubPc 1.87, hexapropyltruxene/SubPc 3.36, and MoO_x/hexapropyltruxene/SubPc 2.49. The change of ratios indicates that apart from the exciton quenching effect, MoO_x layer also seems to reduce the microstructural defects concentration inside the subsequent deposited SubPc layer. This finding suggests that MoO_x layer not only quenches the excitons inside SubPc but also modifies the SubPc film structure. The addition of hexapropyltruxene interlayer between MoO_x and SubPc layer can recover this effect. However, I_{720nm}/I_{620nm} ratio of hexapropyltruxene/SubPc sample is still slightly lower than that of SubPc sample. This may be due to the template effect of hexapropyltruxene on SubPc, which has been observed in GIWAXS measurement.

Table 5.5: Time-resolved photoluminescence lifetimes of SubPc thin films on quartz glass with different interlayers. The emission component lifetime is measured at 620 nm and 720 nm.

Film	wavelength (nm)	τ_1 (ns)	τ_2 (ns)	χ^2 (reduced)
glass/SubPc	620*	0.593		2.971
glass/MoO_x/SubPc		0.576		1.986
glass/ MoO_x/hexapropyltruxene/SubPc		0.674		3.729
glass/hexapropyltruxene/SubPc		0.671		3.02
glass/SubPc	720*	5.018	2.419	1.076
glass/MoO_x/SubPc		3.563	1.302	1.085
glass/ MoO_x/hexapropyltruxene/SubPc		4.786	2.116	1.036
glass/hexapropyltruxene/SubPc		5.546	2.924	1.022

* The 620 nm data sets were fitted with the single exponential model while the 720 nm data sets were fitted with the bi-exponential model.

5.3.8 Time-resolved Photoluminescence (TRPL) Analysis

To further investigate the emission components' lifetimes, time-resolved photoluminescence (TRPL) spectra were measured for the same samples. The results are shown in Figure 5.13. And the instrument response function (IRF) is also plotted together with the experimental results.

Considering the different mechanisms of emission components at 620 and 720 nm [205], we used a single exponential fit to calculate the exciton lifetime at 620 nm, while a bi-exponential fit was utilised to model the component lifetime at 720 nm. The fitted lifetimes of emission components with the reduced χ^2 values [1] are shown in Table 5.5. The exciton lifetimes in different samples are similar to each other, due to the intrinsic short lifetime of excitons at an excitation with 620 nm wavelength. As the emission component at 720 nm is due to trapped excitons in structural defects in

[1] Due to the short lifetime of the excitons, the influence of the instrument response function (IRF) of the TRPL set-up should be considered in the fitting of PL decay. The most appropriate fitting method is the reconvolution fitting method. FluoFit software (PicoQuant GmbH, Germany) was used to perform the reconvolution exponential fitting. Unfortunately, the software does not provide standard errors of the fitted lifetime in our case, though it returned a confidence interval showing the fit is 'fitting' but without exact values. However, the programme also provides the reduced chi-square of each fitting as evidence of goodness-of-fit, which is included in the table.

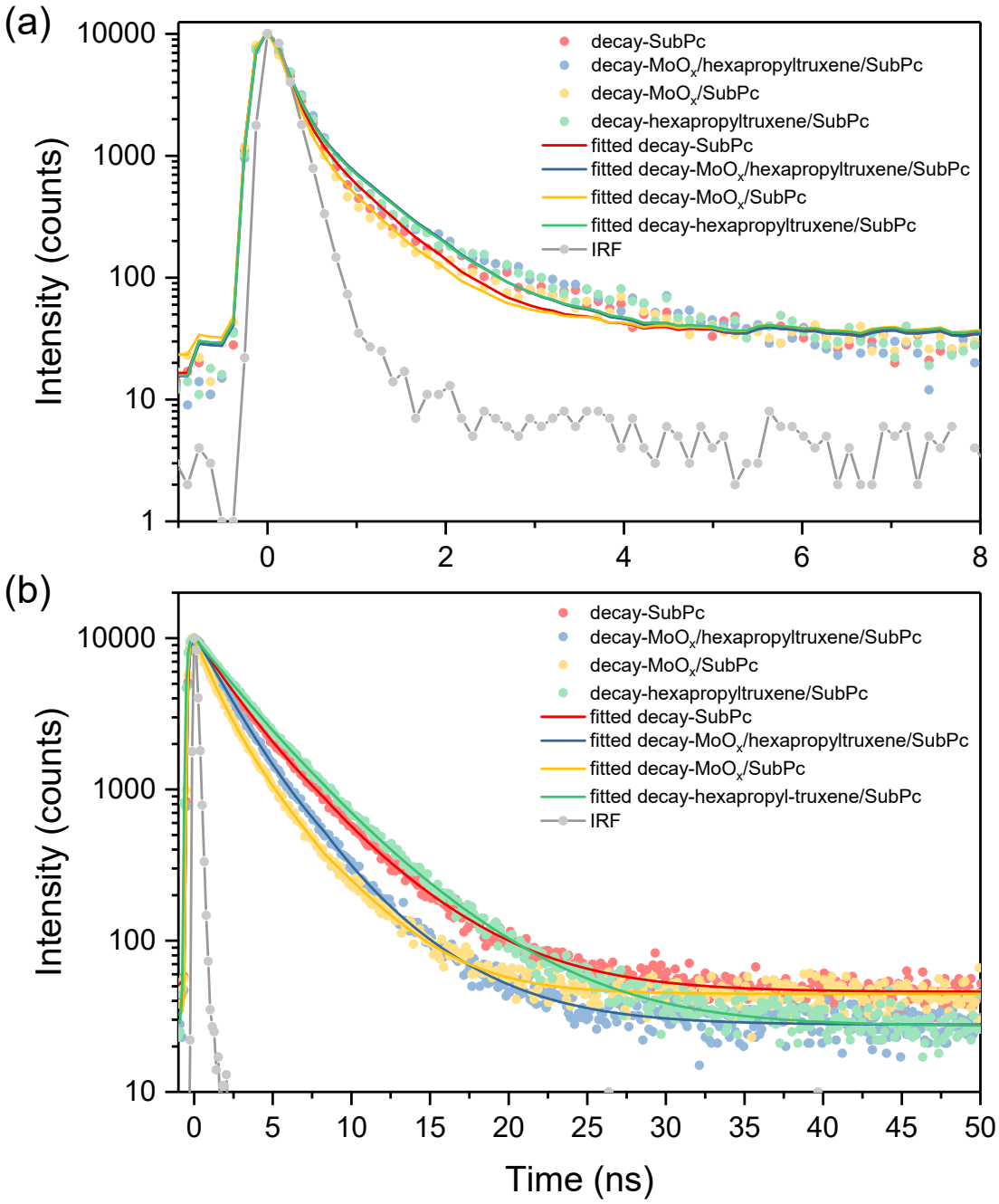


Figure 5.13: TRPL decay dynamics of glass/SubPc(13 nm), glass/MoO_x (5 nm)/SubPc (13 nm), glass/hexapropyltruxene (3.8 nm)/SubPc (13 nm) and glass/ MoO_x (5 nm)/hexapropyltruxene (3.8 nm)/SubPc (13 nm). The IRF is plotted together with the sample data. (a). TRPL decay dynamics at 620 nm wavelength, (b). TRPL decay dynamics at 720 nm wavelength.

SubPc, it is observed to have a longer lifetime than the emission at 620 nm. However, we still find that after inserting the MoO_x layer beneath the SubPc layer, the exciton

lifetime decreases. This result agrees with the quenching effect of the MoO_x layer. The estimated quenching effect (reduction of PL emission component lifetime at 620 nm) is about 3 % calculated according to the classical diffusion equation [205, 206]. After inserting the hexapropyltruxene, the exciton lifetime increases (from 0.576 nm to 0.674 ns). It improves even more than that in the bare SubPc film on glass (increases from 0.593 ns to 0.674 ns). This shows that the hexapropyltruxene layer can reduce the exciton quenching effect of the MoO_x layer. At 720 nm, the lifetime of the emission component decreases when a MoO_x layer is present directly beneath the SubPc layer compared with SubPc on bare glass. The estimated exciton quenching effect (reduction of PL emission component lifetime at 720 nm) is around 40 %. The lifetime increases again after inserting hexapropyltruxene in between MoO_x layer and SubPc layer, but it is still shorter than the ones in the pure SubPc layer (see Table 5.5). For the glass/hexapropyltruxene/SubPc sample, the lifetime of the emission is even longer than it is for the SubPc on glass layer. This behaviour indicates that the hexapropyltruxene layer acts as an exciton blocking layer between MoO_x and SubPc layers. It is worth noting that the exciton/emission component lifetimes of the hexapropyltruxene/SubPc sample at both 620 and 720 nm are longer than those in the glass/SubPc sample. It may indicate that apart from the exciton-blocking effect, the small microstructural changes induced by hexapropyltruxene in the subsequent SubPc layer affects the exciton lifetime, as well. In particular, the emission at 720 nm is caused by the excitons trapped inside the structural defects of the SubPc layer [205].

5.4 Conclusions

By exploring the characteristics of hexapropyltruxene and its application in standard SubPc/C60 planar heterojunction solar cells, we find that it acts as a good interface modifier layer on top of a MoO_x hole contact layer. A maximum of about 20 % of PCE enhancement (from 2.6 % to 3.0 %) was achieved by inserting a 3.8 nm

interlayer between MoO_x and the photovoltaic active donor layer of SubPc. Our characterisation of the thin film microstructure shows that hexapropyltruxene modifies the growth of the subsequently deposited SubPc layer. In-situ GIWAXS and in-situ spectroscopic ellipsometry measurements indicate that insertion of the hexapropyltruxene layer induces a change of the crystal structure of SubPc, which impacts the absorption properties and concentration of crystal structure defects of SubPc. However, absorption changes have only a minor impact on device performance. Looking at time-resolved photoluminescence spectroscopy, we find the enhancement of the PCE is mainly due to improving the blocking of photogenerated excitons from recombining at the MoO_x interface. The excitons are trapped in the defects in SubPc films induced by the hexapropyltruxene layer, which increases the lifetime of photogenerated excitons by ca. 35 %. This shows that hexapropyltruxene can be used with beneficial effects as an interface layer in small molecule OSCs containing SubPc and potentially other 'small molecule' materials, as our results indicate that electrode modification with hexapropyltruxene may offer a potential approach for PCE enhancement.

Chapter 6

Hexapropyltruxene in IMEC Solar Cell Stack

6.1 Introduction

In Chapter 5, we have investigated the function of hexapropyltruxene layer as an interlayer between MoO_x and SubPc layers inside the SubPc/C60 solar stack. The research reveals that the hexapropyltruxene interlayer mainly acts as an exciton blocking layer between MoO_x and SubPc layers. It also presents a weak template growth effect on the growth behaviour of SubPc thin film. However, the PCE of a typical SubPc/C60 solar cell is limited to 3-4% [73, 89, 200, 207], which is much lower in PCE compared to other high-performance OSC stacks. Thus, investigating the usage of hexapropyltruxene in other solar cell stacks with higher PCEs is of significance. In addition, Chapter 5 only explores the influence of hexapropyltruxene interlayer on SubPc, which might be a trivial example. We need to examine if the insertion of hexapropyltruxene interlayer has similar benefits for other donor materials (exciton blocking effect or molecular template growth (MTG) effect). Considering these two reasons, it is of interest to apply hexapropyltruxene as an interlayer in other solar cell stacks.

Among several planar heterojunction stacks, the IMEC stack is a good candidate for our experiment. It has a high PCE (its best reported PCE is 8.4%) [159], high V_{oc}

[69], and a fullerene-free structure [208]. A typical IMEC stack has a solar cell structure as glass/ITO/HCL (e.g. MoO_x or PEDOT:PSS)/α-6T/SubNc/SubPc/BCP/Al. In this thesis, MoO_x was used as HCL and hexapropyltruxene layer was inserted in between MoO_x and α-6T layers to characterize its functions as an interlayer. Figure 6.1 (a) shows the stack of the IMEC stack solar cells fabricated in this chapter and Figure 6.1 (b) illustrates the energy levels of the materials used in this work.

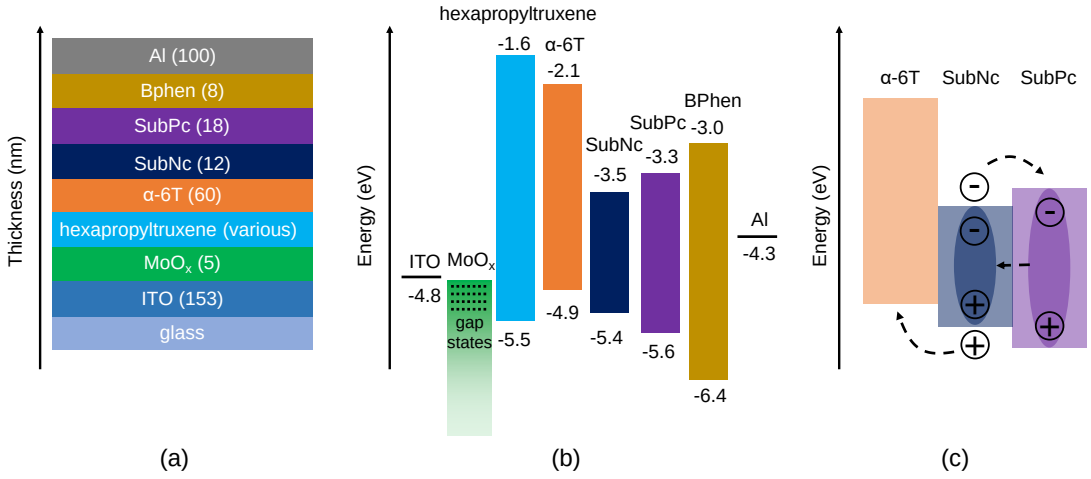


Figure 6.1: Solar cell stack, energy levels of the solar cells, and an explanation of the two-step exciton dissociation mechanism in the IMEC stack. (a). Schematics of the investigated solar cell stacks with the individual layer thickness given in nanometres, (b). Energy levels of materials used in this work. The energy levels of α-6T, SubNc, SubPc, BPhen, and electrodes (UPS & IPES) are taken from literature [158, 201]. The energy levels of MoO_x are normally 9.2-9.7 eV (valence band) and 6.2-6.9 eV (conduction band) [112, 196–198]. The schematic presentation of the energy levels of MoO_x is adjusted due to the shift of the vacuum level [85, 112, 199]. Gap states of MoO_x is shown as dotted lines. The HOMO-LUMO levels of hexapropyltruxene are determined by cyclic voltammetry. (c). A schematic presentation of the two-step exciton dissociation mechanism in the IMEC stack.

This solar cell stack has a high PCE due to a two-step exciton dissociation mechanism illustrated in Figure 6.1 (c). In brief, excitons generated within the SubPc layer can be transferred immediately to the SubNc layer nearby via long-range Föster

energy transfer [158, 159]. Subsequently, the excitons inside SubNc layer dissociate at the interface of SubNc and α-6T. With the full spectrum coverage of the combination of the three absorbing materials, this two-step mechanism helps generate a high photocurrent. Besides, this solar cell stack has a V_{oc} as high as 1 V. All these advantages make the IMEC stack a good solar cell structure with a remarkable PCE.

6.2 Experimental Details

Similar to Chapter 5, thin-film and device samples reported in this chapter were fabricated following the experimental details in Chapter 4. Table 6.1 shows the thicknesses and evaporation rates of each layer of the solar cells fabricated in this chapter. The thin film and solar cell samples were fabricated in vacuum deposition chamber VC-B following the experimental descriptions in Chapter 4.

Table 6.1: Thin film/device stacks in different experiments.

Experiment	Thin film/device stack
Solar cell	glass/ITO/MoO_x (0 or 2.4 nm, 0.1 Å/s)/hexapropyltruxene (various, 0.1 Å/s)/α-6T (60 nm, 1 Å/s)/SubNc (12 nm, 1 Å/s)/SubPc (18 nm, 1 Å/s)/BPhen (8 nm, 1 Å/s)/Al (100 nm, 1.5 Å/s)
XRD, AFM, UV-vis, SSPL, TRPL	glass/MoO_x (2.4 nm, 0.1 Å/s)/hexapropyltruxene (various, 0.1 Å/s)/α-6T (60 nm, 1 Å/s)

XRD measurements of the thin films used in this chapter were carried out via the Rigaku SmartLab system. AFM measurements were undertaken via MFP-3D atomic force microscopy system. TRPL and SSPL experiments were performed via the FluoTime 300 set-up. In TRPL measurement, LDH-P-C-405 laser source was used to generate the 405 nm excitation laser, and 550, 595, 645 nm emission wavelengths of α-6T were monitored. In SSPL, the same laser source was applied. The measuring time interval for each wavelength is 0.5 s.

For solar cell JV measurement, at least four solar cells with an active area of 8.0 mm^2 (defined by the geometric overlap between ITO and Al) were measured for each thickness of hexapropyltruxene. By following a pre-established protocol [64, 65], the mismatch factor for the IMEC stack solar cell is calculated as shown in Table 6.2.

Table 6.2: Solar cell mismatch factor calculation result for IMEC stack.

Solar cell stack	Mismatch factor
IMEC solar cell with 2.4 nm MoO_x and no hexapropyltruxene	1.031
IMEC solar cell with 2.4 nm MoO_x and 0.8 nm hexapropyltruxene	1.029
IMEC solar cell without MoO_x nor hexapropyltruxene	1.029

6.3 Results and Discussion

6.3.1 Current-Voltage (JV) Characterization of Solar Cells (IMEC with MoO_x)

IMEC stack solar cells with an insertion of hexapropyltruxene interlayer which has different layer thicknesses between HTL (MoO_x) and the donor layer (α-6T) were fabricated. Figure 6.2 illustrates the JV curves of the characterized solar cells. Figure 6.3 and Table 6.3 shows the results of the performances of the experimented solar cells.

Table 6.3: IMEC solar cell (with MoO_x) device performance summary of solar cells with different thicknesses of hexapropyltruxene.

Hexapropyltruxene thickness (nm)	J_{sc} ($mA{\cdot}cm^{-2}$)	V_{oc} (V)	FF (%)	PCE (%)
0	9.8 ± 0.2	0.96 ± 0.01	63 ± 1	5.9 ± 0.2
0.8	10.2 ± 0.1	0.96 ± 0.01	63 ± 1	6.1 ± 0.1
2.3	9.8 ± 0.4	0.96 ± 0.01	62 ± 1	5.8 ± 0.3
3.8	9.4 ± 0.5	0.95 ± 0.01	58 ± 1	5.2 ± 0.3

As shown in Figure 6.3, PCE of the solar cells increases slightly with the insertion of 0.8 nm hexapropyltruxene between MoO_x and α-6T (from 5.9% to 6.1%). With the increase of the thickness of hexapropyltruxene interlayer, PCE decreases. There is the same trend of the change in J_{sc}. However, V_{oc} and FF do not decrease dramatically

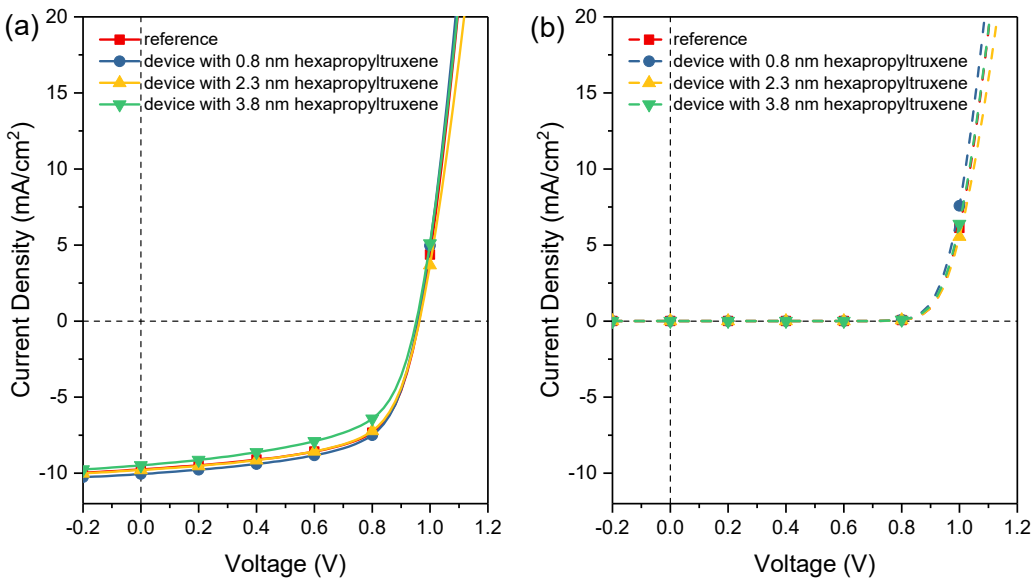


Figure 6.2: JV curves of the solar cells with different thicknesses of a hexapropyltruxene interlayer between MoO_x and α-6T. (a). Solid lines represent the JV curves under illumination. (b). Dashed lines represent the JV curves in the dark.

with the thickness increase of hexapropyltruxene layer. The PCE improvement is mainly due to the increase of J_{sc}. From the JV curve plot in Figure 6.2 we can make the conclusion that the insertion of 0.8 nm hexapropyltruxene increases the J_{sc} of the IMEC solar cells, thus improving the PCE. However, with the thickness of hexapropyltruxene layer becomes large, this improvement effect disappears.

6.3.2 Current-Voltage (JV) Characterization of Solar Cells (IMEC without MoO_x)

To better understand the function of hexapropyltruxene interlayer inside IMEC stack solar cells, the same solar cells without the MoO_x layer as the HTL were fabricated. Figure 6.4 illustrates the JV curve of the corresponding cells. Figure 6.5 and Table 6.4 shows the solar cell performances (PCE, V_{oc}, J_{sc}, and FF).

Figure 6.4 and Figure 6.5 show that the insertion of 0.8 nm hexapropyltruxene between ITO and α-6T layers may slightly increase the J_{sc} of the solar cell (from 9.8 to

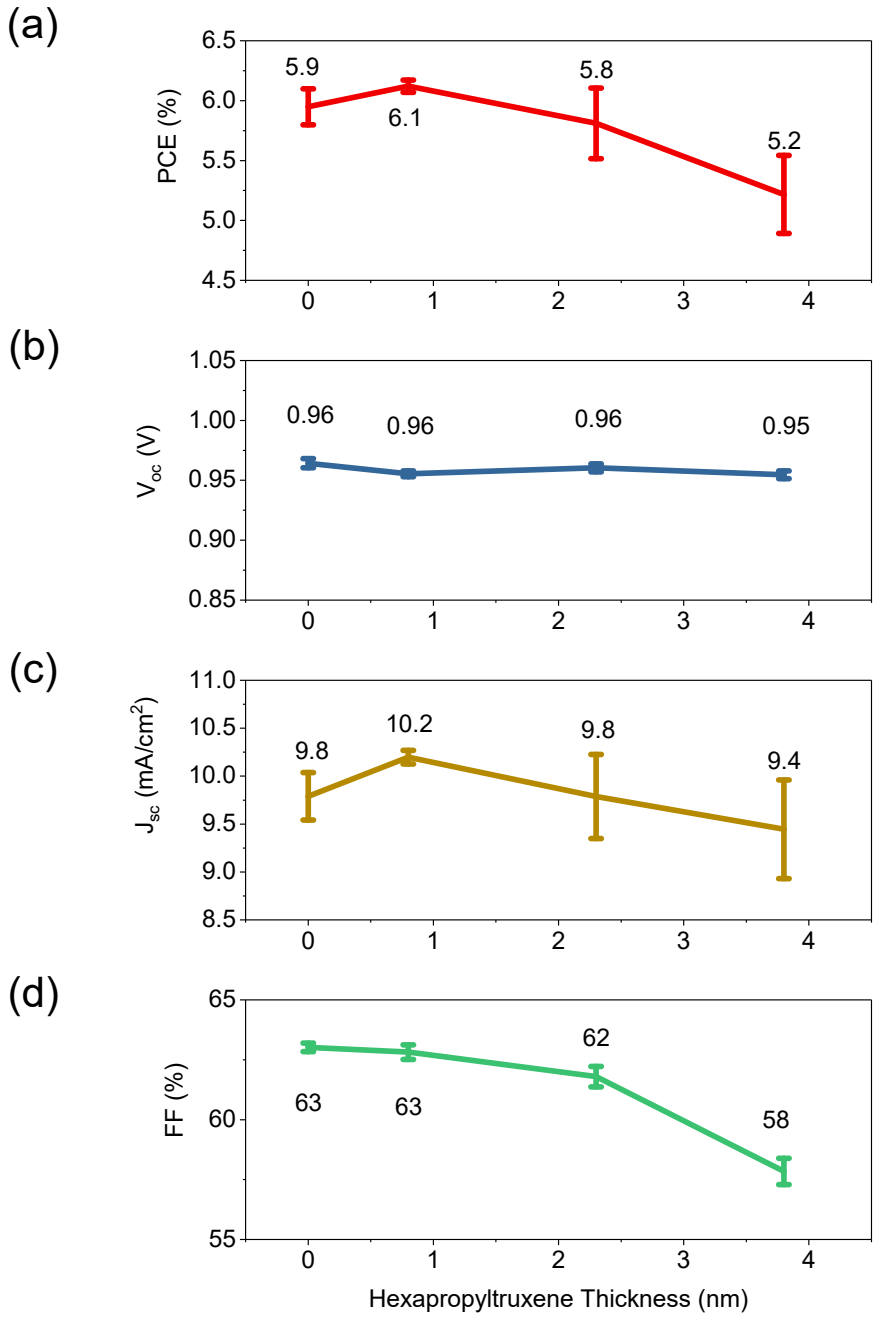


Figure 6.3: Solar cell performance versus the thickness of the hexapropyltruxene layer between MoO_x and α-6T. (a). PCE, (b). V_{oc}, (c). J_{sc}, (d). FF.

10.1 mA/cm^2). However, this minor increment is so small that its contribution to the improvement in PCE can be compensated by the drop of other components such as V_{oc} and FF. From Figure 6.5 we can conclude that the insertion of hexapropyltruxene

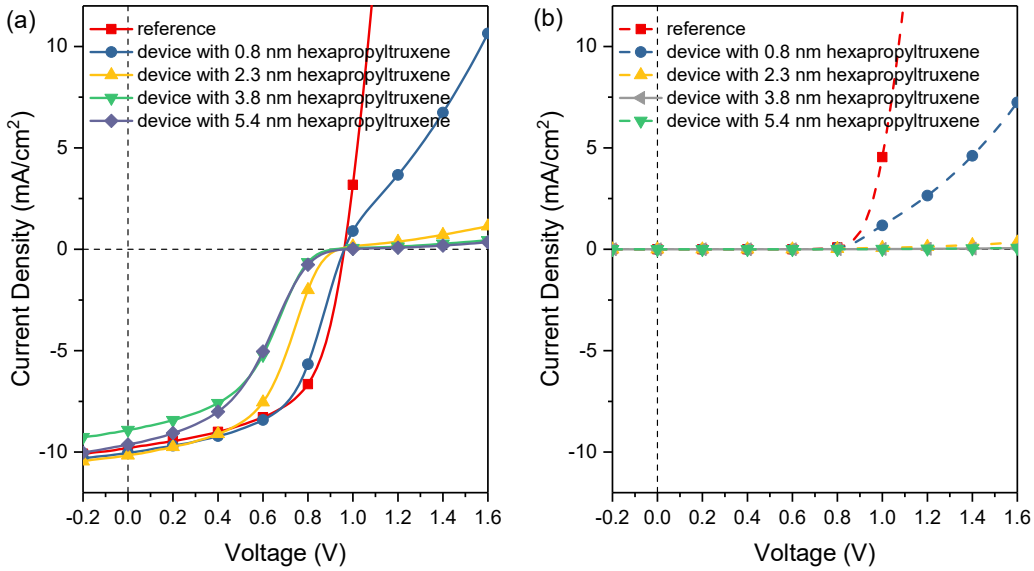


Figure 6.4: JV curves of the solar cells with different thicknesses of a hexapropyltruxene interlayer between ITO and α-6T. (a). Solid lines represent the JV curves under illumination. (b). Dashed lines represent the JV curves in the dark.

Table 6.4: IMEC solar cell (without MoO_x) device performance summary of solar cells with different thicknesses of hexapropyltruxene.

Hexapropyltruxene thickness (nm)	J_{sc} (mA·cm^{-2})	V_{oc} (V)	FF (%)	PCE (%)
0	9.8 ± 0.2	0.96 ± 0.01	58 ± 1	5.5 ± 0.1
0.8	10.1 ± 0.4	0.96 ± 0.01	55 ± 1	5.3 ± 0.2
2.3	10.0 ± 0.3	0.94 ± 0.01	48 ± 1	4.5 ± 0.1
3.8	9.2 ± 0.4	0.92 ± 0.01	41 ± 1	3.5 ± 0.1
5.4	9.4 ± 0.5	0.97 ± 0.01	38 ± 1	3.5 ± 0.1

layer in IMEC stack without MoO_x will not help improve the solar cell performance. The shapes of JV curves of the representative solar cells in Figure 6.4 reveal that hexapropyltruxene is not a good candidate HTL material. When the hexapropyltruxene layer becomes thicker, the S-kink appears in the JV curves. It is due to the mismatch of the energy levels of hexapropyltruxene and ITO, which forms an energy barrier for charge carriers to overcome [204]. The energy barrier can be overcome by the quantum tunnelling effect when the hexapropyltruxene layer is thin enough. With the layer thickness of hexapropyltruxene becomes thick, the effect of the energy

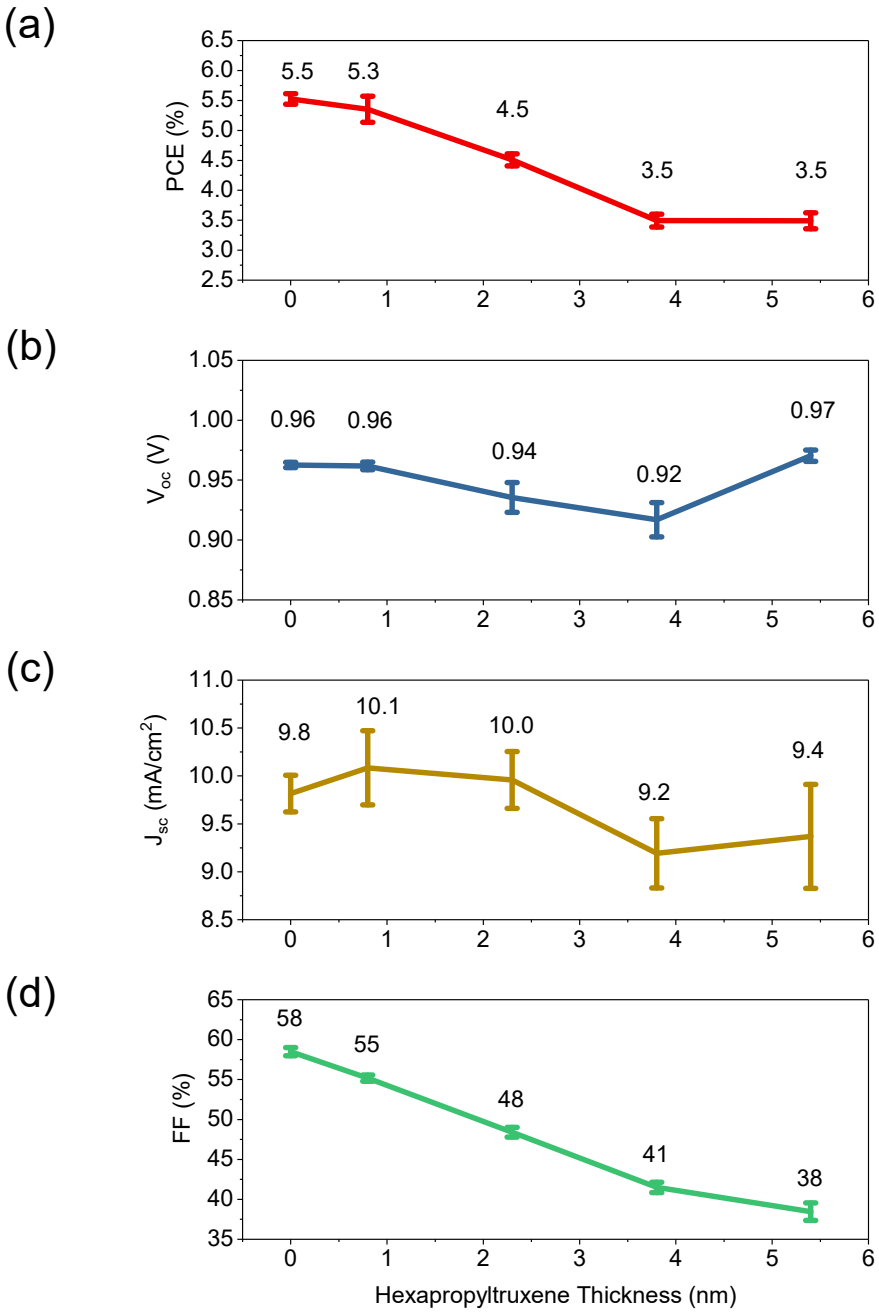


Figure 6.5: Solar cell performance versus the thickness of the hexapropyltruxene layer between ITO and α-6T. (a). PCE, (b). V_{oc}, (c). J_{sc}, (d). FF.

barrier takes in place, and the S-kinks start to increase.

6.3.3 External Quantum Efficiency (EQE) Analysis (IMEC with MoO_x)

To investigate the reason for the short-circuit current (J_{sc}) improvement when adding a 0.8 nm hexapropyltruxene between MoO_x and α-6T in Section 6.3.1, EQE measurements of the corresponding solar cells were performed. The results are shown in Figure 6.6. From the EQE result, we can find that with the insertion of 0.8 nm hexapropyltruxene layer, the EQE of the solar cell increases slightly in the whole stack absorption range. With the increase of the hexapropyltruxene layer thickness, the EQE in the whole stack absorption range drops evenly. This EQE change is different from that in SubPc/C60 solar cell stack shown in Section 5.3.3, which indicates that the hexapropyltruxene layer in IMEC stack may play a different role rather than as an ExBL. This change in the EQE may be caused by the change of absorption behaviour (molecular orientation change or a change in the interference of the stack) or the charge transport behaviour of the active layer.

6.3.4 Device Absorption Simulation

The observation of the EQE change indicates that the EQE diagram increases or decreases evenly in the entire absorption range of the solar cell stack when the thickness of the hexapropyltruxene layer increases. This behaviour is very likely due to a change in the interference pattern change of the solar cell stack. A device absorption simulation of the IMEC solar cell stack with different thicknesses of hexapropyltruxene was performed to examine if the influence of stack interference is the cause of the EQE change. The result is shown in Figure 6.7. In this simulation model, the influence of templating effect of the MoO_x and hexapropyltruxene on α-6T was excluded, i.e. the refractive index of α-6T in this simulation model does not change as the underlying layer (MoO_x and hexapropyltruxene) changes.

From the simulation result, we can find that regardless of the tiny difference in the

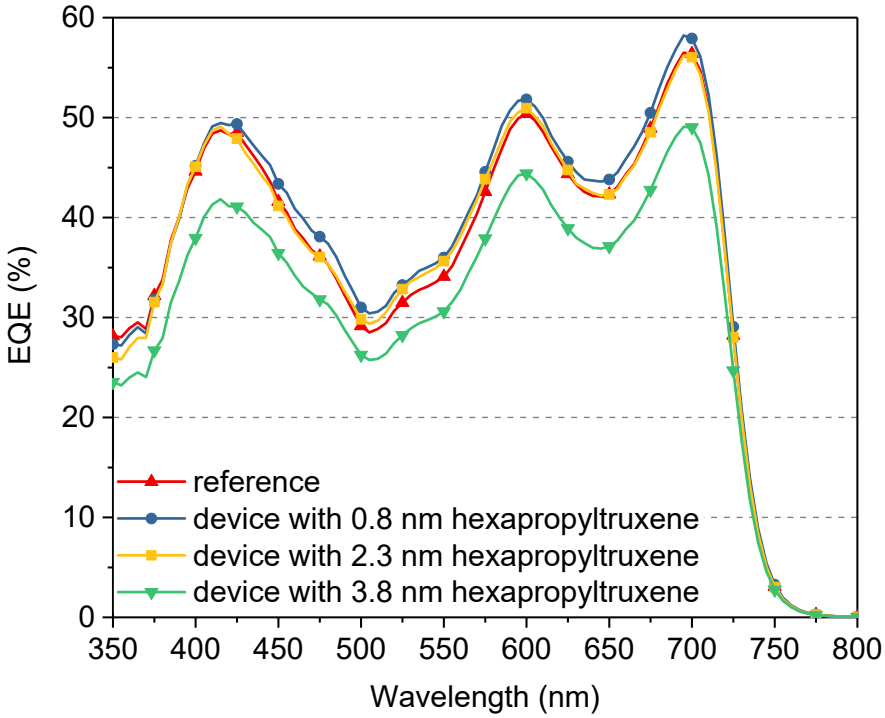


Figure 6.6: EQE of the solar cells with different thicknesses of hexapropyltruxene interlayers between ITO and MoO_x.

region of MoO_x and hexapropyltruxene, the absorption behaviour of the whole solar cell stack with different thicknesses of hexapropyltruxene layers are nearly identical. This simulation result suggests that the change in the thickness of hexapropyltruxnee layer does not have a significant impact on the stack interference behaviour. The increase of solar cell efficiency does not come from the thickness optimization of the solar cell stack. Thus, the change in EQE may be caused by the template effect of hexapropyltruxene (absorption change) or a change in charge transporting, which needs further investigation.

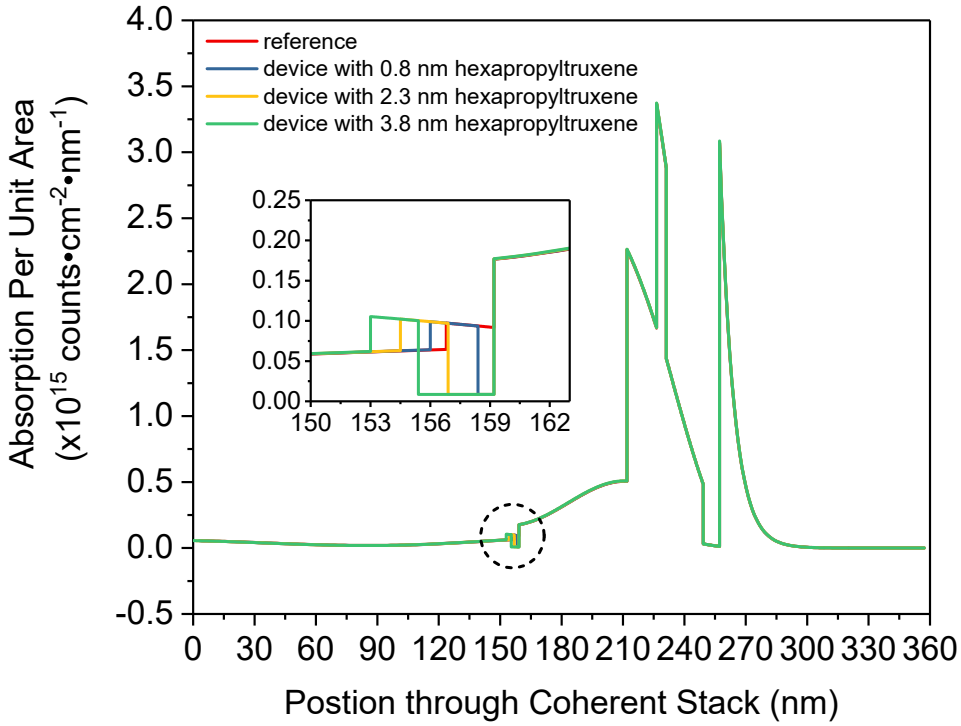


Figure 6.7: Absorption simulation of IMEC solar cell stack with different thicknesses of hexapropyltruxene using a transfer matrix approach. The reference device is the IMEC stack solar cell with MoO_x. The inserted graph is the detailed plot of the dash circled region.

6.3.5 Ultraviolet-visible (UV-vis) Spectroscopy Absorption Analysis

To confirm if there is any templating effect causing the absorption change of α-6T, UV-vis measurements of α-6T thin films on substrates with different additional thin-film layers (MoO_x and hexapropyltruxene) were undertaken. Because the ultra-thin hexapropyltruxene film is sensitive to air and its morphology will change dramatically after being exposed to air, it is difficult to obtain the UV-vis absorption behaviour of the ultra-thin hexapropyltruxene films. The refractive index of hexapropyltruxene and MoO_x obtained from in-situ ellipsometry were used to simulate the absorption and reflection behaviour of the substrates. The UV-vis absorption results are shown in Figure 6.8. Figure 6.8 shows that with the insertion of hexapropyltruxene layer

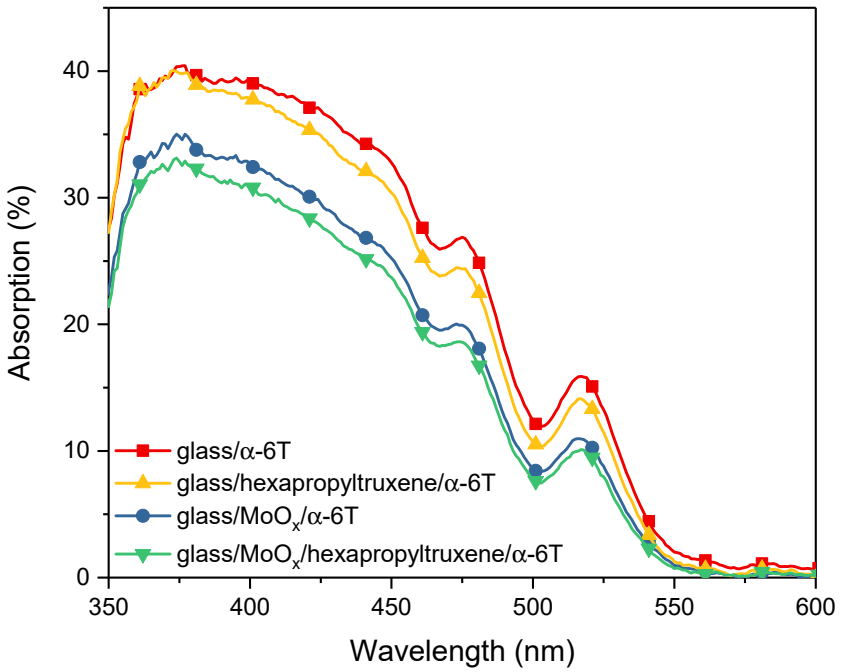


Figure 6.8: UV-vis absorption measurement results of the α-6T thin films on different substrates. The absorption of the substrate glass, hexapropyltruxene, and MoO_x layers have been subtracted. The thin film samples we use are: glass/α-6T (60 nm), glass/MoO_x (2.4 nm)/α-6T (60 nm), glass/MoO_x (2.4 nm)/hexapropyltruxene (0.8 nm)/α-6T (60 nm), glass/hexapropyltruxene (0.8 nm)/α-6T (60 nm).

underneath the α-6T layer, the absorption of α-6T reduces, though the absolute absorption reduction value is approximately 2 %. The reduction ratio is around 5 % to 10 %. From previous solar cell performance analysis, we can find that the small reduction of the α-6T absorption does not influence the solar cell efficiency. By insertion of the hexapropyltruxene layer under the α-6T thin film, α-6T thin film growth is influenced, and the thin film absorbs slightly less light. The reduction in the light absorption of the α-6T thin films after the insertion of hexapropyltruxene does not affect solar cell performance. On the contrary, the solar cells with 0.8 nm hexapropyltruxene have higher J_{sc} and PCE than the reference devices. Thus, a change in absorption is not the major reason for the increase of solar cell performance

after the insertion of hexapropyltruxene interlayer.

However, this absorption behaviour change reflects the change in the α-6T crystal structure in thin films. It suggests that hexapropyltruxene has a weak templating effect on α-6T growth. We also find that with the MoO_x layer, α-6T absorption reduces dramatically. This finding indicates that MoO_x layer has a templating effect on α-6T growth.

6.3.6 X-ray Diffraction (XRD) Analysis

To confirm if the solar cell performance change is caused by any structural change induced via the insertion of hexapropyltruxene, the XRD measurements of the α-6T thin films on different substrates were carried out. The results are shown in Figure 6.9. The background peaks of the glass substrate are subtracted via background fitting. From this figure we can find the XRD peaks for α-6T polymorphs (LT-, HT-, and β-phases) appear in the sample XRD diffractions. The peaks of LT(200) and β(002) are slightly shifted, which is also mentioned in other research [141,209]. According to Christopher Lorch *et al*'s explanation, this phenomenon is due to slightly distorted, more upright standing molecules forming a slightly expanded unit cell [209].

Comparing the XRD results of thin-film samples with/without hexapropyltruxene, we find that there is no noticeable crystal structure change before and after the insertion of hexapropyltruxene layer. A noticeable difference is that after the insertion of hexapropyltruxene layer between MoO_x and α-6T layers, the α-6T LT-phase feature peaks become a little weaker. The change of weakening LT-phase peaks can also be observed from the thin film samples without MoO_x layers. This finding is in agreement with the UV-vis measurement results that hexapropyltruxene has a weak templating effect on α-6T, which induces the α-6T on hexapropyltruxene layer to form less LT-phase. In the meantime, the thin film is a little more disordered. This may clarify the change of α-6T absorption after the insertion of hexapropyltruxene layer. However, an

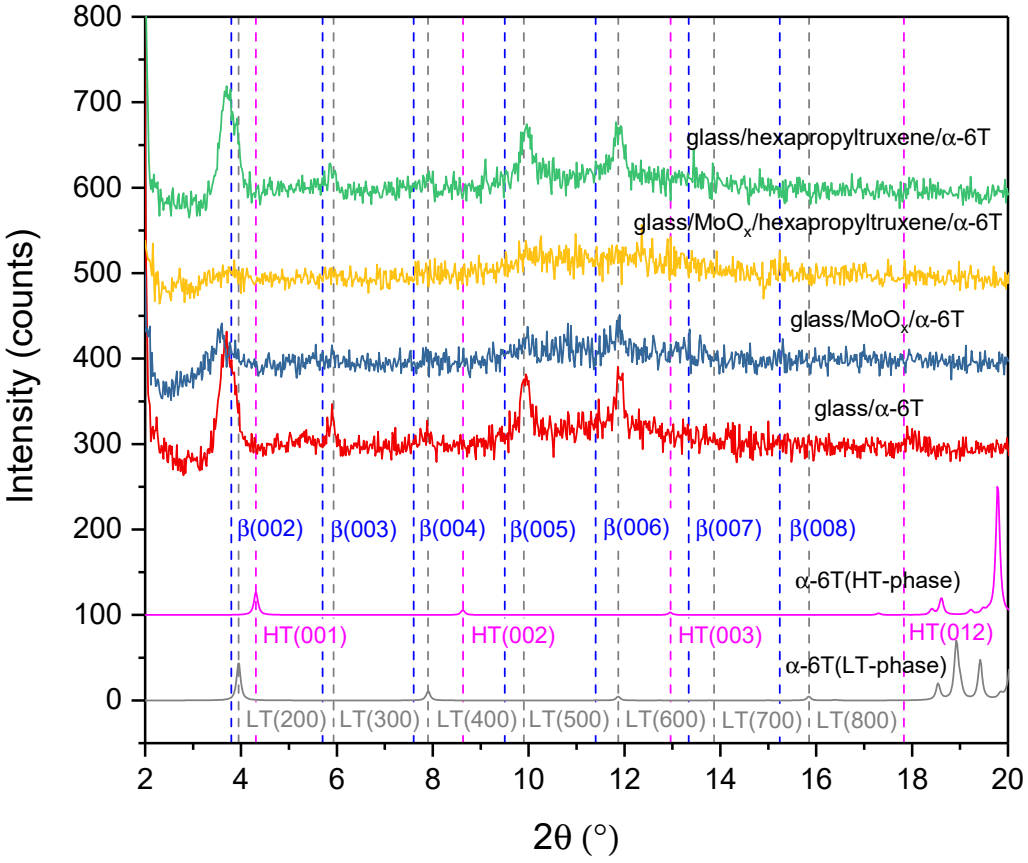


Figure 6.9: XRD measurement of the α-6T thin films on different substrates. The thin film samples we use are: glass/α-6T (60 nm), glass/MoO_x (2.4 nm)/α-6T (60 nm), glass/MoO_x (2.4 nm)/hexapropyltruxene (0.8 nm)/α-6T (60 nm), glass/hexapropyltruxene (0.8 nm)/α-6T (60 nm). The background signal of the glass substrate is subtracted. Powder diffraction pattern of α-6T LT, HT, and β-phases calculated by Mercury software [210] is also plotted at the bottom of the graph. Possible diffraction peaks of α-6T LT, HT, and β-phases are marked as dashed lines in the graph [120, 161, 162, 165]. (To the best of the author's knowledge, the crystallographic information of α-6T β-phase reported in the literature [120, 162] is not sufficient to simulate the powder diffraction profile. Thus, only the possible diffraction peak locations of the β-phase are marked in this figure.)

exciting result appears when we compare the thin film samples with/without MoO_x layer. We can find that after the insertion of MoO_x layer beneath the α-6T layer, the XRD peaks of LT- and HT-phases become much weaker and the peak of β(008) rises. This result indicates that MoO_x layer has a templating effect on the growth of α-6T.

Combining the results of UV-vis and XRD measurements, there seems a connection between the crystallinity of the thin film and the light absorption. If the molecules are oriented correctly, thin films with better crystallinity have higher light absorption.

6.3.7 Atomic Force Microscopy (AFM) Analysis

AFM measurements of the same thin films of the XRD measurements were performed. The result can be found in Figure 6.10. Shown in this figure, α-6T thin films present the typical surface morphology, which is observed by other research reports [120, 134, 160]. α-6T shows a rough surface morphology, with an RMS of approximately 10 nm. Considering the total thickness of α-6T thin film which is 60 nm, 10 nm RMS is a considerably rough surface. This result indicates that the donor and acceptor materials in IMEC stack form an interpenetrating interface. This rough morphology gives the excitons a large interface to be split into free electrons and holes. Besides, this morphology avoids the disadvantages of bulk heterojunctions, such as small or isolated domains which cause trapped charge recombination. Thus, IMEC stack shows a proper morphology for solar cell design.

However, the morphology of α-6T in all the AFM images presents the same node-like or sphere-like shape. From the AFM images, we cannot identify any notable differences among the four thin-film samples. This result indicates that the templating effects of hexapropyltruxene as well as MoO_x layers on the α-6T layer do not affect the surface morphology. Instead, from our XRD and UV-vis analysis, only the crystal structure of α-6T is influenced by these interlayers.

6.3.8 Steady-state Photoluminescence (SSPL) & Time-resolved Photoluminescence (TRPL) Analysis

The previous analysis of XRD, UV-vis, and AFM suggests that hexapropyltruxene has a templating effect on the growth of α-6T thin film. The analysis of the function

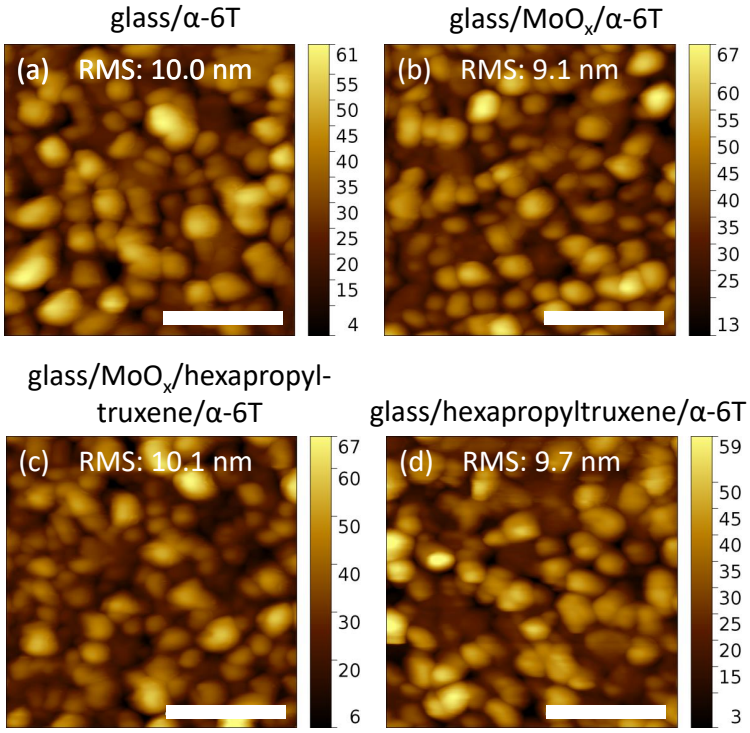


Figure 6.10: AFM height images of the α-6T thin films on different substrates. (a). height image of glass/α-6T (60 nm) thin film; (b). height image of glass/MoO_x (2.4 nm)/α-6T (60 nm) thin film; (c). height image of glass/MoO_x (2.4 nm)/hexapropyltruxene (0.8 nm)/α-6T (60 nm) thin film; (d). height image of glass/hexapropyltruxene (0.8 nm)/α-6T (60 nm) thin film. RMS stands for root mean squared roughness. The scale bar in each image is 400 nm.

of hexapropyltruxene in SubPc/C60 solar cells in Section 5.3.7 suggests hexapropyltruxene works mainly as an ExBL to prevent excitons from quenching between SubPc layer and MoO_x layer. To check if the hexapropyltruxene interlayer between MoO_x and α-6T layers is also acting as an ExBL, both SSPL and TRPL measurements of the same thin film examples as those in the XRD measurement were performed. The results are shown in Figure 6.11 and Figure 6.12.

Figure 6.11 shows the SSPL result. This graph shows that α-6T has three major photoluminescence peaks, which are approximately 550, 595, and 645 nm. The peak locations agree with the previous research [211–213]. In this graph, the intensity of the

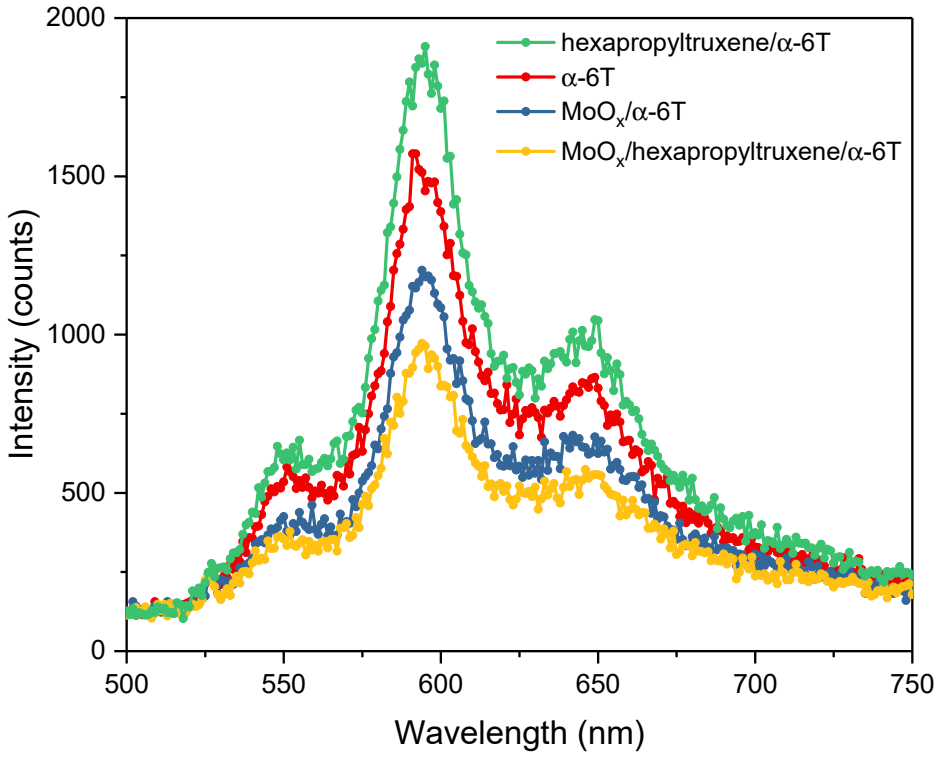


Figure 6.11: SSPL result of the α-6T thin films on different substrates (glass, glass/hexapropyltruxene, glass/MoO_x, and glass/MoO_x/hexapropyltruxene). The samples are excited via a laser with a 410 nm wavelength.

PL peaks of MoO_x/α-6T sample is lower than the bare α-6T sample, which indicates that MoO_x thin film may have the quenching effect on α-6T, too. The intensity of the PL peaks of the hexapropyltruxene/α-6T sample is the strongest, even higher than that of the bare α-6T layer. This result is similar to that in Chapter 5. It may be due to the templating effect of hexapropyltruxene on α-6T. However, the intensity of the PL peaks of MoO_x/hexapropyltruxene/α-6T sample is even lower than the MoO_x/α-6T sample. This contradicts the assumption that hexapropyltruxene layer acts as an ExBL in between MoO_x and α-6T layers. The SSPL result cannot explain if hexapropyltruxene between MoO_x and α-6T layers acts as ExBL or not. To further investigate this question, TRPL measurements were undertaken to track the lifetime

of excitons inside these samples. The result of TRPL is shown in Figure 6.12.

Figure 6.12 illustrates the exciton lifetime of the different samples. From the fitting curves, we can find that the lifetime of the excitons inside different samples is very similar to each other, all of which are very short. This short lifetime of excitons agrees with the previous research [214, 215]. The detailed fitting result [1] is shown in Table 6.5. We use the single-exponential model to fit the results. Researchers have used the single-exponential model, bi-exponential model, and triple-exponential model to simulate the TRPL decay signal of α-6T [212, 216, 217]. However, the photoluminescence mechanism of α-6T is one-step procedure [212, 214]. Thus, the single-exponential model is suitable to describe the exciton decay behaviour within α-6T thin films.

From Table 6.5, we can see that despite the lifetime of excitons at the same wavelength in the four different α-6T samples being very close to each other, there are still minor differences. The samples with hexapropyltruxene interlayers have marginally longer exciton lifetimes than those without hexapropyltruxene interlayers. The TRPL measurement results suggest that hexapropyltruxene layer has a weak exciton blocking effect on α-6T. This may be the reason why the solar cells inserted with 0.8 nm hexapropyltruxene have better performances. However, due to the small difference in fitted lifetimes, this inference needs further supporting evidence.

6.4 Conclusions

The IMEC solar cells show better performances after the insertion of an ultra-thin (0.8 nm) of hexapropyltruxene between MoO_x and α-6T. Considering the slight PCE increase after the insertion of 0.8 nm hexapropyltruxene layer between MoO_x and α-6T, it is first suspected that the improvement may result from the stack interference

[1] For the discussion of the error analysis of the fitting results, please see Section 5.3.8.

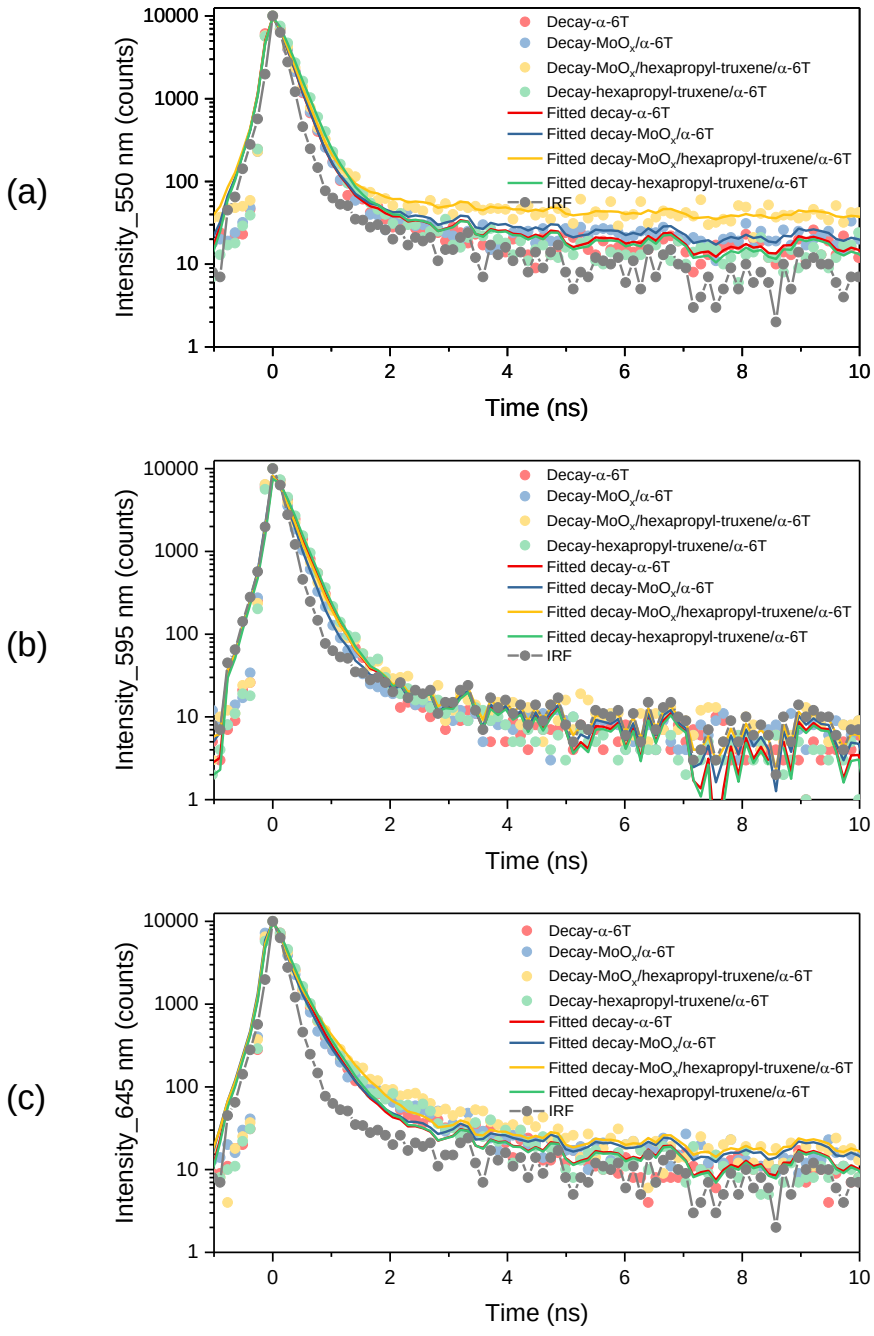


Figure 6.12: TRPL decay dynamics of the α-6T thin films on different substrates. (a). TRPL decay dynamics measured at 550 nm wavelength, (b). TRPL decay dynamics measured at 595 nm wavelength, (c). TRPL decay dynamics measured at 645 nm wavelength.

Table 6.5: Time-resolved photoluminescence lifetimes of α-6T thin films on glass with different interlayers. The emission component lifetime is measured at wavelength of 550 nm, 595 nm, and 645 nm, respectively. The data is fitted with the single-exponential model.

Film	wavelength (nm)	τ_1 (ns)	χ^2 (reduced)
glass/α-6T	550	0.193	38.8
glass/MoO_x/α-6T		0.185	34.8
glass/ MoO_x/hexapropyltruxene/α-6T		0.193	31.3
glass/hexapropyltruxene/α-6T		0.213	37.0
glass/α-6T	595	0.218	28.6
glass/MoO_x/α-6T		0.199	27.1
glass/ MoO_x/hexapropyltruxene/α-6T		0.230	29.8
glass/hexapropyltruxene/α-6T		0.224	31.8
glass/α-6T	645	0.296	46.6
glass/MoO_x/α-6T		0.313	40.2
glass/ MoO_x/hexapropyltruxene/α-6T		0.394	43.0
glass/hexapropyltruxene/α-6T		0.307	42.6

change caused by the stack thickness difference. However, the result of the stack absorption simulation excludes this assumption.

Absorption and structure analysis (UV-vis, XRD and AFM) of the thin films suggests that hexapropyltruxene interlayer has a template growth effect on the growth behaviour of α-6T. It induces the subsequently grown α-6T to grow more amorphously. The absorption of α-6T decreases after the insertion of hexapropyltruxene layer, which means that the induced structural change does not improve the light absorption of α-6T. Photoluminescence analysis reveals that similar to the role in SubPc/C60 stack, the hexapropyltruxene layer acts as a weak ExBL in IMEC stack. Thus, the small improvement of the PCE could be caused by the exciton blocking effect.

From this experiment, a phenomenon that the crystal structure of α-6T within the thin film can be easily induced via MoO_x and hexapropyltruxene layers is observed. The induced grown α-6T thin films present different light absorptions. Such properties in these substrate-induced phase (SIP) materials are useful in designing

high-performance solar cells and other organic thin-film devices like organic transistors. Further research about the SIP properties of α-6T and its application in solar cells needs to be investigated.

Chapter 7

Controlled Growth of α-sexithiophene Polymorphs via Substrate Treatment & Substrate Temperature Variation

This chapter is being prepared for publication to the Journal of ACS Applied Materials & Interfaces.

7.1 Introduction

As discussed in Section 4.1.3, α-6T can show polymorphism. Various polymorphs of α-6T have been discovered both in single crystals and thin films [120]. Previous researches report that the competing growth behaviour of polymorphs of α-6T in thin films can be controlled via substrate temperature [120, 122, 129, 141], light exposure in the process of thin-film growth [134], and post evaporation treatments [80, 209]. Because of the various polymorphs α-6T has, the performance of devices containing this molecule can be tuned by the proportions of different polymorphs in the devices. Servet *et al.* investigated the influence of deposition temperature on structure, orientation, and morphology of vacuum-evaporated α-6T thin films. Pithan *et al.* researched the influence of light on the thin film growth of α-6T. They demonstrated that the α-6T film grows on potassium chloride (KCl) under the illumination of 532 nm light at 1.5 W/cm^2 exhibits an increased purity of the LT-phase compared to

that grown in the dark [134]. Taima *et al.* reported a simple approach to control the crystalline polymorphs of evaporated α-6T by keeping the films in vacuum overnight. After this post evaporation treatment, (lying-down) HT-phase α-6T was partially transformed into (lying-down) LT-phase α-6T, leading to the PCE of solar cells being enhanced from 0.58% to 1.77% [80].

However, the SIP effect of different hole contact layers (HCLs) on the competing growth of α-6T polymorphs have not been studied and reported, yet. Because of the broad application of α-6T in multilayer thin-film devices, it is vital to understand the influence of HCLs on the α-6T polymorph growth. Controllable growth of α-6T SIPs is favourable for the benefit of device fabrication.

In this chapter, α-6T molecules on different substrates with HCLs (ITO glass, ITO/PEDOT:PSS (ca. 20 nm), ITO/MoO_x (5 nm, 0.1 Å/s), and ITO/MeO-TPD (5 nm, 0.1 Å/s)) were prepared to systematically investigate the SIP effect of different HCLs on α-6T. The substrate temperatures at the deposition of α-6T were fixed at 20 °C and 120 °C to study the influence of substrate temperature on α-6T polymorphism. The detailed thin film stack can be found in Figure 7.1 (a) and (b). UV-vis, XRD, AFM, and GIWAXS measurements were performed to characterize the α-6T thin film properties. Corresponding solar cells were fabricated and characterized by JV measurement, EQE, and IQE measurements to examine the influence of polymorphism.

7.2 Experimental Details

Thin film and device samples were fabricated following the procedure described in Chapter 4. The solar cell stack and thin film sample stack are shown in Figure 7.1(b) with energy levels of the materials in Figure 7.1(c). Table 7.1 contains the same information as Figure 7.1(b) but explains detailed evaporation parameters of the stacks. Two sets of thin-film samples and one set of solar cell device samples were

fabricated in the same vacuum chamber for characterisation measurements. The thin film for UV-vis, XRD, and AFM (Thin Film Set 1) were fabricated identically with the solar cells, yet the films in the Thin Film Set 1 excluded the SubPc, BPhen, and Al layers. The thin films for GIWAXS measurement (Thin Film Set 2) were as well identical to the solar cells, excluding BPhen and Al layers. The multilayer thin films fabricated were stored in the same glovebox for measurement.

The substrates (including the HCLs) were treated in different ways to examine the effect of substrate temperature change during evaporation on α-6T polymorphism. For the ease of description, abbreviations were applied to distinguish different samples. In details, "RT" means that the thin film was fabricated with the substrate held at room temperature (20 °C); "120 °C" stands for the treatment that substrate temperature was 120 °C when α-6T thin film was deposited; "ANL" indicates that the substrates of the "ANL"-labelled samples were annealed for the same duration as the "120 °C" samples and then were cooled down to room temperature before the deposition of α-6T. This is a control set of samples to compare the change caused by HCLs being annealed while α-6T was deposited.

Table 7.1: Thin film/device stacks in different experiments.

Experiment	Thin film/device stack
Solar cell	glass/ITO/HCL(MoO_x or MeO-TPD, 5 nm and 0.1 Å/s for each; or PEDOT:PSS ca. 20 nm)/α-6T (60 nm, 1 Å/s) /SubPc (15 nm, 1 Å/s) /BPhen (8 nm, 1 Å/s) /Al (100 nm, 1 Å/s)
UV-vis, XRD, AFM (Thin Film Set 1)	glass/ITO/HCL(MoO_x or MeO-TPD, 5 nm and 0.1 Å/s for each; or PEDOT:PSS, ca. 20 nm)/α-6T (60 nm, 1 Å/s)
GIWAXS (Thin Film Set 2)	glass/ITO/HCL(MoO_x or MeO-TPD, 5 nm and 0.1 Å/s for each; or PEDOT:PSS, ca. 20 nm)/α-6T (60 nm, 1 Å/s) /SubPc (15 nm, 1 Å/s)

GIWAXS was measured at beamline I07 of the Diamond Light Source (Beamtime SI20426-1). A Pilatus P2M detector was put at a sample-detector distance of 420

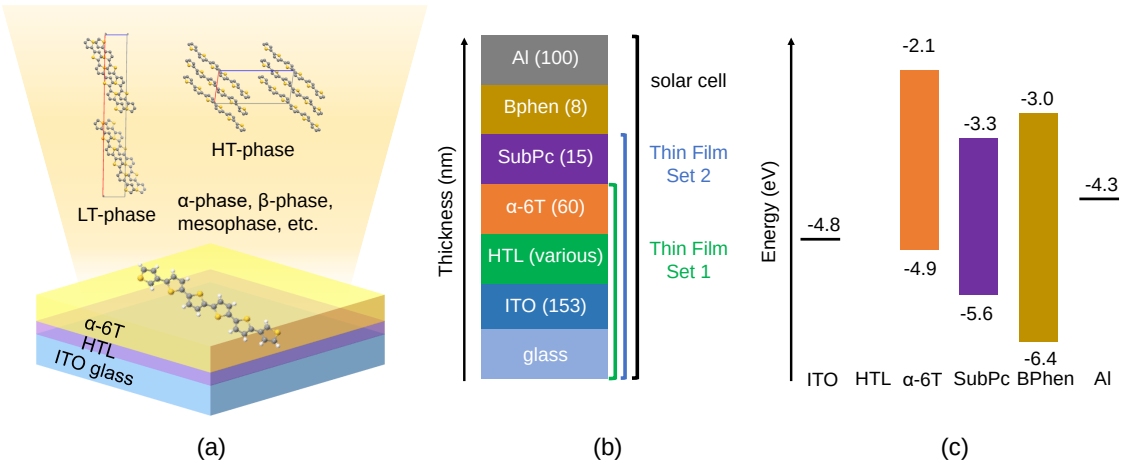


Figure 7.1: Thin film and solar cell stack schematics, with energy levels of the solar cell materials. (a) Schematics of the thin film structure and different α-6T polymorph structures. (b). Schematics of the thin film/solar cell devices with the thickness of each layer in nanometers. (c). Energy levels of the materials in the stacks. The energy levels are measured with UPS & IPES, which are taken from literature [69, 112, 158, 159, 201, 218]. The HCLs in the experiment include PEDOT:PSS (ca. 20 nm), MoO_x (5 nm), and MeO-TPD (5 nm).

mm to measure the data. The incident angle of the X-ray beam on the samples was fixed at ca. 0.15°. The beam energy was 20 keV (wavelength $\lambda = 0.620$ Å), and the exposure time of every image was 5 s. Beam damage was disregarded because the observed signal of the organic thin films does not decrease after several measurements, which is a sign of little beam damage according to Reference [173]. However, it is difficult to conclude whether there is beam damage at the first measurement. The image data was processed by DAWN software [174, 175]. MATLAB was used to re-plot and analyse (Gaussian fit) the image data. The Q-space values of GIWAXS peaks were calculated via DPC toolkit [181] using the single-crystal structure data of the corresponding molecules [155, 161, 162, 165].

7.3 Results and Discussion

7.3.1 Ultraviolet–visible (UV-vis) Spectroscopy Analysis

Since different α-6T polymorphs have their unique crystalline structures, e.g. tilt angle, they consequently have different absorption behaviours. Pithan *et al.* [134] reported different simulated absorption coefficients of HT- and LT-phases of α-6T. In the experiments, the UV-vis absorption measurement was carried out on the thin film samples of the Thin Film Set 1. The result is shown in Figure 7.2. where It can be seen that the absorption behaviour of α-6T depends on the substrate annealing and temperature. If we compare the sample subsets of "RT" and "ANL", we find that for all the substrates with HCLs (if any) (ITO glass, ITO/PEDOT:PSS, ITO/MoO_x, and ITO/MeO-TPD), the absorption of α-6T layers decreases after the annealing treatment of the substrates. It may indicate that the substrate annealing treatment will modify the properties of HCLs, which subsequently lead to the change of growth behaviour of the α-6T layer on top of them. When we compare the "ANL" and "120 °C" subsets, we find that with a substrate temperature increase from 20 °C to 120 °C during the deposition, the α-6T layer absorbs less light, regardless of HCLs. This reduction in the absorption behaviour of α-6T indicates that the substrate temperature increase during evaporation might change the polymorph composition of the α-6T thin film layer.

Additionally, if we look into every sub-figure ("RT", "ANL", and "120 °C" sample subsets) in Figure 7.2, we can observe that for each sample subset, there are differences of α-6T absorption on different HCLs. Take "RT" sample subset in Figure 7.2 as an example, the absorption spectra pattern of α-6T on MoO_x and MeO-TPD have very similar features, and they are both smaller than those on ITO glass and PEDOT:PSS layers. The α-6T absorption peak around 400 nm on different HCLs shows shift of position, e.g. the corresponding peak shifts from ca. 400 nm (glass/RT) to ca. 425 nm (PEDOT:PSS/RT). As discussed in Reference [212, 214], and [219], the peak

shift is attributed to the crystal structure change inside α-6T thin films, which is another sign that different HCLs have different template effect on the polymorph gowth of α-6T. In "ANL" and "120 °C" subsets, the similar absorption trend is again observed. However, the absorption of α-6T on the MoO_x layer is the lowest comparing with α-6T on other HCLs for all sample subsets.

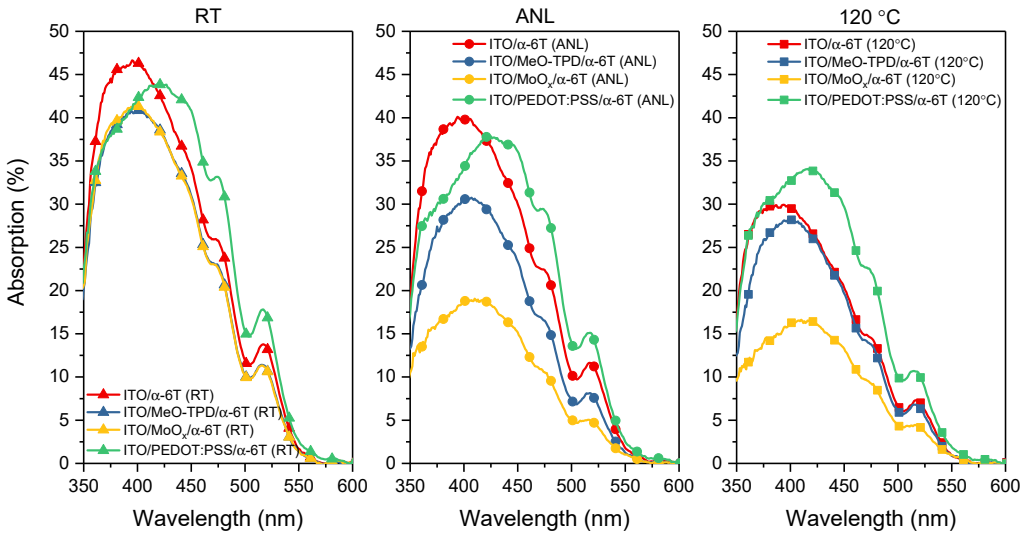


Figure 7.2: UV-vis absorption of α-6T layer in the films of the Thin Film Set 1. Substrates' absorption is subtracted. "RT" indicates that the film was fabricated with the substrate held at room temperature; "120 °C" means that the substrate temperature was 120 °C when α-6T was deposited; "ANL" stands for annealed substrate, which means that the substrates and HCLs (if any) of these samples were annealed for the same duration (13 minutes) of the "120 °C" samples and then were cooled down to room temperature before the α-6T layer was deposited.

7.3.2 X-ray Diffraction (XRD) Analysis

Changes in the absorption behaviour of α-6T suggest that there may be different compositions of α-6T polymorphs in these thin films. To confirm this assumption, XRD measurements of the UV-vis characterized thin film samples were performed. The XRD results are shown in Figure 7.3. With the diffraction pattern of ITO glass is already subtracted from the original data. In the XRD result we find there are diffraction peaks of α-6T LT-, HT- and β-phases. The most distinctive peaks are

LT-phase peaks (LT(200), LT(300), LT(400), LT(500), and LT(600)). The LT(300) and LT(500) peaks are systematically absent in simulated powder diffraction profile. However, they are observed in our case, showing that the crystal lattice of α-6T LT-phase is deformed in the thin films. Besides, the most distinctive ones of β- and HT-phases are β(008), and HT(012) peaks. The peak around 2θ=9.90° could be either LT(500) (2θ=9.90°) or HT(100) (2θ=9.86°). Both of these two peaks are systematically absent in powder diffraction profile. Considering the weak intensities of the other HT-phase peaks and the existence of LT(300) peak in our XRD profile, this peak at 9.90 ° is much more likely the LT(500) peak. All the diffraction peaks of α-6T polymorphs are taken from the literature [120, 161, 162, 165].

Comparing the XRD peak intensities in "RT" and "ANL" subsets, we can observe that after the substrate annealing treatment, generally there is less HT-phase. The LT(500) peak intensity weakens but the LT(600) peak intensity remains the same, indicating a less-deformed crystal lattice of LT-phase in "ANL" films. The β-phase remains similar between "RT" and "ANL" samples.

Similarly, by comparing the "ANL" and "120 °C" sample subsets, we observe that the intensity of LT(500) peak weakens after the increase of substrate temperature. The intensity of β(008) peak does not seem to drop. In samples with MoO_x HCL, the β(008) peak even gets higher intensity with higher substrate temperature. HT(012) peaks in both "ANL" and "120 °C" samples are too weak to be analysed properly. This intensity change indicates that after the increase of the substrate temperature, the crystal lattice of LT-phase is less-deformed, i.e. a more ideal packing of the α-6T LT-phase. This experiment result agrees with the previous research, which reported that α-6T LT-phase is thermally stable [164]. And the α-6T β-phase is reported to be more kinetically favoured [120], i.e. at high substrate temperature there tends to be more β-phase. Thus, it is understandable that there are more β-phase in the "120 °C" thin films than those in the "ANL" subset.

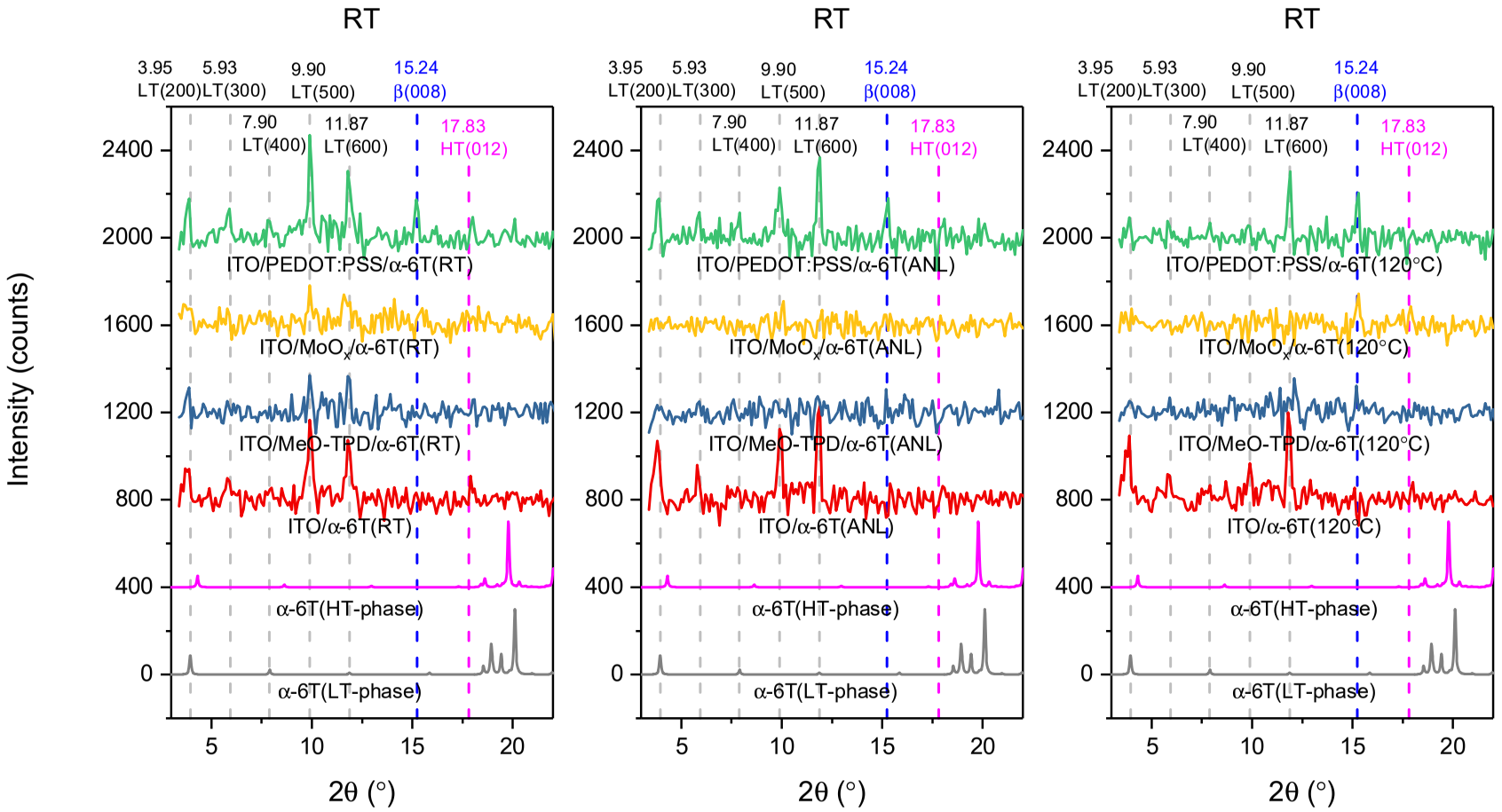


Figure 7.3: XRD measurement of the Thin Film Set 1. Diffraction pattern of ITO glass is subtracted. Powder diffraction pattern of α-6T LT and HT-phases calculated by Mercury software [210] is also plotted at the bottom of the graph. The peak locations of different polymorphs (LT-, HT-, and β-phases) are marked via dashed lines in the graph [120, 161, 162, 165]. (To the best of the author's knowledge, the crystallographic information of α-6T β-phase reported in the literature [120, 162] is not sufficient to simulate the powder diffraction profile. Thus, only the possible diffraction peak locations of the β-phase are marked in this figure.)

For individual subset analysis, in "RT" subset, the XRD result shows that α-6Ts grown on bare ITO substrate and ITO/PEDOT:PSS substrate tend to have diffraction peaks with higher intensity and narrower full width at half maximum (FWHM) ("sharper"), meaning the corresponding thin films have a higher degree of crystallinity and crystallites in these samples have larger domains. In particular, there is a sharp β(008) peak in the ITO/PEDOT:PSS/α-6T(RT) sample, which does not exist in other samples in the same subset. It indicates that the surface condition of PEDOT:PSS is beneficial to the growth of α-6T β-phase. MoO_x and MeO-TPD show similar modification effect on α-6T. The α-6T peaks are weaker, which means the layers grown on top of them are more amorphous. Similar growth behaviours are observed in the "ANL" and "120 °C" sample subsets.

7.3.3 Grazing-incidence Wide-angle X-ray Scattering (GIWAXS) Analysis

Due to the weak signal of XRD measurements, we can only do a qualitative analysis of the XRD results. Further quantitative analysis such as Gaussian fit and Scherrer coherence length analysis was difficult to undertake. Thus, grazing-incidence wide-angle X-ray scattering (GIWAXS) measurement of the thin film stack identical to the solar cell devices (glass/ITO/HCL/α-6T/SubPc, Thin Film Set 2, shown in Figure 7.1 (b)) were carried out in synchrotron light source (Diamond Light Source, UK). The results are shown in Figure 7.4. The diffraction peaks of ITO glass have been subtracted. 2D reciprocal maps with wider Q-space value range are included in Figure A.2 in the Appendix. A list of Q-space values of representative diffraction peaks and their indications of the molecular orientation with respect to the substrate is shown as Table A.1 in the Appendix. For the convenience of analysis, Gaussian fits of the line cut of representative peaks (LT(4-1-1), LT(020), HT(100), β(1-11), and SubPc(-201)) were performed in MATLAB and the results are included in Table 7.2 and Table 7.3. The addition of a SubPc layer in the Thin Film Set 2 comparing with the Thin Film

Set 1 has two purposes: One is to check whether this subsequent layer would modify α-6T layer inside solar cells. The other is to examine if the different α-6T polymorphs influence the growth of SubPc layer.

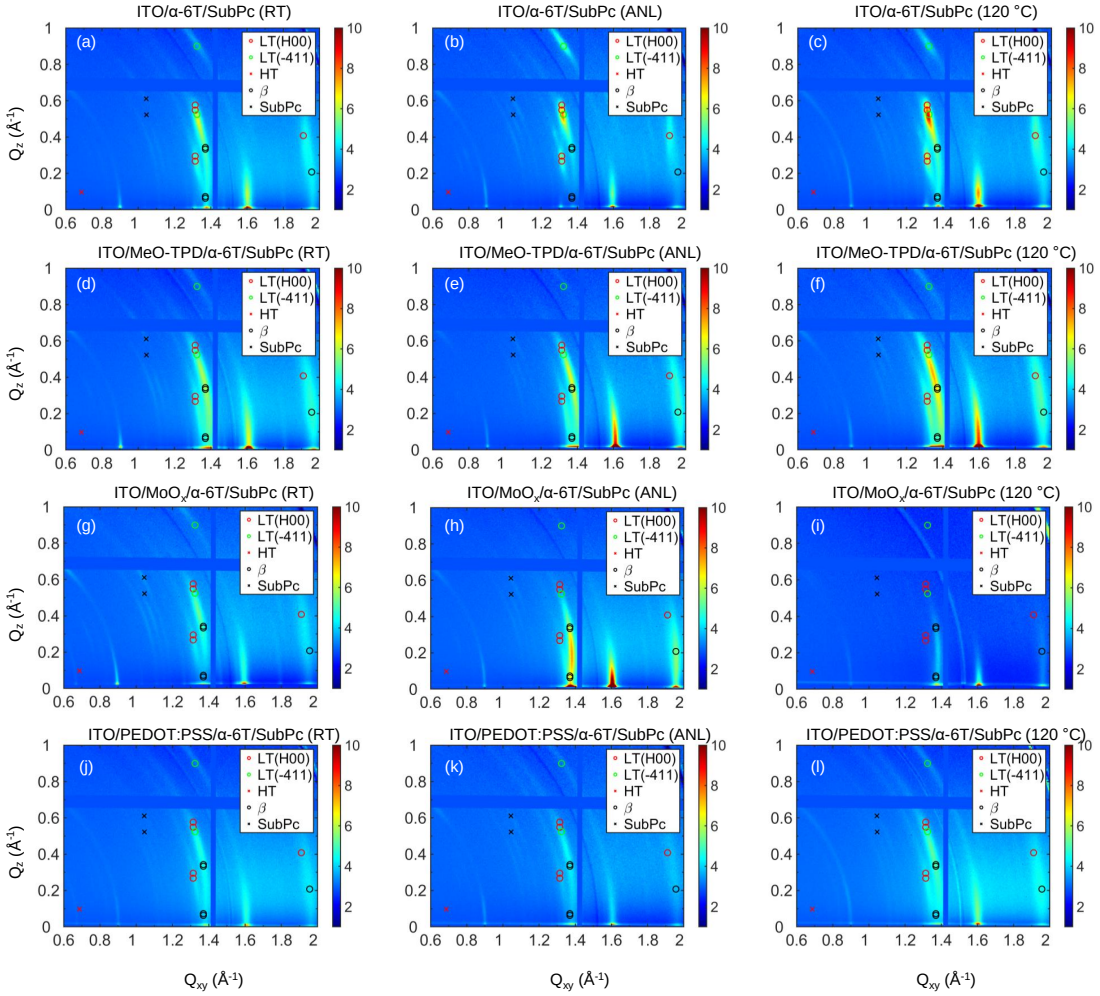


Figure 7.4: Summary of GIWAXS results of the Thin Film Set 2. (a)(b)(c). ITO/α-6T/SubPc thin films at RT, ANL and 120 °C conditions, (d)(e)(f). ITO/MeO-TPD/α-6T/SubPc thin films at RT, ANL and 120 °C conditions, (g)(h)(i). ITO/MoO_x/α-6T/SubPc thin films at RT, ANL and 120 °C conditions, (j)(k)(l). ITO/PEDOT:PSS/α-6T/SubPc thin films at RT, ANL and 120 °C conditions. The diffraction peaks of ITO glass has been already subtracted. LT(H00) (red circle), LT(-411) (green circle), HT (red cross), β (black circle), and SubPc (black cross) stand for (H00) oriented LT-, (-411) oriented LT-, (00L) oriented HT-, (00L) oriented β-phases of α-6T, and SubPc, respectively. Peak locations are calculated via DPCToolkit software from the crystal structures reported by literature [120, 155, 161, 162, 165, 181].

Table 7.2: GIWAXS peak intensity analysis of Figure 7.4. The values shown in this table is fitted peak intensities of the corresponding peaks via Gaussian fitting. For comparison, the background intensity is about 2.8 units. Detailed fitting results including the R-square data (good-of-fit) is available in Table A.2 in the Appendix.

Thin film	Treatment	LT(4-1-1) (standing-up)	LT(020) (lying-down)	HT(100) (lying-down)	β(1-11) (standing-up)	SubPc (-201)	Sub figure in Figure 7.4
ITO/α-6T/SubPc	RT	5.1	3.5	2.9*	5.2	3.1*	(a)
ITO/α-6T/SubPc	ANL	6.7	4.9	2.8*	4.3	3.2*	(e)
ITO/α-6T/SubPc	120 °C	8.0	4.0	2.8*	5.3	3.1*	(i)
ITO/MeO-TPD/α-6T/SubPc	RT	4.7	3.1	2.9*	5.8	3.0*	(b)
ITO/MeO-TPD/α-6T/SubPc	ANL	4.7	2.9*	2.9	6.3	3.1*	(f)
ITO/MeO-TPD/α-6T/SubPc	120 °C	5.9	3.3	2.8*	6.8	3.2*	(j)
ITO/MoO_x/α-6T/SubPc	RT	4.4	3.3	2.9*	4.9*	3.3	(c)
ITO/MoO_x/α-6T/SubPc	ANL	3.6*	3.1*	3.0	6.1	3.2*	(g)
ITO/MoO_x/α-6T/SubPc	120 °C	2.8*	2.9	2.8*	3.5	2.8*	(k)
ITO/PEDOT:PSS/α-6T/SubPc	RT	4.0	3.2	3.0*	4.6	3.1*	(d)
ITO/PEDOT:PSS/α-6T/SubPc	ANL	3.8*	3.1	2.9*	4.3*	3.2*	(h)
ITO/PEDOT:PSS/α-6T/SubPc	120 °C	4.4	3.2	3.0*	5.1	3.2*	(l)

Note: The * mark means the corresponding value is the intensity value of the centre pixel of peak collected manually, because either the peak intensity is too weak for the fitting program to find a proper Gaussian curve or the good-of-fit is poor (R-square < 0.7).

Table 7.3: Scherrer coherence length analysis of Figure 7.4. The values shown in this table are the calculated Scherrer coherence length (in Å) from the Gaussian function fitting of the peaks. Detailed fitting results including the R-square data is available in Table A.2 in the Appendix.

Thin film	Treatment	LT(4-1-1) (standing-up)	LT(020) (lying-down)	β(1-11) (standing-up)	Sub figure in Figure 7.4
ITO/α-6T/SubPc	RT	56.8	52.6	37.7	(a)
ITO/α-6T/SubPc	ANL	64.1	87.2	31.9	(e)
ITO/α-6T/SubPc	120 °C	67.4	64.4	34.8	(i)
ITO/MeO-TPD/α-6T/SubPc	RT	44.2	44.1	36.8	(b)
ITO/MeO-TPD/α-6T/SubPc	ANL	53.1	N/A	48.9	(f)
ITO/MeO-TPD/α-6T/SubPc	120 °C	59.2	38.2	42.8	(j)
ITO/MoO_x/α-6T/SubPc	RT	39.9	29.9	25.5	(c)
ITO/MoO_x/α-6T/SubPc	ANL	N/A	N/A	51.3	(g)
ITO/MoO_x/α-6T/SubPc	120 °C	N/A	60.2	28.3	(k)
ITO/PEDOT:PSS/α-6T/SubPc	RT	37.4	52.2	31.0	(d)
ITO/PEDOT:PSS/α-6T/SubPc	ANL	28.4	N/A	30.1	(h)
ITO/PEDOT:PSS/α-6T/SubPc	120 °C	38.2	42.2	34.0	(l)

From the GIWAXS result, we can see the coexistence of LT-, HT-, and β-phases of α-6T. Similar with the XRD result, among the three polymorphs, LT- and β-phases have distinctive diffraction peaks. The diffraction peaks of HT-phase have much lower intensities, which makes it challenging to distinguish them from the background. The diffraction patterns in this research agree with previous reports of α-6T thin films [129, 209], which did not mention the existence of the HT-phase. Comparing with the XRD results, GIWAXS measurement results reveal more details about the polymorph composition within the films. A combination of (H00) and (-411) oriented LT-phase α-6T is discovered. A schematic presentation of the molecular orientation of α-6T polymorphs with different parallel planes is shown in Figure A.3. It suggests that the α-6T molecules in (H00) oriented LT-phase and (00L) oriented β-phase are "standing-up", while those in (-411) oriented LT-phase and (00L) oriented HT-phase are "lying-down". Thus, we can predict that with less "standing-up" ((H00) oriented LT-phase and (00L) oriented β-phase) but more "lying-down" ((-411) oriented LT-phase and (00L) oriented HT-phase) molecules, the corresponding α-6T thin film absorbs more light.

From Table 7.2, we can see the LT(020) peak is weak in ITO/MeO-TPD, ITO/MoO_x, and ITO/PEDOT:PSS samples, but distinctive in bare ITO samples. This result shows (-411) oriented ("lying-down") α-6T LT-phase has a preference of the underlying HCLs. LT(4-1-1) and β(1-11) peaks of α-6T samples on ITO, ITO/MeO-TPD, and ITO/PEDOT:PSS are stronger in "120 °C" samples rather than the "ANL" ones, except that the sample on ITO/MoO_x have low intensity of LT peaks. Sherrer coherence length analysis in Table 7.3 shows the same trend of the crystalinity of the (H00) oriented LT- and (00L) oriented β-phases (both "standing-up"). This finding agrees with our XRD analysis. The higher substrate temperature in evaporation, the more "standing-up" LT- and β-phases will exist within the α-6T thin films. HT (100) peak intensity values are small, which is almost as the same as the background. It is

difficult to make any meaningful conclusions from HT (100) peak intensities.

Individual analysis of each substrate treatment subset reveals some interesting findings: The LT(4-1-1) and LT(020) peak intensities are strong in the ITO samples and they have high values of the calculated Scherrer coherence lengths, meaning bare ITO substrates seem to provide a good surface environment for both "standing-up" and "lying-down" oriented LT-phase to grow large domains. There are more β-phase and less LT-, HT-phases in MeO-TPD and MoO_x samples. For MoO_x samples, the diffraction peaks are broadened, and only a few peaks can be identified, which means the α-6T molecules are much more disordered in these samples. The peak intensities of all three α-6T polymorphs on PEDOT:PSS samples are a bit weaker than those on bare ITO substrates, and the Scherrer coherence lengths of the LT- and β-phases in PEDOT:PSS samples are smaller, which suggests these samples have a smaller degree of crystallinity and smaller crystallite domains.

To systematically investigate the relationship between the microstructure of α-6T thin films and their optical properties, diagrams based on Table 7.2, Table 7.3, and Figure 7.2 are shown in Figure 7.5. In these diagrams, GIWAXS peak intensities/Scherrer coherence length are the X-axis and the coverage areas of corresponding UV-vis curves in Figure 7.2 are integrated and normalized as the Y-axis. Linear fits of the data points except ITO/MoO_x/α-6T (120 °C) and ITO/MoO_x/α-6T (ANL) are plotted as dashed lines in sub-figures. Pearson's r (indication of the correlation) and R^2 of each fit are included in each sub-figure. From Figure 7.5 (a), we can see a negative correlation between the LT(4-1-1) ("standing-up") peak intensity and the UV-vis absorption of α-6T thin films. The same trend also can be observed in Figure 7.5 (c) for the relation between the β(1-11) ("sanding-up") peak intensity and the UV-vis absorption of α-6T thin films. The linear fitting of the correlation between the LT(020) ("lying-down") peak intensity and the UV-vis absorption of α-6T thin films in Figure 7.5 (b) fails. It might be due to the fact that the fraction of the

"lying-down" oriented LT-phase within the films is small and it's strongly affected by the presence of the "standing-up" oriented LT-phase majority. The peak intensities of the HT-phase are too low to be analysed closely, but Figure 7.5 (d) might indicate a rough positive correlation between the HT(100) peak intensity and absorption of α-6T thin film. Similar correlations are also found between the Scherrer coherence length of α-6T polymorphs and the UV-vis absorption of α-6T thin film. These findings suggest that apart from the α-6T films on ITO/MoO_x, the α-6T films on other HCLs have less absorption of light if there are more "standing-up" oriented LT- and β-phases within the films. The different trend observed from the α-6T film on ITO/MoO_x might be due to a disordered crystallite structure within α-6T thin films.

Combining the UV-vis absorption result together with the XRD and GIWAXS measurement results, we can find that the absorption of the light is associated with the composition α-6T polymorphs in the thin films. With less "standing-up" ((H00) oriented LT-phase and (00L) oriented β-phase) but more "lying-down" ((-411) oriented LT-phase and (00L) oriented HT-phase) molecules, the α-6T thin film has better absorption. This result is in agreement with the previous research about the different absorption behaviour of α-6T polymorphs [164].

In the GIWAXS measurement results, SubPc peaks can hardly be identified because of their low intensities, which agrees with our previous in-situ GIWAXS observation of SubPc in Figure 5.9. In addition, many SubPc peaks overlap with the diffraction peaks of α-6T polymorphs. The weak SubPc peaks may indicate that SubPc layers in these solar cell stacks are not well crystallised. However, we can identify some weak peaks of SubPc, e.g. SubPc (-200), SubPc (1-2-1), and SubPc (-201) peaks in every sub-graph in Figure A.2 in the Appendix. Their locations and intensities do not change dramatically among the sub-graphs. The peak intensity of SubPc (-201) is recorded in Table 7.2. It shows its intensity is weak and does not change between different HCLs and substrate treatments. Particularly, only in

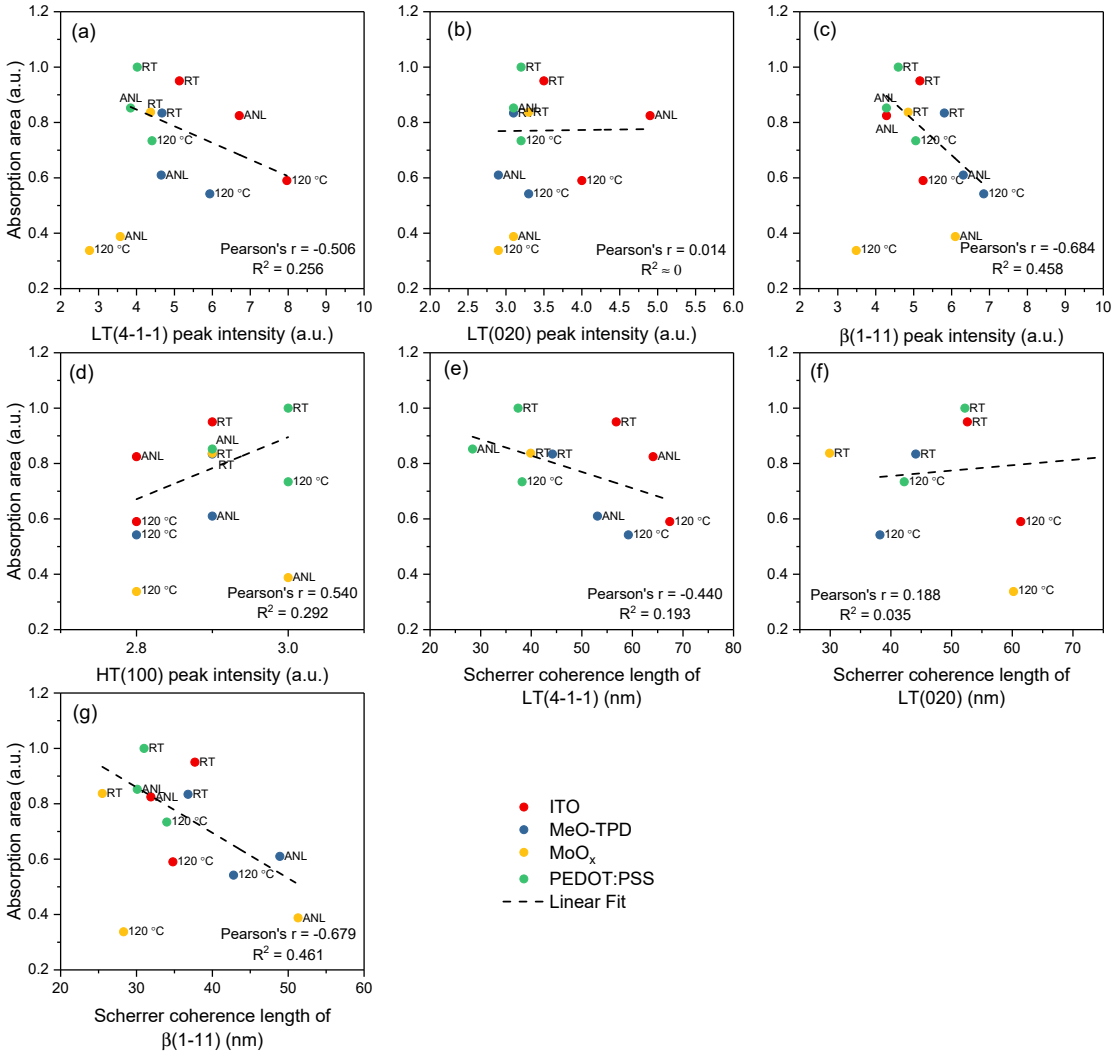


Figure 7.5: Comparison of GIWAXS peak intensity, Scherrer coherence length, and UV-vis absorption. GIWAXS peak intensities/Scherrer coherence length are the X-axis and the areas of UV-vis curves in Figure 7.2 are integrated and normalized as the Y-axis in this diagram. Linear fits of the data points except ITO/MoO_x/α-6T (120 °C) and ITO/MoO_x/α-6T (ANL) are plotted as dashed lines in sub-figures. Pearson's r (indication of the correlation) and R^2 of each fit are included in each sub-figure.

ITO/MoO_x/α-6T/SubPc (120 °C) thin-film sample the diffraction peaks of SubPc cannot be identified by eye. This result suggests that SubPc layers on top of different α-6T layers tend to remain the same semi-amorphous crystal structure.

7.3.4 Atomic Force Microscopy (AFM) Analysis

To further analyse the reason why modification of the substrate surface can induce the competing growth of diverse polymorphs of α-6T, we undertook AFM measurements of the different substrates as well as the subsequent α-6T layers. The root mean square roughness (RMS) of the images are included in Table 7.4 for comparison. The AFM images of the substrates are shown in Figure 7.6. From the AFM images, we confirm that the annealing treatment of the substrates (ANL) modifies the substrate surface. Without treatment, the surface morphology of MeO-TPD (RT) is worm-like, with domains connecting each other. After the annealing treatment, the MeO-TPD thin-film seems to dewet, and the domains separate from each other. This is due to the low glass transition temperature of MeO-TPD (67 °C) [220]. The RMS rises from 1.5 nm to 3.5 nm. For MoO_x thin film, even though the roughness changes minimal (from 0.6 nm to 0.5 nm), we can still find the annealing process reduces the domains of MoO_x. For PEDOT:PSS layer, annealing treatment introduces some node-like features. Thus, the roughness of the film grows from 0.7 nm to 0.9 nm. The surface morphology of the bare ITO does not seem to have noticeable change after the annealing treatment.

Table 7.4: Summary of root mean square roughness (RMS) of the AFM heigh images in Figure 7.6 and 7.7.

Thin film	RMS (nm)		
Treatment	RT	ANL	120 °C
ITO	0.5	0.5	-
ITO/MeO-TPD	1.5	3.5	-
ITO/MoO_x	0.6	0.5	-
ITO/PEDOT:PSS	0.7	0.9	-
ITO/α-6T	8.8	11.2	9.7
ITO/MeO-TPD/α-6T	7.1	10.2	4.6
ITO/MoO_x/α-6T	7.0	6.1	6.0
ITO/PEDOT:PSS/α-6T	8.9	8.8	6.7

Shown in Figure 7.7, subsequently deposited α-6T layer on "RT", "ANL", and

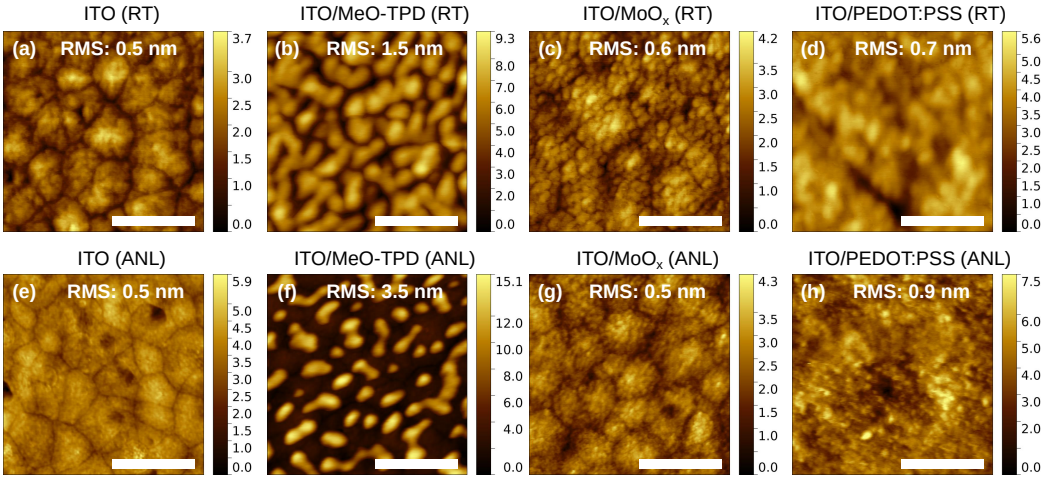


Figure 7.6: AFM height images of different HCLs. (a). ITO substrate without thermal treatment; (b). ITO/MeO-TPD sample without thermal treatment; (c). ITO/MoO_x sample without thermal treatment; (d). ITO/PEDOT:PSS sample without thermal treatment; (e). ITO substrate with annealing treatment (120 °C for 13 minutes, the same for (f), (g), and (h)); (f). ITO/MeO-TPD sample with annealing treatment; (g). ITO/MoO_x sample with annealing treatment; (h). ITO/PEDOT:PSS sample with annealing treatment. RMS stands for root mean squared roughness. The scale bar in each image is 400 nm. The unit in height image is nm.

"120 °C" substrates form similar node-like features. It agrees with the previous research [160]. However, the size of domains and roughness of the surface vary depending on the HCL substrate and temperature. We can find that the surface roughness of α-6T on annealed ITO glass and annealed MeO-TPD layer becomes larger than the other ones in the same "ANL" categories. Except of the α-6T on the bare ITO glass, the domain size and roughness of α-6T on other substrates at 120 °C become smaller comparing with the "RT" and "ANL" subsets. However, we cannot directly distinguish the polymorph type of α-6T via AFM morphology images. Details about the fundamental kinetics of template growth effect need to be conducted in future researches.

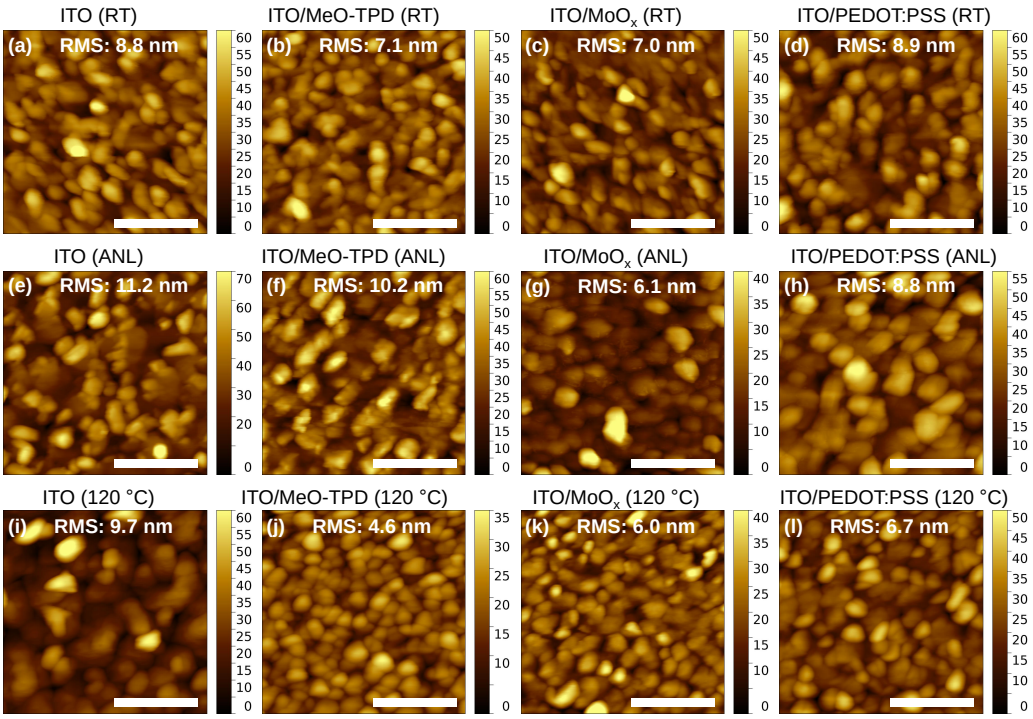


Figure 7.7: AFM height images of α-6T on different HCLs. (a). ITO/α-6T(RT) sample; (b). ITO/MeO-TPD/α-6T(RT) sample; (c). ITO/MoO$_x$/α-6T(RT) sample; (d). ITO/PEDOT:PSS/α-6T(RT) sample; (e). ITO/α-6T(ANL) sample; (f). ITO/MeO-TPD/α-6T(ANL) sample; (g). ITO/MoO$_x$/α-6T(ANL) sample; (h). ITO/PEDOT:PSS/α-6T(ANL) sample; (i). ITO/α-6T(120 °C) sample; (j). ITO/MeO-TPD/α-6T(120 °C) sample; (k). ITO/MoO$_x$/α-6T(120 °C) sample; (l). ITO/PEDOT:PSS/α-6T(120 °C) sample. RMS stands for root mean squared roughness. The scale bar in each image is 400 nm. The unit in height image is nm.

7.3.5 Current-Voltage (JV) Characterization of Solar Cells

Finally, the corresponding solar cells (solar cell stack structure shown in Figure 7.1 (b)) were fabricated to investigate the influence on device performance caused by the fractional change in α-6T polymorphs. The solar cell performance result is summarized in Table 7.5. The JV curve of the representative solar cells (whose performance is closest to the average performance) are included in Figure 7.8. JV curves of solar cells with MeO-TPD show S-kinks. It is caused by the energy level misalignment of these two layers (IP$_{MeO-TPD}$=5.07 eV, whose value is larger than IP$_{\alpha-6T}$=4.9

eV) [69, 204, 221]. For solar cells with bare ITO glass or MoO_x, we find that PCE of "RT" and "ANL" subsets are similar to each other while solar cells in the "120 °C" subset have lower PCE comparing to "RT" and "ANL" sublets. For solar cells with PEDOT:PSS, both "ANL" and "120 °C" solar cells have lower PCE than the "RT" subsets, however the PCE of the "120 °C" subset is marginally higher than "ANL" subset. From Table 7.5 we can find that the change of solar cell PCE is mainly caused by the alteration of J_{sc}.

Table 7.5: Device performance summary of solar cells with different HCLs and substrate treatments.

HCL	Subset	J_{sc}(mA·cm^{-2})	V_{oc} (V)	FF	PCE (%)
ITO	RT	5.8 ± 0.1	1.07 ± 0.01	0.52 ± 0.02	3.1 ± 0.1
MeO-TPD	RT	5.1 ± 0.1	1.00 ± 0.02	0.48 ± 0.01	2.4 ± 0.1
MoO_x	RT	5.5 ± 0.1	1.07 ± 0.01	0.58 ± 0.01	3.4 ± 0.1
PEDOT:PSS	RT	6.4 ± 0.1	1.07 ± 0.01	0.57 ± 0.01	3.9 ± 0.1
ITO	ANL	5.7 ± 0.1	1.07 ± 0.01	0.56 ± 0.01	3.4 ± 0.2
MeO-TPD	ANL	5.4 ± 0.1	1.07 ± 0.01	0.54 ± 0.01	3.1 ± 0.1
MoO_x	ANL	3.8 ± 0.1	1.04 ± 0.01	0.60 ± 0.01	2.3 ± 0.2
PEDOT:PSS	ANL	4.6 ± 0.3	1.06 ± 0.01	0.57 ± 0.01	2.8 ± 0.2
ITO	120 °C	4.2 ± 0.4	1.08 ± 0.01	0.57 ± 0.01	2.6 ± 0.1
MeO-TPD	120 °C	3.8 ± 0.1	1.07 ± 0.01	0.52 ± 0.01	2.1 ± 0.1
MoO_x	120 °C	2.4 ± 0.1	1.07 ± 0.01	0.61 ± 0.01	1.6 ± 0.1
PEDOT:PSS	120 °C	5.7 ± 0.1	1.09 ± 0.01	0.55 ± 0.01	3.3 ± 0.1

A diagram of correlation between the UV-vis absorption of α-6T and J_{sc} is shown in Figure 7.9. From this figure we can see a positive corelation between these two parameters. J_{sc} mainly depends on the UV-vis absorption of α-6T. Together with the previous microstructural analysis, we bridge the relationship between microstructure (polymorphs) within α-6T thin films and the corresponding solar cell performance: less "standing-up" ((H00) oriented LT-phase and (00L) oriented β-phase) but more "lying-down" ((-411) oriented LT-phase and (00L) oriented HT-phase) molecules leads to better UV-vis absorption, which results in better solar cell performance.

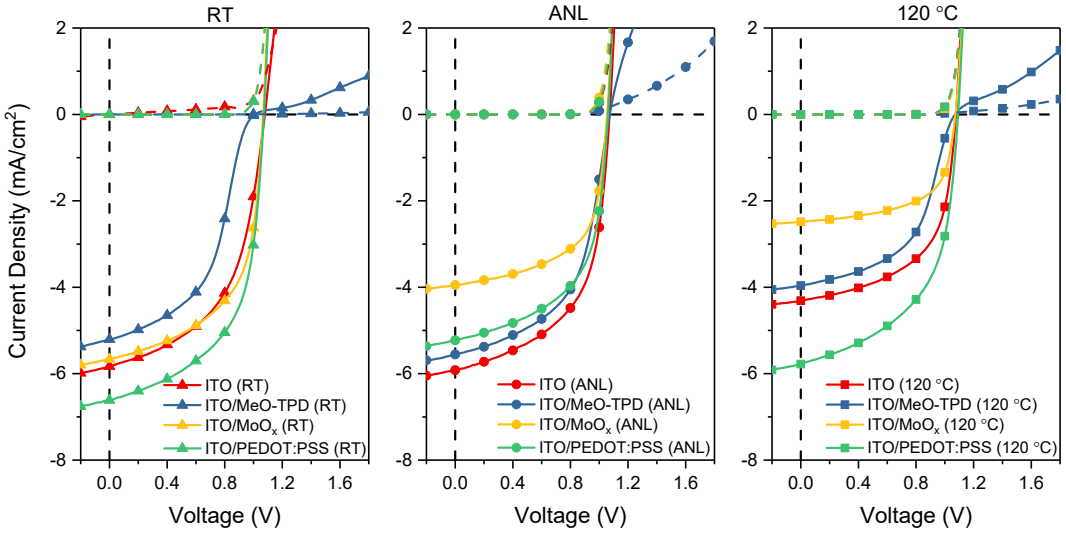


Figure 7.8: JV curve summary of solar cells with different HCLs and substrate treatments. The straight lines are illuminated JV curves and the dashed lines are dark JV curves. The full solar cell stack is glass/ITO/HCL(MoO_x or MeO-TPD, 5 nm; or PEDOT:PSS ca. 20 nm)/α-6T (60 nm) /SubPc (15 nm) /BPhen (8 nm) /Al (100 nm).

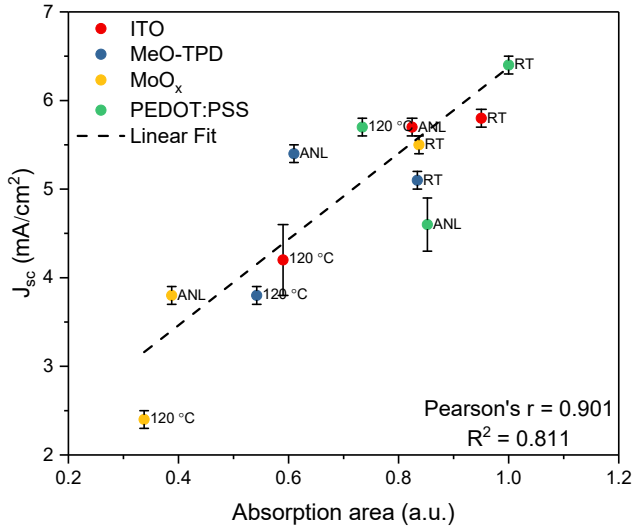


Figure 7.9: Comparison of UV-vis absorption and J_{sc}. The areas of UV-vis curves in Figure 7.2 are integrated and normalized as the X-axis, and the J_{sc} values of the OSCs are the Y-axis in this diagram. The linear fit of the data points is plotted as a dashed line in the figure. Pearson's r (indication of the correlation) and R^2 of each fit are included in the figure.

7.3.6 External Quantum Efficiency (EQE) and Internal Quantum Efficiency (IQE) Analysis

In order to confirm this assumption, external quantum efficiency (EQE) measurements of the corresponding solar cells were performed. The results are shown in Figure 7.10. Comparing the EQE results with UV-vis absorption analysis, we observe they show the same trend in the absorption range of α-6T (350 nm - 550 nm). As for devices with the same HCL, devices in the "RT" subset have better EQE performance than those in "ANL" subset. The ones in the "120 °C" subset have the lowest EQE. In each subset, devices with PEDOT:PSS show the best EQE, devices without HCL come second, the ones with MoO_x rank the last. However, in the absorption range of SubPc (500 nm - 650 nm), we also find similar decrease trend of EQE performance, but the peak shift of EQE is much smaller than that in the α-6T absorption range. The IQE result is shown in Figure 7.11. From the IQE plot, we can see the same trend of IQE decrease with the change of the substrate and deposition temperature as in EQE result.

The change of EQE/IQE in α-6T absorption range is mainly due to the different light absorption properties of the α-6T layer within the stack, which is caused by the polymorph composition differences as discussed before.

The minor change of EQE/IQE in SubPc absorption range seems to be caused by the change of microstructure within the α-6T layer. One possible explanation could be as followed. The π-π stacking orientation in the "lying-down" oriented molecules is closer to the perpendicular direction of the solar cell stack. This structure potentially helps increase the mobility of charge carriers in the perpendicular direction. Thus, it reduces the recombination of the charge carriers transferred from SubPc layer, leading to better EQE/IQE results. However, it might be just an add-on effect apart from the absorption change we discussed before.

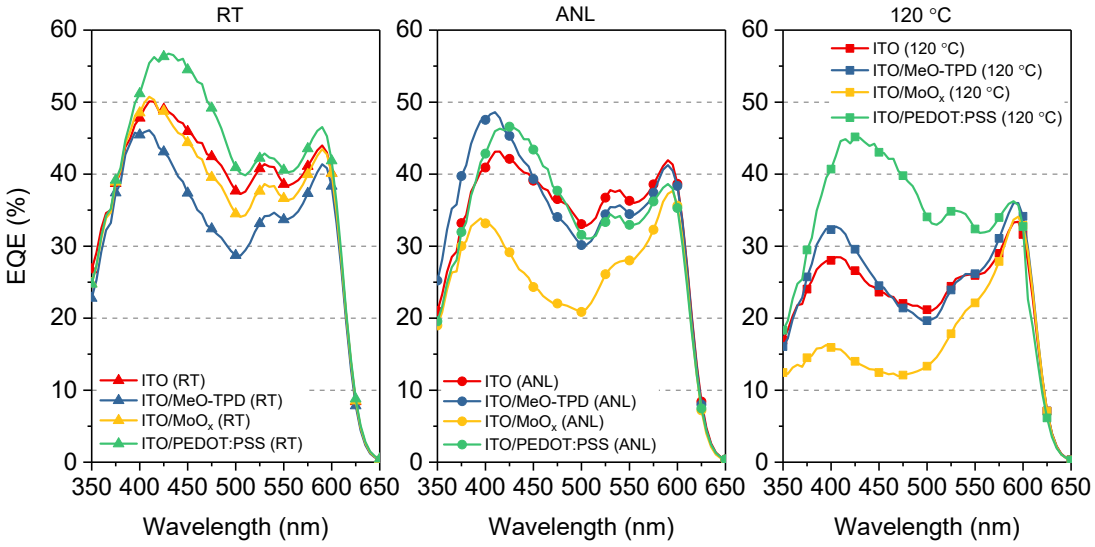


Figure 7.10: EQE summary of solar cells with different HCLs and substrate treatments. The full solar cell stack is glass/ITO/HCL(MoO_x or MeO-TPD, 5 nm; or PEDOT:PSS ca. 20 nm)/α-6T (60 nm) /SubPc (15 nm) /BPhen (8 nm) /Al (100 nm). α-6T absorbs light with a wavelength range from 350 to 550 nm.SubPc absorbs light with a wavelength range from 500 to 650 nm.

Combing IQE and EQE results and considering the polymorph composition analysis, we can conclude that there is a clear relationship between the α-6T polymorph composition and the device performance. The devices with less "standing-up" ((H00) oriented LT-phase and (00L) oriented β-phase) but more "lying-down" ((-411) oriented LT-phase and (00L) oriented HT-phase) molecules will have higher light absorption. Thus, it helps increase the performance of the solar cell.

7.4 Conclusions

By investigating into the growth of α-6T polymorphs in thin films, it is found that widely-used HCLs (MoO_x, PEDOT:PSS, and MeO-TPD) have substrate-induced phase (SIP) effect on the growth of α-6T. Thin film characterization meaurements such as UV-vis, XRD, and GIWAXS show competing growth model of LT-, HT-, and β-phases of α-6T on different HCLs. Mainly because of the different tilt angles of crystallites within these polymorphs, they show different light absorption proper-

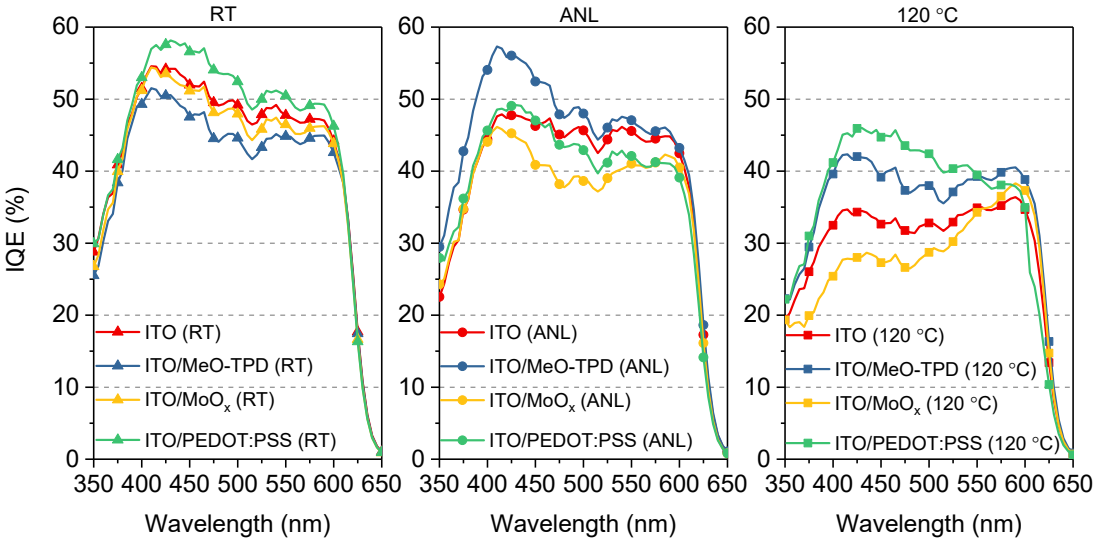


Figure 7.11: IQE summary of solar cells with different HCL and substrate treatment. The full solar cell stack is glass/ITO/HCL(MoO_x or MeO-TPD, 5 nm; or PEDOT:PSS ca. 20 nm)/α-6T (60 nm) /SubPc (15 nm) /BPhen (8 nm) /Al (100 nm). α-6T absorbs light with a wavelength range from 350 to 550 nm.SubPc absorbs light with a wavelength range from 500 to 650 nm.

ties. Together with studying the corresponding OSC devices, it is found that with less "standing-up" ((H00) oriented LT-phase and (00L) oriented β-phase) but more "lying-down" ((-411) oriented LT-phase and (00L) oriented HT-phase) molecules in the film, the thin film tends to absorb more light in α-6T absorption range. These improvements help increase the performance of the corresponding OSCs. Regarding to specific HCL, PEDOT:PSS is found to be the most suitable HCL to achieve the best device performance. In addition, the results about substrate temperature control illustrate the importance of the substrate temperature in thin film and device fabrication. With higher substrate temperature (120 °C), there forms more "standing-up" oriented α-6T molecules ((H00) oriented LT-phase and (00L) oriented β-phase) than "lying-down" oriented α-6T molecules ((-411) oriented LT-phase and (00L) oriented HT-phase) in the thin film, which leads to lower light absorption and poorer OSC device performance. Last but not least, the coexistence of different α-6T polymorphs in the device does not necessarily affect the growth of subsequently deposited SubPc

layer significantly.

This finding helps us understand the polymorphism of α-6T better. It shows the device application of SIPs in growing thin films via vacuum deposition. And it helps guide further investigation into the controlled growth of small molecules which have multiple polymorphs, e.g. pentacene. And it will potentially help us efficiently control the polymorph fraction in thin-film devices, leading to desirable OSC and organic transistor device performances.

Chapter 8

Conclusions and Outlook

8.1 Conclusions

This thesis investigates the effect of a new molecule, hexapropyltruxene as an interlayer in vacuum-deposited small molecule organic solar cells (SMOSCs). Besides, it studies the substrate-induced phase (SIP) effect of different HCLs on the growth of α-6T polymorphs and its applications in SMOSCs.

The effect of hexapropyltruxene interlayer in vacuum-deposited SMOSC architecture: glass/ITO/MoO_x/hexapropyltruxene/SubPc/C60/BPhen/Al was investigated first. It is found that a 3.8 nm hexapropyltruxene interlayer between the MoO_x hole contact and SubPc is sufficient to improve the PCE in SubPc/C60 fullerene solar cells from 2.6% to 3.0%, achieving a ca. 15 % performance improvement. While the absorption stays roughly the same, the comparison of external and internal quantum efficiencies reveals a significant increase in SubPc's contribution to the current for light with wavelengths between 520 and 600 nm. The microstructural investigations demonstrate changes to the surface and bulk of SubPc grown atop a hexapropyltruxene interlayer indicating that the latter acts as a templating layer in a similar way as MoO_x. However, the improvement in PCE is found to be mainly via reduced exciton quenching at the MoO_x contact with the insertion of the hexapropyltruxene layer.

To apply the hexapropyltruxene as an interlayer in other solar cell stacks, the interlayer function of hexapropyltruxene is examined again in the IMEC solar cell

stack. The results of device performance show that the insertion of a thin layer (0.8 nm) of hexapropyltruxene between MoO_x and α-6T layers will slightly increase the PCE of solar cells. The main reason for the PCE enhancement is the increase of the J_{sc}, though the enhancement is small. The JV curve of IMEC device without MoO_x but inserted with hexapropyltruxene layer shows S-kink features, which indicates the hexapropyltruxene interlayer cannot act as a hole transporting layer (HTL). Further EQE analysis indicates that the J_{sc} increase does not come from the change in EQE as that in the SubPc/C60 solar cell stack. Stack absorption simulation reveals that the increase of the PCE does not come from a change in interference pattern caused by thickness change. Photoluminescence measurement also reveals that there is no dramatic difference in the exciton lifetime between before and after the insertion of hexapropyltruxene interlayer, but only a weak one. The above analysis suggested that hexapropyltruxene can act as a weak MTG material in IMEC stack solar cells. Besides, the XRD analysis of the α-sexithiophene (α-6T) thin film on the MoO_x layer and the hexapropyltruxene layer indicates that the thin layer beneath α-6T will induce the growth of polymorphism of α-6T. UV-vis and AFM measurement of the same samples also confirm this phenomenon. It turns out that hexapropyltruxene has template growth effect on α-6T. The hexapropyltruxene layer induces the α-6T crystal to grow more amorphously. It inspires us to explore the behaviour of α-6T substrate-induced-phases (SIPs) on different HCLs and its application in the solar cells.

To continue the exploration of α-6T SIPs observed in last chapter, vacuum deposited α-6T thin films on substrates with HCLs (if any) (ITO glass, ITO/PEDOT:PSS, ITO/MoO_x, and ITO/MeO-TPD) are fabricated at 20 °C ("low") and 120 ("high") substrate temperature, with control samples of α-6T deposited at 20 °C on 120 °C pre-annealed substrates. The growth of α-6T polymorphs (HT-, LT-, and β-phases) is studied via ordinary XRD, GIWAXS, AFM, and UV-vis absorption measurements.

The competing growth of α-6T polymorphs is observed with ordinary XRD and GIWAXS measurement.

These experiment results indicate that (H00) oriented LT-phase and (00L) orientated β-phase are the major polymorphs in α-6T layers. The α-6T molecules in these two phases have a "standing-up" orientation. Meanwhile, there exist small fractions of (-411)oriented LT-phase and (H00) orientated HT-phase within the α-6T layers, the molecules in which have a "lying-down" orientation. Both the (H00) and (-411) oriented LT-phase has a preference to grow on bare ITO substrates. The (00L) oriented β-phase tends to grow on MeO-TPD and MoO_x layers. And the (00L) oriented HT-phase has a preference for growing on PEDOT:PSS layer. Meanwhile, it is found that substrate temperature also plays an important role in the competing growth of α-6T polymorphs. With higher (120 °C) substrate temperature, less (-411) oriented LT- and (00L) oriented HT-phase is formed while more (H00) oriented LT- and (00L) oriented β-phase are generated. The fractions of these different polymorphs within the α-6T layer determines its light absorption. Thin films with less "standing-up" but more "lying-down" molecules show better UV-vis absorption, which is confirmed via UV-vis absorption measurements. The device measurement results (JV, EQE, and IQE) confirm the thin film characterization results. From the analyses of microstructural measurement results and the device performance results, we bridge the relationship between microstructure (polymorphs) within α-6T thin films and the corresponding solar cell performance: more (-411) oriented LT-phase and (00L) oriented HT-phase, less (H00) oriented LT-phase and (00L) oriented β-phase of α-6T leads to better UV-vis absorption, which results in better solar cell performance.

These findings help us understand the preferred growth of α-6T polymorphs on different HCLs at low (20 °C) and high (120 °C) substrate temperature and the relationship of polymorphism of the thin film with device performance. These findings are beneficial in guiding the HCL selection for vacuum deposited SMOSC manufacturing.

8.2 Outlook

The first part of the thesis discusses the potential application of hexapropyltruxene as an interlayer within SMOSCs. Due to the limitation of time and equipment availability, the function of hexapropyltruxene interlayer was examined only with two typical SMOSC stacks (SubPc/C60 and IMEC stacks). However, new materials such as non-fullerene acceptors are widely researched [222, 223] and breakthroughs in PCE are made recently [224, 225], which encourages the researchers to investigates the applications of hexapropyltruxene in these new solar cell stacks. In addition, hexapropyltruxene can be resolved in many common solvents, which make it convenient to be solution-processed. It is also worthwhile to investigate its application possibility in solution-processed solar cells.

In this thesis, the hexapropyltruxene molecule is the only derivative of truxene-based materials being systematically investigated. The experimental results show that it has potential applications as an interlayer within SMOSCs. Considering there are quantities of truxene-based materials [147], these positive results encourage future researchers to look into other truxene-based materials to improve the performance of solar cell devices. Materials such as truxenone, isotruxene, and their derivatives are of interest to be further investigated about their functions within solar cells [147, 157].

The second part of this thesis provides researchers with an alternative perspective towards polymorphism control as well as its relationship with HCLs and substrate temperature at evaporation. It is reported that in-situ measurement of α-6T growth on top of silicon substrates has been researched to investigate the dominant growing polymorph of α-6T at different temperature [141]. However, in-situ investigation of the α-6T growth on top of different HCLs remains to be carried out, in order to have an in-depth understanding of the competing growth behaviour of the different polymorphs on HCLs. The ex-situ measurement results in this thesis reveal some facts about the competing growth of polymorphs, but the further in-situ measurement is of

importance to understand the dynamic mechanism of the competing growth process, e.g. which polymorph dominate the growth at which growing stage. Also, since many other molecules such as pentacene have polymorphism phenomena, it is of interest to have an investigation into other molecule systems.

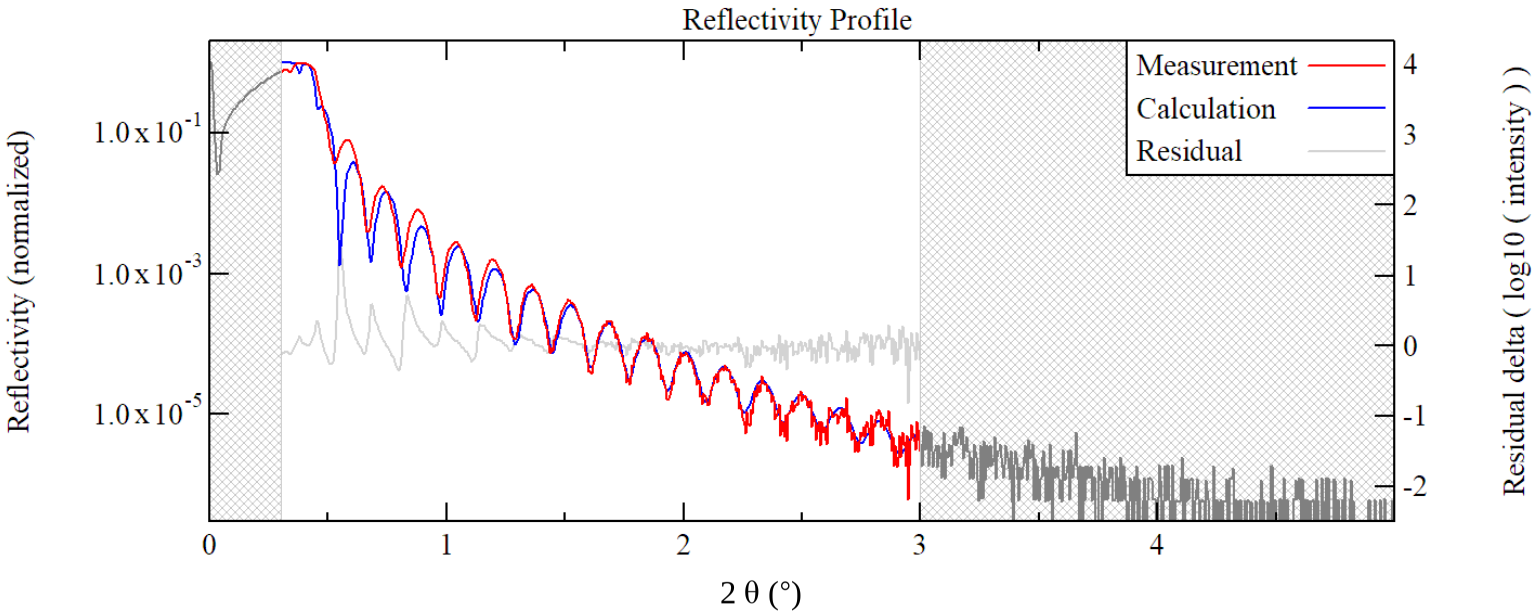
Appendix A

Appendix

Table A.1: List of the Q-space values of representative GIWAXS diffraction peaks.

Crystal plane	Q_{xy} (Å^{-1})	Q_z (Å^{-1})	Parallel plane*	Molecular orientation with respect to the substrate**
α-6T LT (4-1-1)	1.314	0.5484	(H00)	standing up
α-6T LT (4-11)	1.314	0.576	(H00)	standing up
α-6T LT (3-2-1)	1.91	0.4078	(H00)	standing up
α-6T LT (4-2-1)	1.91	0.5484	(H00)	standing up
α-6T LT (-4-11)	1.324	0.5242	(-411)	lying down
α-6T LT (020)	1.324	0.8997	(-411)	lying down
α-6T LT (2-1-1)	1.314	0.2673	(H00)	standing up
α-6T LT (2-11)	1.314	0.2949	(H00)	standing up
α-6T HT (100)	0.6874	0.0966	(00L)	"lying down" (more tilted than LT(H00))
α-6T β (-1-14)	1.37	0.3332	(00L)	standing up
α-6T β (1-11)	1.37	0.3427	(00L)	standing up
α-6T β (-1-12)	1.37	0.0629	(00L)	standing up
α-6T β (1-1-1)	1.37	0.0723	(00L)	standing up
α-6T β (1-20)	1.956	0.2075	(00L)	standing up
SubPc (-201)	1.044	0.6107	(00L)	-
SubPc (1-2-1)	1.046	0.5221	(H00)	-
SubPc (-200)	1.044	0	(00L)	-

*: The plane of the unit cell that is parallel to the substrate.
**: A schematic presentation of the molecular orientation of α-6T polymorphs with different parallel planes is included in Figure A.3.



Layer	Thickness by QCM (nm)	Fitted thickness by XRR (nm)	Fitted density by XRR (g/cm^3)	Fitted roughness by XRR (nm)
SubPc	20	21.1	1.66	0.6
Hexapropyltruxene	30	32.5	1.34	2.0
glass	-	-	2.38	0.9

*R^2 of the fitting is 0.055 and χ^2 of the fitting is 0.0455.

Figure A.1: X-ray reflectivity (XRR) Analysis of a glass/hexapropyltruxene/SubPc thin film sample. Thicknesses of individual layers are included in the inset table.

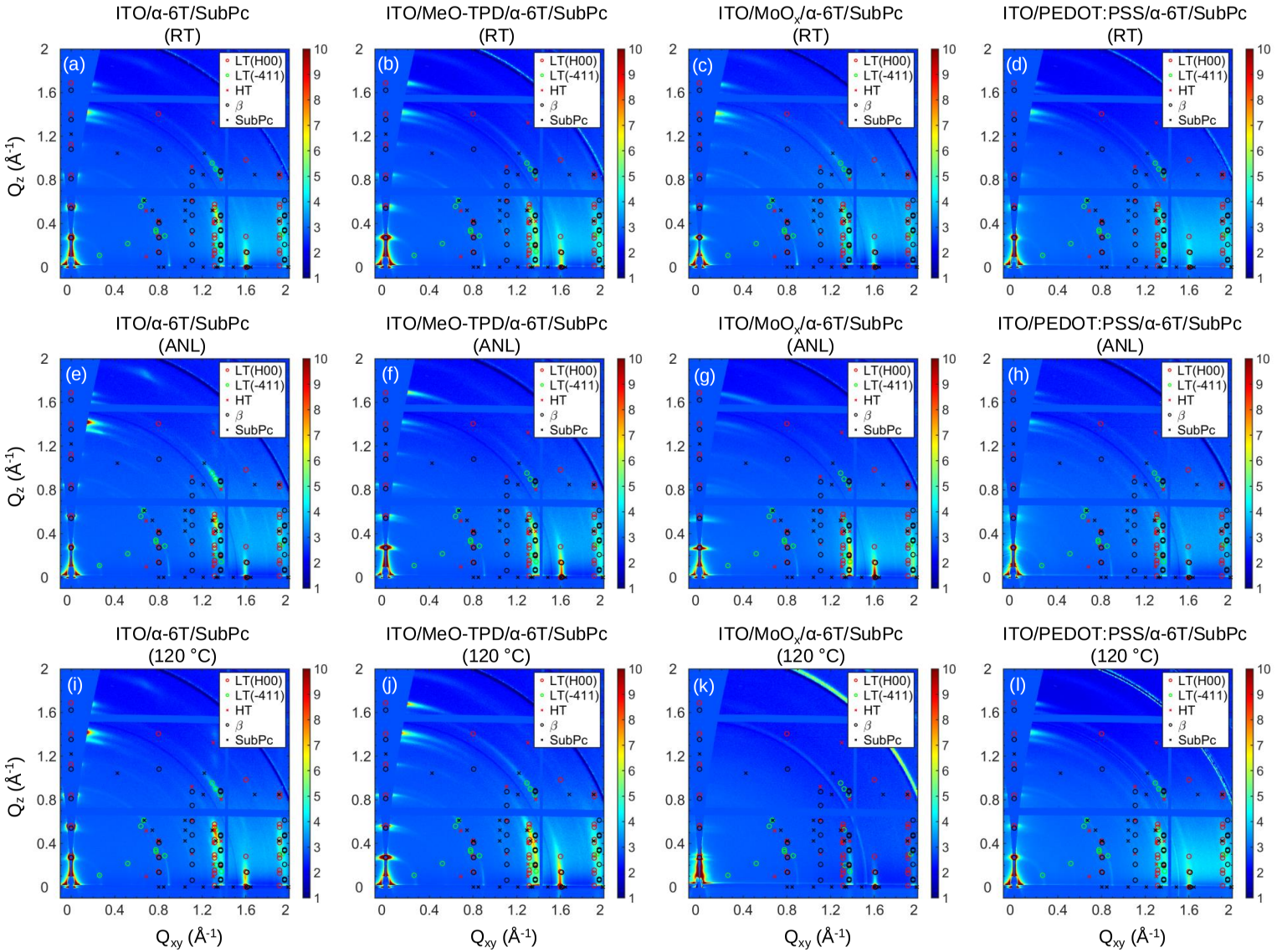


Figure A.2: Summary of GIWAXS results of Thin Film Set 2. (a)(e)(i). ITO/α-6T/SubPc thin films at RT, ANL and 120 °C conditions, (b)(f)(j). ITO/MeO-TPD/α-6T/SubPc thin films at RT, ANL and 120 °C conditions, (c)(g)(k). ITO/MoO_x/α-6T/SubPc thin films at RT, ANL and 120 °C conditions, (d)(h)(l). ITO/PEDOT:PSS/α-6T/SubPc thin films at RT, ANL and 120 °C conditions. LT(H00) (red circle), LT(-411) (green circle), HT (red cross), β (black circle), and SubPc (black cross) stand for (H00) oriented LT-, (-411) oriented LT-, HT-, β-phases of α-6T, and SubPc, respectively. Peak locations are calculated via DPCToolkit software from the crystal structures reported by literature [120, 155, 161, 162, 165, 181].(The figure is tilted 90 ° to show more features in details.)

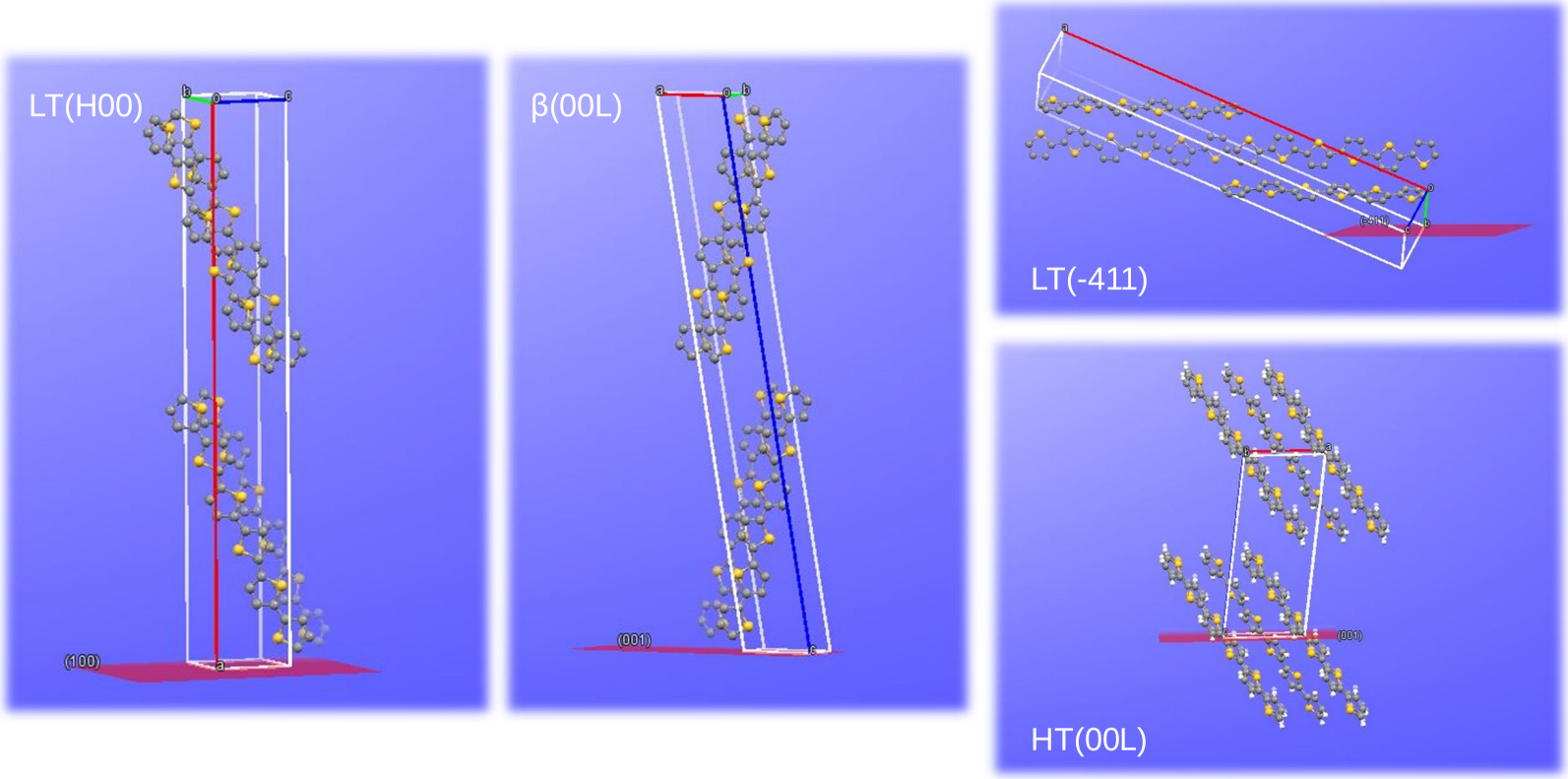


Figure A.3: Schematic presentation of the molecular orientation of α-6T polymorphs with different parallel planes. The plane of the unit cell that is parallel to the substrate in draw in red. The tilt angle of molecules in HT-phase is smaller than those in LT-phase (4.1), meaning molecules in (00L) oriented HT phase is more "lying down" oriented than those in (H00) oriented LT-phase.

Table A.2: GIWAXS peak intensity (I) analysis with R-square (R^2) data.

Polymorph peak	Treatment	LT (4-1-1)		LT (-4-11)		LT (020)		LT (2-1-1)		HT (100)		β (-1-14)		β (1-11)		SubPc (-201)		SubPc (1-2-1)	
Sample		I	R^2	I	R^2	I	R^2	I	R^2	I	R^2	I	R^2	I	R^2	I	R^2	I	R^2
ITO/α-6T/SubPc	RT	5.1	0.98	6.0	0.98	3.5	0.90	4.8	0.91	2.9	0.28	5.1	0.85	5.2	0.93	3.1	0.54	N/A	0.60
ITO/α-6T/SubPc	ANL	6.7	0.99	7.7	0.98	4.9	0.94	5.3	0.92	2.9	0.33	4.3	0.87	4.3	0.87	3.2	0.49	3.2	0.92
ITO/α-6T/SubPc	120 °C	8.0	0.98	9.0	1.00	4.0	0.87	6.1	0.93	2.9	0.33	5.2	0.80	5.3	0.92	3.1	0.52	3.1	0.00
ITO/MeO-TPD/α-6T/SubPc	RT	4.7	0.97	5.0	0.96	3.1	0.89	4.4	0.71	3.8	0.54	5.8	0.97	5.8	0.92	3.0	0.57	3.1	0.66
ITO/MeO-TPD/α-6T/SubPc	ANL	4.7	0.95	5.0	0.89	2.9	0.16	4.3	0.84	2.9	0.83	6.3	0.96	6.3	0.93	3.1	0.67	5.5	0.25
ITO/MeO-TPD/α-6T/SubPc	120 °C	5.9	0.97	6.4	0.99	3.3	0.80	5.2	0.91	2.9	0.67	6.8	0.93	6.8	0.95	3.2	0.29	3.2	0.85
ITO/MoO_x/α-6T/SubPc	RT	4.4	0.96	4.7	0.91	3.3	0.85	4.1	0.91	2.9	0.64	4.8	0.62	4.9	0.60	3.3	0.68	3.3	0.88
ITO/MoO_x/α-6T/SubPc	ANL	3.6	0.14	3.8	0.77	3.1	0.05	3.9	0.72	3.0	0.77	6.2	0.96	6.1	0.97	3.1	0.72	3.3	0.36
ITO/MoO_x/α-6T/SubPc	120 °C	2.8	0.00	2.8	0.10	2.9	0.92	2.9	0.56	N/A	0.37	3.5	0.56	3.5	0.79	2.9	0.62	2.8	0.10
ITO/PEDOT:PSS/α-6T/SubPc	RT	4.0	0.84	4.2	0.90	3.2	0.89	4.0	0.89	3.0	0.62	4.6	0.88	4.6	0.72	3.1	0.45	3.1	0.02
ITO/PEDOT:PSS/α-6T/SubPc	ANL	3.8	0.61	4.0	0.80	3.1	0.64	3.7	0.30	2.9	0.59	4.3	0.76	4.3	0.69	3.1	0.32	3.4	0.06
ITO/PEDOT:PSS/α-6T/SubPc	120 °C	4.4	0.92	4.6	0.90	3.2	0.87	4.3	0.69	3.0	0.57	5.0	0.49	5.1	0.88	N/A	0.23	3.2	0.15

Table A.3: GIWAXS Scherrer coherence length (SCL) analysis with R-square (R^2) data.

Polymorph peak	Treatment	LT (4-1-1)		LT (-4-11)		LT (020)		LT (2-1-1)		HT (100)		β (-1-14)		β (1-11)		SubPc (-201)		SubPc (1-2-1)	
Sample		SCL	R^2	SCL	R^2	SCL	R^2	SCL	R^2	SCL	R^2	SCL	R^2	SCL	R^2	SCL	R^2	SCL	R^2
ITO/α-6T/SubPc	RT	56.8	0.98	59.8	0.98	52.6	0.90	40.0	0.91	3.2	0.28	32.6	0.85	37.7	0.93	22.9	0.54	1.0	0.60
ITO/α-6T/SubPc	ANL	64.1	0.99	76.0	0.98	87.2	0.94	53.6	0.92	6.4	0.33	31.6	0.87	31.9	0.87	33.4	0.49	76.0	0.92
ITO/α-6T/SubPc	120 °C	67.4	0.98	74.5	1.00	61.4	0.87	49.8	0.93	33.9	0.33	36.6	0.80	34.8	0.92	25.1	0.52	1.6	0.00
ITO/MeO-TPD/α-6T/SubPc	RT	44.2	0.97	49.2	0.96	44.1	0.89	22.0	0.71	1.3	0.54	33.1	0.97	36.8	0.92	24.2	0.57	12.4	0.66
ITO/MeO-TPD/α-6T/SubPc	ANL	53.1	0.95	56.1	0.89	20.7	0.16	33.6	0.84	20.2	0.83	48.4	0.96	48.9	0.93	29.3	0.67	1.4	0.25
ITO/MeO-TPD/α-6T/SubPc	120 °C	59.2	0.97	57.4	0.99	38.2	0.80	35.1	0.91	33.5	0.67	38.8	0.93	42.8	0.95	22.0	0.29	62.0	0.85
ITO/MoO_x/α-6T/SubPc	RT	39.9	0.96	43.0	0.91	29.9	0.85	27.0	0.91	16.0	0.64	27.1	0.62	25.5	0.60	36.3	0.68	54.7	0.88
ITO/MoO_x/α-6T/SubPc	ANL	14.0	0.14	22.6	0.77	2.5	0.05	20.4	0.72	4.7	0.77	47.7	0.96	51.3	0.97	25.0	0.72	5.5	0.36
ITO/MoO_x/α-6T/SubPc	120 °C	3.3	0.00	17.2	0.10	60.2	0.92	24.3	0.56	0.9	0.37	26.4	0.56	28.3	0.79	33.1	0.62	16.9	0.10
ITO/PEDOT:PSS/α-6T/SubPc	RT	37.4	0.84	39.2	0.90	52.2	0.89	28.1	0.89	15.1	0.62	30.5	0.88	31.0	0.72	13.9	0.45	3.4	0.02
ITO/PEDOT:PSS/α-6T/SubPc	ANL	28.4	0.61	36.9	0.80	38.6	0.64	17.3	0.30	25.7	0.59	19.1	0.76	30.1	0.69	34.3	0.32	2.7	0.06
ITO/PEDOT:PSS/α-6T/SubPc	120 °C	38.2	0.92	39.4	0.90	42.2	0.87	25.1	0.69	37.2	0.57	27.0	0.49	34.0	0.88	0.7	0.23	14.0	0.15

Appendix B

List of Publications

B.1 Journal Publications

1. Ye H., Kesava S. V., Hardigree J. F. M., Brown R. E., Mazzotta G., Warren R., Skabara P. J., & Riede M. Efficiency enhancement of small molecule organic solar cells using hexapropyltruxene as an interface layer, *Journal of Materials Chemistry C* **8**, 4909 (2020).

2. Duan H., Jha A., Li X., Tiwari V.,Ye H., Nayak P. K., Zhu X., Li Z., Martinez T. J., Thorwart M. & Miller R. J. D. Intermolecular vibrations mediate ultrafast singlet fission, *Science Advances* **6**, 38 (2020).

B.2 Conference Contributions

1. Ye H., Kesava S. V., Hardigree J. M., Brown R. E., Mazzotta G., Warren R., Skabara P. J., & Riede M. PCE enhancement of small molecule organic solar cells using hexapropyltruxene as an interface layer, poster, *14th International Conference on Organic Electronics*, Bordeaux, June 2018.

2. Ye H., Lauritzen A., & Riede M., Controlled growth of α-sexithiophene polymorphs via substrate pre-treatment & temperature and its application in organic solar cells, poster, *14th International Symposium on Functional π-Electron Systems*, Berlin, June 2019.

Bibliography

[1] Max Roser, H. R. & Ortiz-Ospina, E. World population growth. *Our World in Data* (2019). Https://ourworldindata.org/world-population-growth.

[2] Energy, B. BP energy outlook 2019 edition .

[3] Keeling, C. D. *et al.* Exchanges of atmospheric CO_2 and $13CO_2$ with the terrestrial biosphere and oceans from 1978 to 2000. I. Global aspects (2001).

[4] Covert, T. R., Greenstone, M. & Knittel, C. R. Will we ever stop using fossil fuels? *Ssrn* **30**, 117–138 (2016).

[5] Jenkinson, D. S., Adams, D. & Wild, A. Model estimates of CO_2 emissions from soil in response to global warming. *Nature* **351**, 304 (1991).

[6] Norby, R. J. & Luo, Y. Evaluating ecosystem responses to rising atmospheric CO_2 and global warming in a multi-factor world. *New Phytologist* **162**, 281–293 (2004).

[7] Boo, K.-O., Kwon, W.-T. & Baek, H.-J. Change of extreme events of temperature and precipitation over korea using regional projection of future climate change. *Geophysical Research Letters* **33** (2006).

[8] Diffenbaugh, N. S. *et al.* Quantifying the influence of global warming on unprecedented extreme climate events. *Proceedings of the National Academy of Sciences* **114**, 4881–4886 (2017).

[9] Teixeira, E. I., Fischer, G., Van Velthuizen, H., Walter, C. & Ewert, F. Global hot-spots of heat stress on agricultural crops due to climate change. *Agricultural and Forest Meteorology* **170**, 206–215 (2013).

[10] Rosenzweig, C., Iglesius, A., Yang, X.-B., Epstein, P. R. & Chivian, E. Climate change and extreme weather events-implications for food production, plant diseases, and pests (2001).

[11] Field, C. B., Campbell, J. E. & Lobell, D. B. Biomass energy: the scale of the potential resource. *Trends in ecology & evolution* **23**, 65–72 (2008).

[12] Gürbüz, A. The role of hydropower in sustainable development. *History* **20**, 25–000 (2006).

[13] Leung, D. Y. & Yang, Y. Wind energy development and its environmental impact: A review. *Renewable and sustainable energy reviews* **16**, 1031–1039 (2012).

[14] Jäger-Waldau, A. Photovoltaics and renewable energies in europe. *Renewable and Sustainable Energy Reviews* **11**, 1414–1437 (2007).

[15] Haszeldine, R. S. Carbon capture and storage: how green can black be? *Science* **325**, 1647–1652 (2009).

[16] Pietzcker, R. C., Stetter, D., Manger, S. & Luderer, G. Using the sun to decarbonize the power sector: The economic potential of photovoltaics and concentrating solar power. *Applied Energy* **135**, 704–720 (2014).

[17] Pimentel, D. *et al.* Renewable energy: economic and environmental issues. *BioScience* **44**, 536–547 (1994).

[18] Breyer, C. *et al.* On the role of solar photovoltaics in global energy transition scenarios. *Progress in Photovoltaics: Research and Applications* **25**, 727–745 (2017).

[19] Zhang, H., Baeyens, J., Degrève, J. & Cacères, G. Concentrated solar power plants: Review and design methodology. *Renewable and sustainable energy reviews* **22**, 466–481 (2013).

[20] Müller-Steinhagen, H. & Trieb, F. Concentrating solar power. *A review of the technology. Ingenia Inform QR Acad Eng* **18**, 43–50 (2004).

[21] Barlev, D., Vidu, R. & Stroeve, P. Innovation in concentrated solar power. *Solar energy materials and solar cells* **95**, 2703–2725 (2011).

[22] Fuqiang, W. *et al.* Progress in concentrated solar power technology with parabolic trough collector system: a comprehensive review. *Renewable and Sustainable Energy Reviews* **79**, 1314–1328 (2017).

[23] Khan, J. & Arsalan, M. H. Solar power technologies for sustainable electricity generation–a review. *Renewable and Sustainable Energy Reviews* **55**, 414–425 (2016).

[24] Bhatia, S. *Advanced renewable energy systems,(Part 1 and 2)* (WPI Publishing, 2014).

[25] Green, M. A. *et al.* Solar cell efficiency tables (version 54). *Progress in Photovoltaics: Research and Applications* **27**, 565–575 (2019).

[26] Martín-Martínez, S., Cañas-Carretón, M., Honrubia-Escribano, A. & Gómez-Lázaro, E. Performance evaluation of large solar photovoltaic power plants in spain. *Energy conversion and management* **183**, 515–528 (2019).

[27] Johnstone, B. *Switching to solar: what we can learn from Germany's success in harnessing clean energy* (Prometheus Books, 2010).

[28] Palz, W. *Solar power for the world: what you wanted to know about photovoltaics*, vol. 4 (CRC press, 2013).

[29] Wang, X. & Barnett, A. The evolving value of photovoltaic module efficiency. *Applied Sciences* **9**, 1227 (2019).

[30] the Mechanical Engineering Industry Association (VDMA). International technology roadmap for photovoltaics (itrpv) results 2018 (tenth edition) (2019).

[31] Blakers, A. Development of the perc solar cell. *IEEE Journal of Photovoltaics* **9**, 629–635 (2019).

[32] Braun, S., Hahn, G., Nissler, R., Pönisch, C. & Habermann, D. Multi-busbar solar cells and modules: high efficiencies and low silver consumption. *Energy Procedia* **38**, 334–339 (2013).

[33] Lazard, N. Lazard's levelized cost of energy analysis–version 13.0 (2019).

[34] YCharts, I. I. First solar: Thanks for the subsidies (2010). URL `https://www.forbes.com/sites/investor/2010/07/01/first-solar-thanks-for-the-subsidies/`.

[35] Williamson, K. First solar on the patent throne for solar pv (2011). URL `http://www.renewableenergyfocus.com/view/22234/first-solar-on-the-patent-throne-for-solar-pv/`.

[36] Fraunhofer, I. Photovoltaics report. *Fraunhofer ISE, Freiburg* (2019).

[37] Baharwani, V., Meena, N., Dubey, A., Brighu, U. & Mathur, J. Life cycle analysis of solar pv system: a review. *International Journal of Environmental Research and Development* **4**, 183–190 (2014).

[38] Powell, D. M. *et al.* The capital intensity of photovoltaics manufacturing: barrier to scale and opportunity for innovation. *Energy & Environmental Science* **8**, 3395–3408 (2015).

[39] Kumar, A., Bieri, M., Reindl, T. & Aberle, A. G. Economic viability analysis of silicon solar cell manufacturing: Al-bsf versus perc. *Energy Procedia* **130**, 43–49 (2017).

[40] Swarup, A. & Khare, P. S. Organic solar pv cells: promising option for meeting future energy requirements (2015). URL http://www.supersmartenergy.com/organic-solar-photovoltaic-cells-promising-option-for-meeting-future-energy-

[41] The Future of Things. Neuber lightweight solar panel bags (2019). URL https://thefutureofthings.com/4380-neuber-lightweight-solar-panel-bags/.

[42] Ma, A. Hanergy, Audi sign deal for solar-roof cars (2017). URL https://www.caixinglobal.com/2017-08-24/hanergy-audi-sign-deal-for-solar-roof-cars-101135153.html.

[43] Wild, E. A quick run-down of BIPV (2014). URL https://www.solarpowerworldonline.com/2014/12/quick-run-bipv/.

[44] NREL, N. Best research-cell efficiency chart (2019).

[45] Würfel, P. & Würfel, U. *Physics of solar cells: from basic principles to advanced concepts* (John Wiley & Sons, 2016).

[46] Tress, W. *Organic Solar Cells: Theory, Experiment, and Device Simulation* (Springer, 2014).

[47] Dechun, Z. 4 - Chemical and photophysical properties of materials for OLEDs. In Buckley, A. (ed.) *Organic Light-Emitting Diodes (OLEDs)*, Woodhead Publishing Series in Electronic and Optical Materials, 114 – 142 (Woodhead Publishing, 2013).

[48] Huheey, J. E., Keiter, E. A., Keiter, R. L. & Medhi, O. K. *Inorganic chemistry: principles of structure and reactivity* (Pearson Education India, 2006).

[49] Schwoerer, M. & Wolf, H. C. *Organic molecular solids* (John Wiley & Sons, 2007).

[50] Po, R., Carbonera, C., Bernardi, A. & Camaioni, N. The role of buffer layers in polymer solar cells. *Energy & Environmental Science* **4**, 285 (2011).

[51] Armin, A. *et al.* Quantum efficiency of organic solar cells: Electro-optical cavity considerations. *ACS Photonics* **1**, 173–181 (2014).

[52] Fei, Z. *et al.* Correction to: An alkylated indacenodithieno[3,2-b]thiophene-based nonfullerene acceptor with high crystallinity exhibiting single junction solar cell efficiencies greater than 13% with low voltage losses (adv. mater., (2018), 30, (1705209), 10.1002/adma. *Advanced Materials* **30**, 1705209 (2018).

[53] Zhang, H. *et al.* Over 14% efficiency in organic solar cells enabled by chlorinated nonfullerene small-molecule acceptors. *Advanced Materials* **1800613**, 1–7 (2018).

[54] Zhao, W. *et al.* Molecular optimization enables over 13% efficiency in organic solar cells. *Journal of the American Chemical Society* **139**, 7148–7151 (2017).

[55] Xu, X. *et al.* Realizing over 13% efficiency in green-solvent-processed nonfullerene organic solar cells enabled by 1,3,4-thiadiazole-based wide-bandgap copolymers. *Advanced Materials* **1703973**, 1703973 (2017).

[56] Cui, Y. *et al.* Over 16% efficiency organic photovoltaic cells enabled by a chlorinated acceptor with increased open-circuit voltages. *Nature communications* **10**, 2515 (2019).

[57] Huang, Y., Kramer, E. J., Heeger, A. J. & Bazan, G. C. Bulk Heterojunction Solar Cells: Morphology and Performance Relationships. *Chem. Rev.* **114**, 7006–7043 (2014).

[58] Li, G., Zhu, R. & Yang, Y. Polymer solar cells. *Nature Photonics* **6**, 153–161 (2012).

[59] Su, Y.-W., Lan, S.-C. & Wei, K.-H. Organic photovoltaics. *Mater. Today (Oxford, U. K.)* **15**, 554–562 (2012).

[60] Scharber, M. C. & Sariciftci, N. S. Efficiency of bulk-heterojunction organic solar cells. *Progress in Polymer Science* **38**, 1929–1940 (2013).

[61] Brabec, C. J. *et al.* Polymer–fullerene bulk-heterojunction solar cells. *Advanced Materials* **22**, 3839–3856 (2010).

[62] Brabec, C. J., Heeney, M., McCulloch, I. & Nelson, J. Influence of blend microstructure on bulk heterojunction organic photovoltaic performance. *Chemical Society reviews* **40**, 1185–1199 (2011).

[63] Christoforo, G. batch-iv-analysis (2019). URL `https://github.com/greyltc/analysis-software`.

[64] Shrotriya, V. *et al.* Accurate measurement and characterization of organic solar cells. *Advanced Functional Materials* **16**, 2016–2023 (2006).

[65] American Society for Testing and Materials. ASTM Standard E973, standard test method for determination of the spectral mismatch parameter between a photovoltaic device and a photovoltaic reference cell **12**, 1–3 (2010).

[66] Golder, J. *et al.* Unconventional anode interlayer universally improving solar cell efficiency. *Journal of Physics D: Applied Physics* **51** (2018).

[67] Yin, Z., Wei, J. & Zheng, Q. Interfacial materials for organic solar cells: Recent advances and perspectives. *Advanced Science* **3**, 1–37 (2016).

[68] Song, Q. L., Li, C. M., Wang, M. L., Sun, X. Y. & Hou, X. Y. Role of buffer in organic solar cells using C60 as an acceptor. *Applied Physics Letters* **90**, 071109 (2007).

[69] Nikolis, V. C. *et al.* Reducing voltage losses in cascade organic solar cells while maintaining high external quantum efficiencies. *Advanced Energy Materials* **1700855**, 1–8 (2017).

[70] Ghorashi, S. M. B., Behjat, A. & Ajeian, R. The effect of a buffer layer on the performance and optimal encapsulation time of ITO/CuPc/C60/buffer/Cu bilayer cells. *Solar Energy Materials and Solar Cells* **96**, 50–57 (2012).

[71] Chan, M. Y. *et al.* Efficient organic photovoltaic devices using a combination of exciton blocking layer and anodic buffer layer. *Journal of Applied Physics* **100** (2006).

[72] Bergemann, K. J., Amonoo, J. a., Song, B., Green, P. F. & Forrest, S. R. Surprisingly High Conductivity and Efficient Exciton Blocking in Fullerene/Wide-Energy-Gap Small Molecule Mixtures. *Nano letters* **15**, 3994–9 (2015).

[73] Barito, A. *et al.* Recovering lost excitons in organic photovoltaics using a transparent dissociation layer. *Journal of Applied Physics* **113** (2013).

[74] Yang, J., Yan, D. & Jones, T. S. Molecular template growth and its applications in organic electronics and optoelectronics. *Chemical Reviews* **115**, 5570–5603 (2015).

[75] Wang, Z., Zhou, Y., Miyadera, T., Chikamatsu, M. & Yoshida, Y. Constructing nanostructured donor/acceptor bulk heterojunctions via interfacial templates for efficient organic photovoltaics. *ACS Applied Materials & Interfaces* acsami.7b13989 (2017).

[76] Lorch, C. *et al.* Templating effects of α-sexithiophene in donor-acceptor organic thin films. *Journal of Physical Chemistry C* **119**, 23211–23220 (2015).

[77] Sullivan, P., Jones, T. S., Ferguson, A. J. & Heutz, S. Structural templating as a route to improved photovoltaic performance in copper phthalocyanine/fullerene (C60) heterojunctions. *Applied Physics Letters* **91**, 2005–2008 (2007).

[78] Rand, B. P. *et al.* The impact of molecular orientation on the photovoltaic properties of a phthalocyanine/fullerene heterojunction. *Advanced Functional Materials* **22**, 2987–2995 (2012).

[79] Wang, Z., Miyadera, T., Yamanari, T. & Yoshida, Y. Templating effects in molecular growth of blended films for efficient small-molecule photovoltaics (2014).

[80] Taima, T. *et al.* Sexithiophene-based photovoltaic cells with high light absorption coefficient via crystalline polymorph control. *The Journal of Physical Chemistry C* **121**, 19699–19704 (2017).

[81] Opitz, A. Energy level alignment at planar organic heterojunctions: influence of contact doping and molecular orientation. *Journal of Physics: Condensed Matter* **29**, 133001 (2017).

[82] Wang, Z. *et al.* Structural influences on charge carrier dynamics for small-molecule organic photovoltaics. *Journal of Applied Physics* **116**, 0–7 (2014).

[83] Tokito, S., Noda, K. & Taga, Y. Metal oxides as a hole-injecting layer for an organic electroluminescent device **2750**, 1–5 (1996).

[84] Girotto, C., Voroshazi, E., Cheyns, D., Heremans, P. & Rand, B. P. Solution-processed MoO_3 thin films as a hole-injection layer for organic solar cells. *ACS applied materials & interfaces* **3**, 3244–7 (2011).

[85] Cattin, L. *et al.* MoO3 surface passivation of the transparent anode in organic solar cells using ultrathin films. *Journal of Applied Physics* **105**, 1–7 (2009).

[86] Jin, F. *et al.* Interface engineering of organic schottky barrier solar cells and its application in enhancing performances of planar heterojunction solar cells. *Scientific Reports* **6**, 26262 (2016). URL `http://www.nature.com/articles/srep26262`.

[87] Verreet, B., Müller, R., Rand, B. P., Vasseur, K. & Heremans, P. Structural templating of chloro-aluminum phthalocyanine layers for planar and bulk heterojunction organic solar cells. *Organic Electronics: physics, materials, applications* **12**, 2131–2139 (2011).

[88] Nakayama, Y. *et al.* Origins of improved hole-injection efficiency by the deposition of MoO 3 on the polymeric semiconductor poly(dioctyifluorene-alt-benzothiadiazole). *Advanced Functional Materials* **19**, 3746–3752 (2009).

[89] Lin, C. F. *et al.* Chloroboron subphthalocyanine/C60 planar heterojunction organic solar cell with N,N-dicarbazolyl-3,5-benzene blocking layer. *Solar Energy Materials and Solar Cells* **122**, 264–270 (2014).

[90] Ran, N. A. *et al.* Impact of interfacial molecular orientation on radiative recombination and charge generation efficiency. *Nature Communications* **8**, 1–9 (2017).

[91] Wang, Z. *et al.* Understanding device-structure-induced variations in open-circuit voltage for organic photovoltaics. *ACS applied materials & interfaces* **7**, 10814–22 (2015).

[92] Kang, C.-m. *et al.* 1 GHz pentacene diode rectifiers enabled by controlled film deposition on sam-treated au anodes. *Advanced Electronic Materials* **2**, 1500282 (2016).

[93] Ha, Y. E. *et al.* Inverted type polymer solar cells with self-assembled monolayer treated ZnO. *Journal of Physical Chemistry C* **117**, 2646–2652 (2013).

[94] Bain, C. D. & Whitesides, G. M. Modeling organic surfaces with self-assembled monolayers. *Advanced Materials* **1**, 110–116 (1989).

[95] Fenwick, O. *et al.* Thermochemical nanopatterning of organic semiconductors. *Nature Nanotechnology* **4**, 664–668 (2009).

[96] Holdcroft, S. Patterning π-conjugated polymers. *Advanced Materials* **13**, 1753–1765 (2001).

[97] Kim, C., Cao, Y., Soboyejo, W. O. & Forrest, S. R. Patterning of active organic materials by direct transfer for organic electronic devices. *Journal of Applied Physics* **97** (2005).

[98] Jones, A. O., Chattopadhyay, B., Geerts, Y. H. & Resel, R. Substrate-induced and thin-film phases: Polymorphism of organic materials on surfaces. *Advanced Functional Materials* **26**, 2233–2255 (2016).

[99] Chou, C. T. *et al.* Effect of substrate temperature on orientation of subphthalocyanine molecule in organic photovoltaic cells. *Thin Solid Films* **520**, 2289–2292 (2012).

[100] Ramadan, A. J. *et al.* Exploring high temperature templating in non-planar phthalocyanine/copper iodide (111) bilayers. *Journal of Materials Chemistry C: Materials for optical and electronic devices* **3**, 461–465 (2014).

[101] Cho, S. W. *et al.* Probing the effect of relative molecular orientation on the photovoltaic device performance of an organic bilayer heterojunction using soft x-ray spectroscopies. *Applied Physics Letters* **100**, 1–5 (2012).

[102] Heutz, S., Cloots, R. & Jones, T. S. Structural templating effects in molecular heterostructures grown by organic molecular-beam deposition. *Applied Physics Letters* **77**, 3938 (2000).

[103] Chauhan, K. V., Sullivan, P., Yang, J. L. & Jones, T. S. Efficient organic photovoltaic cells through structural modification of chloroaluminum phthalocyanine / fullerene heterojunctions. *J. Phys. Chem. C* **114**, 3304–3308 (2010).

[104] Wang, T. *et al.* Growing ultra-flat organic films on graphene with a face-on stacking via moderate molecule-substrate interaction. *Scientific Reports* **6**, 28895 (2016).

[105] Duhm, S. *et al.* Orientation-dependent ionization energies and interface dipoles in ordered molecular assemblies. *Nature Materials* **7**, 326–332 (2008).

[106] Zhou, Y. *et al.* Glancing angle deposition of copper iodide nanocrystals for. *Nano letters* **12**, 4146–4152 (2012).

[107] Rochford, L. A. *et al.* Structural templating in a nonplanar phthalocyanine using single crystal copper iodide. *Advanced Materials Interfaces* **2**, 2–5 (2015).

[108] Jo, S. B. *et al.* Boosting photon harvesting in organic solar cells with highly oriented molecular crystals via graphene-organic heterointerface. *ACS Nano* **9**, 8206–8219 (2015).

[109] Singha Roy, S., Bindl, D. J. & Arnold, M. S. Templating highly crystalline organic semiconductors using atomic membranes of graphene at the Anode/organic interface. *Journal of Physical Chemistry Letters* **3**, 873–878 (2012).

[110] Zhang, L., Roy, S. S., Hamers, R. J., Arnold, M. S. & Andrew, T. L. Molecular orientation-dependent interfacial energetics and built-in voltage tuned by a template graphene monolayer. *Journal of Physical Chemistry C* **119**, 45–54 (2015).

[111] McDonough, T. J. *et al.* Triplet exciton dissociation and electron extraction in graphene-templated pentacene observed with ultrafast spectroscopy. *Phys. Chem. Chem. Phys.* **19**, 4809–4820 (2017).

[112] Duan, H. *et al.* Interface modification of organic photovoltaics by combining molybdenum oxide (MoOx) and molecular template layer. *Thin Solid Films* **574**, 146–151 (2015).

[113] Holmes, D., Kumaraswamy, S., Matzger, A. J. & Vollhardt, K. P. C. On the nature of nonplanarity in the [n] phenylenes. *Chemistry–A European Journal* **5**, 3399–3412 (1999).

[114] Campbell, R., Robertson, J. M. & Trotter, J. The crystal structure of hexacene, and a revision of the crystallographic data for tetracene. *Acta crystallographica* **15**, 289–290 (1962).

[115] Schiefer, S., Huth, M., Dobrinevski, A. & Nickel, B. Determination of the crystal structure of substrate-induced pentacene polymorphs in fiber structured thin films. *Journal of the American Chemical Society* **129**, 10316–10317 (2007).

[116] Fritz, S. E., Martin, S. M., Frisbie, C. D., Ward, M. D. & Toney, M. F. Structural characterization of a pentacene monolayer on an amorphous sio2 substrate

with grazing incidence x-ray diffraction. *Journal of the American Chemical Society* **126**, 4084–4085 (2004).

[117] Mannsfeld, S. C., Virkar, A., Reese, C., Toney, M. F. & Bao, Z. Precise structure of pentacene monolayers on amorphous silicon oxide and relation to charge transport. *Advanced Materials* **21**, 2294–2298 (2009).

[118] Jung, M.-C. *et al.* Flat-lying semiconductor–insulator interfacial layer in dntt thin films. *ACS applied materials & interfaces* **7**, 1833–1840 (2015).

[119] Wedl, B. *et al.* Crystallisation kinetics in thin films of dihexyl-terthiophene: the appearance of polymorphic phases. *RSC advances* **2**, 4404–4414 (2012).

[120] Servet, B. *et al.* Polymorphism and charge transport in vacuum-evaporated sexithiophene films. *Chemistry of Materials* **6**, 1809–1815 (1994).

[121] Diao, Y., Myerson, A. S., Hatton, T. A. & Trout, B. L. Surface design for controlled crystallization: The role of surface chemistry and nanoscale pores in heterogeneous nucleation. *Langmuir* **27**, 5324–5334 (2011).

[122] Destri, S., Mascherpa, M. & Porzio, W. Mesophase formation in a-sexithienyl at high temperature-an x-ray diffraction study. *Advanced Materials* **0**, 43–45 (1993).

[123] Mattheus, C. C. *et al.* Identification of polymorphs of pentacene. *Synthetic metals* **138**, 475–481 (2003).

[124] Siegrist, T. *et al.* A polymorph lost and found: The high-temperature crystal structure of pentacene. *Advanced materials* **19**, 2079–2082 (2007).

[125] Wang, X., Garcia, T., Monaco, S., Schatschneider, B. & Marom, N. Effect of crystal packing on the excitonic properties of rubrene polymorphs. *CrystEngComm* **18**, 7353–7362 (2016).

[126] Matsukawa, T. *et al.* Polymorphs of rubrene crystal grown from solution. *Japanese Journal of Applied Physics* **49**, 085502 (2010).

[127] Milita, S., Servidori, M., Cicoira, F., Santato, C. & Pifferi, A. Synchrotron x-ray investigation of tetracene thin films grown at different deposition fluxes. *Nuclear Instruments and Methods in Physics Research Section B: Beam Interactions with Materials and Atoms* **246**, 101–105 (2006).

[128] Brillante, A., Bilotti, I., Della Valle, R. G., Venuti, E. & Girlando, A. Probing polymorphs of organic semiconductors by lattice phonon raman microscopy. *CrystEngComm* **10**, 937–946 (2008).

[129] Moser, A. *et al.* A disordered layered phase in thin films of sexithiophene. *Chemical Physics Letters* **574**, 51–55 (2013).

[130] Siegrist, T. *et al.* Enhanced physical properties in a pentacene polymorph. *Angewandte Chemie International Edition* **40**, 1732–1736 (2001).

[131] Heinrich, M. A. *et al.* Enantiotropic polymorphism in di-indenoperylene. *The Journal of Physical Chemistry C* **111**, 18878–18881 (2007).

[132] Sharp, J. H. & Abkowitz, M. Dimeric structure of a copper phthalocyanine polymorph. *The Journal of Physical Chemistry* **77**, 477–481 (1973).

[133] Saijo, H., Kobayashi, T. & Uyeda, N. Epitaxial growth of a new polymorph of cu-phthalocyanine on graphite. *Journal of Crystal Growth* **40**, 118–124 (1977).

[134] Pithan, L. *et al.* Light controls polymorphism in thin films of sexithiophene. *Crystal Growth and Design* **15**, 1319–1324 (2015).

[135] Porzio, W., Destri, S., Mascherpa, M. & Bruckner, S. Structual aspects of oligothienyl series from X-ray powder diffraction data. *Acta Polymerica* **44**, 266–272 (1993).

[136] Giri, G. *et al.* Tuning charge transport in solution-sheared organic semiconductors using lattice strain. *Nature* **480**, 504 (2011).

[137] Diao, Y. *et al.* Understanding polymorphism in organic semiconductor thin films through nanoconfinement. *Journal of the American Chemical Society* **136**, 17046–17057 (2014).

[138] Drummy, L. F. & Martin, D. C. Thickness-driven orthorhombic to triclinic phase transformation in pentacene thin films. *Advanced Materials* **17**, 903–907 (2005).

[139] Bayliss, S. M. *et al.* Templating effects in the growth of metal-free phthalocyanine polymorphic double layers. *Advanced Materials* **12**, 202–206 (2000).

[140] Caridi, A., Kulkarni, S. A., Di Profio, G., Curcio, E. & Ter Horst, J. H. Template-induced nucleation of isonicotinamide polymorphs. *Crystal Growth & Design* **14**, 1135–1141 (2014).

[141] Lorch, C. *et al.* Growth of competing crystal phases of α-sexithiophene studied by real-time in situ X-ray scattering. *Journal of Physical Chemistry C* **119**, 819–825 (2015).

[142] Reischl, D. *et al.* Surface-induced polymorphism as a tool for enhanced dissolution: The example of phenytoin. *Crystal Growth and Design* **15**, 4687–4693 (2015).

[143] Hiremath, R., Varney, S. W. & Swift, J. A. Selective growth of a less stable polymorph of 2-iodo-4-nitroaniline on a self-assembled monolayer template. *Chemical Communications* 2676–2677 (2004).

[144] Hiremath, R., Basile, J. A., Varney, S. W. & Swift, J. A. Controlling molecular crystal polymorphism with self-assembled monolayer templates. *Journal of the American Chemical Society* **127**, 18321–18327 (2005).

[145] Placencia, D. *et al.* Organic photovoltaic cells based on solvent-annealed, textured titanyl phthalocyanine/C60 heterojunctions. *Advanced Functional Materials* **19**, 1913–1921 (2009).

[146] Conboy, J. C. *et al.* Impact of solvent vapor annealing on the morphology and photophysics of molecular semiconductor thin films. *The Journal of Physical Chemistry B* **102**, 4516–4525 (1998).

[147] Goubard, F. & Dumur, F. Truxene: a promising scaffold for future materials. *RSC Adv.* **5**, 3521–3551 (2015).

[148] Zong, X. *et al.* Design of truxene-based organic dyes for high-efficiency dye-sensitized solar cells employing cobalt redox shuttle (2012).

[149] Zhang, G., Rominger, F. & Mastalerz, M. Fused π-extended truxenes via a threefold borylation as the key step. *Chemistry - A European Journal* **22**, 3084–3093 (2016).

[150] Pérez, E. M. *et al.* Concave tetrathiafulvalene-type donors as supramolecular partners for fullerenes. *Angewandte Chemie - International Edition* **46**, 1847–1851 (2007).

[151] Molina-Ontoria, A., Gallego, M., Echegoyen, L., Pérez, E. M. & Martín, N. Organic solar cells based on bowl-shaped small-molecules. *RSC Adv.* **5**, 31541–31546 (2015).

[152] Wang, J. *et al.* A new thermal-stable truxene-based hole-transporting material for perovskite solar cells. *Dyes and Pigments* **125**, 399–406 (2016).

[153] Ramadan, A. J. *et al.* Organic/inorganic epitaxy: commensurate epitaxial growth of truxenone on Cu (111). *RSC Adv.* **6**, 17125–17128 (2016).

[154] Kinoshita, Y., Takenaka, R. & Murata, H. Independent control of open-circuit voltage of organic solar cells by changing film thickness of MoO_3 buffer layer. *Applied Physics Letters* **92**, 2008–2010 (2008).

[155] Virdo, J. D., Lough, A. J. & Bender, T. P. Redetermination of the crystal structure of boron subphthalocyanine chloride (Cl-BsubPc) enabled by slow train sublimation. *Acta Crystallographica Section C Structural Chemistry* **72**, 297–307 (2016).

[156] Morse, G. E., Gong, I., Kawar, Y., Lough, A. J. & Bender, T. P. Crystal and solid-state arrangement trends of halogenated boron subphthalocyanines. *Cryst Growth Des* **14**, 2138–2147 (2014).

[157] Nielsen, C. B. *et al.* Efficient truxenone-based acceptors for organic photovoltaics. *J. Mater. Chem. A* **1**, 73–76 (2013).

[158] Endres, J., Pelczer, I., Rand, B. P. & Kahn, A. Determination of energy level alignment within an energy cascade organic solar cell. *Chemistry of Materials* acs.chemmater.5b03857 (2016).

[159] Cnops, K. *et al.* 8.4% efficient fullerene-free organic solar cells exploiting long-range exciton energy transfer. *Nature Communications* **5**, 1–6 (2014).

[160] Lovinger, A. J. *et al.* Morphology of alpha-hexathienyl thin-film-transistor films. *Journal of Materials Research* **10**, 2958–2962 (1995).

[161] Horowitz, G. *et al.* Growth and characterization of sexithiophene single crystals. *Chemistry of Materials* **7**, 1337–1341 (1995).

[162] Siegrist, T. *et al.* The crystal structure of the high-temperature polymorph of a-hexathienyl (a-6T / HT). *Journal of Materials Research* **10**, 2170–2173 (1995).

[163] Antolini, L., Horowitz, G., Kouki, F. & Garnier, F. Polymorphism in oligothiophenes with an even number of thiophene subunits. *Advanced Materials* **10**, 382–385 (1998).

[164] Klett, B., Cocchi, C., Pithan, L., Kowarik, S. & Draxl, C. Polymorphism in α-sexithiophene crystals: Relative stability and transition path. *Physical Chemistry Chemical Physics* **18**, 14603–14609 (2016).

[165] Servet, B. *et al.* X-ray determination of the crystal structure and orientation of vacuum evaporated sexithiophene films. *Advanced Materials* **5**, 461–464 (1993).

[166] Nicklin, C. *et al.* Minerva: A facility to study microstructure and interface evolution in realtime under vacuum. *Review of Scientific Instruments* **88**, 103901 (2017).

[167] GmbH, C. User manual evap300 modular deposition system (2014).

[168] Als-Nielsen, J. & McMorrow, D. *Elements of modern X-ray physics* (John Wiley & Sons, 2011).

[169] Le Bail, A. *Powder diffraction: theory and practice* (Royal Society of Chemistry, 2008).

[170] Bragg, W. L. The specular reflection of x-rays. *Nature* **90**, 410 (1912).

[171] Birkholz, M. *Thin film analysis by X-ray scattering* (John Wiley & Sons, 2006).

[172] Langford, J. I. & Wilson, A. Scherrer after sixty years: a survey and some new results in the determination of crystallite size. *Journal of applied crystallography* **11**, 102–113 (1978).

[173] Rivnay, J., Mannsfeld, S. C., Miller, C. E., Salleo, A. & Toney, M. F. Quantitative determination of organic semiconductor microstructure from the molecular to device scale. *Chemical Reviews* **112**, 5488–5519 (2012).

[174] Basham, M. *et al.* Data Analysis WorkbeNch (DAWN). *Journal of Synchrotron Radiation* **22**, 853–858 (2015).

[175] Filik, J. *et al.* Processing two-dimensional X-ray diffraction and small-angle scattering data in DAWN 2. *Journal of Applied Crystallography* **50**, 959–966 (2017).

[176] Allen, F. H. *et al.* The cambridge crystallographic data centre: computer-based search, retrieval, analysis and display of information. *Acta Crystallographica Section B: Structural Crystallography and Crystal Chemistry* **35**, 2331–2339 (1979).

[177] Gražulis, S. *et al.* Crystallography Open Database (COD): an open-access collection of crystal structures and platform for world-wide collaboration. *Nucleic acids research* **40**, D420–D427 (2011).

[178] Warren, B. E. *X-ray Diffraction* (Courier Corporation, 1990).

[179] Guinier, A. *X-ray diffraction in crystals, imperfect crystals, and amorphous bodies* (Courier Corporation, 1994).

[180] Breiby, D. W., Bunk, O., Andreasen, J. W., Lemke, H. T. & Nielsen, M. M. Simulating x-ray diffraction of textured films. *Journal of Applied Crystallography* **41**, 262–271 (2008).

[181] Hailey, A. K., Hiszpanski, A. M., Smilgies, D. M. & Loo, Y. L. The Diffraction Pattern Calculator (DPC) toolkit: A user-friendly approach to unit-cell lattice

parameter identification of two-dimensional grazing-incidence wide-angle X-ray scattering data. *Journal of Applied Crystallography* **47**, 2090–2099 (2014).

[182] Fujiwara, H. *Spectroscopic ellipsometry: principles and applications* (John Wiley & Sons, 2007).

[183] Abou-Ras, D., Kirchartz, T. & Rau, U. *Advanced characterization techniques for thin film solar cells* (John Wiley & Sons, 2016).

[184] Ramamurthy, V. & Schanze, K. S. *Organic photochemistry and photophysics* (CRC Press, 2005).

[185] Balzani, V., Ceroni, P. & Juris, A. *Photochemistry and photophysics: concepts, research, applications* (John Wiley & Sons, 2014).

[186] Wenger, B. *et al.* Consolidation of the optoelectronic properties of $CH_3NH_3PbBr_3$ perovskite single crystals. *Nature Communications* **8**, 590 (2017).

[187] Ostrikov, K., Neyts, E. C. & Meyyappan, M. Plasma Nanoscience: from Nano-Solids in Plasmas to Nano-Plasmas in Solids. *Advances in Physics* **62**, 113–224 (2013). 1306.6711.

[188] Eperon, G. E. *et al.* Formamidinium lead trihalide: a broadly tunable perovskite for efficient planar heterojunction solar cells. *Energy & Environmental Science* **7**, 982–988 (2014).

[189] Santra, K. *et al.* What is the best method to fit time-resolved data? a comparison of the residual minimization and the maximum likelihood techniques as applied to experimental time-correlated, single-photon counting data. *Journal of Physical Chemistry B* **120**, 2484–2490 (2016).

[190] Wahl, M. Time-correlated single photon counting. *Technical Note* 1–14 (2014).

[191] He, B.-L., Dong, B. & Li, H.-L. Preparation and electrochemical properties of Ag-modified TiO_2 nanotube anode material for lithium–ion battery. *Electrochemistry Communications* **9**, 425–430 (2007).

[192] Li, Y. *et al.* Nitrogen-doped graphene nanosheets as cathode materials with excellent electrocatalytic activity for high capacity lithium-oxygen batteries. *Electrochemistry Communications* **18**, 12–15 (2012).

[193] Sylvester-Hvid, K. O. *et al.* Analyzing poly(3-hexyl-thiophene):1-(3-methoxy-carbonyl)propyl-1-phenyl- (6,6) C61 bulk-heterojunction solar cells by UV-visible spectroscopy and optical simulations. *Journal of Applied Physics* **102** (2007).

[194] Nečas, D. & Klapetek, P. Gwyddion: an open-source software for SPM data analysis. *Open Physics* **10** (2012).

[195] Centurioni, E. Generalized matrix method for calculation of internal light energy flux in mixed coherent and incoherent multilayers. *Appl. Opt.* **44**, 7532–7539 (2005).

[196] Wang, F., Tan, Z. & Li, Y. Solution-processable metal oxides/chelates as electrode buffer layers for efficient and stable polymer solar cells. *Energy Environ. Sci.* **8**, 1059–1091 (2015).

[197] Zhang, M. L., Irfan, Ding, H. J., Gao, Y. L. & Tang, C. W. Organic Schottky barrier photovoltaic cells based on MoO_x/C-60. *Applied Physics Letters* **96** (2010).

[198] Yang, J.-P. *et al.* Mechanism for doping induced p type C_{60} using thermally evaporated molybdenum trioxide (MoO_3) as a dopant. *Journal of Physics: Condensed Matter* **28**, 185502 (2016).

[199] Kim, D. Y., So, F. & Gao, Y. Aluminum phthalocyanine chloride/C60 organic photovoltaic cells with high open-circuit voltages. *Solar Energy Materials and Solar Cells* **93**, 1688–1691 (2009).

[200] Mutolo, K. L., Mayo, E. I., Rand, B. P., Forrest, S. R. & Thompson, M. E. Enhanced open-circuit voltage in subphthalocyanine/C60 organic photovoltaic cells. *Journal of the American Chemical Society* **128**, 8108–8109 (2006).

[201] Burlingame, Q. *et al.* Centimetre-scale electron diffusion in photoactive organic heterostructures. *Nature* **554**, 77–80 (2018).

[202] Tress, W. & Inganäs, O. Simple experimental test to distinguish extraction and injection barriers at the electrodes of (organic) solar cells with S-shaped current-voltage characteristics. *Solar Energy Materials and Solar Cells* **117**, 599–603 (2013).

[203] Tress, W., Leo, K. & Riede, M. Influence of hole-transport layers and donor materials on open-circuit voltage and shape of I-V curves of organic solar cells. *Advanced Functional Materials* **21**, 2140–2149 (2011).

[204] Tress, W., Corvers, S., Leo, K. & Riede, M. Investigation of driving forces for charge extraction in organic solar cells: Transient photocurrent measurements on solar cells showing s-shaped current-voltage characteristics. *Advanced Energy Materials* **3**, 873–880 (2013).

[205] Gommans, H., Schols, S., Kadashchuk, A., Heremans, P. & Meskers, S. C. J. Exciton diffusion length and lifetime in subphthalocyanine films. *Journal of Physical Chemistry C* **113**, 2974–2979 (2009).

[206] Pope, M. & Swenberg, C. E. *Electronic processes in organic crystals and polymers*, vol. 2 (Oxford University Press New York, 1999).

[207] Barito, A. *et al.* Universal design principles for cascade heterojunction solar cells with high fill factors and internal quantum efficiencies approaching 100%. *Advanced Energy Materials* **4**, 1–10 (2014).

[208] Huang, P.-H., Wang, Y.-H., Ke, J.-C. & Huang, C.-J. Investigation of various active layers for their performance on organic solar cells. *Materials* **9**, 667 (2016).

[209] Lorch, C. *et al.* Growth and annealing kinetics of α-sexithiophene and fullerene C60mixed films. *Journal of Applied Crystallography* **49**, 1266–1275 (2016).

[210] Macrae, C. F. *et al.* Mercury csd 2.0–new features for the visualization and investigation of crystal structures. *Journal of Applied Crystallography* **41**, 466–470 (2008).

[211] Yassar, A. *et al.* Exciton coupling effects in the absorption and photoluminescence of sexithiophene derivatives. *Journal of Physical Chemistry* **99**, 9155–9159 (1995).

[212] Horowitz, G., Valat, P., Garnier, F., Kouki, F. & Wintgens, V. Photoinduced spontaneous and stimulated emission in sexithiophene single crystals. *Optical Materials* **9**, 46–52 (1998).

[213] Meinardi, F. *et al.* Intrinsic excitonic luminescence in odd and even numbered oligothiophenes. *Physical Review Letters* **89**, 157403/1–157403/4 (2002).

[214] Periasamy, N., Danieli, R., Ruani, G., Zamboni, R. & Taliani, C. Location of the low-energy $1A_g$ state in a polythiophene oligomer by two-photon absorption spectroscopy: α-sexithienyl. *Physical Review Letters* **68**, 919–922 (1992).

[215] Nunzi, J. M., Pfeffer, N., Charra, F. & Fichou, D. Picosecond photoinduced dichroism in sexithiophene thin films. *Chemical Physics Letters* **215**, 114–119 (1993).

[216] Takahashi, Y. *et al.* Prominent charge-transfer state at α-sexithiophene/C60 interface. *Journal of the Physical Society of Japan* **82**, 1–4 (2013).

[217] Watanabe, K. *et al.* Ultrafast decay dynamics of excited and charged states in alpha- sexithienyl film as revealed by femtosecond transient absorption and picosecond fluorescence spectroscopy. *Journal of Physical Chemistry B* **101**, 1510–1519 (1997).

[218] Kahn, A., KOCH, N. & GAO, W. Energy levels of CuPc and PTCBI 1–20 (2003).

[219] Sun, L. *et al.* Layer resolved evolution of the optical properties of α-sexithiophene thin films. *Physical Chemistry Chemical Physics* **14**, 13651 (2012).

[220] Thelakkat, M., Fink, R., Haubner, F. & Schmidt, H.-W. Synthesis and properties of novel hole transport materials for electroluminescent devices. In *Macromolecular Symposia*, vol. 125, 157–164 (Wiley Online Library, 1998).

[221] Tietze, M. L., Burtone, L., Riede, M., Lüssem, B. & Leo, K. Fermi level shift and doping efficiency in p-doped small molecule organic semiconductors: a photoelectron spectroscopy and theoretical study. *Physical Review B* **86**, 035320 (2012).

[222] Yan, C. *et al.* Non-fullerene acceptors for organic solar cells. *Nature Reviews Materials* **3**, 1–19 (2018).

[223] Chen, W. & Zhang, Q. Recent progress in non-fullerene small molecule acceptors in organic solar cells (OSCs). *Journal of Materials Chemistry C* **5**, 1275–1302 (2017).

[224] Yuan, J. *et al.* Single-junction organic solar cell with over 15% efficiency using fused-ring acceptor with electron-deficient core. *Joule* **3**, 1140–1151 (2019).

[225] Meng, L. *et al.* Organic and solution-processed tandem solar cells with 17.3% efficiency. *Science* **361**, 1094–1098 (2018).